UNIVERSITY OF MONS

Faculté de Médecine, Pharmacie et Sciences Biomédicales

Laboratoire de Neurosciences

Facilitating Vision Restoration: Brain Plasticity After Monocular Vision Loss and Multidisciplinary Interventions

Antonio Caballero Tapia

Dissertation submitted in fulfilment of the requirements for the degree of Doctor in Biomedical and Pharmaceutical Sciences.

Thesis supervisor	Prof. Laurence Ris	University of Mons, Belgium
Co-supervisor	Prof. Lut Arckens	Katholieke Universiteit Leuven, Belgium
Chair of the jury	Prof. Giovanni Briganti	University of Mons, Belgium
Secretary of the jury	Dr. Agnès Villers	University of Mons, Belgium
Reviewers	Dr. Asli Ayaz	NERF-VIB, Flanders, Belgium
	Prof. Ana Cebolla	Université libre de Bruxelles, Belgium
	Prof. Javier Márquez Ruiz	Universidad Pablo de Olavide, Spain

Academic year 2025 - 2026

UNIVERSITY OF MONS

Faculté de Médecine, Pharmacie et Sciences Biomédicales

Laboratoire de Neurosciences

Facilitating Vision Restoration: Brain Plasticity After Monocular Vision Loss and Multidisciplinary Interventions

---

Antonio Caballero Tapia

Dissertation submitted in fulfilment of the requirements for the degree of Doctor in Biomedical and Pharmaceutical Sciences.

Thesis supervisor	Prof. Laurence Ris	University of Mons, Belgium
Co-supervisor	Prof. Lut Arckens	Katholieke Universiteit Leuven, Belgium
Chair of the jury	Prof. Giovanni Briganti	University of Mons, Belgium
Secretary of the jury	Dr. Agnès Villers	University of Mons, Belgium
Reviewers	Dr. Asli Ayaz	NERF-VIB, Flanders, Belgium
	Prof. Ana Cebolla	Université libre de Bruxelles, Belgium
	Prof. Javier Márquez Ruiz	Universidad Pablo de Olavide, Spain

Academic year 2025 - 2026

Acknowledgements

I would like to express my deepest gratitude to Professor Laurence Ris, for her constant support, dedication, and trust throughout these years. Thank you for guiding me from my very first steps in research through to the completion of this thesis, for your patience, your advice, and for believing in me even during the most challenging moments. Your availability, scientific rigor, and ability to guide me with both clarity and generosity have been fundamental to the successful completion of this work. I feel fortunate to have carried out such an important stage of my career under your supervision, in an environment where I have always felt respected, supported, and motivated to keep learning. I will always be grateful for welcoming me into your laboratory and giving me the opportunity to join a Belgian doctoral program as a foreign student. Your trust allowed me to embrace this challenge away from my home country and to grow both professionally and personally. Thank you for opening the doors of your lab to me and for giving me the opportunity to grow as both a researcher and as a person.

I would like to express my most sincere and heartfelt gratitude to Professor Guy Cheron. Over the past years, I have had the privilege of learning from his vast expertise and knowledge in the field of neuroelectrophysiological recordings. Thanks to his dedication, patience, and generosity, I have been able to train in every practical and theoretical aspect of this discipline: from handling the equipment, machines, and electrodes, to working with animals, acquiring and interpreting recordings, and designing experiments. Everything I know today in this area, I owe in large part to his teaching, his guidance, and his remarkable ability to share his passion for this field of research. However, my gratitude goes far beyond the academic sphere. Throughout these years, Guy has not only been a scientific mentor but also an invaluable personal support. During the most challenging moments I faced throughout my time in Belgium, he was always there to help me, offering his support, his understanding, and often standing up for me when I needed it the most. Thanks to him, I was able to overcome difficulties that extended far beyond the laboratory, and I always felt supported, respected, and valued. I am deeply grateful for all that I have learned under his guidance, for the trust he placed in me, and for the sincere friendship we have built over time. It has truly been a privilege to count on his mentorship and his support, both professionally and personally.

I would like to extend my deepest thanks to Dominique Ristori, whom I came to know thanks to Guy, whose constant support was likewise decisive for the completion of this thesis. Thanks to her, I benefited from the analysis of event-related spectral perturbations and inter-trial coherence across frequency bands using EEGLAB, which underpins an essential part of my results. I know

she devoted countless hours at the screen to obtain these analyses and to adapt the software to animal recording data, an effort for which I am profoundly grateful. Her rigour in preparing and validating the procedures, as well as her readiness to accompany me as the results emerged, were crucial in enabling steady, confident progress. Beyond the academic sphere, her support and timely counsel made a difference when I needed them most; her personal warmth, generosity, and hospitality consolidated a relationship of trust and friendship that transcends the scientific realm.

I would also like to express my sincere gratitude to Professor Lut Arckens for her involvement, generosity, and availability throughout these years. Although we belonged to different universities, her engagement with my work has been constant and fundamental, both in guiding me scientifically and in enriching my ideas throughout my PhD journey. Thanks to her advice, her suggestions for improvement, and the many discussions we have shared, I have been able to further develop my project and strengthen my critical thinking. Her feedback, always precise and constructive, has been essential in shaping and deepening many of the results presented in this thesis. I am particularly grateful for her kindness in integrating me into her group, for giving me the opportunity to present my work during their meetings, and for introducing me to so many researchers with whom I have had the chance to exchange ideas and discuss my project. Her support and contributions have been a constant source of motivation. Being able to count on her experience, her vision, and her network has undoubtedly been a privilege that has positively shaped this important stage of my career.

I would also like to extend my heartfelt thanks to my lab colleagues Agnès Villers, Aurore Latragna, and Damiana Leo. Since my arrival, Agnès became a constant point of reference: she guided me patiently through the laboratory procedures, shared her experience with admirable clarity, and did not hesitate to devote extra time to resolving doubts, reviewing protocols, and helping me to plan each stage of the work. Her sense of rigour, both in the preparation and in the execution and documentation of the experiments, her attention to detail, and her ability to detect potential errors in good time were decisive in raising the quality of this thesis. I am also grateful for the numerous discussions of results, her critical reading of drafts, presentations, and figures, and her readiness to help at times of pressure, when the urgent threatened to eclipse the important. On a personal level, her closeness and warmth made my settling-in far easier; with her support, Mons and the laboratory quickly became a welcoming place. From her I learned not only procedures and good practice, but a way of working grounded in generosity, intellectual honesty, and collegiality. I feel fortunate to have built with Agnès a sincere friendship that goes beyond the strictly academic. Although Aurore and Damiana left the lab a few years ago, I would still like to acknowledge the significant help they gave me during the time we worked together. Thanks to them, my first steps in this journey were much easier, and I will always have very fond memories of their support, their kindness, and their valuable advice.

I would like to dedicate a few words of special thanks to Thomas Peteau, our lab technician, for all the help he has given me throughout these years. Beyond his technical expertise, which has been invaluable in solving countless practical issues in the daily life of the lab, I am especially grateful for his kindness, his approachability, and the friendship we have also built outside of work. Thank you for your support, for the good moments we have shared, and for always being ready to lend a hand, both professionally and personally.

Finally, I would like to express my deepest gratitude to Les Amis des Aveugles et Malvoyants, a Belgian non-profit association with over 140 years of history, dedicated to supporting the autonomy, well-being, and inclusion of people with visual impairments. Thanks to their long-standing commitment in areas such as guide dogs, education, functional rehabilitation, and research programs in health and accessibility, they have made the completion of this PhD possible. Their generous financial support has been fundamental in covering the costs of this project and in supporting scientific activities such as conferences, international exchanges, and advanced training. I am truly grateful for their trust and for making it possible for this work to be carried out in an environment that has fostered both scientific and personal growth.

I would like to dedicate these final words to those who have undoubtedly been my greatest support throughout this journey: my family and my partner. Without you, none of this would have been possible.

To my sister, Ana, who was still a child when I started this PhD and is now a young woman beginning her university studies, I want to thank you for your support, your affection, and the closeness you have shown me despite the distance. I am sorry for not being more present during these years as you grew and found your own path; it pains me to have missed so many important moments in your life. But I want you to know that I have always carried with me an immense pride in seeing you become the person you are today. Your maturity, courage, and generosity inspire me more than you can imagine.

To my father, Antonio, to whom I owe not only the opportunity to pursue my education but also the values and understanding of the world that have brought me here. You have carried on your shoulders the weight of the effort that allowed me to dedicate myself to what I have always dreamed of. Through your example, you have taught me the true meaning of hard work, perseverance, commitment, and, above all, honesty and the value of one's word. There is no greater lesson than that. I know well that this thesis is also, in many ways, yours.

To my mother, Yolanda, who has always been my source of inspiration, my role model, and my refuge. Since I was a child, you have taught me to look at life with curiosity, freedom, and without fear of dreaming. You never clipped my wings; on the contrary, you always encouraged me to fly even further. You helped me build my dreams, to pursue them, and never to give up. Despite the

thousands of kilometers that separated us, you always found a way to stay close. Whenever you had the chance, you travelled all the way to Mons to be with me, to show me that even from afar, a mother never stops caring for her child. Thank you for your unconditional love, your strength, and for teaching me to be who I am.

And finally, to Ana Belén, the love of my life, my companion on this journey. Thank you for your courage in embarking on this adventure by my side, for leaving everything behind in Spain to come with me, without knowing the language, without certainties, but with the hope and trust that have supported every step we have taken together. It has not been easy. We have faced difficult moments, we have overcome many challenges, but we have also grown, learned, and shared a life that has taught me that there is no greater fortune than having you by my side. There are not enough pages in this thesis to express what you mean to me. Thank you for your love, your patience, your unwavering support, and for always being my best friend.

Abstract

Monocular vision loss induces a profound reorganisation of the primary visual cortex (V1), yet it remains unclear to what extent such plasticity can be modulated with minimally invasive clinical interventions. This thesis evaluates whether transcranial direct current stimulation (tDCS), cholinergic enhancement with donepezil, and a structured visual stimulation protocol modify V1 plasticity after monocular enucleation in rodents. The work is articulated in a sequence of objectives that include (i) the multimodal physiological characterisation of V1 under normal conditions, (ii) systematic comparison with the post-enucleation state, and (iii) testing each intervention separately and in combination, using local field potential (LFP) and unit activity recordings in awake animals, with spectral analysis (power and phase coherence) using the maxima of ERSP (Event-Related Spectral Perturbation) and ITC (Inter-Trial Coherence) as mesoscopic biomarkers of plasticity. Electrode placement in the binocular and monocular zones of V1 was validated; standardised visual, auditory, and somatosensory stimulations were applied in control animals, enucleated animals without treatment, and animals treated with epicranial tDCS, donepezil, and the combination for 15 days synchronised with visual training.

In the reference physiology, V1 acted as a multisensory node with brief latencies and an oscillatory profile dominated by beta, accompanied by robust inter-trial phase coherence. Following enucleation, event-related potential components did not change markedly, but a spectral reconfiguration was observed: power and phase coherence to visual stimuli decreased, and increased selectively to auditory and somatosensory stimuli, with beta (and, to a lesser extent, delta) as a sensitive axis of the intermodal readjustment.

Each treatment generated a distinct neurophysiological profile. tDCS selectively increased alpha power during auditory stimulation and attenuated the somatosensory response across the spectrum, although by itself it did not restore the lost visual organisation. Donepezil showed an overall depressant effect on power and coherence in V1 with the protocol applied. The tDCS + donepezil combination did not act as a non-specific amplifier: it tended to “focus” plasticity, with indications of power/coherence increase in theta during visual stimulation and of a reduction in auditory-somatosensory interference, suggesting a bias from cross-modal plasticity towards visual intramodality for the residual visual information.

Taken together, plasticity after monocular vision loss is not epiphenomenal but steerable. Spectral biomarkers (beta for non-visual inputs and theta for visual inputs), together with temporal metrics of coherence, offer operational principles for designing and monitoring rehabilitation and visual restoration strategies that combine electrical neuromodulation and cholinergic potentiation.

Abbreviations

A2E	N-retinylidene-N-retinyl-ethanolamine
AAV	Adeno-associated virus
ABCA4	ATP binding cassette subfamily A member 4
ACC	Anterior Cingulate Cortex
AD	Alzheimer's disease
ADA	American Diabetes Association
AES	Anterior ectosylvian cortex/sulcus
AMD	Age related macular degeneration
AnG	Angular gyrus
AP	Anteroposterior
AVT	Audiovisual training
BDI	Beck Depression Inventory
BOLD	Blood-oxygen-level dependent
CBF	Cerebral blood flow
CFT	Central foveal thickness
CI	Confidence interval
CSD	Current source density
CT	Corticothalamic
DALYs	Disability-adjusted life years
DC	Direct current
DCCT	Diabetes Control and Complications Trial
DFC	Dorsolateral prefrontal cortex
DiL	1, I'-dioctadecyl-3.3,3',3'-tetramethyl- indocarbocyanine perchlorate
dLGN	Dorsal lateral geniculate nucleus
DPZ	Donepezil (Sigma-Aldrich, D6821-10MG)
DMO	Diabetic macular oedema
DNPZ	Donepezil
DR	Diabetic retinopathy

DRSS	Diabetic Retinopathy Severity Scale
DTI	Diffusion tensor imaging
dTRD	Diabetic tractional retinal detachment
EEG	Electroencephalogram or Electroencephalography
EQ-5D	EuroQol 5-dimension questionnaire
ERG	Electroretinography
ERP	Event-related potential
ERSP	Event-related spectral perturbation
ETDRS	Early treatment diabetic retinopathy study
fMRI	Functional magnetic resonance imaging
GA	Geographic atrophy
GBD	Global Burden of Disease
GHQ-12	General Health Questionnaire-12
HbA1c	Hemoglobin A1c (glycated hemoglobin)
HRQoL	Health-related quality of life
IMT	Implantable miniature telescope
ITC	Inter-trial coherence
LGN	Lateral geniculate nucleus
LFP	Local field potential
MD	Mean deviation
MEG	Magnetoencephalography
MMN	Mismatch negativity
MSVI	Moderate-to-severe vision impairment
MTG	Middle temporal gyrus
MUA	Multi-unit activity
NPDR	Non-proliferative diabetic retinopathy
OCT	Optical coherence tomography
PCV	Polypoidal choroidal vasculopathy
PD	Pneumatic displacement
PDR	Proliferative diabetic retinopathy

PET	Positron emission tomography
PPV	Pars plana vitrectomy
PRIMA	Photovoltaic retinal implant (subretinal)
PSTH	Peri-stimulus time histogram
RIDE	Phase III randomized trial of ranibizumab for DME/DMO (NCT00473382)
RISE	Phase III randomized trial of ranibizumab for DME/DMO (NCT00473330)
RNA	Ribonucleic acid
RP	Retinitis pigmentosa
RPE	Retinal pigment epithelium
RPE65	Retinal pigment epithelium-specific 65 kDa protein (gene)
RPGR	Retinitis pigmentosa GTPase regulator (gene)
RR	Risk ratio
s	Seconds
sFlt-1	Soluble VEGF receptor-1 (VEGFR-1)
SD	Standard deviation
SE	Standard error
SMH	Submacular hemorrhage
SUA	Single-unit activity
t	Time
tDCS	Transcranial direct current stimulation
UKPDS	UK Prospective Diabetes Study
URE	Uncorrected refractive error
VA	Visual acuity
VEGF	Vascular endothelial growth factor
VEGF-A	Vascular endothelial growth factor A
VISTA	Phase III aflibercept trial in DMO
VIVID	Phase III aflibercept trial in DMO
V1	Primary visual cortex
VWFA	Visual word form area
WDCR	Whole-dataset confound regression

WHO	World Health Organization
YLDs	Years lived with disability
eLFP	Evoked local field potential
ms	Milliseconds
p	p-value
tACS	Transcranial alternating current stimulation
tES	Transcranial electrical stimulation
µA	Microampere
µV	Microvolts

Table of Contents


Introduction

Introduction

1. Visual Impairment: Clinical Context and Therapeutic Challenges

1.1. Global prevalence of vision loss

Visual impairment represents a major public health concern worldwide, affecting individuals across all age groups and socioeconomic backgrounds. According to the World Report on Vision by the World Health Organization (WHO), over 2.2 billion people globally live with some form of visual impairment, with at least 1 billion of these cases being preventable or unaddressed due to lack of access to basic care such as refractive correction or cataract surgery (World Health Organization, 2019). The International Agency for the Prevention of Blindness (IAPB) further estimates that as of 2020, approximately 43 million people are blind, 295 million suffer from moderate-to-severe vision impairment (MSVI), and over 510 million live with uncorrected presbyopia, a condition especially prevalent in individuals over 40 years of age (R. Bourne et al., 2020; World Health Organization, 2019) (**Figure 1**).

Trends over recent decades reveal a significant increase in the global burden of vision loss. Between 1990 and 2019, the number of people affected by visual impairment increased by 91.46%, and in 2019 alone, vision loss was responsible for approximately 12.6 million disability-adjusted life years (DALYs), the vast majority of which were years lived with disability (YLDs). This upward trend is largely driven by population growth and aging, with the highest prevalence observed in individuals aged 50 years and older. Between 1990 and 2021, DALYs due to blindness and vision loss more than doubled, underscoring a persistent and growing global challenge (Chen et al., 2024; Que et al., 2025).

Among the leading causes of vision loss worldwide are uncorrected refractive errors (URE), age-related macular degeneration (AMD), glaucoma, and diabetic retinopathy (DR), all conditions that predominantly affect older adults.

In 2020, an estimated 3.7 million people were blind and 157 million had moderate to severe visual impairment due to URE. Although the absolute number of cases increased since 2000, the age-standardised prevalence of blindness from URE declined by 30.5%, reflecting improvements in access to vision correction services. A persistent gender disparity was also observed, with a female-to-male ratio of 1.05:1 for blindness and 1.08:1 for MSVI, indicating a greater impact on women (Vision Loss Expert Group of the Global Burden of Disease Study, Little, et al., 2024).

In 2020, age-related macular degeneration caused blindness in 1.85 million people and MSVI in 6.23 million. The prevalence of AMD increases markedly with age, particularly after the age of 70, and is virtually absent in individuals under 50. These figures are influenced by regional burdens, which were concentrated in high-income regions. Although, once again, the absolute number of cases increased, the age-standardised prevalence declined slightly between 2000 and 2020, likely due to improvements in screening and therapeutic interventions (Vision Loss Expert Group of the Global Burden of Disease Study, Furtado, et al., 2024).

In 2020, an estimated 1.07 million people were blind and 3.28 million had moderate to severe visual impairment due to diabetic retinopathy, accounting for 2.5% of all global blindness. DR disproportionately affected women across most super-regions, with the highest age-standardised prevalences observed in Latin America and the Caribbean, as well as in North Africa and the Middle East. Between 2000 and 2020, there was a notable increase in blindness from DR among women, particularly in South Asia and Southeast Asia (Vision Loss Expert Group of the Global Burden of Disease Study, Curran, et al., 2024).

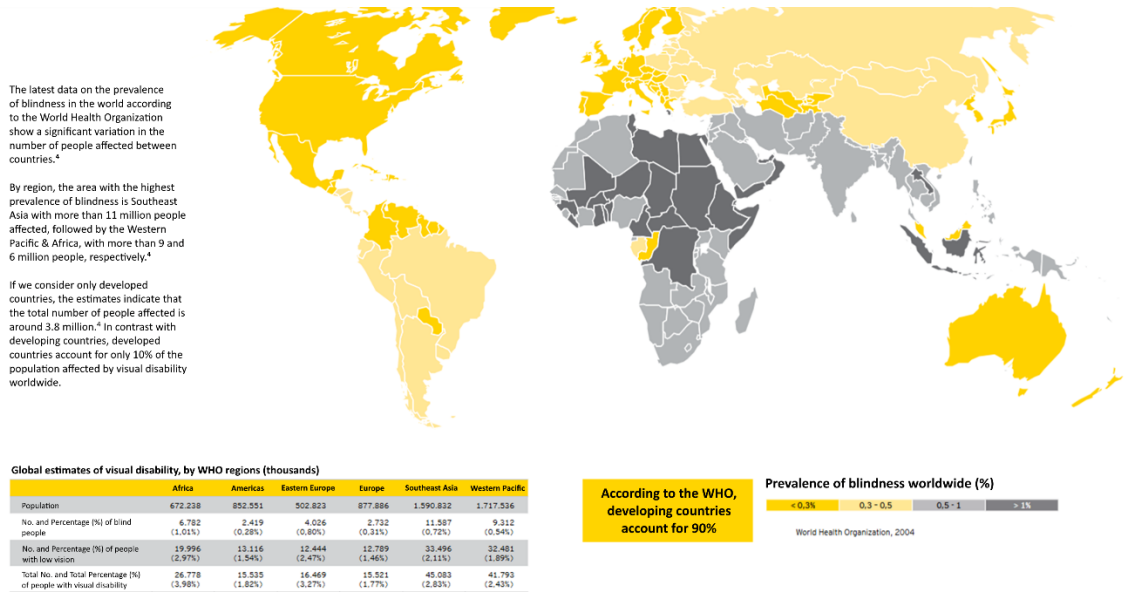

Figure 1. Global prevalence of blindness (%) by country and WHO regional estimates of visual impairment. The map classifies prevalence into four categories: <0.3%, 0.3-0.5%, 0.5-1%, and >1% (darker shades indicate higher prevalence). The inset summarises that ≈90% of people with visual impairment live in developing countries. The lower table details, by WHO region, the population and the number/percentage of people who are blind and those with low vision. Source: (Gómez-Ulla de Irazazábal & Ondategui-Parra, 2012)

Finally, another meta-analysis identified glaucoma as the leading global cause of irreversible blindness, with 3.61 million people blind and 4.14 million with MSVI in 2020. The condition primarily affects individuals aged 60 and over, with age-standardised prevalence particularly high in sub-Saharan Africa and Southeast Asia. The study also noted that, although the total number of cases increased, age-standardised rates declined slightly between 2000 and 2020, reflecting improved awareness and detection. As glaucoma is often asymptomatic until advanced stages, this highlights the need for early diagnostic strategies targeting older populations (Vision Loss Expert Group of the Global Burden of Disease Study, Bourne, et al., 2024).

Together, these data highlight the magnitude, demographic concentration, and socioeconomic inequities of visual impairment, reinforcing the need for more inclusive strategies to prevent avoidable blindness and improve global vision health.

1.2. Vision loss in Europe

Vision loss represents a growing challenge in Europe, particularly in the context of an ageing population. Although European countries generally exhibit lower prevalence rates than the global average, the absolute number of affected individuals has steadily increased over recent decades. In 2020, it was estimated that approximately 2.8 million people were blind and 29 million had MSVI in Europe and other high-income countries, accounting for around 10% of the global burden. This trend reflects not only greater longevity but also the persistence of structural inequalities in access to ophthalmic services.

Marked differences exist between European subregions. Eastern Europe continues to show higher rates of blindness and visual impairment than Central and Western Europe, although it has made significant progress in recent decades. In contrast, some high-income regions such as North America have experienced recent increases in age-standardised prevalence, suggesting that progress in eye health is not necessarily irreversible. Meanwhile, Western Europe maintains some of the most favourable indicators, though it too faces the challenges associated with an ageing population.

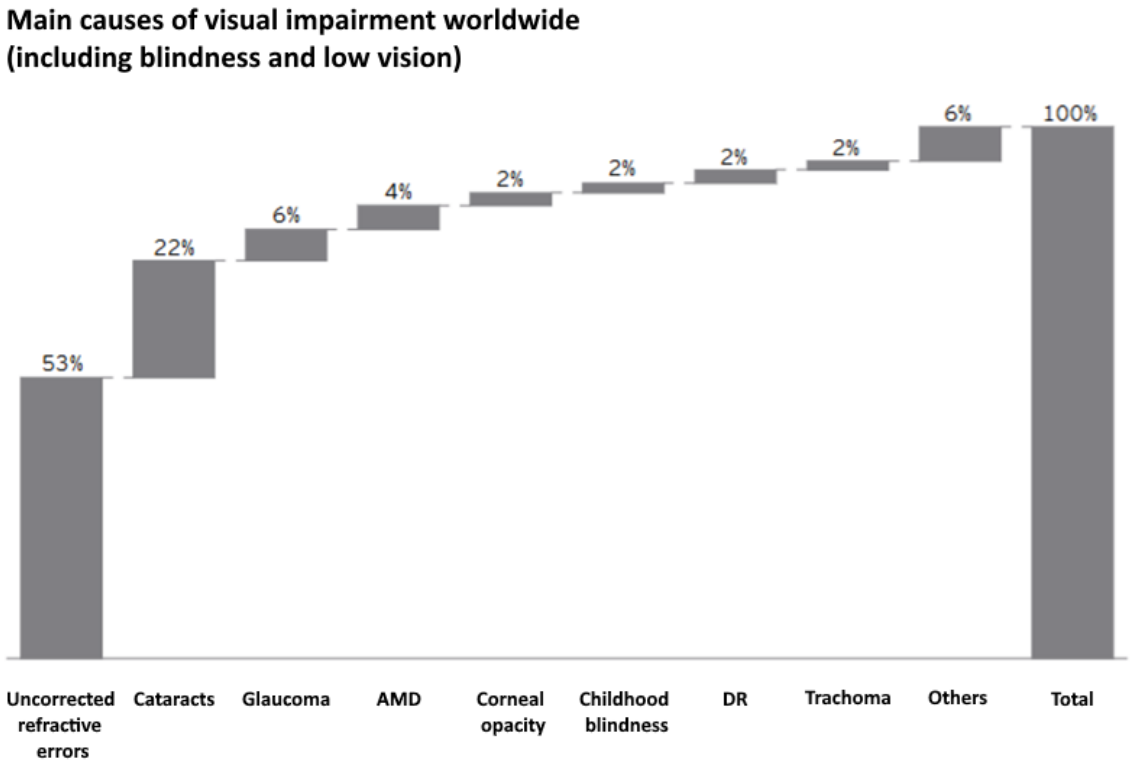

Figure 2. Leading causes of visual impairment worldwide (including blindness and low vision) and their relative contribution. The "waterfall" chart shows the percentage attributable to each cause up to the global total of 100%: uncorrected refractive errors (53%), cataract (22%), glaucoma (6%), AMD-age-related macular degeneration (4%), corneal opacity (2%), childhood blindness (2%), DR-diabetic retinopathy (2%), trachoma (2%), and other causes (6%). Source: The Global Economic Cost of Visual Impairment (2010), based on Resnikoff et al., 2008.

The most common causes of vision loss in Europe include uncorrected refractive errors, age-related macular degeneration, glaucoma, and diabetic retinopathy (**Figure 2**). Most of these conditions disproportionately affect older individuals, and in many cases, such as presbyopia or refractive errors, they could be addressed through simple, accessible interventions. However, barriers to early diagnosis and equitable coverage of basic eye care services persist, particularly among women and in areas with limited healthcare resources.

While substantial progress has been made in reducing age-standardised prevalence, the overall burden of vision loss in Europe remains far from resolved. Current trends highlight the need to sustain and strengthen strategies for prevention, early detection, and treatment, with particular focus on vulnerable populations and the persistent regional disparities across the continent (Vision Loss Expert Group of the Global Burden of Disease Study & the GBD 2019 Blindness and Vision Impairment Collaborators, 2025).

There are also less prevalent inherited diseases that contribute significantly to visual deterioration. One example is Stargardt disease (STGD1), a juvenile-onset macular dystrophy of genetic origin, with an estimated prevalence ranging from 1 in 8,000 to 1 in 10,000 individuals. It affects both sexes equally and typically manifests in childhood or adolescence, although adult-onset cases have also been reported. The disease progresses to central vision loss, while peripheral vision is generally preserved. Despite its lower absolute impact, its early onset poses additional challenges in terms of educational, occupational, and social inclusion (Orphanet, 2024).

In absolute terms, it is estimated that between 26 and 30 million people in Europe live with some form of visual impairment. This includes approximately 2.55 million individuals who are blind and 23.8 million with low vision, meaning that roughly 1 in every 30 Europeans is affected by vision loss. These numbers are expected to increase due to population ageing and the rising prevalence of chronic eye diseases (Facts and figures | European Blind Union).

Notably, longitudinal data reflect a sustained decline in the overall prevalence of vision loss in Europe over recent decades. Between 1990 and 2015, the age-standardised prevalence of blindness in high-income European countries decreased from 0.26% to 0.15%, while MSVI declined from 1.74% to 1.27%. This progress represents a significant improvement in population eye health across the region, largely driven by advances in prevention, early diagnosis, and the treatment of leading causes of blindness.

Among the most impactful developments has been the refinement of cataract surgery techniques, which significantly reduced the burden of what had long been the most common cause of blindness in the region. Expanded access to specialised ophthalmic services has further supported this trend. At the same time, screening programmes for diabetic retinopathy have facilitated earlier detection of diabetes-related visual complications, particularly in populations where diabetes is becoming more prevalent. Additionally, improved clinical management of AMD, through anti-angiogenic therapies and systematic follow-up, has contributed to the stabilisation or slowing of visual decline in many patients.

Despite these notable gains, the burden of vision loss in Europe remains a pressing public health concern. Ongoing demographic shifts, particularly population ageing, are expected to increase the number of people affected by chronic eye conditions. Furthermore, persistent regional and gender-based disparities in access to basic eye care services continue to hinder progress towards equitable visual health outcomes. Sustained investment in prevention, early detection, and treatment, particularly among vulnerable groups, will be essential to consolidating the advances made and addressing the unmet needs that remain across the continent (R. R. A. Bourne et al., 2018).

In Belgium, blindness and visual impairment represent a significant health and social issue, affecting both personal autonomy and professional inclusion. It is estimated that, on average, there are 1.4 blind individuals per 1,000 inhabitants. However, this does not account for people with low vision, whose prevalence is presumed to be much higher but remains difficult to quantify due to the lack of accurate official data. This statistical limitation highlights the partial invisibility of this population and underscores the need for improved epidemiological monitoring.

The demographic profile of blind individuals in Belgium is clearly age-related: approximately 65% are over the age of 60, reflecting the strong link between ageing and vision loss. This has important implications not only for healthcare but also for labour market participation, the provision of social support, and the design of accessible public policies.

Despite the development of assistive technologies and a legal framework supportive of inclusion, people with visual impairments in Belgium continue to face major obstacles in accessing and retaining employment. Key challenges include reading written information, navigating the physical workspace, and confronting prejudice or a lack of awareness among employers. Nonetheless, the country benefits from an active and specialised support network which provides counselling services, workplace adaptations, and financial support for both employees and employers.

There are also successful examples of labour market integration in sectors such as banking, call centres, human resources, logistics, and information technology. These cases have been made possible using assistive technologies such as video magnifiers, screen enlargement software, screen readers, braille displays, and other spatial and organisational adjustments. They demonstrate that blindness, when accompanied by appropriate tools, does not constitute an insurmountable barrier to employment but rather presents a technical and organisational challenge that can be effectively addressed (Ligue Braille *et al.*, 2020).

1.3. Life with vision loss

Visual acuity

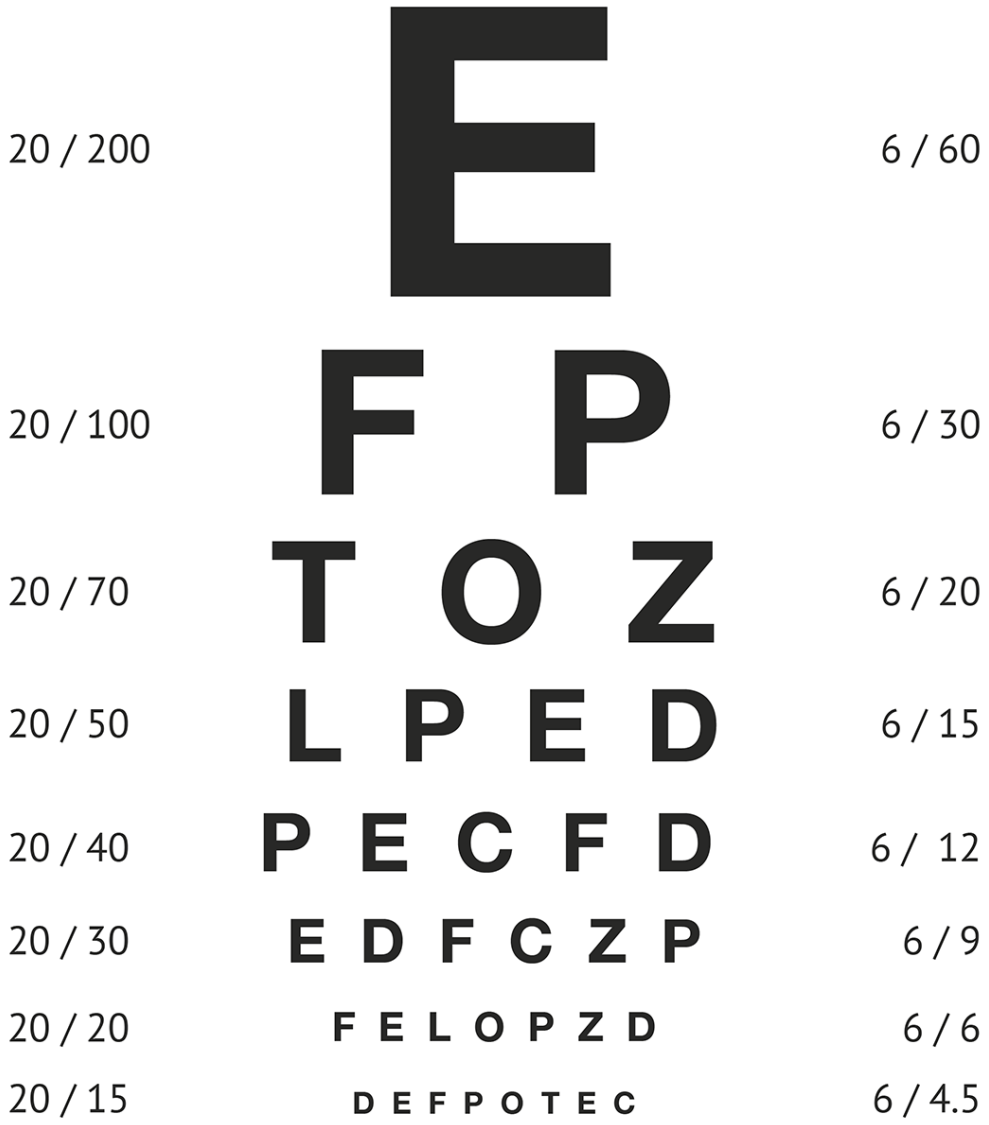

Figure 3. Snellen optotype for the assessment of visual acuity. The letters decrease in size on each line. Acuity is recorded as a fraction 20/x (left column) or 6/x (right column), where the numerator is the test distance (20 feet ≈ 6 m) and the denominator indicates the smallest line correctly identified. 20/20 (6/6) corresponds to vision considered normal; higher values (e.g., 20/40 or 6/12) indicate lower acuity; 20/200 (6/60) is used as a threshold for legal blindness in several countries. Used in screening and clinical follow-up. Source: https://medschool.co/signs/reduced-visual-acuity

Visual acuity is a measure of the eye's ability to resolve fine detail and is commonly expressed using the Snellen notation, where the numerator indicates the testing distance and the denominator represents the distance at which a person with normal vision can discern the same optotype (**Figure 3**). For example, a visual acuity of 5/200 means that what a person with normal sight can identify at 200 feet (≈60 meters) must be brought to 5 feet (≈1.5 meters) for the tested individual to see it with the same clarity. This level of vision corresponds to profound visual impairment and

meets the U.S. criteria for legal blindness (≤20/200 in the better-seeing eye) (Holladay & FACS MSEE, 2004; Lennie & Van Hemel, 2002).

Vision loss, even at moderate levels, has a significant and well-documented impact on quality of life, particularly in areas such as functional autonomy, mental health, and social integration. Numerous studies have shown that both visual impairment itself and the underlying ocular diseases contribute to an overall decline in physical and emotional well-being. This impact is not limited to older adults; it also affects adolescents and young adults. For instance, a recent global study on the burden of uncorrected refractive errors estimated that more than 157 million individuals aged 15 to 49 live with vision loss due to URE, most without adequate correction. This negatively affects vision-related quality of life, access to education, and work capacity. The study emphasises that even mild levels of visual impairment are associated with functional difficulties, anxiety, social isolation, and increased dependence, particularly during formative and economically productive stages of life (Assi et al., 2021).

A population-based study conducted in Finland using data from 2000 and 2011 examined the relationship between chronic eye diseases (including glaucoma, cataracts, and retinal degeneration), loss of visual acuity, and health-related quality of life (HRQoL), as well as their impact on mental health. Among the conditions studied, retinal degeneration was associated with the greatest decline in HRQoL, while untreated cataracts and glaucoma had a more moderate impact (**Figure 4**).

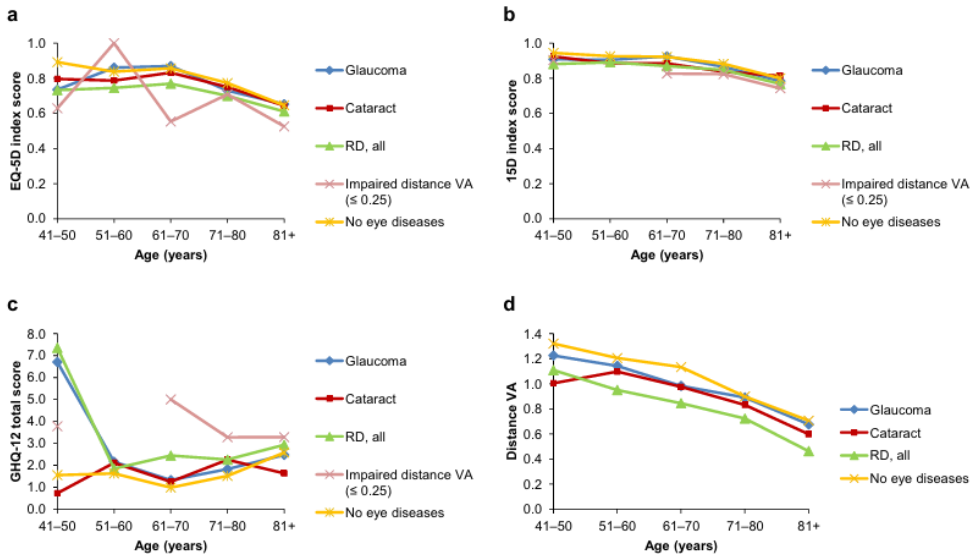

Figure 4 illustrates the relationship between age, eye diseases, and quality of life using four key indicators. Visual acuity (VA) measures the ability to see clearly; values equal to or below 0.25 indicate significant vision loss. The EQ-5D and 15D are standardised indices of health-related quality of life, with lower scores

reflecting poorer overall health status. The GHQ-12, meanwhile, assesses psychological distress, with higher scores indicating worse mental health.

Panels (a) and (b) show that quality of life declines with age and is significantly lower among individuals with retinal degeneration or visual impairment. Panel (c) indicates that those with low vision report higher levels of psychological distress, particularly in the 61-70 age group. Finally, panel (d) demonstrates that visual acuity progressively worsens with age and is lowest among patients with eye diseases, especially those with retinal degeneration.

Taken together, the data suggest that functional vision loss has a greater impact on quality of life and mental health than the mere diagnosis of an ocular condition (Purola et al., 2021).

Using standardised assessment tools such as the EQ-5D, 15D, Beck Depression Inventory (BDI), and General Health Questionnaire (GHQ-12), the study found that individuals with vision loss reported lower quality of life and higher levels of psychological distress compared to those with preserved vision (Purola et al., 2021).

Recent studies have highlighted the strong association between visual impairment and mental health in both adults and older individuals, underscoring the need for a comprehensive clinical approach that addresses not only functional but also emotional aspects. On the one hand, evidence shows that a substantial proportion of individuals with legal blindness experience depressive symptoms and varying degrees of dependence in activities of daily living. This suggests that the loss of visual autonomy has a direct impact on psychological well-being (Osaba et al., 2019). On the other hand, qualitative research has shown that many individuals with visual impairments face significant barriers in recognising or expressing symptoms of anxiety or depression. These difficulties are often linked to stigma, a lack of accessible information, and limited initiative on the part of healthcare professionals to address mental health concerns (Van Munster et al., 2021).

Global initiatives focused on fall prevention, such as those proposed by the international group referenced in Montero et al. 2021, highlight the importance of personalised clinical strategies that integrate functional, cognitive, and psychological factors, particularly in older adults. These recommendations advocate for a multidisciplinary, person-centred approach based on the P4 model (personalisation, prediction, prevention, and participation), which emphasises individualised risk assessment, shared decision-making, and the tailoring of interventions to each patient's specific needs, preferences, and living environment.

Cataract surgery has been associated with a significant reduction in long-term mortality risk among the Medicare population. The protective effect was more pronounced in older patients, women, and individuals with a moderate burden of systemic disease or more severe cataracts. These findings support the hypothesis that the benefits of cataract surgery may extend beyond

visual improvement, positively influencing overall functioning and survival (Tseng et al., 2016). Vision loss in older adults is associated with an increased risk of injury-related accidents, particularly falls. This relationship is especially significant when visual deterioration affects central or peripheral vision, and even moderate levels of impairment are clearly linked to a higher risk of injury. However, individuals with severe visual impairment may not exhibit as elevated a risk, possibly due to voluntary mobility restrictions or more cautious behaviour that reduces their exposure to hazardous situations (Kulmala et al., 2008; Patino et al., 2010).

Visual impairment has been associated with an increased risk of mortality, both directly and indirectly. In a longitudinal study involving over 100,000 adults, vision loss was not found to be statistically significantly associated with suicide; however, an indirect effect was identified through poorer self-reported health and a higher burden of medical comorbidities. This suggests that visual impairment may act as a cumulative vulnerability factor (Lam, 2008). Another study found that reduced visual acuity was linked to an increased risk of all-cause mortality, an effect mediated by functional disability in activities of daily living. These findings underscore that vision loss not only compromises quality of life but may also exacerbate general frailty, thereby increasing the risk of fatal outcomes (Christ et al., 2014).

Visual impairment is associated with a higher prevalence and faster progression of cognitive decline in older adults. The coexistence of visual and cognitive problems in this population is more common than many other recognised neurological conditions. In particular, individuals with age-related macular degeneration show higher rates of cognitive impairment, poorer performance on memory and language tests, and an increased risk of dementia. Although no clear genetic link has been identified between this ocular disease and cognitive decline, a significant functional correlation does exist. In children, visual impairment is often present alongside developmental disorders such as cerebral palsy or Down syndrome, making it difficult to isolate its direct impact on cognitive or academic performance. However, some studies suggest that children with vision loss tend to perform worse on intellectual assessments, particularly in cases of unrecognised or untreated comorbidities. Although a link between vision and cognition has been established, the mechanisms underlying this association remain unclear. Several hypotheses have been proposed, including the negative impact of visual deficits on cognitive stimulation, neuroplastic changes in the brain triggered by sensory loss, and shared genetic, medical, or environmental factors that affect both the eye and the brain. Socioeconomic status and lifestyle factors may also act as confounding variables (Welp et al., 2016).

Vision loss entails a considerable economic burden for both affected individuals and society as a whole. In Portugal, it has been estimated that people with visual impairments generate annual productivity losses exceeding €1.5 million, with reduced labour force participation identified as

the primary contributing factor. In addition, younger age, higher educational attainment, and better quality of life were associated with higher employment rates. Although greater severity of vision loss showed a negative trend in relation to employability, this association did not reach statistical significance in the multivariate analysis (Marques et al., 2019). A study conducted in Germany estimated a total annual cost of approximately €49.6 billion associated with blindness and visual impairment, considering not only direct medical expenses but also indirect costs such as productivity loss and informal care provided by family members. The magnitude of these costs increased significantly with the severity of visual impairment. These findings underscore the substantial economic impact of vision loss from a societal perspective (Chuvarayan et al., 2020).

Beyond direct economic impact and measurable productivity losses, visual impairment also significantly affects job quality, employment stability, and professional well-being among those affected. According to data collected across 12 European countries, individuals with reduced vision consistently report lower levels of job satisfaction, fewer opportunities for promotion and learning, greater job insecurity, and insufficient workplace recognition. This population also expresses heightened concern about their ability to maintain employment due to health-related limitations, which frequently leads to a greater propensity for early retirement. These observations reinforce the notion that vision loss not only restricts employability in quantitative terms, but also deteriorates the subjective experience of work, increasing psychosocial vulnerability in a domain that is key to social inclusion and personal autonomy (Mojon-Azzi et al., 2010).

1.4. Common retinal diseases

Retinopathies encompass a heterogeneous group of diseases affecting the retina and can generally be classified into two broad categories: hereditary and acquired (non-hereditary). Hereditary retinopathies, such as retinitis pigmentosa, Stargardt disease, and various other retinal dystrophies, are caused by specific genetic mutations and typically present in early or middle life, following a progressive course and, in many cases, lacking curative treatment options. In contrast, non-hereditary retinopathies include conditions such as diabetic retinopathy and age-related macular degeneration (AMD), which develop as a result of systemic diseases or ageing. These are more common among adult and older populations, and their progression may be influenced by modifiable factors such as metabolic control, smoking, and diet.

Stargardt disease

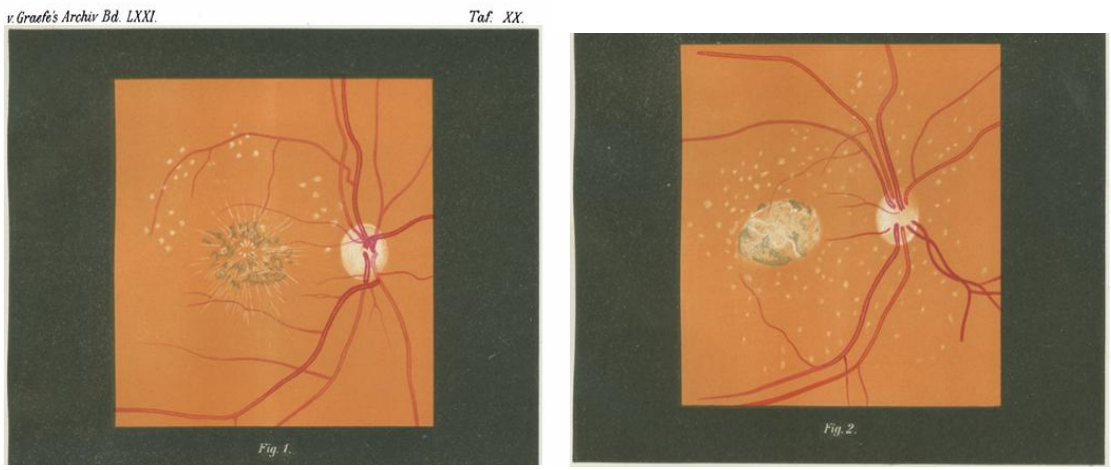

Figure 5. These figures serve as pioneering visual testimonies of the foundational clinical observations of Stargardt disease:

Fig.1: early-stage case, showing radial striations and macular mottling.

Fig.2: more advanced case, with dense macular lesion and broader perifoveal involvement.

They offer an artistic yet medically accurate representation of what would now be observed in fundus autofluorescence or OCT (optical coherence tomography) imaging, namely, central atrophy and subretinal deposits (Stargardt, 1909).

Stargardt disease is an inherited macular dystrophy characterised by progressive degeneration of the retinal pigment epithelium (RPE) and central photoreceptors, primarily cones, leading to irreversible loss of central vision. The first systematic clinical description was provided by Karl Stargardt in 1909 (**Figure 5**), who analysed multiple familial cases of progressive visual loss during adolescence. He identified symmetrical and bilateral involvement of the macula, with central scotomas affecting red and green perception, while peripheral visual fields and night vision remained intact. Stargardt noted that fundoscopic findings included irregular yellow-grey lesions, perifoveal white flecks, amorphous pigment deposits, and loss of the foveal reflex. In advanced stages, he described macular atrophy with visible sclerotic choroidal vessels, whereas the peripheral retina and retinal vessels remained largely unaffected (Stargardt, 1909).

Stargardt disease is classified within the group of inherited retinal degenerations (IRDs) and represents the most common form of macular dystrophy in patients under the age of 50, with an estimated prevalence of 1 in 10,000. It is primarily caused by biallelic mutations in the *ABCA4* (ATP binding cassette subfamily A member 4) gene, which encodes a retinoid transporter protein expressed in the outer segments of both cone and rod photoreceptors. Loss of *ABCA4* function disrupts the transport of all-trans-retinal, leading to the accumulation of lipofuscin, particularly A2E (N-retinylidene-N-retinyl-ethanolamine), within the RPE, resulting in cellular toxicity.

Stargardt disease has a marked phenotypic heterogeneity of the disease: in some patients, involvement is limited to the macula, while others show widespread cone and rod dysfunction, with progression toward a cone-rod dystrophy phenotype. The electroretinogram (ERG) findings range from preserved peripheral function to generalised cone and rod dysfunction, depending on disease stage. Imaging techniques such as fundus autofluorescence reveal loss of the foveal reflex, a mottled pattern of hyper- and hypoautofluorescence, and typically a peripapillary sparing. Optical coherence tomography (OCT) shows outer retinal thinning and loss of the RPE in the foveal region (Sahel et al., 2015).

Retinitis pigmentosa

Retinitis pigmentosa (RP) is the most common inherited retinal dystrophy, with an estimated prevalence of approximately 1 in 4,000 individuals in the general population (Bruninx & Lepièce, 2020). It is a progressive degenerative condition that initially affects the rod photoreceptors, responsible for peripheral and night vision, and in later stages involves cone photoreceptors, ultimately leading to loss of central visual acuity and, in some cases, complete blindness (Bruninx & Lepièce, 2020; Openshaw et al., 2008).

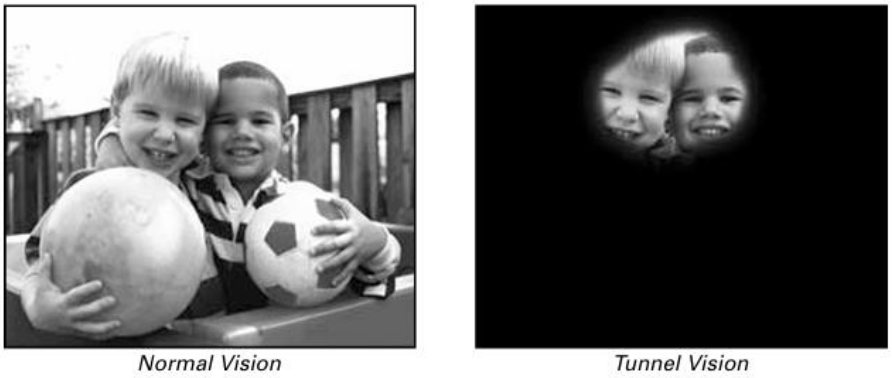

Figure 6. Visual comparison between normal vision (left) and tunnel vision (right), a hallmark of advanced-stage retinitis pigmentosa. Progressive loss of peripheral visual field is one of the most characteristic symptoms of the disease. Source: Kellogg Eye Center, University of Michigan.

Early clinical symptoms typically include nyctalopia (night blindness) and a gradual reduction in peripheral visual fields. These symptoms often progress to annular scotomas and concentric tunnel vision (**Figure 6**). In early stages, visual acuity is often preserved, even though the visual field is shrinking (Bruninx & Lepièce, 2020; Openshaw et al., 2008). Although some individuals

worry about total blindness, complete loss of vision is rare; most patients eventually meet criteria for legal blindness, defined as vision worse than 20/200 or a visual field less than 20 degrees in both eyes (Openshaw et al., 2008).

RP may occur in both familial and sporadic forms. All major modes of inheritance have been described, including autosomal dominant (15-25%), autosomal recessive (20-30%), and X-linked (10-15%) forms (Openshaw et al., 2008). Additionally, 20-30% of cases are syndromic, occurring as part of systemic conditions such as Usher or Bardet-Biedl syndrome (Bruninx & Lepièce, 2020). While many patients have a family history, up to 40-50% of RP cases appear isolated, either due to new mutations or undiagnosed mild cases in relatives (Openshaw et al., 2008). To date, more than 100 genes have been implicated in the pathogenesis of RP (Bruninx & Lepièce, 2020), and over 55 genes have been confirmed as causative in clinical genetic studies (Openshaw et al., 2008). Ophthalmoscopically, RP typically presents with bone spicule-shaped pigment deposits, narrowing of retinal vessels, and a pale, waxy optic disc. In some cases, macular oedema may occur, contributing to central vision deterioration (Bruninx & Lepièce, 2020).

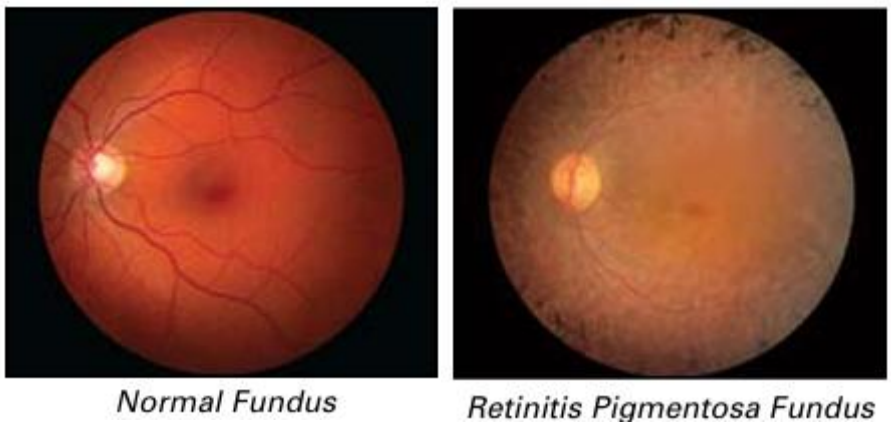

Figure 7. Comparison between a normal fundus and a fundus affected by retinitis pigmentosa (RP). The RP retina shows characteristic features such as generalized retinal pallor, attenuation of retinal vessels, and peripheral pigment deposits in a bone-spicule pattern. Source: Kellogg Eye Center, University of Michigan.

Diagnosis involves a combination of functional and structural assessments. Key tests include visual field testing, which monitors the gradual constriction of peripheral vision; electroretinography, which evaluates rod and cone response and can detect dysfunction before clinical signs appear; and optical coherence tomography to examine retinal structure and identify macular changes such as oedema. Additional evaluations such as fundus photography and fluorescein angiography may support the diagnosis or rule out other retinal disorders (Openshaw et al., 2008) (**Figure 7**).

Given its often early onset and progressive course, RP can significantly impact daily life, education, and employment. However, with adequate support, most individuals lead independent and fulfilling lives. Children and adolescents benefit from individualized educational plans and peer support, while adults often continue working with reasonable adaptations. Emotional support, low vision services, and legal protections such as the Americans with Disabilities Act play a key role in maintaining autonomy and quality of life (Openshaw et al., 2008).

Age-related macular degeneration (AMD)

AMD is the leading cause of vision loss in adults over the age of 60 in industrialised countries. It is an acquired, progressive degenerative disease of the retina that affects the macula, the central region responsible for high-resolution vision. While AMD results in central vision loss, peripheral vision remains unaffected, meaning it does not lead to complete blindness (Apte, 2021; Mehta, 2015). AMD presents in two main clinical forms. The dry (nonexudative) form, which accounts for approximately 85-90% of cases, is characterised by the accumulation of yellowish subretinal deposits known as *drusen* and progressive geographic atrophy (GA) of the retinal pigment epithelium (Mehta, 2015). The wet (exudative or neovascular) form, although less common (10-15%), is responsible for the majority of severe vision loss. It is defined by the growth of abnormal choroidal blood vessels beneath the retina, often accompanied by subretinal or intraretinal fluid and haemorrhages (Apte, 2021; Mehta, 2015) (**Figure 8**).

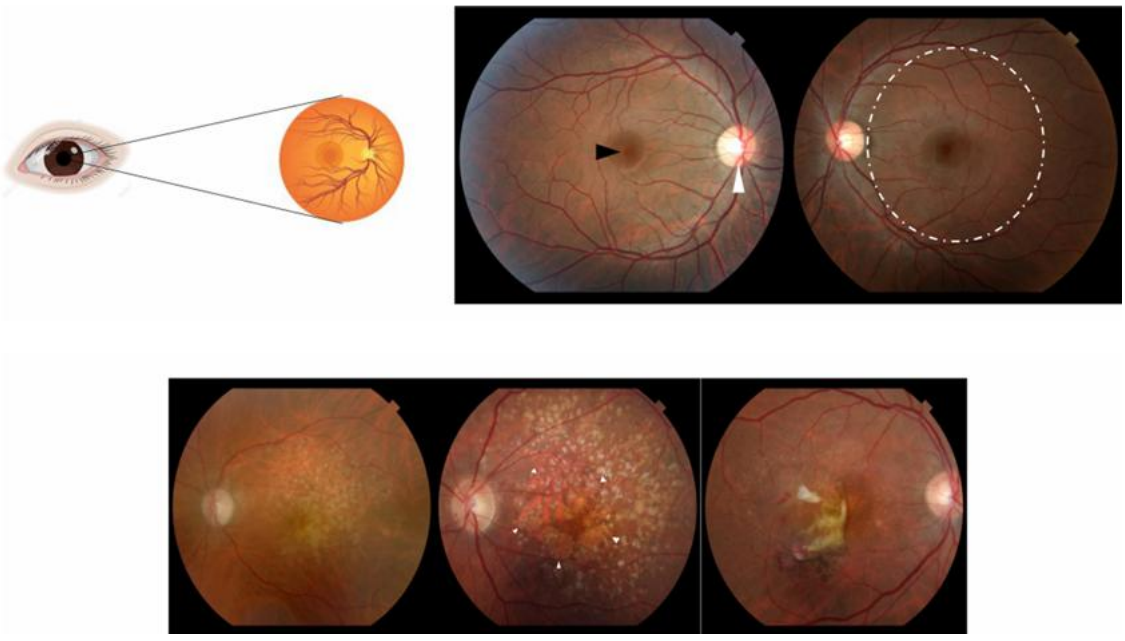

Figure 8. Macular anatomy and progression of age-related macular degeneration. The top row first shows a diagram of the eye illustrating how vision is focused on the macula; this is followed by fundus

photographs of a healthy eye in which the macula (dashed circle), the fovea (black arrow), and the optic nerve (white arrow) are indicated. The bottom row illustrates, via biomicroscopic photographs, the clinical progression of AMD: intermediate with yellowish deposits (drusen); advanced dry with geographic atrophy (GA) and mottled pale areas; and neovascular ("wet") with haemorrhage and subretinal fluid. Source: Apte, 2021.

Clinically, patients may initially be asymptomatic, particularly in early or intermediate stages. When symptoms do appear, they often include blurred or reduced central vision, metamorphopsia (distortion of straight lines), central scotomas (dark or blank areas in central vision), and difficulty reading or seeing in low light conditions. Diagnosis is based on clinical findings from a dilated fundus examination and supported by multimodal imaging. Optical coherence tomography is the primary non-invasive tool used to detect *drusen*, fluid accumulation, retinal atrophy, or thickening. Fundus autofluorescence offers insights into retinal pigment epithelium health and the presence of lipofuscin accumulation, while fluorescein angiography is useful for identifying neovascular membranes in wet AMD (Apte, 2021; Mehta, 2015) (**Figure 9**). Additional functional tests, such as dark adaptometry, microperimetry, and multifocal electroretinography, can detect early visual deficits even in the presence of preserved visual acuity (Apte, 2021).

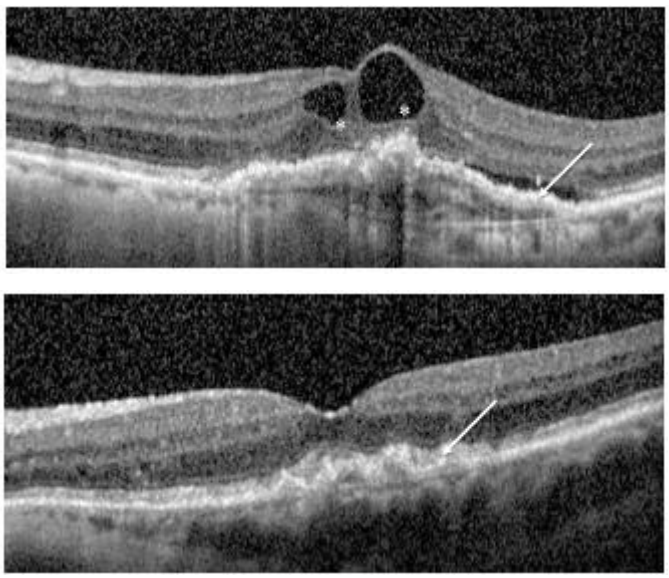

Figure 9. Optical coherence tomography (OCT) in age-related macular degeneration (AMD). Top: neovascular or "wet" form, with intraretinal (asterisks) and subretinal (arrow) fluid. Bottom: dry/atrophic form, with drusen (arrow) located at the level of the retinal pigment epithelium. Adapted from Mehta (2015).

The prevalence of AMD increases significantly with age, particularly after the age of 75. It is more common among individuals of European ancestry and is influenced by both environmental and genetic factors. Modifiable risk factors include smoking, hypertension, elevated body mass index, and prolonged exposure to ultraviolet or blue light. Moreover, genetic polymorphisms, particularly in the CFH and ARMS2 genes, are strongly associated with susceptibility to and progression of the disease (Apte, 2021; Mehta, 2015).

In terms of management, dry AMD currently has no curative treatment. However, progression can be slowed in patients with intermediate or advanced disease through dietary supplementation based on the AREDS2 formulation, which includes vitamins C and E, zinc, copper, lutein, and zeaxanthin. This approach has been shown to reduce the risk of progression to advanced AMD by up to 25% (Mehta, 2015).

For wet AMD, the introduction of intravitreal anti-VEGF therapies, such as ranibizumab, aflibercept, and bevacizumab, has significantly improved prognosis. These treatments reduce the risk of moderate vision loss to below 10% over two years and can even lead to substantial visual improvement in a considerable proportion of patients.

The socioeconomic burden of AMD is considerable, with global costs estimated to exceed USD 300 billion, including more than USD 250 billion in direct healthcare expenses such as imaging, clinical management, and anti-VEGF therapy. As the population continues to age, these costs are expected to rise sharply in the coming decades (Apte, 2021).

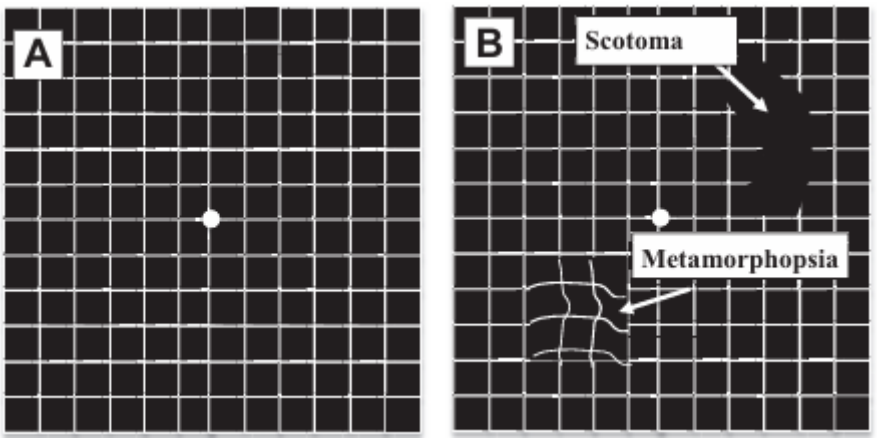

Figure 10. The Amsler grid is a simple and effective tool for self-monitoring of central vision in patients with age-related macular degeneration. (A) Normal perception: all lines appear straight. (B) Pathological perception: central vision distortions such as metamorphopsia (wavy lines) and scotomas (dark or missing areas) can indicate disease progression and should prompt immediate ophthalmologic evaluation. Adapted from Mehta (2015).

Early detection and prompt treatment initiation are critical for preserving visual function. Patients are encouraged to self-monitor using tools such as the Amsler grid or home-based technologies like the ForSeeHome device, which can detect subtle changes indicative of progression from dry to wet AMD (Mehta, 2015) (**Figure 10**). In advanced cases, where visual acuity remains limited despite treatment, rehabilitation with low vision aids and environmental adaptations can help maintain independence and quality of life. Regular ophthalmological follow-up is essential for detecting disease progression or recurrence in a timely manner, particularly in patients with unilateral neovascular AMD or previously inactive disease (Apte, 2021; Mehta, 2015).

Diabetic retinopathy (DR)

DR is the most common cause of new cases of blindness in adults aged 20 to 74 years. It is a progressive microvascular complication of diabetes mellitus, affecting nearly all patients with type 1 diabetes and the majority of those with type 2 diabetes over time (Fong et al., 2004; Kataoka et al., 2023). DR results from chronic hyperglycaemia, which damages the retinal microvasculature and disrupts the blood-retina barrier, leading to increased vascular permeability, ischaemia, and neurodegeneration.

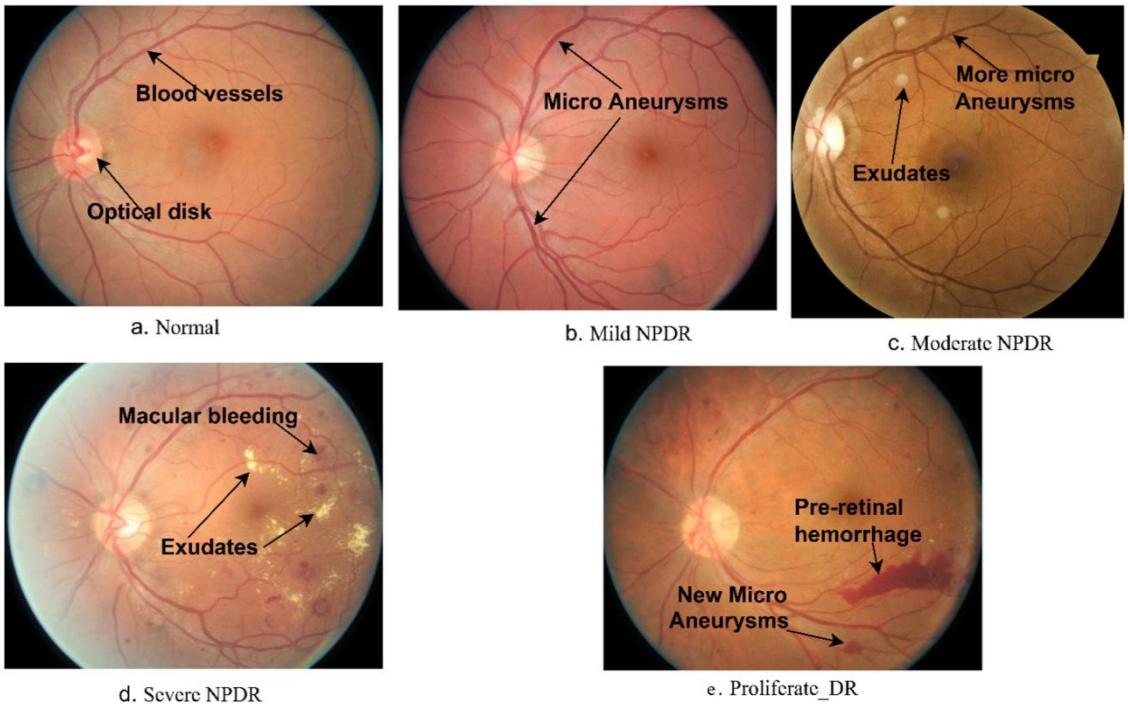

Figure 11. Representative colour fundus photographs illustrating the clinical stages of diabetic retinopathy (DR). (a) Normal retina showing intact retinal blood vessels and optic disc. (b) Mild non-proliferative DR

(NPDR) characterized by the presence of microaneurysms. (c) Moderate NPDR with increased numbers of microaneurysms and the appearance of hard exudates. (d) Severe NPDR demonstrating macular hemorrhage and extensive exudates. (e) Proliferative DR (PDR) with pathological neovascularization and pre-retinal hemorrhage (Alshahrani et al., 2023).

DR progresses through defined clinical stages. Non-proliferative diabetic retinopathy (NPDR) is the initial phase, characterised by microaneurysms, retinal haemorrhages, venous beading, and intraretinal microvascular abnormalities. As ischaemia advances, the condition may progress to proliferative diabetic retinopathy (PDR), marked by pathological neovascularisation of the retina and posterior vitreous surface. These fragile new vessels are prone to rupture, resulting in vitreous haemorrhage, fibrovascular proliferation, and tractional retinal detachment, potentially leading to irreversible vision loss. Additionally, diabetic macular oedema (DMO), caused by vascular leakage and fluid accumulation in the macula, can occur at any stage and is a major cause of central vision loss in diabetic patients (Fong et al., 2004; Kataoka et al., 2023) (**Figure 11**).

Although DR may remain asymptomatic in its early stages, advanced disease often presents with symptoms such as blurred or fluctuating vision, floaters, or sudden vision loss due to vitreous haemorrhage or retinal detachment. Diagnosis is based on dilated fundus examination, stereoscopic retinal photography, and imaging techniques including OCT for detecting macular oedema, and fluorescein angiography for identifying neovascularisation.

Several factors influence the risk and progression of DR. Duration of diabetes is the strongest predictor: in patients with type 1 diabetes, the prevalence of retinopathy rises from 8% at three years to 80% at fifteen years post-diagnosis. Notably, up to 21% of individuals with type 2 diabetes present with DR at the time of diagnosis. Other important risk factors include poor glycaemic control, hypertension, hyperlipidaemia, puberty, pregnancy, and cataract surgery.

Glycaemic and blood pressure control are well-established interventions for delaying both the onset and progression of DR. The Diabetes Control and Complications Trial (DCCT) demonstrated a 76% reduction in retinopathy onset and a 54% reduction in progression with intensive insulin therapy in type 1 diabetes. Similarly, the UK Prospective Diabetes Study (UKPDS) showed that every 1% reduction in HbA1c was associated with a 35% decrease in the risk of microvascular complications, including DR. Tight blood pressure control has also been shown to reduce retinopathy progression and vision loss.

Guidelines from the American Diabetes Association (ADA) recommend that individuals with type 1 diabetes undergo a comprehensive dilated eye examination within 3-5 years of diagnosis (after age 10), while those with type 2 diabetes should be screened at the time of diagnosis. Follow-up should occur annually, or more frequently depending on disease severity. In pregnant

women with pre-existing diabetes, eye examinations are recommended during the first trimester and at intervals throughout pregnancy, as DR may progress rapidly in this context (Fong et al., 2004).

1.5. Current clinical treatments and limitations

Pharmacological

The current therapeutic landscape for age-related macular degeneration (AMD) is dominated by intravitreal anti-VEGF agents, which remain the gold standard for the neovascular form. Ranibizumab, aflibercept, and brolucizumab have demonstrated strong efficacy in preserving and improving visual acuity, although their short intraocular half-life necessitates frequent dosing (Heier et al., 2012; Galindo-Camacho et al., 2022; Rosenfeld et al., 2006). Faricimab, a bispecific antibody inhibiting both VEGF-A (vascular endothelial growth factor A) and angiopoietin-2, has recently expanded treatment options by enabling extended dosing intervals of up to four months with non-inferior visual outcomes compared to aflibercept. The port delivery system Susvimo offers a further step toward reducing treatment burden through sustained intravitreal release of ranibizumab (Hoffmann & La Roche Ltd, 2022).

Several strategies aim to address the limitations of repeated injections. Gene therapy approaches are being developed to transform retinal cells into long-term biofactories producing anti-angiogenic proteins such as aflibercept or sFlt-1, delivered via viral vectors (AAV (Adeno-associated virus), lentiviral) or non-viral carriers. Regenerative medicine is also advancing, with transplantation of retinal pigment epithelium cells derived from embryonic or induced pluripotent stem cells showing early safety and functional improvement, although challenges such as tumorigenesis risk and immune compatibility remain (Galindo-Camacho et al., 2022).

The management of diabetic macular oedema has evolved from macular laser photocoagulation, established by the Early Treatment Diabetic Retinopathy Study as the historical standard of care, towards pharmacologic approaches targeting vascular endothelial growth factor (VEGF). Anti-VEGF therapy is now considered the first-line treatment for centre-involved DMO, given its superior efficacy in improving visual acuity and retinal anatomy compared with laser (Lim et al., 2025).

Ranibizumab, a monoclonal antibody fragment that inhibits VEGF-A, has shown sustained benefits in the phase III RIDE and RISE trials. Over 36 months, continuous monthly treatment led to gains of ≥15 Early Treatment Diabetic Retinopathy Study (ETDRS) letters in up to 51% of

patients, with durable reductions in central foveal thickness (CFT) and a decreased risk of progression to PDR. Delayed initiation of ranibizumab, as seen in sham-treated patients crossing over in the third year, resulted in smaller visual gains, underscoring the importance of early treatment (Brown et al., 2013).

Aflibercept, a recombinant fusion protein with high affinity for VEGF-A, VEGF-B, and placental growth factor, demonstrated comparable efficacy in the VISTA and VIVID trials, with dosing every 8 weeks after a loading phase maintaining visual gains similar to monthly injections. At 100 weeks, approximately one-third of treated eyes achieved ≥15-letter gains, and a significant proportion showed a ≥2-step improvement in Diabetic Retinopathy Severity Scale (DRSS) scores (Brown et al., 2015). Other anti-VEGF agents, such as bevacizumab, have also been used off-label with evidence of benefit, although large comparative studies suggest aflibercept may provide greater improvement in patients with worse baseline vision.

Intravitreal corticosteroids, including dexamethasone and fluocinolone acetonide implants, remain an option, particularly for pseudophakic patients or those insufficiently responsive to anti-VEGF therapy, given their anti-inflammatory and anti-permeability effects. However, their use is limited by higher risks of intraocular pressure elevation and cataract formation. Laser photocoagulation still has a role as a focal/grid approach in selected cases, especially when oedema is non-centre-involved or as adjunctive therapy to pharmacologic treatment (Lim et al., 2025).

Long-term data from RIDE and RISE confirm that intraocular anti-VEGF therapy with ranibizumab offers a substantially better approach to treating DMO than historical standard care, reducing visual morbidity associated with chronic disease and establishing a new standard of care (Brown et al., 2013).

Surgical

In patients with proliferative diabetic retinopathy and recent vitreous haemorrhage causing a reduction in visual acuity to 5/200 or worse for at least one month, early vitrectomy has been shown to provide a clear benefit in those with type 1 diabetes and severe vitreous haemorrhage, whereas no such advantage has been demonstrated in type 2 diabetes, for which a more conservative approach may be appropriate (The Diabetic Retinopathy Vitrectomy Study Research Group, 1985). More than 70% of patients achieve improved visual acuity following diabetic vitrectomy; however, central or fovea-involving tractional retinal detachment, poor preoperative visual acuity, iris neovascularization, and the absence of prior panretinal photocoagulation are associated with less favourable outcomes (Shaikh et al., 2024). On the other hand, pars plana

vitrectomy (PPV) in patients with diabetic tractional retinal detachment (dTRD) shows a low retinal reattachment failure rate of 5.9% after a single surgery, while the mean final visual acuity was approximately 20/175 Snellen, indicating limited vision despite anatomical success (McCullough et al., 2023). Other authors have shown that pars plana vitrectomy improves vision and restores macular architecture in tractional diabetic macular oedema; however, adding internal limiting membrane peeling does not significantly affect either functional or anatomical outcomes (6-month follow-up), consistent with meta-analyses that show no long-term benefits (Khattab et al., 2022).

Pneumatic displacement (PD), which consists of the intravitreal injection of an expansile gas to displace blood away from the fovea, is used as a surgical alternative for the management of submacular hemorrhage (SMH), a complication that can occur in conditions such as age-related macular degeneration (AMD), polypoidal choroidal vasculopathy (PCV), and retinal macroaneurysms. The procedure may be performed alone or in combination with anti-VEGF agents and, in some cases, recombinant tissue plasminogen activator (rtPA). This approach allows for faster visual recovery compared with pharmacologic monotherapy but requires the patient to maintain a face-down position for several days and may be associated with complications such as ocular hypertension or cataract progression. Subretinal displacement has been proposed as an alternative to conventional PD. This technique involves the direct injection of air into the subretinal space following rtPA, generating greater pressure to mobilize the clot. Although it eliminates the need for a face-down position and reduces the risk of gas-induced ocular hypertension, it carries a higher risk of macular hole formation (Wai Wong et al., 2018). Another procedure is the use of the implantable miniature telescope (IMT) for vision loss in end-stage AMD. This intraocular device, implanted in a single eye, is designed to magnify images and project them onto retinal areas unaffected by AMD, thereby potentially improving central vision. However, high-quality evidence is still insufficient to establish its safety and effectiveness (Gupta et al., 2018).

1.6. Recent advances in vision restoration

In a recent study on RP, gene therapy was conducted for the treatment of inherited retinal dystrophies caused by biallelic mutations in the RPE65 gene, including both Leber congenital amaurosis type 2 (LCA2) and retinitis pigmentosa type 20 (RP20). After one year, 65% of treated patients showed improvement compared with controls, with additional gains in light sensitivity and visual fields, while best-corrected visual acuity demonstrated a favourable trend without reaching statistical significance in all cases. Regarding safety, adverse events were mostly mild

and transient (ocular inflammation, transient ocular hypertension, cataract), with no serious events directly attributable to the treatment (Russell et al., 2017). In patients with X-linked retinitis pigmentosa caused by RPGR mutations, a study evaluated subretinal gene therapy, which involves injecting under the retina a viral vector (AAV-based) carrying a functional copy of the RPGR gene to restore photoreceptor function. The results demonstrated an acceptable safety profile (adverse events were mild to moderate, expected and manageable, such as transient intraocular inflammation and elevated intraocular pressure; serious events were rare) along with improvements in functional vision and retinal sensitivity, supporting the progression of this trial to phase 3 in this severe form of retinitis pigmentosa (Michaelides et al., 2024). In a pioneering study in the field of visual restoration, advanced RP was treated using optogenetic therapy, in which a gene was delivered into retinal ganglion cells to render them light-sensitive through ChrimsonR, a protein responsive to amber light. As ganglion cells do not naturally capture images, the patient wore special glasses equipped with a camera that converted visual scenes into adapted light impulses projected directly onto the retina. Following therapy and several months of training with the device, the patient achieved a partial recovery of visual function, being able to detect, localize, count, and even correctly touch objects, tasks that had been impossible before treatment. Furthermore, subsequent electroencephalography (EEG) tests confirmed that the visual information reached and activated the occipital cortex (Sahel et al., 2021) (**Figure 12**).

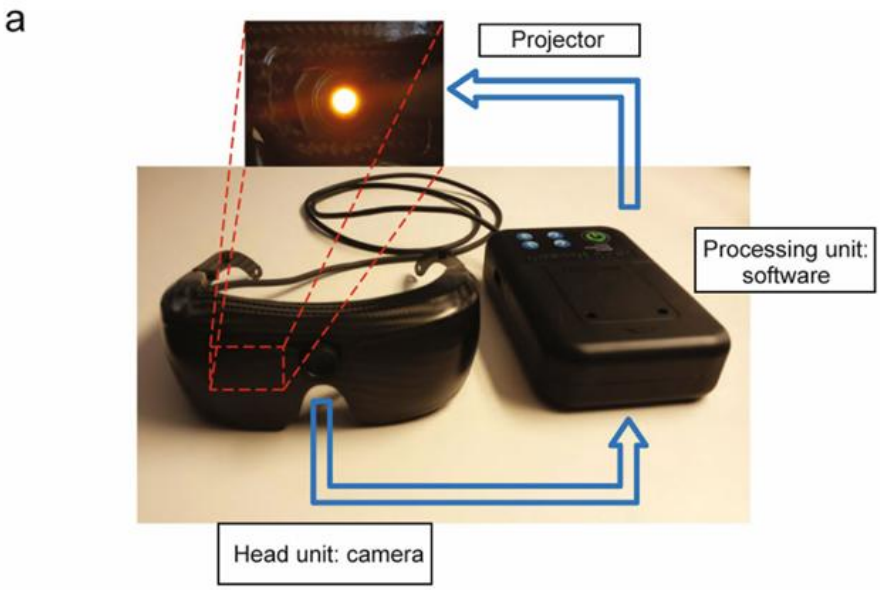

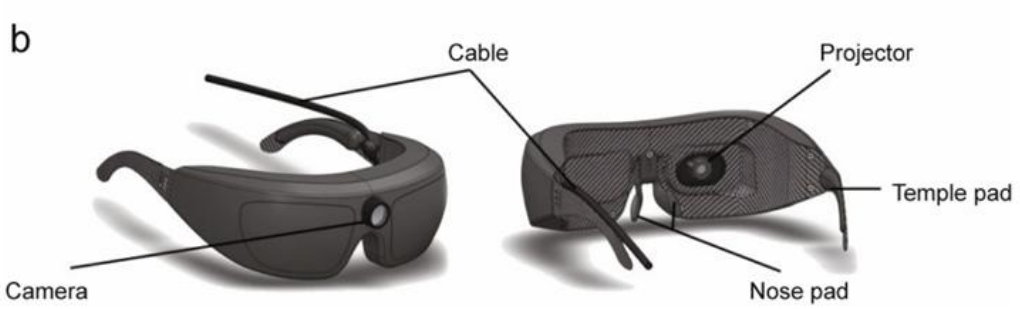

Figure 12. Light stimulation glasses. a. The GS030-MD device consists of two interconnected components. The head-mounted unit includes a camera that captures, in real time, what is in front of the patient. This information is transferred to a processing unit, which converts the images into simplified light patterns and sends them back to the head-mounted unit. There, a small projector projects the light directly onto the retina of the treated eye. b. Front and rear views of the glasses. The camera is located centrally, facing outward, while the projector is aligned with the pupil of the treated eye, with the possibility of adjustment according to each patient's interpupillary distance (Sahel et al., 2021).

In Taiwan, a clinical case was reported in which an Argus II retinal prosthesis system was implanted in a patient with advanced RP and high myopia. The device consists of 60 electrodes that directly stimulate surviving retinal cells to generate visual perceptions. In this patient, most electrodes functioned properly after surgery. Following prolonged rehabilitation, functional improvements were achieved, including the ability to localize lights and distinguish large objects such as televisions or furniture, without serious complications (Hsu et al., 2019) (**Figure 13**).

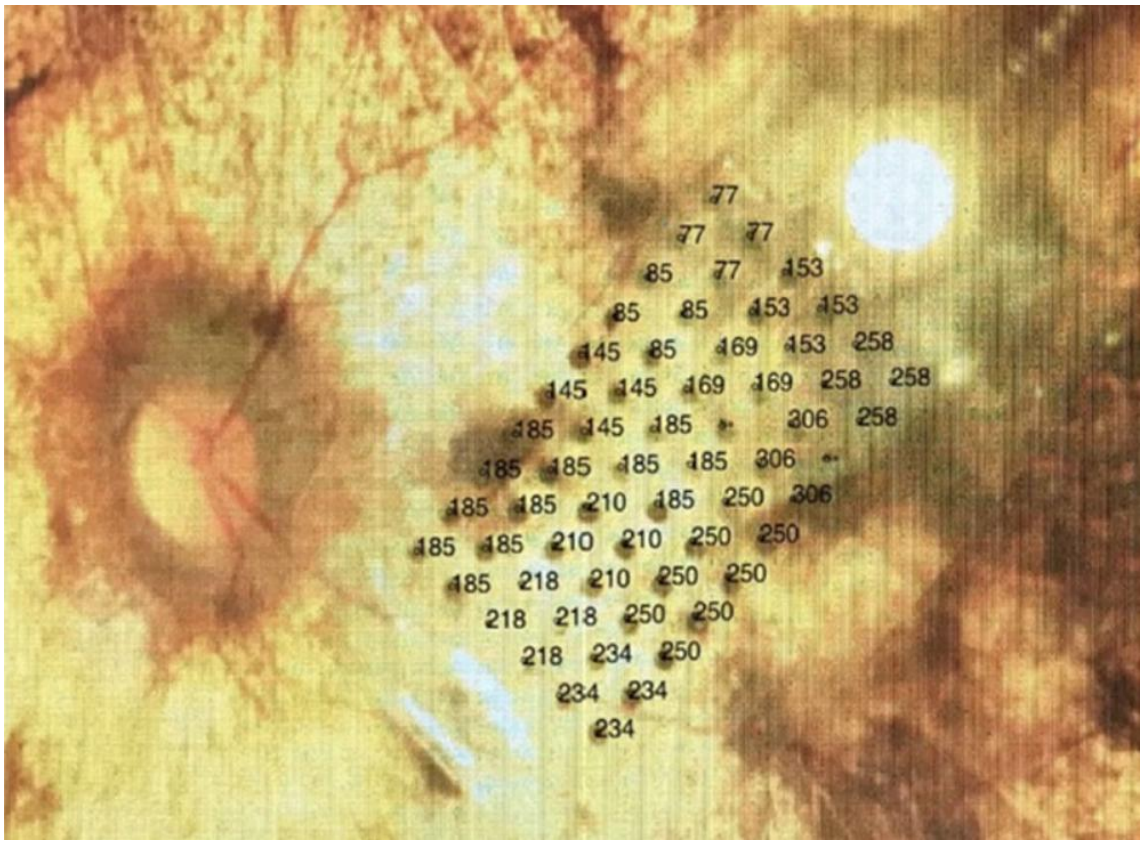

Figure 13. Thresholds for each quad were measured for the amount of electrical current necessary to produce visual percepts. In 11 of 15 quads, a low current amplitude (below 233 µA) could induce a visual perception. For the four remaining quads, the thresholds for visual perception ranged from 250 to 306 µA (Hsu et al., 2019).

In 2018, another group presented the initial results of the electronic retinal implant Alpha AMS in patients with end-stage RP. In this study, a subretinal microchip was implanted in six patients who no longer had useful light perception. The device captures incoming light and converts it into electrical signals that directly stimulate the inner retinal layers, thereby partially restoring visual function by stimulating surviving inner retinal neurons. The results were promising: five of the six patients improved their ability to localize objects on a table, recognize simple shapes, or distinguish grayscale contrasts when the implant was activated. In some cases, patients were even able to read the position of clock hands or identify everyday items such as plates or cutlery. Participants also anecdotally reported improvements in daily activities, including navigating within the home, recognizing doors and windows, distinguishing car lights, or even perceiving mountain silhouettes against the sky. Regarding safety, complications such as conjunctival erosion and retinal detachment were observed, though both were managed successfully (**Figure 14**) (Edwards et al., 2018).

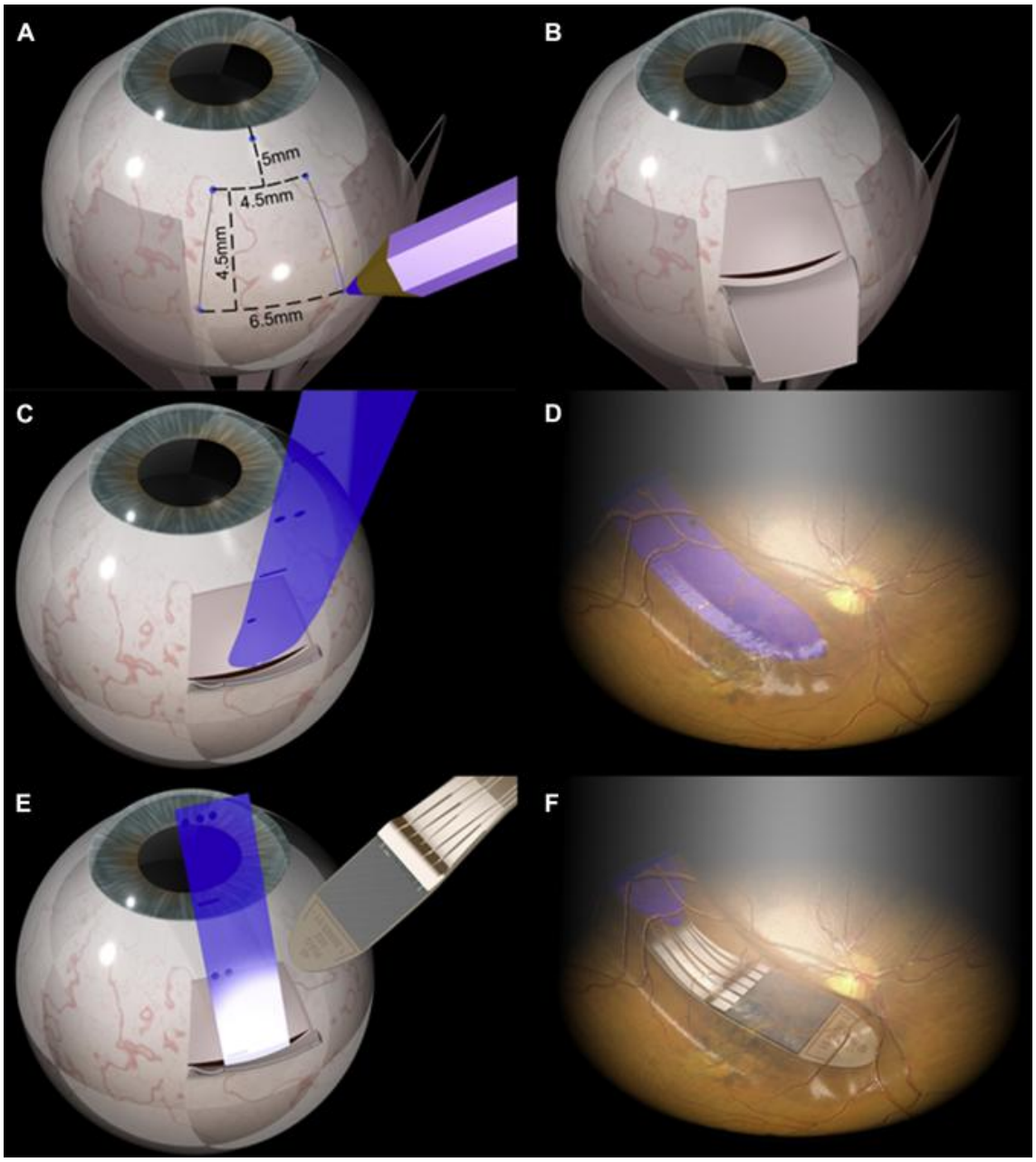

Figure 14. Surgical procedure for the implantation of a subretinal microchip. (A, B) A partial-thickness scleral flap based at the fornix is created. (C) After vitrectomy and induction of a localized retinal detachment, a guiding foil is introduced through a full-thickness incision in the sclera and choroid. (D) The foil is positioned beneath the fovea, and (E, F) the chip is advanced along the same trajectory into the subretinal space, at which point the guiding foil is removed (Edwards et al., 2018).

Similarly, in a human clinical trial, the wireless subretinal PRIMA implant was evaluated for the restoration of central vision in five patients with geographic atrophy due to age-related macular degeneration. The device is a 2-mm photovoltaic microchip with 378 pixels, placed beneath the macula, and it operates in conjunction with special glasses equipped with a camera that captures images and projects them onto the retina using infrared light. Each pixel of the chip converts this

optical information into electrical impulses that stimulate the remaining inner retinal neurons. In two of the five patients the chip was not positioned precisely in the intended area, but all patients recovered at least light perception and simple shapes within the scotoma of their macula. The three patients with optimal chip placement achieved prosthetic visual acuities ranging from 20/460 to 20/550, sufficient to recognize letters and short words. Importantly, the procedure did not lead to worsening of the patients' natural peripheral vision (Palanker et al., 2020).

Transplantation of human embryonic stem cell (hESC)-derived cells into the subretinal space has been tested in patients with dry AMD and Stargardt disease. After nearly two years of follow-up, no tumors, severe immune rejections, or abnormal proliferations of the transplanted cells were detected. In most patients, pigmented patches were observed in the retina, consistent with survival of the transplanted retinal pigment epithelium (RPE). More than half of the treated eyes experienced improvements in visual acuity (≥15 letters in some cases), whereas untreated eyes remained stable or worsened. In addition, patients reported vision-related quality-of-life improvements, including enhanced ability in near and distance activities as well as peripheral vision (Schwartz et al., 2015). Another human trial tested a bioengineered retinal pigment epithelium (RPE) implant derived from human embryonic stem cells on a synthetic parylene membrane, designed to treat advanced dry age-related macular degeneration in five patients. One patient gained 17 letters in visual acuity testing, and two showed improvement in fixation stability, while none of the implanted eyes lost vision. Moreover, the implant remained stable at the site of atrophy and demonstrated signs of integration with the host retina (Kashani et al., 2018).

In Stargardt disease associated with *ABCA4* mutations, a phase I/IIa trial was conducted in 22 adult patients using subretinal injection of a lentiviral vector (EIAV-ABCA4) carrying a healthy copy of the gene. The treatment was generally well tolerated, with adverse events mostly related to surgery (e.g., conjunctival hemorrhage, transient elevations in intraocular pressure), and only one case of chronic ocular hypertension as a serious ocular event. No clinically meaningful improvements in visual acuity or visual fields attributable to the therapy were observed. Structural changes were variable: in one high-dose patient, a significant reduction of the characteristic yellow flecks was documented, while in several others progression of retinal pigment epithelium atrophy was more pronounced in the treated eye (Parker et al., 2022). Another group conducted a phase I clinical trial of gene therapy in patients with geographic atrophy secondary to advanced dry age-related macular degeneration (AMD). The approach consisted of a single intravitreal injection of JNJ-1887, a viral vector designed to produce soluble CD59, a protein that inhibits formation of the membrane attack complex of the complement system (implicated in retinal damage). After two years of follow-up, the treatment was well tolerated, with no serious therapy-related adverse events. Ocular inflammation occurred in 29% of patients, but was mild and resolved with topical corticosteroids or, in some cases, observation alone. Although the sample

size was small, the high-dose group showed a slowing of lesion growth over time (Heier et al., 2024).

Although numerous examples of clinical and experimental treatments for visual restoration have been presented, a long road still lies ahead. At some point along that path, one must ask whether, if vision could one day be fully restored or most visual disorders eliminated, the brain would be able to once again interpret and process this reestablished visual information, or whether plasticity-related changes may prevent classically visual neurons from ever truly 'seeing' again. For example, in India, a woman born with dense congenital cataracts lived nearly 12 years in a state of practical blindness until she underwent surgery in which the cataracts were removed in a single procedure. Initially, she struggled to identify the objects around her, but gradually she learned to recognize her family members, household items, and to navigate her environment. Twenty years later, researchers tested the extent to which she had developed vision. They found that although her visual acuity remained limited (with blurred vision), she was able to recognize faces, distinguish shapes, and use her sight to work and lead an independent life (Ostrovsky et al., 2006).

2. Neocortical Dynamics and Sensory Integration

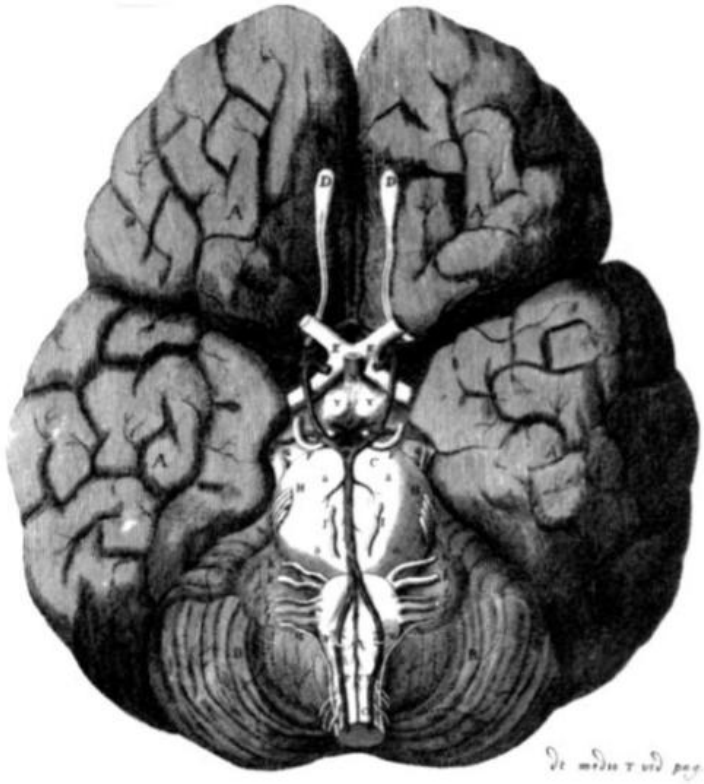

Figure 15. Inferior view of the human brain, illustrated by Christopher Wren in Cerebri Anatome (1664). This image shows the base of the human brain in anatomical detail, including structures such as the optic nerves and brainstem. It was drawn by Christopher Wren as part of the collaborative work led by Thomas Willis, and represents one of the earliest systematic attempts to describe brain anatomy from a functional perspective. The work marked the beginning of modern neuroanatomy, combining empirical observation with natural philosophy. Reproduced by permission from Hughes JT, Thomas Willis 1621-1675: His Life and Works (RSM Press, 1991) (O'Connor, 2003).

The scientific concept of the cerebral cortex has evolved over time, from the earliest descriptions of the brain in the 17th century B.C. in an ancient Egyptian papyrus, where clinical cases and both spinal and cerebral lesions were documented (Van Middendorp et al., 2010), to Andreas Vesalius' *De humani corporis fabrica* (1543), which, through illustrations produced by artists from Titian's school, provided detailed depictions of the human body and corrected long-accepted misconceptions derived from animal dissections (Zampieri et al., 2015), followed by Thomas Willis' *Cerebri Anatome* (1664) (**Figure 15**), which marked a turning point in the anatomy of the brain and nerves. His ideas about the brain were closely tied to his views on the soul, and in this

work he described the arterial system at the base of the brain, now known as the circle of Willis (O'Connor, 2003).

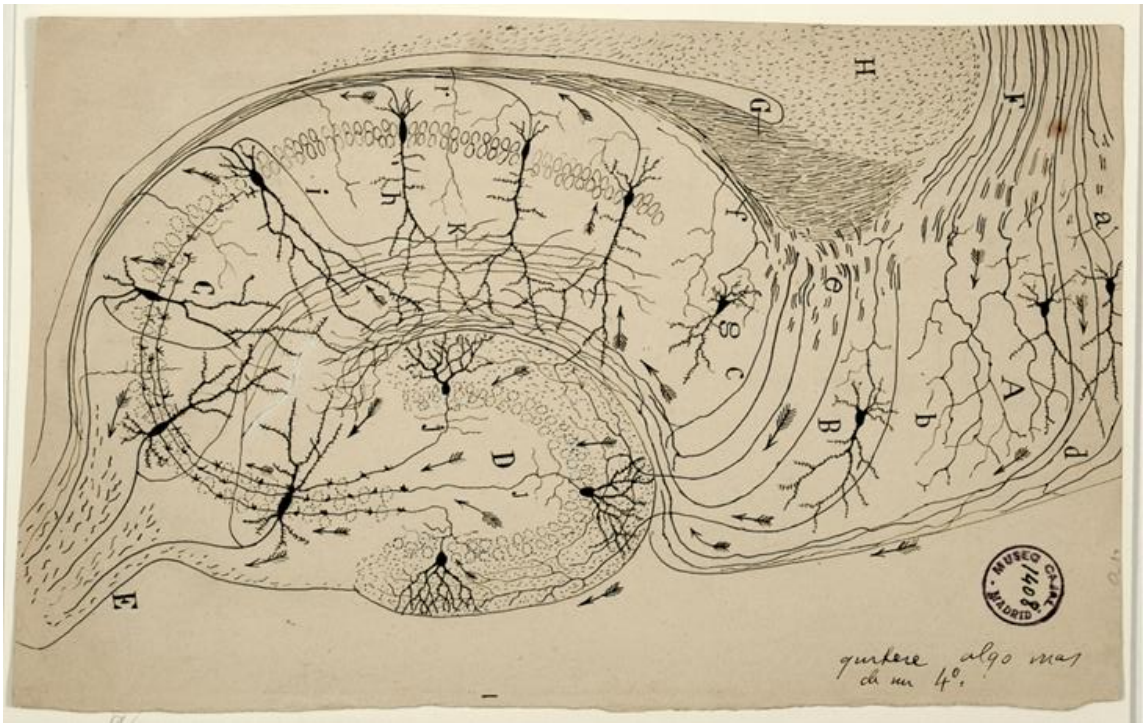

Figure 16. Schematic representation of the hippocampal structure and connectivity, published by Santiago Ramón y Cajal in 1901. This classic drawing shows individual neurons and the direction of signal flow within the hippocampus, marked with arrows. Key anatomical structures include the dentate gyrus (D), Ammon's horn (C), the subiculum (B), and the fimbria (E), among others. Cajal's illustration reflects the groundbreaking use of Golgi staining to map the cellular organization and connections of the brain. [Image from Legado Cajal, Instituto Cajal (CSIC), Madrid] (Rozo et al., 2024).

Key figures in the regional cytoarchitecture of the cortex include Theodor Meynert, who in 1867 described five cortical layers, and up to eight in the visual cortex; Vladimir Betz, who identified a population of giant pyramidal cells in the motor cortex (now known as 'Betz cells'), noting that they were confined to the precentral cortex and linked them to motor function; and finally William Bevan-Lewis, who in 1882 refined the five- versus six-layer cortical model, designating the ganglionic layer as the site of the giant cells and providing detailed illustrations of Betz cells (Triarhou, 2021). But it was not until 1909 that Korbinian Brodmann, in his landmark work *Vergleichende Lokalisationslehre*, organized the human cortex into 48 areas. He emphasized, however, that no single area could by itself explain complex functions. He insisted on the networked cooperation of multiple regions, and he also criticized simplistic explanations such as those of Flechsig, who associated cortical areas with 'association centers' based on myelination.

Brodmann further rejected the notion that a single cell type could define a function. Instead, he argued that what truly mattered were patterns of cellular organization and their connections, an insight that closely anticipates what is now understood as functional connectivity in neuroscience (Zilles, 2018). Concluding with Santiago Ramón y Cajal, one of the fathers of modern neuroscience, who in 1888 demonstrated, through his histological preparations using the Golgi stain, which he himself refined, that neurons are independent units, with processes ending freely rather than in continuity. In doing so, he laid the foundation of the so-called neuron doctrine, thereby cementing the basis of modern neuroscience (Rozo et al., 2024) (**Figure 16**).

In 1957, Vernon Mountcastle introduced the concept that the cerebral cortex is organized into 'cortical columns,' an idea that profoundly changed the way the brain is understood. By recording the activity of individual neurons in the somatosensory cortex of cats while applying different mechanical stimuli to the body (e.g., moving hairs, pressing the skin, rotating joints, or stimulating deep fascia), he observed that each neuron responded to a very specific type of stimulus. The neurons exhibited small, well-defined receptive fields on the contralateral side of the body. The concept of the cortical column emerged when Mountcastle inserted the electrode perpendicularly into the cortex and found that vertically aligned neurons (from the surface down to the deeper layers) shared the same type of response and the same receptive field. He concluded that the basic functional unit of the cortex is a column of neurons (a few hundred microns in diameter) that processes the same type of sensory information (Mountcastle, 1957). Just two years later, Hubel and Wiesel (1959) conducted a study on the receptive fields of individual neurons in the striate cortex of cats, aiming to understand how cortical cells respond to light stimuli by comparing their organization with that of neurons in the retina and the lateral geniculate nucleus. They demonstrated that the visual cortex does not simply replicate the retinal signal, but rather extracts new properties from the visual stimulus, such as orientation, edges, and direction of movement. This work marked the beginning of a revolution in visual neuroscience (Hubel & Wiesel, 1959).

At the end of the 20th and the beginning of the 21st century, the neocortex came to be approached as a canonical circuit repeated in columns or patches, with excitatory spiny cells (pyramidal neurons) providing interlaminar and lateral excitation, shaped by GABAergic inhibitory interneurons. In the classical scheme, thalamic input arrives at layer 4, which projects to layers 2/3; the superficial layers then recruit layers 5 and 6, with layer 5 sending outputs to subcortical structures, while layers 5/6 provide feedback projections to other areas and layer 6 influences layer 4 (cortico→thalamic loops and return to input layers). Although this pattern is general, variants exist depending on the cortical area. Recurrent and lateral connections allow small inputs to be amplified by the local microcircuitry (Douglas & Martin, 2004).

2.1. Structure and function of the neocortex

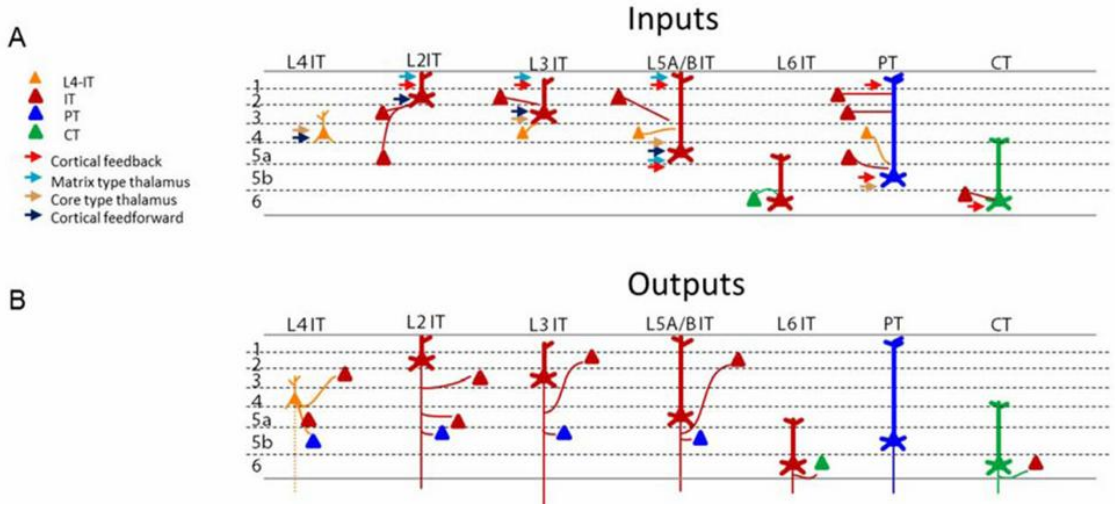

Figure 17. Hypothetical excitatory connectivity between major cortical excitatory cell classes. Panel (A) shows the proposed patterns of excitatory inputs to six main excitatory neuron types across cortical layers, while panel (B) depicts their outputs. Connectivity includes projections from other cortical neurons (feedback and feedforward) and from matrix- and core-type thalamic inputs. The model is based primarily on data from rodent barrel and motor cortex, with some projections omitted due to limited or conflicting evidence. For visualization clarity, inputs and outputs are often shown within the same layer, although most synapses occur on perisomatic dendrites (Harris & Shepherd, 2015).

But how are neocortical circuits organized? The neocortex implements a common processing strategy to handle multimodal sensation, motor control, and cognitive functions, such that the same circuit plan is quantitatively adapted in each area to the demands of its processing. Within this plan, excitatory neurons are organized into three major classes: intratelencephalic (IT) neurons, distributed across layers 2-6 and uniquely responsible for connecting both hemispheres as well as other telencephalic structures; pyramidal tract (PT) neurons, large pyramidal cells of layer 5B that constitute the primary output pathway to multiple subcerebral targets (brainstem, spinal cord, thalamus, basal ganglia) in addition to local branches; and corticothalamic (CT) neurons of layer 6, which project back to the thalamus and modulate thalamo-cortical exchange. These classes exhibit asymmetric and sequential local connectivity with multiple points of entry and exit: layer 4 IT cells rapidly receive thalamic input and transform it; layer 2/3 IT neurons integrate and redistribute information (typically via sparse coding in vivo); layer 5B PT neurons aggregate computations and transmit them to subcortical targets (with denser coding); and layer 6 CT neurons adjust gain and information flow (highly sparse activity), thereby ensuring that the cortex flexibly receives, integrates, decides, and modulates according to task and state. The

excitatory scaffold is regulated by a conserved sequential inhibitory circuit comprising three principal classes: Vip interneurons (Htr3a subclass, predominant in layers 2/3 and 1), which receive corticocortical inputs and primarily suppress other interneurons; Sst interneurons, which inhibit the dendrites of excitatory cells as well as Pvalb interneurons; and Pvalb interneurons, which receive strong feedforward thalamic and corticocortical inputs and perform perisomatic inhibition, enabling behaviour-dependent disinhibition or attenuation (e.g., during locomotion or whisking), with effects varying by area. The remaining connections are interareal, following hierarchical feedforward and feedback routes with characteristic laminar origins and targets, mediated by distinct IT subclasses. This organization enables the combination of ascending sensory evidence with descending context and goals (attention, prediction), and explains how quantitative variations (cell density, synaptic strength, sublamination of layer 4) built upon a shared blueprint generate functional specializations spanning perception, action, and cognition (Harris & Shepherd, 2015) (**Figure 17**).

Using more modern techniques such as single-nucleus RNA sequencing and spatial transcriptomics (MERFISH), the human cerebral cortex (neocortex) can be defined as a mosaic of eight analysed areas (M1, S1, A1, V1, DFC, ACC, MTG, AnG) that share a canonical cellular plan of 24 neuronal and glial subclasses present across all regions. Their identity does not depend on possessing 'unique' types, but rather on the quantitative combination (proportions) and transcriptomic signature of these same types. This quantitative cytoarchitecture means that, although the basic catalogue is common, each area is distinguished by how much of each subclass it contains and how its genes are expressed. Excitatory neurons show the greatest areal variation (whereas inhibitory neurons are more uniform across areas). Moreover, spatial gradients exist such that transcriptomic similarity decreases with distance along the cortical sheet. For instance, V1 stands out for its specialization: expansion and diversity of L4 IT, a high E:I ratio (≈4.5:1 globally and up to 10:1 in L6), specific corticothalamic and interneuronal types, and multiple consensus types enriched within this region (Jorstad et al., 2023).

2.2. Multisensory integration

Perceiving the environment is not a simple task. Although individuals are exposed throughout life to stimuli from multiple modalities, such as vision, hearing, and touch, reconstructing reality in the brain relies on multisensory input. Moreover, the most crucial aspect of creating a coherent and accurate perception involves the combination of sensory inputs. This process has been extensively studied primarily at the mesoscopic level using techniques such as EEG (electroencephalography) (Bertonati et al., 2023; Rossi Sebastiano et al., 2024) and fMRI

(functional magnetic resonance imaging) (Alwashmi et al., 2024) in human subjects. Studies in primates, which also investigate sensory integration, conclude that possibly the entire neocortex is in some way multisensory, implying that the senses do not function independently during the cognitive process of reconstructing reality in the brain (Ghazanfar & Schroeder, 2006; Kayser & Logothetis, 2007). Other research in rodents suggests that the mechanism behind sensory integration resides in different neuronal microcircuits that operate in parallel and are flexibly recruited based on factors such as the stimulus characteristics and behavioural constraints (Meijer et al., 2019; Oude Lohuis et al., 2024; Xu et al., 2020).

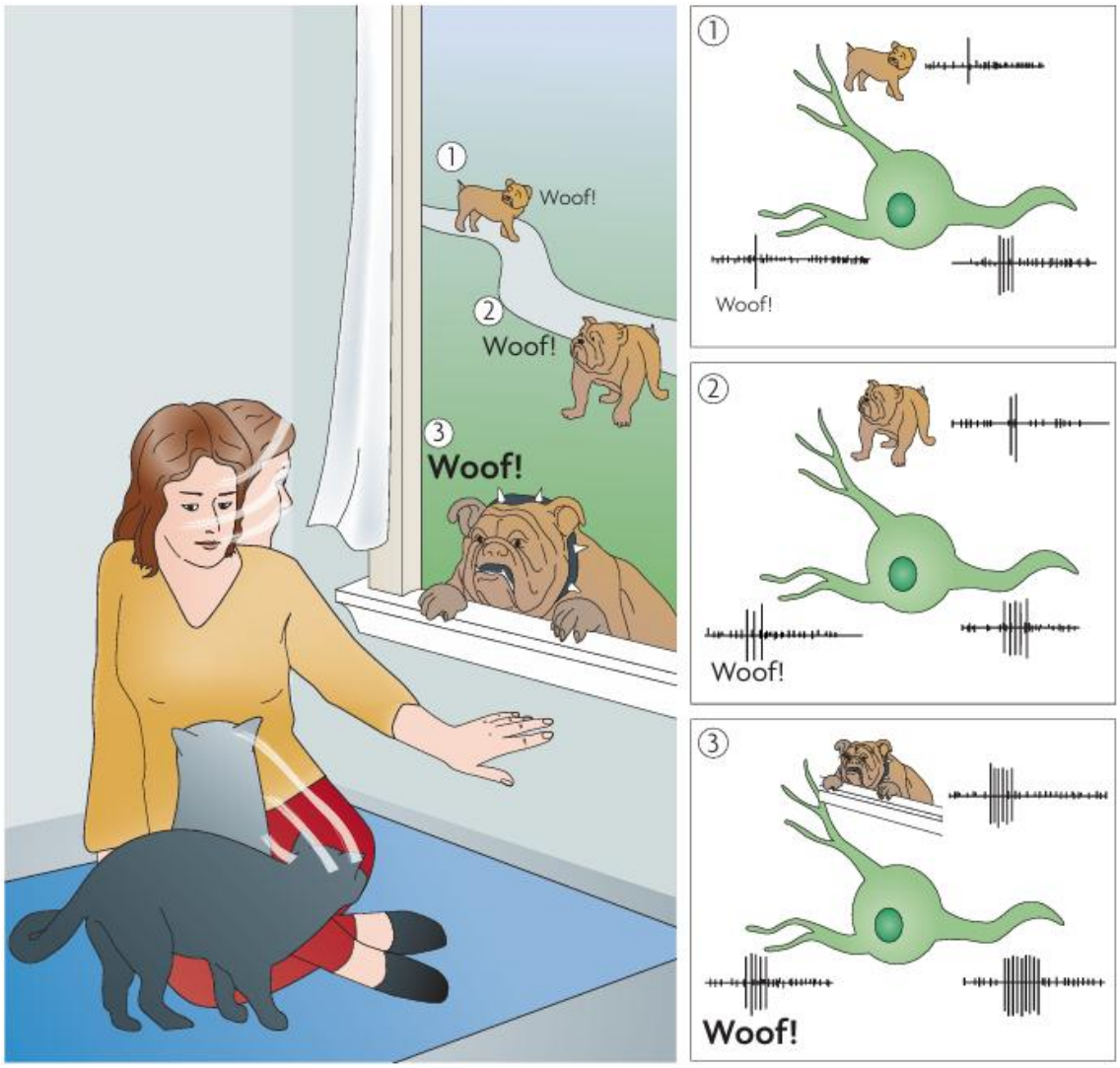

Figure 18. Multisensory integration enhances detection and response depending on stimulus strength. The figure illustrates how a woman and her cat respond to an approaching dog using both auditory and visual cues. When the dog is distant and signals are weak (top), the brain combines inputs from both senses in a superadditive way, producing a stronger-than-expected neural response. As the dog gets closer and sensory cues become stronger (middle and bottom), integration becomes additive and eventually subadditive, where

the combined response is still greater than either single input but no longer exceeds their sum. This principle reflects how multisensory integration is most beneficial under low-salience conditions (Stein & Stanford, 2008).

There are several cortical regions where multisensory neurons are found, such as the anterior ectosylvian cortex (AES) in cats or the superior temporal sulcus (STS) in primates. At the neuronal level, multisensory integration is said to occur when the response to a combined stimulus (e.g., a light and a sound together) is significantly different from the response to the most effective unimodal stimulus alone, whether as multisensory enhancement or multisensory depression. This process is governed by several principles: the spatial principle, in which stimuli from different senses must coincide in space to be effectively integrated; the temporal principle, in which stimuli must also coincide in time (although the 'integration window' can be broad); inverse effectiveness, whereby the less effective the individual stimuli, the greater the benefit of their integration; and super additivity, in which the integrated response in some cases exceeds the arithmetic sum of the individual responses. But the cortex itself also carries out multisensory integration, albeit in a more complex fashion, for instance by considering semantic congruence (such as associating a face with a voice). It can generate perceptual illusions (such as the McGurk effect or ventriloquism) and further contributes to higher cognitive functions including language, memory, and decision-making (Stein & Stanford, 2008) (**Figure 18**). Other authors define it as the process by which the brain combines information from different senses to generate a unified perception or behaviour. This phenomenon is not simply about registering multiple stimuli, but about actively fusing them to optimize detection, identification, and responses to environmental events. They emphasize that multisensory integration can be observed both at the behavioural and neuronal level and is likewise measured by comparing the response to a combined stimulus (Stevenson et al., 2014) (**Figure 19**).

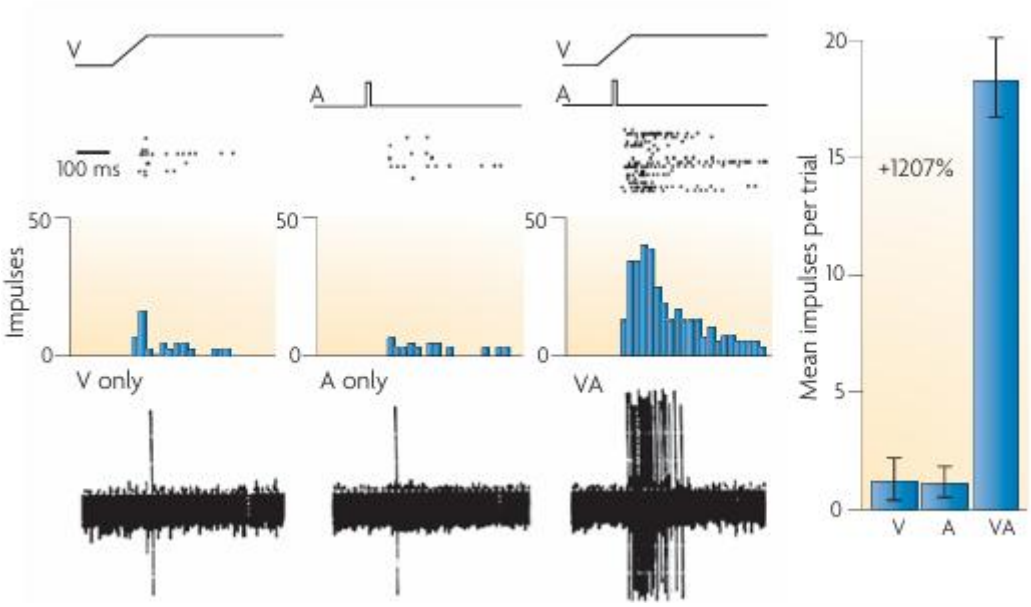

Figure 19. Multisensory enhancement in a single superior colliculus neuron. The figure shows the neuronal response to visual (V), auditory (A), and combined visual-auditory (VA) stimuli in a superior colliculus neuron. Raster plots, histograms, and oscillograms illustrate that the combined VA stimulus elicits a markedly greater response than either unisensory input alone. The bar graph on the right quantifies this enhancement, revealing a superadditive effect (+1207%), a hallmark of multisensory integration. This response exceeds the sum of the individual components, demonstrating the nonlinear nature of sensory integration at the neuronal level (Stein & Stanford, 2008).

2.3. Multisensory neocortex

This question has fuelled ongoing debate within the scientific community, with an extensive body of literature supporting the view that multisensory processing is a fundamental property of the neocortex. The typical view is that multisensory integration is a process restricted to higher-order brain regions and occurs only after information has been processed within lower-level, modality-specific sensory cortices. However, multisensory research has given rise to a new perspective on brain organization and perception, in which the convergence and integration of different senses within low-level cortices is the norm (Murray et al., 2016).

The classical idea that the mammalian neocortex is organized into six layers, each with specific neuronal types and connections, and that these layers are fundamental for information processing, is being increasingly challenged by the scientific community. For example, Guy & Staiger (2017) used the reeler mouse model, which carries a mutation in the reelin protein and develops a brain without normal cortical lamination, where neurons are intermixed rather than arranged in layers.

Their findings were striking despite this disorganization, the reeler mouse retains largely normal sensory functions. Its somatosensory and visual systems display organized maps, and the animal is capable of perception, learning, and memory almost comparable to that of a normal mouse.

On the other hand, functional magnetic resonance imaging (fMRI) has been used to investigate how the human brain integrates visual and auditory information during speech perception, with a focus on the phenomenon of lipreading. These studies conclude that the visual perception of speech can activate the same brain areas as auditory speech perception, supporting the idea that the brain integrates sensory inputs at an early and automatic stage, probably at a prelexical level (before words are identified as such). Interestingly, this may also explain phenomena such as the McGurk effect, in which what we see can alter what we believe we hear (Calvert et al., 1997).

QR code and URL linking to a BBC Horizon video that demonstrates the McGurk effect: mismatched visual (/ga/ or /fa/) with an audio /ba/ makes most listeners perceive /da/; watch once with eyes open and again with eyes closed to notice the shift. Scan the code or visit:

https://youtu.be/2k8fHR9jKVM?si=9hVemXdhCxhkPkl4

In another study, the existence of direct anatomical connections between the auditory and visual cortices in the human brain was investigated. Although it is known that sounds can influence visual perception, the precise neural pathways underlying this effect had remained unclear. Previous studies in primates had demonstrated direct axonal connections between auditory and visual areas, but such connections had not been confirmed in humans. Using diffusion tensor imaging (DTI) combined with probabilistic tractography, water diffusion in the white matter was modelled and thousands of fibre trajectories were estimated from each seed region voxel. The analyses examined fibres crossing to the contralateral hemisphere, reaching the thalamus or cerebellum, or projecting toward the occipital cortex. The study suggested the existence of white matter tracts directly connecting the auditory and visual cortices (in humans), providing structural evidence to support multisensory integration and crossmodal plasticity (Beer et al., 2011). Perception itself is a multisensory and dynamic process, and therefore inherently requires multisensory integration. This integration is not an isolated phenomenon, but rather a manifestation of how the brain as a whole combines information in a flexible and adaptive manner, which is essential for learning, communication, and survival (van Atteveldt et al., 2014).

Bennett's model of a neocortical microcircuit repeated across macrocolumns integrates well with this multisensory view of the brain. If all macrocolumns share the same architecture and perform the same computations, as Bennett argues, then it is not surprising that multisensory integration is not restricted to higher hierarchical levels but also occurs in primary sensory cortices. Rerouting studies have shown that when visual information is redirected to the auditory cortex, it can be

processed as if it were vision, suggesting that the function of a cortical region depends more on the type of input it receives than on its internal structure (Bennett, 2020).

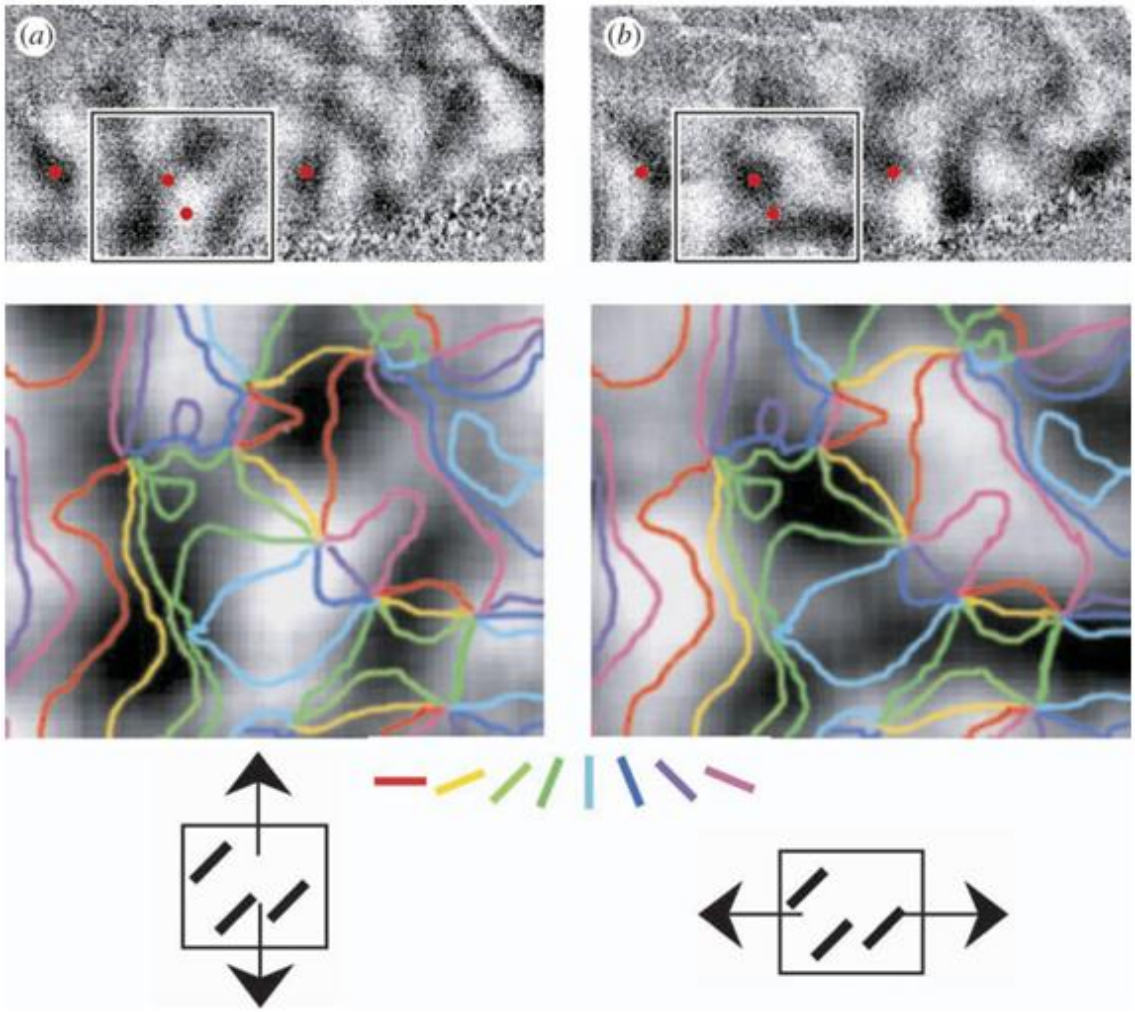

Figure 20: Context-dependent activation in V1. Optical imaging from ferret primary visual cortex in response to short 45° bars moving (a) vertically and (b) horizontally. Top: difference maps shown in grayscale; the inset outlines the region enlarged below. Coloured lines: iso-orientation contours taken from an independent grating-angle map; each colour denotes a different preferred orientation and is shown only as a reference to the orientation map, not as an additional signal. Red dots: fiducials to align the same cortical region between (a) and (b). Icons: direction/axis of stimulus motion. Note that, despite identical orientation (45°), the activation pattern differs markedly with motion direction, consistent with the conclusion that population activity is not fixed by a static "orientation map" alone but emerges from the integration of spatiotemporal stimulus parameters (data from Basole et al., 2003)(Horton & Adams, 2005).

Another striking example comes from the long-debated concept of the cortical column. For decades, columns were considered the fundamental building blocks of neocortical organization, providing a canonical unit repeated across the cortical sheet. However, Horton & Adams (2005) reviewed fifty years of research and concluded that columns may not have a necessary or universal

function. Their analysis showed that some species possess ocular dominance or orientation columns, while others lack them entirely, yet both exhibit comparable perceptual abilities (**Figure 20**). Even within the same species, or in different cortical regions of the same individual, columns can vary dramatically in size or even be absent without any obvious functional deficit. This variability undermines the idea that columns are indispensable processing units. Instead, it supports a more flexible view of neocortical organization, in which perception and cognition emerge from distributed and dynamic networks rather than from rigid, modular units (**Figure 21**). This perspective aligns well with the notion of the neocortex as a multisensory and adaptive system, capable of integrating diverse inputs across modalities.

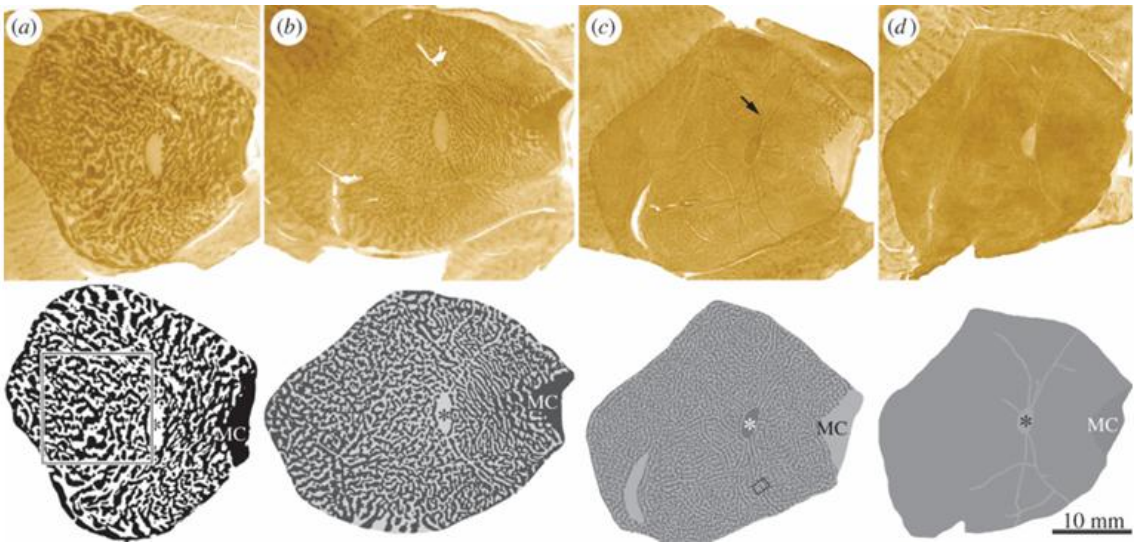

Figure 21. Variability in the expression of ocular dominance columns across individuals. Cytochrome oxidase staining of layer 4C in the striate cortex of four squirrel monkeys after enucleation of one eye. The examples illustrate a wide spectrum: from well-defined, large columns (a) to intermediate (b), fine (c), and nearly absent columns (d). Despite this variability, all animals retain normal visual perception, suggesting that ocular dominance columns are not essential for cortical function. This variability challenges the notion of a fixed, canonical architecture and supports the view of the neocortex as a flexible and adaptive system (Horton & Adams, 2005).

Taken together, these findings challenge the traditional notion of the neocortex as a rigidly modular structure defined by canonical columns or laminar architecture. Instead, evidence from both animal models and human studies supports a view of the neocortex as a dynamic and multisensory system, where functional organization emerges flexibly from distributed networks rather than fixed structural units. The variability of columnar expression across species and

individuals, and the context-dependent activation of cortical circuits, emphasize that perception and cognition rely less on uniform microarchitecture than on the brain's capacity for adaptive integration. This perspective not only reframes our understanding of cortical organization but also highlights multisensory processing as a fundamental and unifying principle of neocortical function.

2.4. Multisensory V1

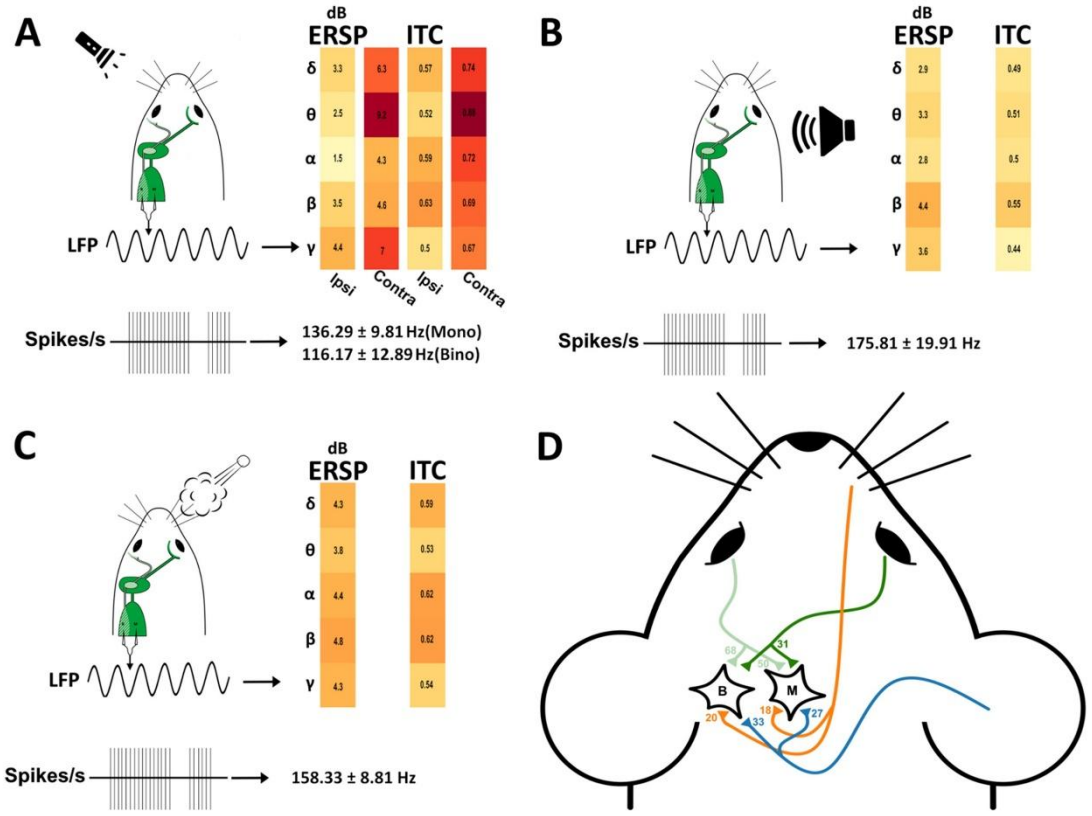

Figure 22. Differential processing of sensory stimuli in V1. (A-C) Neural responses to ipsilateral visual, auditory, and somatosensory stimulation. Each panel illustrates the stimulus type (top), the corresponding local field potential (LFP) response, multi/single-unit firing rate, and spectral analysis of the evoked activity. Heatmaps show ERSP (dB) and inter-trial coherence (ITC) across different frequency bands (δ, θ, α, β, and γ). (D) Example neurons from the monocular (M) and binocular (B) regions of V1 and their respective sensory inputs. Response latency diagram summarising the estimated latencies for each sensory modality. Somatosensory input exhibits the shortest response time (18 ms), auditory input activates V1 at 30 ms, while visual stimulation leads to longer latencies: 50-68 ms for ipsilateral stimulation and 31 ms for contralateral stimulation.

In recent studies such as that of Caballero Tapia et al. 2025, it is highlighted that the primary visual cortex (V1) is driven mainly by contralateral visual input, but it can also be modulated by auditory and somatosensory stimuli, showing notable differences in response latency and neuronal firing rate. These findings add to a growing body of literature that questions the traditional view that multisensory integration occurs exclusively at higher cortical stages following independent processing in specific sensory areas. Indeed, electrophysiological and anatomical studies in humans and primates have demonstrated that early cortical regions, classically considered unisensory, integrate information from multiple modalities at very early stages of cortical processing (J. J. Foxe & Schroeder, 2005; Schroeder & Foxe, 2005).

In the aforementioned study by Caballero Tapia et al. 2025, they reported differences in terms of latency and firing rate between the monocular and binocular regions of V1. They also described an interesting finding that the non-visual stimuli used in the study evoked responses in V1 more rapidly than those evoked via visual stimulation. This has also been described in other works such as J. Foxe & Simpson, 2002.

It has also been described how the beta frequency band may play a transversal role in multisensory integration; in other cortices, this band participates in sensorimotor integration and higher functions (Baker, 2007; Lalo et al., 2007), and in humans it has been linked to sensory gating phenomena (Hong et al., 2008). In the model used in this study by Caballero Tapia et al. 2025, ipsilateral visual stimulation and contralateral somatosensory stimulation increased beta coherence (see Figure 22A, C), in line with observations in the human somatosensory cortex (Cheron et al., 2007). Moreover, beta has been associated with improvements in visual perception during rehabilitation (Cho et al., 2015) and with the global modulation of visual information transmission (Dubey et al., 2023; Wróbel, 2000). On the other hand, in awake primates beta oscillations have been linked to phase-dependent mechanisms of short-term synaptic plasticity (Womelsdorf & Hoffman, 2018; Zanos et al., 2018), in keeping with its role in attention, learning and cortical reorganisation, and with its consistent presence irrespective of stimulus modality (Mongillo et al., 2008; Singer, 2017). Gamma activity, by contrast, increased with visual stimulation (Figure 22A), consistent with its role in active visual processing, while alpha synchronisation was the weakest except in the somatosensory condition, in line with alpha suppression during active tasks (Toscani et al., 2010). These patterns relate to findings on intersensory switching in human EEG, where switching modality reduces sensory alpha coherence and increases frontal theta, suggesting an attentional cost and cortical reconfiguration (Vanneau et al., 2024); the increase in theta coherence with contralateral repetition could reflect a similar mechanism of anticipatory preparation. In comparative terms across stimulation modalities, the auditory modality evoked lower gamma power and coherence, for example (Figure 22B), than those evoked by somatosensory and visual inputs. This cannot be attributed to

perceptual limitations for the frequency band employed, as high-frequency hearing loss in C57BL/6J mice begins above ≈18 kHz (Heffner et al., 2001), and the auditory stimuli used were in the mid-low frequency range. Possible auditory or mechanoreceptive contamination of the somatosensory air-puff stimulus was also considered. Measurements showed that the air-puff did not exceed 30 dB against a background noise of 60-70 dB, and no systematic eyelid closures were observed; moreover, the latencies recorded after the air-puff were consistent with rapid somatosensory transmission to V1. Although a minor contribution of auditory or ocular signals cannot be completely excluded, the controls implemented and the temporal signatures support the conclusion that V1 was genuinely activated by somatosensory input.

One possible explanation for why somatosensory stimulation induced generalised increases in power and phase coherence is that this could be due to its functional proximity to S1 and to the sensitivity of beta and gamma to such input (Figure 22C) (Kisley & Cornwell, 2006). Some authors have shown that V1 significantly influences S1 activity in mice of the same strain, without full reciprocity from S1→V1 (Dinh et al., 2024), which may help explain the active response of V1 to somatosensory input (Massé et al., 2016). In humans, early somatosensory evoked potentials (frontal N30 component) increase when tactile stimulation is accompanied by visual observation of the stimulated hand, probably via beta modulation and reorganisation of ongoing oscillations (Cebolla & Cheron, 2015; Rossi et al., 2002).

At the neuronal level, it has been reported that V1 neurones not only respond to visual stimuli, but also encode variables such as decision and reward, reinforcing the view of V1 as a multisensory area that integrates non-visual information (Zhang & Zador, 2023). In this vein, audio-somatosensory integration in V1 may require higher firing rates owing to the complexity of cross-modal interaction: temporal congruence in audiovisual input has been shown to increase firing rates, whereas incongruence suppresses them (Meijer et al., 2017; Wang et al., 2008). Other authors report earlier latencies evoked by auditory than by visual stimuli in V1 (≈27 ms for auditory versus ≈40 ms for visual) (Oude Lohuis et al., 2024), and S1 shows somatosensory responses at ≈10 ms, consistent with latencies of ≈18 ms in V1 for somatosensory input (Ahissar et al., 2000) (Figure 22D). Cross-modal interactions have also been documented in other cortices: in the ferret auditory cortex, ≈15% of primary neurones are modulated by vision, rising to nearly 50% in higher-order auditory areas (Bizley et al., 2007); in mouse S1, visual stimuli modulate tactile processing via theta and gamma oscillations (see Figure 22A, C), and inactivation of V1 with lignocaine indicates that V1-S1 connections are critical for this modulation, although tactile responses do not disappear completely, suggesting additional subcortical support (Sieben et al., 2013).

On the other hand, it is worth noting that these effects of multisensory integration may be related to plastic states facilitated by locomotion, since locomotion increases firing rates in V1 and improves visual encoding by reducing noise and response times, suggesting a better adaptation of V1 for efficient multisensory processing (Dadarlat & Stryker, 2017; Stryker, 2014). In addition, specific inhibitory networks can modulate this integration: VIP interneurones, implicated in cortical plasticity, can facilitate the incorporation of non-visual signals by adjusting firing rates (Y. Fu et al., 2015; Mesik et al., 2015), while PV+ interneurones may contribute to sensory selection via gamma synchronisation (Womelsdorf et al., 2014).

2.5. Relevance for vision loss and sensory substitution

As previously mentioned, vision loss has a profound impact on patients' quality of life. Consequently, there has always been considerable interest in finding a "substitute" for the loss of visual input, such as sensory substitution devices (SSDs), which convert visual information into auditory or tactile stimuli (e.g., Braille or the vOICe). Although significant limitations remain, whether due to technical challenges, the lack of standardized training, cost, discomfort, or social factors, SSDs hold promising potential; however, their practical adoption remains limited (Maidenbaum et al., 2014).

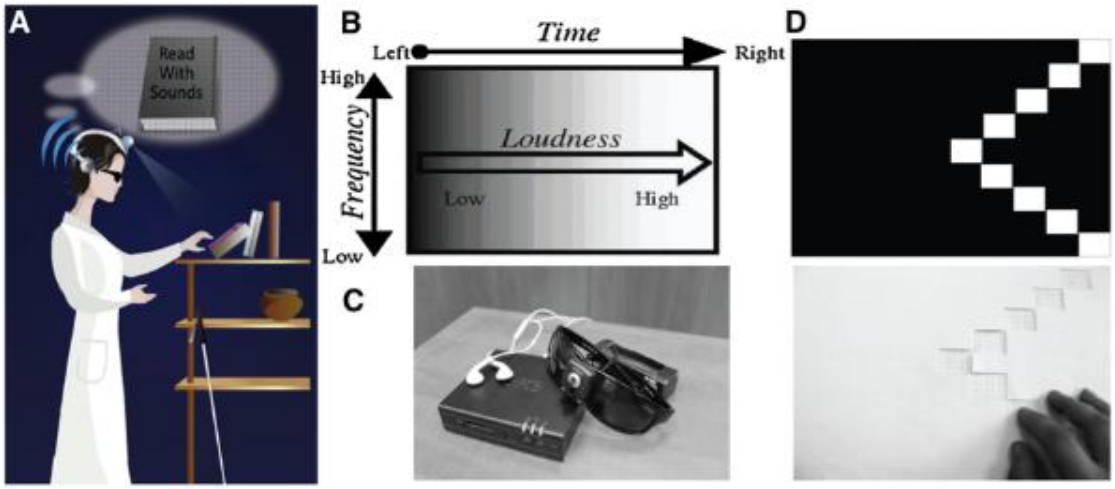

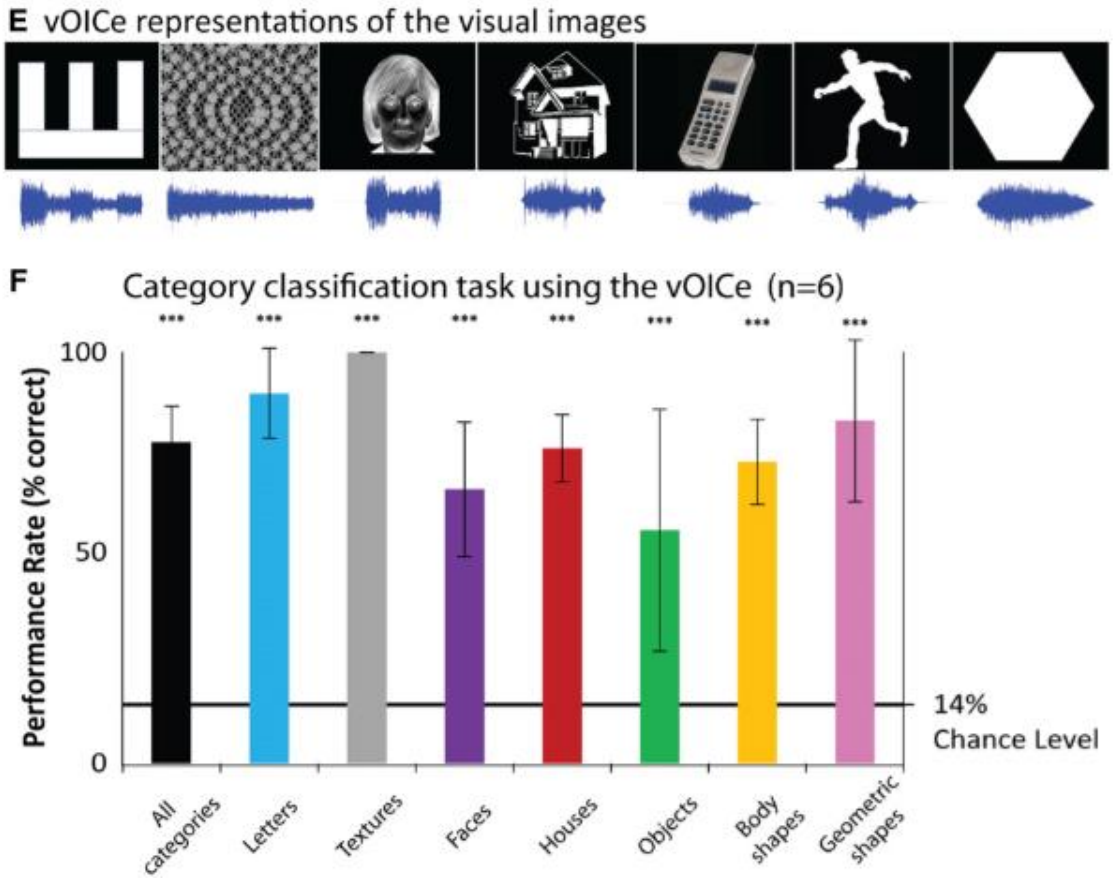

Figure 23. "Visual" Performance in Blind Users of the vOICe Sensory Substitution Device after Training. Visuo-auditory sensory substitution is employed to convey visual information to blind individuals through their intact auditory channel. The vOICe transformation algorithm scans each image from left to right, such that time and stereo panning correspond to the horizontal axis, pitch frequency to the vertical axis, and sound intensity to pixel brightness. The mobile kit of the device includes a lightweight camera mounted on glasses, a portable computing unit (such as a computer or smartphone), and headphones. To facilitate learning, tangible feedback of the images was provided, identical to those presented through the vOICe. The two-dimensional training program comprised hundreds of stimuli organized into structured categories, including Hebrew letters, textures, faces, houses, everyday objects and tools, body postures, and geometric shapes. Accuracy in the category-classification task after training (n = 6) averaged 78.1% ± 8.8% (SD), which was significantly above chance level (14%, $p < 0.00005$). No differences were observed between performance with letters and with the other categories ($p > 0.05$, corrected for multiple comparisons). Error bars represent standard deviation, and statistical significance is indicated relative to chance level ($p < 0.05$, **$p < 0.005$, ***$p < 0.0005$) (Striem-Amit et al., 2012).*

The lateral occipital tactile-visual (LOtv) region of the brain is specialized in processing object shape. Logically, one might expect this associative area to be active only when receiving visual input or tactile input (e.g., object palpation). However, it can also be activated when individuals listen to specialized sounds that represent object shape through the vOICe system, though only if

the individual has learned to extract shape information from those sounds. If the association is limited to linking a sound with an object without encoding its shape, the LOtv region will not be engaged. Moreover, this constitutes a clear case in which neural activity can be associated with distinct sensory inputs, as both sighted and blind individuals can be trained in this system and thereby activate this shape-recognition region through sound (Amedi et al., 2007). Similarly, another region of the left ventral occipito-temporal cortex, normally specialized in the visual recognition of letters in sighted individuals, the Visual Word Form Area (VWFA), can be specifically and selectively activated in blind individuals by letters encoded through the vOICe system, as compared to other auditory stimuli representing objects, faces, houses, and so forth (Striem-Amit et al., 2012) (**Figure 23**).

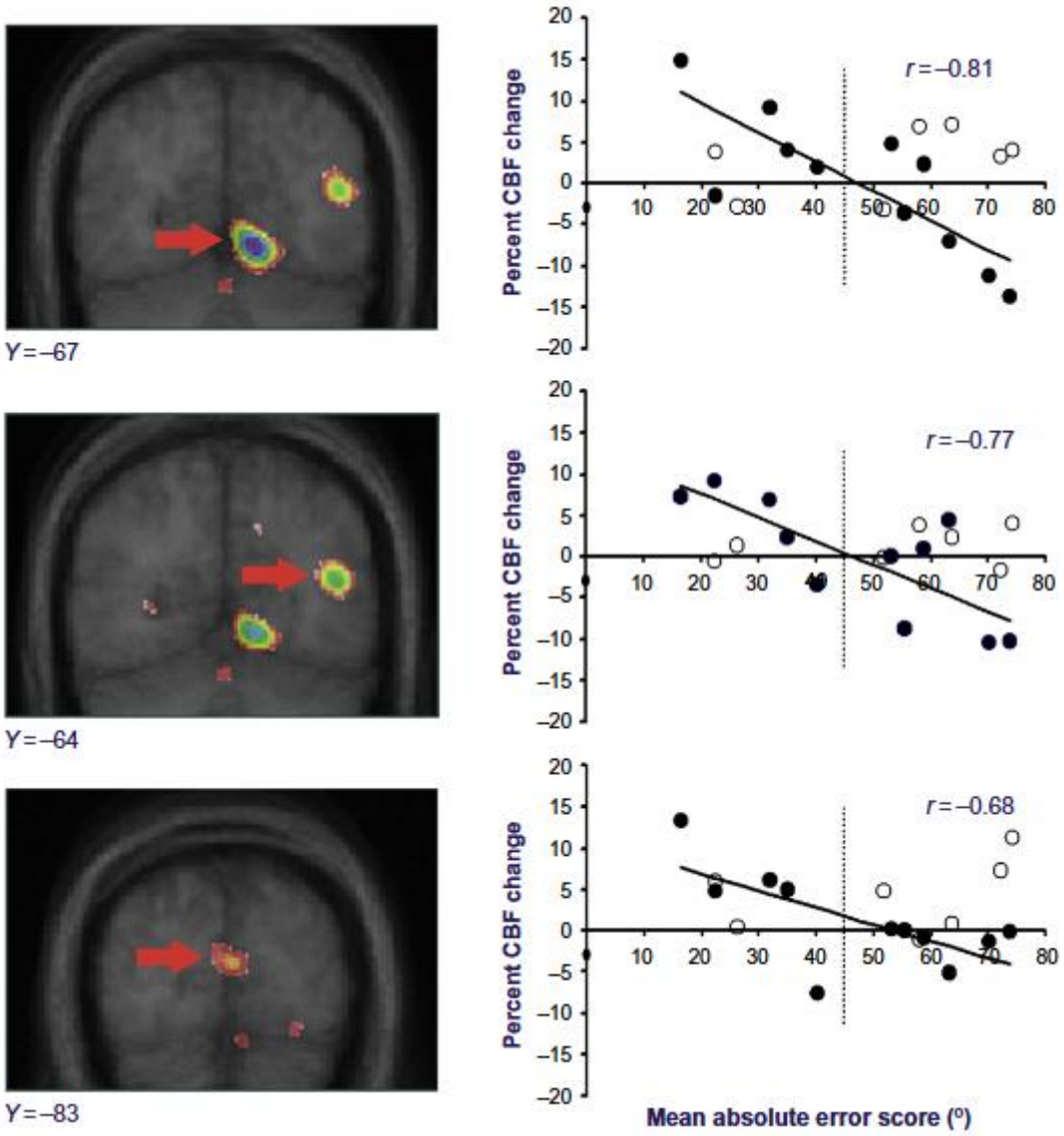

Figure 24. Correlation between performance in a monaural sound localization task and brain activation measured by PET (positron emission tomography) in blind subjects. Brain images show regions of the occipital cortex, ventral extrastriate (top), dorsal extrastriate (middle), and striate (bottom), where activity

was related to accuracy in auditory localization. Black circles represent blind participants, and white circles represent sighted controls; regression lines were fitted to the data from the blind group. These findings illustrate how the occipital cortex, typically devoted to vision, can be recruited to process auditory information in the absence of visual experience, providing evidence of functional reorganization of the brain following blindness (Frasnelli et al., 2011).

In a natural and general manner, blind individuals may develop advantages in other senses, particularly audition and touch. Behavioural findings have documented enhanced sound localization, faster performance in auditory and tactile attention tasks, and greater tactile precision in activities such as Braille reading or texture discrimination. At the cerebral level, it has been described how the occipital cortex, typically devoted to vision, is recruited to process auditory, tactile, or even olfactory information, evidencing a profound functional reorganization. In chronically deaf patients, improvements have been observed in visual attention and in the perception of stimuli in the peripheral visual field, while neuroimaging studies show that auditory areas can be reorganized to respond to visual stimuli, further indicating cross-modal plasticity (Frasnelli et al., 2011) (**Figure 24**).

Beyond the potential of sensory substitution devices, these findings must be understood within the broader framework of brain plasticity after sensory loss. Blind individuals often develop enhanced tactile acuity, superior auditory localization, and improved verbal memory, while deaf individuals show more efficient peripheral and motion-related visual processing. Such compensatory behaviours reflect cortical reorganization, with occipital areas in the blind and auditory areas in the deaf recruited to process remaining inputs. Human and animal studies suggest that this cross-modal plasticity likely involves the unmasking of pre-existing cortico-cortical connections and shifts in connectivity and is strongly influenced by the timing of deprivation. Although the brain remains plastic in adulthood, changes are more robust when loss occurs early in life. Plasticity, however, is not always beneficial: in some cases, it may hinder outcomes of vision-restoration or cochlear implants. For rehabilitation, this duality highlights the need for strategies that enhance adaptive reorganizations while minimizing negative effects, such as combining targeted training with non-invasive brain stimulation. A nuanced understanding of plasticity is essential to design interventions that truly improve quality of life in individuals with sensory loss (Merabet & Pascual-Leone, 2010).

3. Visual System and Plasticity: Scope and Limits

3.1. Structure and function of the visual cortex

The human primary visual cortex (V1) undergoes five developmental stages across the lifespan. In the first year, the foundations of vision and plasticity are rapidly established through changes in excitatory and inhibitory receptors. Between 1 and 4 years of age, vision improves with experience and substantial variability in plasticity mechanisms emerges, facilitating learning. From 5 to 11 years, many visual functions reach maturity and synaptic mechanisms stabilize, progressively reducing plasticity. During adolescence and early adulthood (12-55 years), complex abilities such as face perception continue to refine, while plasticity gradually declines, though a useful margin for treatment remains. After 55 years of age, visual functions and plasticity decline, accompanied by structural and neurobiological changes associated with aging. Taken together, V1 displays a prolonged and dynamic developmental trajectory that shapes both normal vision and therapeutic potential (Siu & Murphy, 2018).

Visual information reaching the cortex begins in the retina. There, after phototransduction and the initial neuronal interactions, the only signal transmitted to the brain is a continuous stream of action potentials traveling along the axons of the ganglion cells. These axons form the optic nerve, cross at the chiasm, and ultimately project to the dorsal lateral geniculate nucleus (dLGN) of the thalamus, which acts as a relay station before reaching the cortex. Within the LGN, information remains organized into distinct layers: magnocellular layers, which receive input from large ganglion cells and are characterized by fast transmission; parvocellular layers, which receive input from smaller cells and preserve fine details of the image; and intercalated or koniocellular layers, which are associated with colour information. This division is preserved when the fibres reach the primary visual cortex: magnocellular projections terminate in sublayer 4Cα, parvocellular projections in sublayer 4Cβ, and koniocellular projections in the so-called “blobs” of layers 2/3. Once inside V1, however, the information does not remain confined to the recipient layer (Schmolesky, 2005) (**Figure 25**).

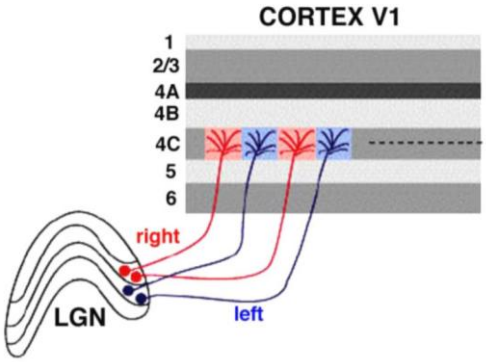

Figure 25. Ocular segregation in primary visual cortex (V1). Schematic of thalamocortical projections from the lateral geniculate nucleus (LGN) to layer 4C of V1, where afferents from each eye remain segregated in alternating ocular dominance columns (red: right eye; blue: left eye). In upper layers (2/3) these signals begin to converge, giving rise to binocular integration (Schmolesky, 2005).

The primary visual cortex in macaques is highly specialized, characterized by an exceptionally high density of neurons and synapses arranged in a laminar fashion (**Figure 26**). Nearly half of the neurons are located in Layer IV, reflecting its role as the principal recipient of thalamic afferents (O'Kusky & Colonnier, 1982). In parallel, a substantial population of GABAergic interneurons (≈15%) is distributed unevenly across layers, with their terminals precisely organized within the territories receiving input from the LGN. This arrangement suggests that local GABA-mediated inhibition constitutes a key structural mechanism for transforming thalamic input into the specific receptive field properties of V1 (Fitzpatrick et al., 1987). Furthermore, pyramidal neurons in V1 are arranged in vertical modules defined by clusters of apical dendrites and by cones of pyramidal cells in layers IVA/IVB, whose apical dendrites ascend in bundles to layers II/III. These modules thus represent basic units that, when combined through afferent input, may give rise to functional columnar systems (Peters & Sethares, 1991).

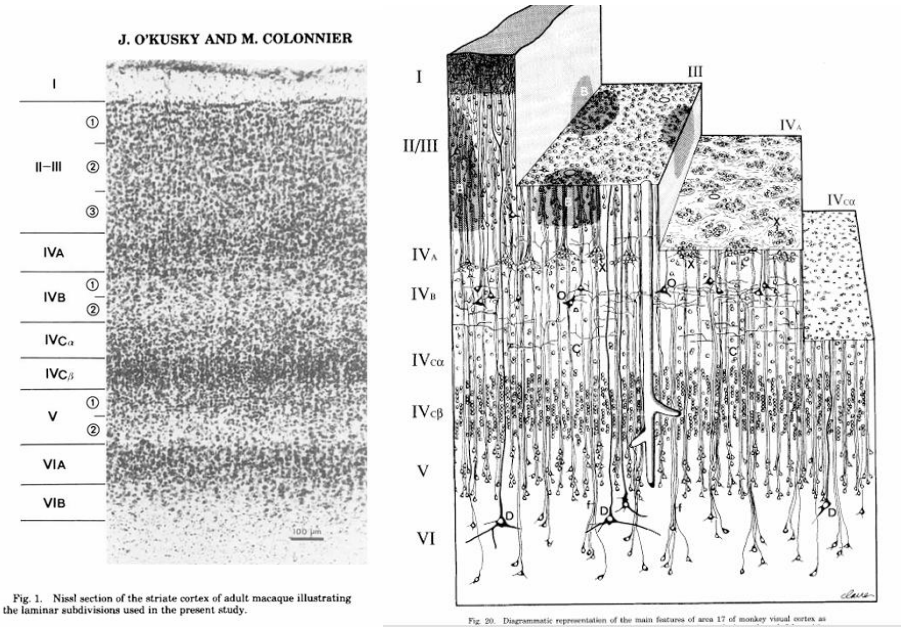

Figure 26. Laminar organization of area 17 (V1) in the macaque. Left: Nissl-stained section of the striate cortex showing the layers and sublayers as defined by O'Kusky & Colonnier (1982) for the quantitative analysis of neurons, glia, and synapses. Right: Schematic representation of the arrangement of pyramidal neurons and their apical dendrites across the layers, including the clusters and cones of pyramidal cells in the sublayers of IV, as described by Peters & Sethares (1991), highlighting the vertical modular organization that underlies the columnar architecture of V1.

The images received by the eyes are two flat projections, one per eye, but through a process known as binocular vision both signals are integrated, and their small differences are exploited to perceive depth, an ability referred to as stereopsis. In V1, neurons exhibit three fundamental properties related to binocular vision. The first is ocular dominance, that is, the tendency of each neuron to respond more strongly to one eye than to the other, which, as mentioned earlier, depends on how thalamic (dLGN) inputs reach the visual cortex. The second property is interocular matching of orientation preference, meaning that neurons ultimately respond similarly to lines and edges presented to either eye. The third is selectivity for binocular disparity, referring to the ability of certain neurons to detect the small positional differences between the two retinal images in order to compute depth. It remains unclear how inhibitory circuits participate in these processes, how the different cortical layers contribute, or what role structures such as the thalamus play before the information reaches the cortex. Moreover, results vary depending on the species studied: mice are valuable because of the genetic tools available, but animals such as ferrets or tree shrews provide visual systems more closely resembling those of primates (Cang et al., 2023) (**Figure 27**).

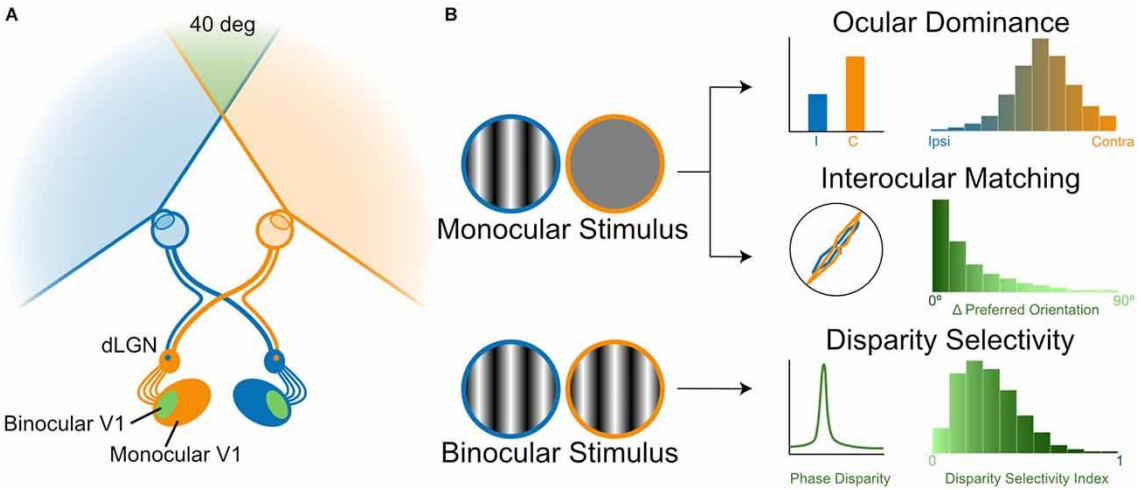

Figure 27. How the brain combines information from both eyes. In mice, each eye sends part of its nerve fibers to the same side of the brain and part to the opposite side. This arrangement allows the primary visual cortex (V1) to receive input from both eyes within the binocular field of view (approximately 40°). In this region, three key properties of binocular vision can be measured: (1) ocular dominance, when a neuron responds more strongly to one eye than to the other; (2) interocular matching of orientation, when the neuron learns to prefer the same orientation of lines or edges in both eyes; and (3) disparity selectivity, when the neuron detects small positional differences between the two retinal images and thereby contributes to depth perception (Cang et al., 2023).

Regarding the third principle, one group investigated this mechanism through neural intelligence. They explained that, in the early stages of vision (areas V1-V3), neurons represent disparity using a mechanism like cross-correlation: they compare images from both eyes but respond to both correct and false matches, thereby generating an ambiguous signal. As information advances along the visual hierarchy (areas V3A/B, V7, hV4, and hMT+), an additional process emerges, termed cross-matching, which filters out false matches and produces a more stable representation of depth. Using fMRI and random-dot stereogram stimuli (correlated, anticorrelated, and semi-correlated), it was shown that early visual areas privilege cross-correlation, whereas higher areas shift toward cross-matching. In parallel, a deep neural network (GC-Net) was trained to predict disparity in natural scenes. Although not explicitly designed to mimic the brain, the network exhibited a strikingly similar transformation: its initial layers operated like cross-correlation, intermediate layers combined both strategies, and final layers predominantly implemented cross-matching. In conclusion, both the human visual system and artificial neural networks appear to share a common computational principle: transforming ambiguous cross-correlation signals into robust representations through cross-matching, thereby enabling coherent depth perception (Wundari et al., 2025).

3.2. Mechanisms of cortical plasticity

The idea of plasticity was introduced by Cajal in 1892, when he spoke of 'cerebral gymnastics': the possibility that mental exercise could multiply interneuronal connections. In 1894, he explicitly used the term 'plasticity' to describe how neurons could adapt, branch, and form new connections in response to learning or experience. He also employed metaphors such as that of the brain as a garden, in which pyramidal cells are trees that, with intelligent cultivation, grow additional branches and bear more fruit (Rozo et al., 2024).

As previously mentioned, visual loss or deficiency has a profound impact on human life. However, visual functions can still be carried out by other cortical regions while brain plasticity remains high, as in childhood. Indeed, there are reports of children lacking an occipital cortex, either due to developmental absence or following hemispherectomy, who nevertheless retained visual sensitivity (Holloway, 2000; Werth, 2006). According to Heinen and Skavenski, no neural activity was observed within the lesion projection zone (LPZ) until three weeks after retinal lesioning (Heinen & Skavenski, 1991), whereas other authors have reported substantial changes only after two months (Darian-Smith & Gilbert, 1995), and still others have described reorganization within hours or even minutes post-lesion (Chino et al., 1992).

In V1, two different and well-studied forms of plasticity can occur. The first is intramodal plasticity. In adult mice, following optic nerve lesion, cortical reorganization has been observed, whereby signals from the intact eye are potentiated. Functional imaging revealed an immediate shift in ocular dominance towards the intact eye, due to the loss of responses from the injured eye, followed by a delayed increase in intact-eye responses after one to two weeks. This finding demonstrates that even in adulthood, the visual cortex retains the capacity for ocular dominance plasticity, a phenomenon previously thought to be restricted to early developmental stages (Vasalauskaite et al., 2019). The other type of plasticity is intermodal, or cross-modal. In adult animals (P120), it has been shown that recovery from monocular enucleation is not solely a visual process but a multimodal one. After the initial adjustment of the remaining eye, the deprived visual cortex gradually recruits inputs from auditory and somatosensory regions, revealing a clear cross-modal contribution to functional restoration. At earlier ages, such as P90, this cross-modal involvement is only beginning to emerge, resulting in an incomplete and transitional pattern of recovery. These findings underscore that multimodal plasticity strengthens progressively with age, becoming a defining mechanism of adult cortical adaptation and compensating for the reduced capacity of traditional ocular dominance shifts (Nys et al., 2014). Experiments in mice older than 110 days have shown that deprivation of whiskers or audition induces a transient shift

in ocular dominance, driven by an increased response to the ipsilateral eye. This is remarkable, since ocular plasticity, specifically, shifts in dominance induced by monocular deprivation, does not normally occur at this age. In other words, the manifestation of the phenomenon takes place within the visual modality, although its cause is cross-modal. This effect is further accompanied by synaptic strengthening in layer 4, a shift of the excitation/inhibition balance toward excitation, and dependence on NMDA receptors (Teichert et al., 2019). These findings have been reinforced by subsequent studies showing that cross-modal sensory deprivation can reopen plasticity mechanisms in the adult visual cortex. In particular, Rodríguez et al. (2018) demonstrated that one week of transient deafness restores the ability of thalamocortical synapses to express long-term potentiation (cross-modal reinstatement of TC-LTP) and accelerates ocular dominance plasticity. Importantly, this effect does not replicate classical juvenile plasticity based on the depression of closed-eye responses but instead occurs through an accelerated potentiation of open-eye responses, revealing a modality-specific form of plasticity characteristic of the adult brain.

3.3. Limits of plasticity after sensory loss

Van Brussel and colleagues introduced the concept of "windows of plasticity" in V1 in mice. These windows are highly relevant to the aims of the present project, as they depend on several factors, including species differences and the methodology used to assess plasticity. In their work, cortical reactivation after monocular enucleation was shown to follow a layer- and time-specific sequence: an initial reactivation of supragranular layers spreading from the binocular zone into the surrounding monocular cortex after approximately three weeks, followed later, between five and seven weeks, by the recovery of infragranular layers. Importantly, this latter recovery appeared to begin at the borders with nonvisual cortex and coincided with hyperactivation of adjacent somatosensory and auditory areas (Van Brussel et al., 2011). Therefore, in the present study we conducted a systematic investigation to determine the time point after enucleation at which a typical visual response would first emerge in V1 of C57BL/6 mice. Other authors reveal the existence of a presensitive period during adolescence, in which the capacity for visual cortical recovery is reduced. When monocular enucleation is performed at postnatal day 45 (P45), binocular regions regain activity relatively quickly, but monocular cortex areas remain persistently hypoactive, even after seven weeks. This incomplete reactivation differs from the robust and widespread recovery observed in adults. These findings indicate that adolescence is not simply an extension of the critical period of ocular dominance plasticity, but a distinct stage where the cortex shows limited potential to compensate for visual loss (Nys et al., 2014). In

juvenile mice, monocular deprivation during the critical period (the critical period for ocular dominance plasticity in rodents begins at the end of the third postnatal week; see Maffei *et al*., (2010)) readily induces a shift in ocular dominance in the primary visual cortex. However, this type of plasticity declines progressively with age, and in animals older than 110 days no changes are observed following monocular deprivation.

Amblyopia in children, commonly known as "lazy eye," arises when an imbalance in the input from both eyes occurs during the critical period of visual development, for example due to strabismus or monocular deprivation. Under these conditions, neurons in the primary visual cortex shift their ocular dominance toward the non-deprived eye, leading to a loss of sensitivity in the affected eye. If this situation is not corrected in time, before the end of the critical period, deficits in visual acuity and in depth perception through stereopsis become permanent. Furthermore, the maturation of specific inhibitory circuits has been shown to be crucial for both the opening and closure of the critical period. In addition, several "molecular brakes" have been identified that limit the capacity for reorganization beyond childhood, explaining why untreated amblyopia becomes irreversible. Finally, this line of research has opened the possibility of exploring strategies to reopen windows of plasticity in the adult brain, with a view toward future therapies for amblyopia (Cang et al., 2023).

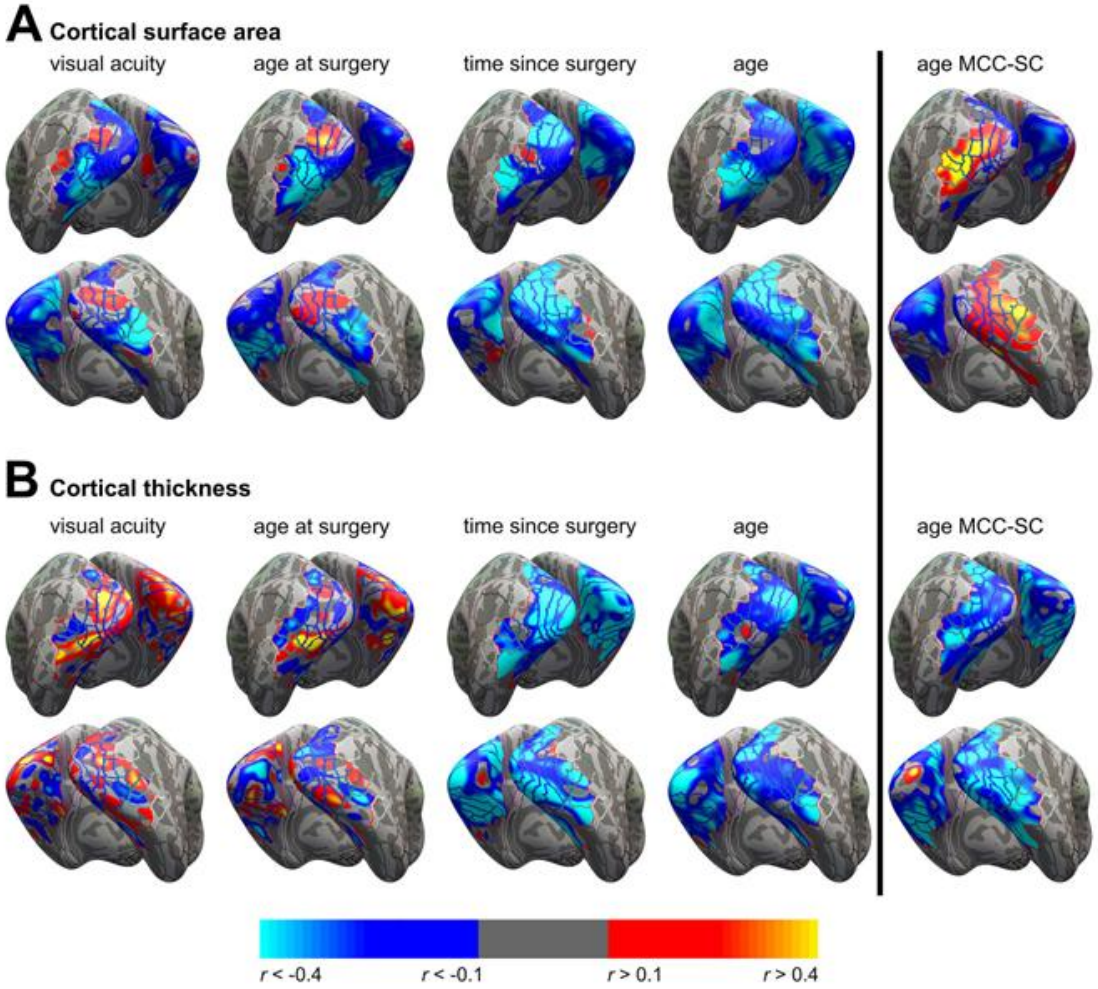

Figure 28. Brain projections representing correlation values between different clinical variables (visual acuity, age at surgery, time since surgery, and chronological age) and two structural measures: cortical surface area (A) and cortical thickness (B). Overall, poorer visual acuity after surgery was associated with reduced cortical surface area and increased thickness in visual regions. Colours indicate the strength and direction of the correlation (red/yellow: positive, blue/light blue: negative). The final column displays correlation patterns with age in a control group with normal vision (Hölig et al., 2023).

A study conducted in India has challenged the long-held belief that if a child does not receive visual stimulation during the so-called 'critical periods' of development (the first years of life), the brain would no longer be able to learn to see properly later on. The group examined children and adolescents in India who had been blind from bilateral cataracts since before their first year of life and did not undergo surgery until between 8 and 17 years of age. After surgery, many patients showed remarkable improvements in contrast sensitivity, that is, the ability to detect differences in light and patterns in the environment. In some cases, improvements were even faster than those typically observed in infants who develop vision normally. Although not all patients progressed equally, surprisingly, the age at which surgery was performed did not

determine the magnitude of improvement, suggesting that visual cortical plasticity may persist far longer than previously assumed (Kalia et al., 2014). On the other hand, also in India, researchers investigated the related question of what happens to the visual cortex if a person is born blind, later regains sight through surgery, but spends years without visual input. Using magnetic resonance imaging, they measured two aspects of the visual cortex, cortical surface area and cortical thickness, in 21 patients born with dense congenital cataracts (causing blindness from birth) who underwent surgery months or even years later. They found that individuals who recovered vision after congenital cataracts had a smaller visual cortical surface area and a thicker cortex compared to people with normal vision. These structural changes were similar to those observed in individuals with lifelong congenital blindness. In contrast, patients who lost vision later in childhood due to cataracts and then underwent surgery did not show such alterations. Moreover, the more abnormal the cortical structure, the poorer the visual acuity after surgery. This study therefore demonstrates the existence of a sensitive period in early brain development: if the brain does not receive visual input during the first months or years of life, the architecture of the visual cortex fails to develop normally. Although some vision can be recovered after surgery, cortical structure does not fully normalize, limiting functional recovery (Hölig et al., 2023) (**Figure 28**). Other studies confirm that there is an optimal window for surgery to restore vision, typically between 4 and 8 weeks of life, although this timing carries an increased risk of glaucoma. More importantly, however, achieving good visual outcomes in some children with unilateral congenital cataract depends primarily on early detection, consistent optical correction, and balanced patching therapy, rather than on the automatic choice of intraocular lens implantation in very young infants (Lambert, 2023).

3.4. The challenge of reactivating adult visual cortex

The loss of a sensory modality can trigger cross-modal plasticity, that is, the functional reorganization of the brain to enhance the use of preserved senses. In adults, this plasticity does not rely on large-scale structural changes but rather on the capacity of existing circuits to reorganize through functional plasticity processes. Such processes include long-term potentiation (LTP), long-term depression (LTD), and homeostatic mechanisms that regulate neuronal activity. Within this context, metaplasticity, understood as the “plasticity of plasticity”, acquires particular importance. A central model is the sliding threshold framework, which proposes that the threshold for inducing LTP or LTD is dynamically adjusted according to the neuron’s prior activity, thereby ensuring both network stability and adaptability to new conditions. This framework is expressed in two main scenarios: in sensory cortices deprived of their original modality, where latent inputs

from other senses can be strengthened and recruit the region for new functions; and in the cortices of preserved senses, where feedforward connections are reinforced and lateral connections weakened, thereby increasing selectivity and precision of sensory processing (Lee, 2023). The study by Teichert builds on this established framework and presents a novel finding: deprivation of a non-visual sense, such as whisker touch or audition, can transiently reinstate ocular plasticity in adult mice in which such capacity was no longer expected. Notably, this change in ocular dominance does not require monocular deprivation but emerges spontaneously after three days of non-visual sensory deprivation, driven by an increased response of the ipsilateral eye while contralateral input remains stable. Moreover, the effect is transient: after seven days ocular dominance levels return to baseline, suggesting the action of homeostatic mechanisms that stabilize the cortical network following the adaptation phase (Teichert et al., 2019).

4. Electrophysiological Approaches and Experimental Model

4.1. A brief history of brain electrophysiology

The development of electrophysiology as a scientific discipline dates to the seventeenth century, when the Dutch microscopist Jan Swammerdam laid the experimental foundations for studying the relation between nerves and muscles. Working with frog preparations, he showed that nerve stimulation elicited muscle contraction, an early, clear demonstration of tissue excitability. A century later Luigi Galvani revolutionized the field. In *De Viribus Electricitatis in Motu Musculari Commentarius* (1791), after a decade of experiments conducted with his wife Lucia Galeazzi and his nephew Giovanni Aldini, Galvani showed that electrical stimuli could trigger contraction even in isolated limbs. He advanced the idea of "animal electricity," comparing biological tissues to a Leyden jar, and argued that living systems possess intrinsic electrical properties. Galvani's claims sparked a famous debate with Alessandro Volta, whose work led to the first electric battery. Beyond science, this debate resonated culturally and has often been linked to Mary Shelley's *Frankenstein* (Verkhratsky et al., 2006).

During the nineteenth century, Galvani's central premise, endogenous bioelectricity, was vindicated. Carlo Matteucci demonstrated "injury currents," potentials between damaged and intact muscle, while Emil du Bois-Reymond developed sensitive instrumentation and recorded what he termed "action currents" in nerves and muscles. Their work transformed electrophysiology from descriptive observations of twitches into a quantitative biophysics of nerve and muscle function (Marshall, 1987). In parallel, technical innovations such as Gabriel

Lippmann's capillary electrometer (1872), Augustus Waller's first human electrocardiograms (1887), and, crucially, Willem Einthoven's string galvanometer (early 1900s) made it possible to record electrical activity with precision, laying the foundations of modern electrocardiography and the clinical mapping and diagnosis of arrhythmias (Micheli, 2011).

A decisive leap came with the analysis of the squid giant axon. In 1939 Alan Hodgkin and Andrew Huxley obtained the first intracellular recordings of an action potential, revealing a characteristic depolarization-repolarization sequence with overshoot. After World War II they adopted and refined the voltage-clamp technique originally introduced by Kenneth Cole and George Marmont, which allowed them to isolate ionic currents underlying excitability. Between 1947 and 1952 they built a comprehensive mathematical model of the action potential, introducing the gating variables *m*, *n*, and *h* to describe the time- and voltage-dependent behaviour of sodium and potassium conductances. Their equations, computed with mechanical calculators, reproduced the data with striking accuracy and inaugurated computational neuroscience. For these contributions Hodgkin, Huxley, and John Eccles shared the 1963 Nobel Prize (Schwiening, 2012).

In 1924 Hans Berger recorded the first human electroencephalogram (EEG), building on earlier observations by Richard Caton. Berger's careful work revealed rhythmic brain waves, introduced the concept of alpha-wave blocking, and provided early electrical evidence for the cortical basis of epilepsy, shifting views of seizures toward identifiable patterns of cerebral dysrhythmia (Brigo et al., 2025).

Electrophysiology reshaped auditory science. Building on nineteenth-century physiology (Johannes Müller, Emil du Bois-Reymond), Hermann von Helmholtz's theory of hearing, and Alfonso Corti's 1851 histology, researchers in the 1930s attempted direct stimulation of the auditory organ in humans (e.g., Andreef et al., 1934). In 1957 André Djourno and Charles Eyriès performed the first cochlear implant, and William House followed in 1961. Subsequent multichannel work (e.g., Blair Simmons, 1964) paved the way for modern implants, which have transformed outcomes for people with profound hearing loss (Rizzi, 2011). The field continues to mature not only through experimental success but also through methodological self-correction. As emphasized by Giacomo Rizzolatti, negative or null results can be pivotal for pruning false positives and refining experimental design; openness to such outcomes is essential for cumulative progress (Massimino, 2025).

In recent years, all-optical electrophysiology combined with human iPSC-derived neuronal models has enabled high-throughput, near patch-clamp-resolution measurements at single-cell, millisecond scales. By manipulating FMR1/FMRP levels and assessing multiparametric electrophysiological phenotypes, studies have linked molecular perturbations to neuronal function

and dysfunction, providing scalable assays that open new avenues into the cellular bases of human neurophysiology and disease biology (Fink et al., 2024).

Finally, new computational frameworks have been proposed for modelling EEG that do not change signal acquisition but rather how signals are read and modelled. One such direction integrates pretrained foundation models with neuro-inspired algorithms, such as spiking neural networks (SNNs) and Hierarchical Temporal Memory (HTM), together with Hebbian learning, to capture temporal dynamics and variability. With surrogate-gradient training and, where appropriate, neuromorphic hardware, these hybrid systems aim to mitigate long-standing challenges of EEG analysis, non-stationarity, low signal-to-noise ratio, and inference latency, while improving accuracy, robustness, and interpretability for applications ranging from seizure detection to emotion recognition and Alzheimer's diagnosis (Cui et al., 2024).

4.2. Overview of single/multi-unit and LFP recordings

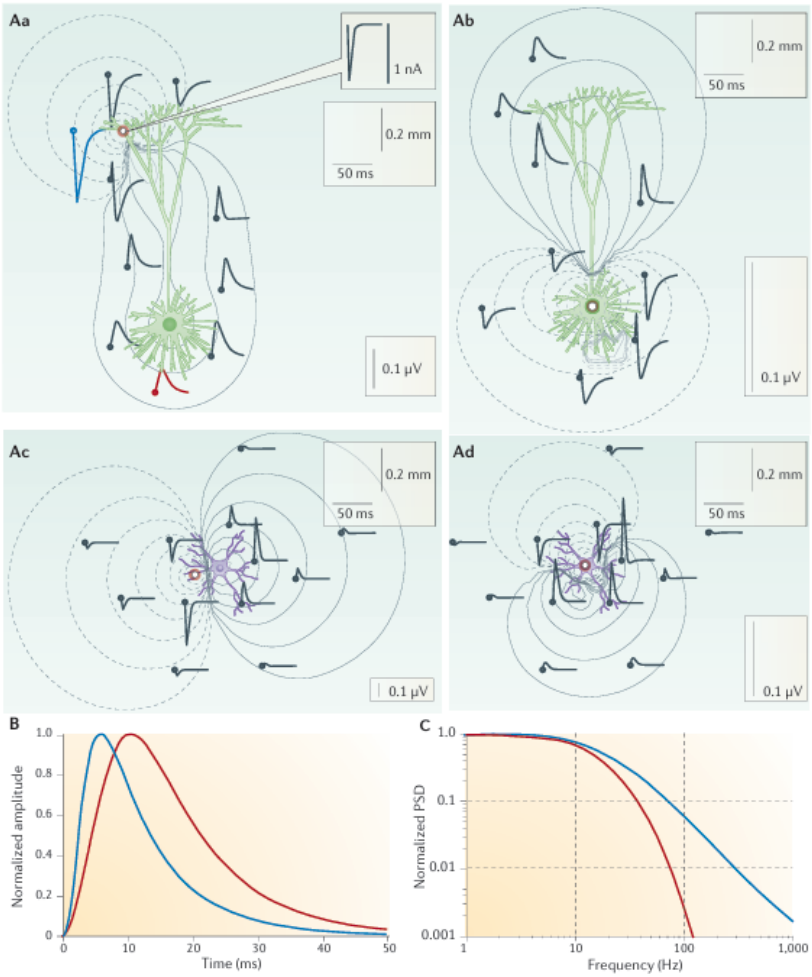

Figure 29. Local field potentials (LFPs) calculated following synaptic activation of individual neurons. (A) Example showing how the location of an excitatory synapse (white circle) in different parts of the dendrite of a layer 5 pyramidal neuron (Aa: apical dendrite; Ab: soma) or of a layer 4 stellate neuron (Ac: distal dendrite; Ad: soma) determines the spatial distribution of extracellular current sources and sinks, and consequently the shape of the LFP recorded at nearby electrodes. (B) Normalized amplitude of LFPs recorded near the synapse (blue) or near the soma (red), illustrating the dendritic filtering effect: signals closer to the synapse have greater amplitude and occur earlier in time than those recorded near the soma. (C) Normalized power spectral density of the signals in (B), showing how synapse location influences the frequency filtering of the LFP. Adapted from Einevoll et al. (2013), Nature Reviews Neuroscience, 14(11), 770-785.

The local field potential (LFP) is an electrical signal recorded inside the brain that reflects the joint activity of populations of neurons within a relatively small volume of brain tissue. It is obtained with small intracerebral electrodes and corresponds to the low-frequency component (approximately below 500 Hz) of the extracellular signal. Unlike individual action potentials,

which are brief and discrete, the LFP provides a continuous measure of synaptic integration and other membrane currents in the neurons near the electrode (Einevoll et al., 2013) (**Figure 29**).

The origin of the LFP lies in the summation of transmembrane currents flowing across neuronal membranes. The main contribution comes from synaptic currents: excitatory, mediated by AMPA and NMDA receptors, and inhibitory, largely mediated by GABA receptors. As these currents flow into or out of the dendrites and somas of neurons, they generate electrical dipoles that spread through the extracellular medium and are recorded as potential fluctuations. Other sources also contribute, including action potentials (when many occur synchronously), calcium spikes producing slower and more prolonged currents, intrinsic membrane currents, and phenomena associated with glia or the extracellular environment (Buzsáki et al., 2012).

The geometry of neurons and their spatial organization is a crucial factor. For example, pyramidal cells have long apical dendrites arranged in parallel, favouring the summation of their currents and the generation of strong, coherent signals. In contrast, neurons with more spherically distributed dendrites tend to cancel out their contributions. For this reason, most cortical LFPs are attributed to the activity of pyramidal neurons and to the way they receive excitatory and inhibitory synapses along their dendritic trees (Buzsáki et al., 2012; Einevoll et al., 2013).

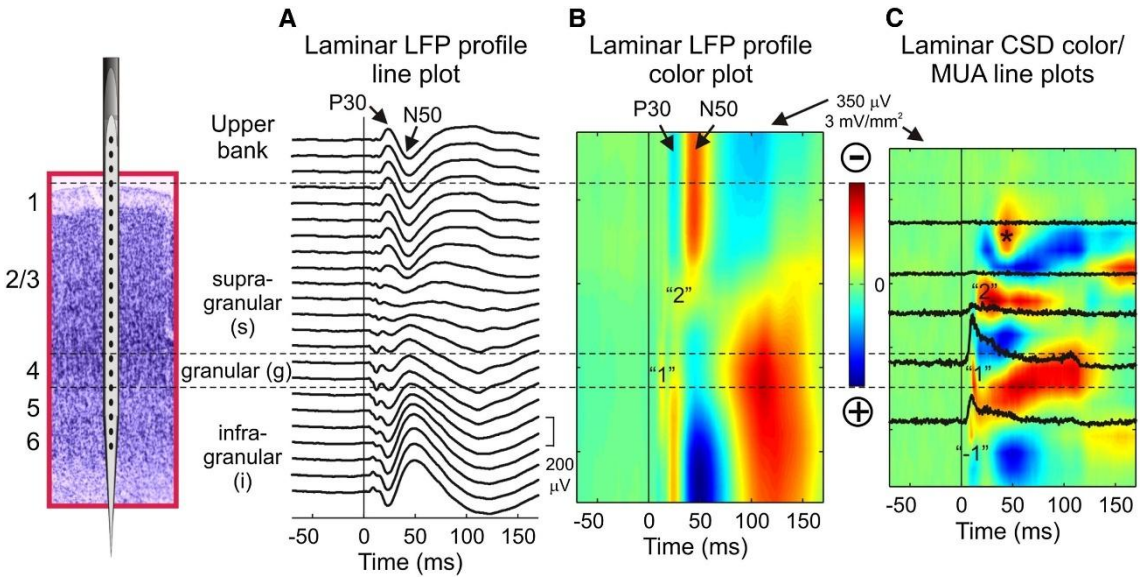

Figure 30. Laminar patterns of auditory responses in LFP, CSD, and MUA in auditory cortex. Responses to the best-frequency (BF) tone at one site in A1. (A) LFP traces recorded at 23 depths using a laminar electrode with 100 µm spacing between contacts (schematic at left). (B) Color map representation of the laminar LFP profile shown in (A); negative deflections are shown in red and positive deflections in blue. (C) Current source density (CSD) profile derived from the second derivative of the LFP profile shown in (A) and (B); red indicates sinks of extracellular current (associated with net inward transmembrane current flow), while blue indicates extracellular sources (net outward current). Superimposed are multiunit activity

(MUA) responses selected from channels 2, 6, 10, 15, and 19. Thin vertical lines across all panels mark stimulus onset. In this example, the MUA peak in channel 15 coincided with the maximum LFP negativity and with the current sink (CSD) in layer 4, which was used to analyze the lateral propagation of signals. The asterisk marks a superficial sink giving rise to the N50 component. Adapted from Kajikawa & Schroeder (2011), Neuron, 72(5), 847-858.

Despite what its name suggests, the LFP is not purely "local". While electrodes mainly capture the activity of neurons within a few hundred microns, they also pick up signals propagated from more distant regions due to volume conduction. This means that currents generated millimetres away can influence the recording. Thus, LFPs should be interpreted as a mixture of local and remote sources, rather than as the activity of just a few neurons near the electrode (**Figure 30**) (Herreras, 2016; Kajikawa & Schroeder, 2011).

The LFP is considered part of the family of field potentials. When recorded from the scalp it is called the electroencephalogram (EEG), from the cortical surface the electrocorticogram (ECoG), and within the brain the LFP. All share the same biophysical basis, transmembrane currents that, according to volume conductor theory and Maxwell's equations, generate electric fields, but they differ in spatial resolution and degree of invasiveness (Buzsáki et al., 2012; Pesaran et al., 2018).

From an analytical perspective, LFPs are primarily studied in the spectral domain and in their relationship to other recordings such as neuronal spikes. The power spectrum of an LFP typically decays following an approximate 1/f law, reflecting the mixture of fast and slow processes that generate it. Within this trend, characteristic oscillations emerge, such as theta, alpha, beta, gamma, or ripples, that correspond to network rhythms with specific functional meanings, for example in memory, attention, or motor planning (Einevoll et al., 2013; Pesaran et al., 2018). The relationship between spikes and field (spike-field coherence) is used to study how individual neuronal discharges are coupled to population rhythms.

However, interpretation of the LFP is complex and nuanced. A common misconception is that LFP polarity (positive or negative) directly indicates excitation or inhibition. In reality, polarity depends on the geometry of current sinks and sources and can invert depending on electrode position relative to the neuronal dipole. Another misunderstanding is to assume that LFPs are exclusively local; numerous studies have shown that much of the signal may originate from remote sources. Similarly, LFP amplitude does not correlate simply with the amount of neuronal activity: spatial organization and synchrony weigh more heavily than the absolute firing rate (Herreras, 2016; Kajikawa & Schroeder, 2011).

In recent years, inhibitory interneurons have been shown to play a central role in generating LFPs. Recordings in humans and primates have demonstrated that postsynaptic currents triggered by

inhibitory spikes contribute substantially, often more than excitatory currents, to the focal signals observed in LFPs. This highlights that oscillatory rhythms and the recorded dynamics largely reflect the action of local inhibitory networks (Teleńczuk et al., 2017).

The LFP has diverse applications. In basic research it is used to study mechanisms of sensory processing, cognition, attention, and memory. In clinical contexts, it is applied in the study of epilepsy and Parkinson's disease, since pathological oscillations are clearly detectable in the LFP. It is also employed in brain-machine interfaces: being more stable and easier to record chronically than spikes, the LFP provides a robust signal for controlling neuroprostheses or brain stimulation systems (Einevoll et al., 2013).

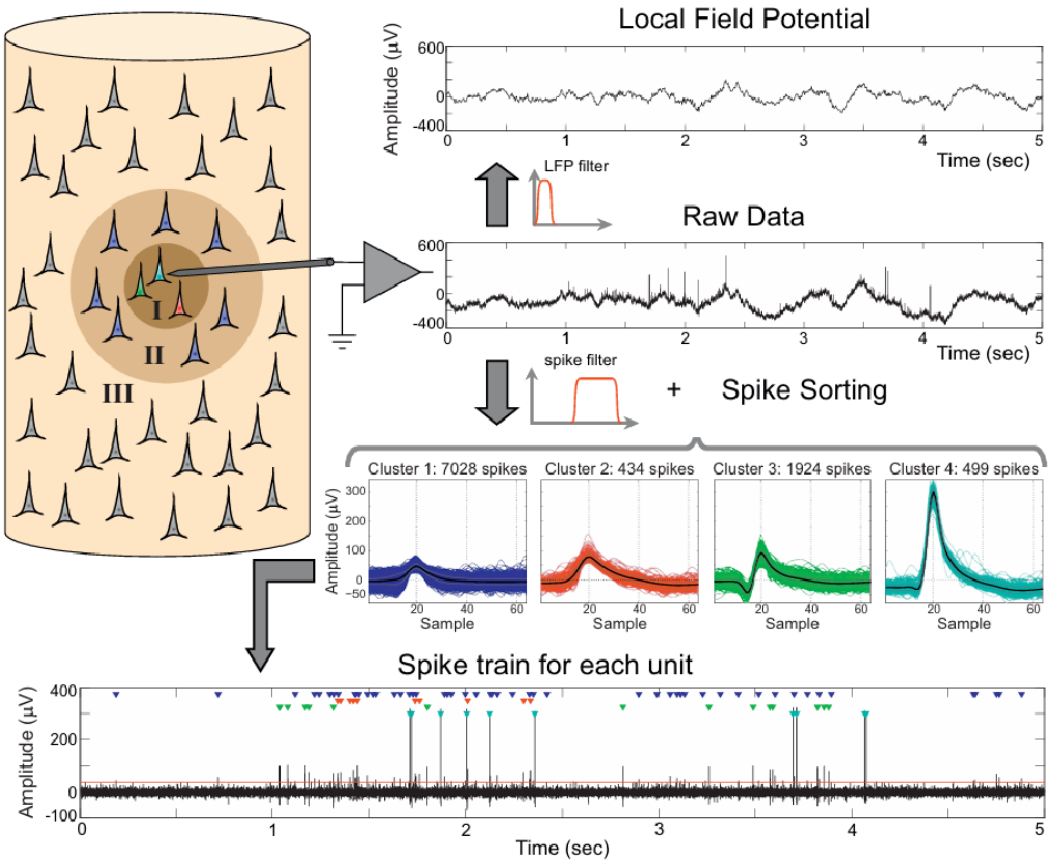

Figure 31. Diagram of the process for recording and analyzing extracellular signals. From the raw signal, low-frequency filtering yields local field potentials (LFPs), while high-frequency filtering reveals spike activity. These spikes can be grouped into a multiunit activity (MUA) cluster or, through spike sorting techniques, assigned to individual units (SUA). The example illustrates how a single recording contains both population-level and single-neuron information (adapted from Rey et al., 2015).

Other approaches to studying cortical activity have involved the recording of MUA and SUA (Single-Unit Activity), this one refers to the activity of a single neuron. To obtain it, a process of

spike detection and classification, known as spike sorting, is required. This procedure consists of identifying electrical discharges (action potentials) in the extracellular signal, classifying them according to their waveform, and assigning them to a specific cell (**Figure 31**). SUA therefore allows high temporal resolution analysis of how an individual neuron responds to stimuli or participates in a cognitive or motor task (Rey et al., 2015). Owing to this precision, SUA has been pivotal in both clinical and experimental neurophysiology. For example, it has contributed to understanding the organization of motor cortex and to the development of brain-computer interfaces capable of restoring movement in people with paralysis (Cash & Hochberg, 2015). However, SUA recordings present practical limitations: they are unstable over the long term, rely on complex classification algorithms, and depend on neuronal signals being sufficiently strong and consistent to be distinguished from those of other cells (Rey et al., 2015).

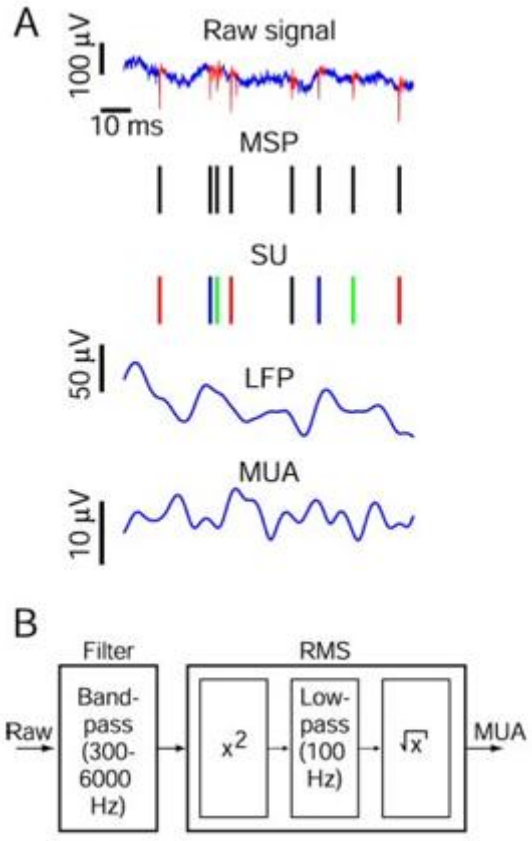

Figure 32. Decomposition of an extracellular signal into its different components. Panel A shows how, from a single raw recording, multiple spikes (MSP), single-unit activity (SUA) after classification, LFPs as slow oscillations, and MUA as energy in the high-frequency range can be derived. Panel B outlines the calculation of MUA through filtering and RMS (adapted from Stark & Abeles, 2007).

In contrast, Multiunit Activity (MUA) refers to the combined activity of several neurons located near the electrode. It is obtained by filtering the high-frequency components of the signal (approximately 300-6000 Hz) and reflects the summation of spikes from a local neuronal population, without requiring assignment of each discharge to a specific cell (**Figure 32**). This means that MUA is easier to obtain than SUA, since it does not require exhaustive classification and is more stable over time. Furthermore, MUA maintains a high correlation with motor, sensory, or cognitive information processed by the neuronal group. Indeed, studies in primates have shown that with only a few MUA recordings it is possible to predict arm movements with good accuracy, sometimes even more robustly than with SUA or with local field potentials (LFPs) (Stark & Abeles, 2007).

Comparison between SUA and MUA highlights a trade-off between resolution and practicality. SUA provides the most detailed and precise view of neuronal activity, making it possible to study the fine physiology of each cell and its specific properties. MUA, on the other hand, offers a more global measure that is much easier to obtain and maintain stable, which makes it particularly useful for long-term applications such as implantable neural interfaces (Ahmadi et al., 2021). In addition, recent research suggests that both MUA and SUA can be inferred from more robust signals such as LFPs, underscoring the interdependence of these recording types and the potential of combining them to extract richer information (Ahmadi et al., 2021; Burns et al., 2010).

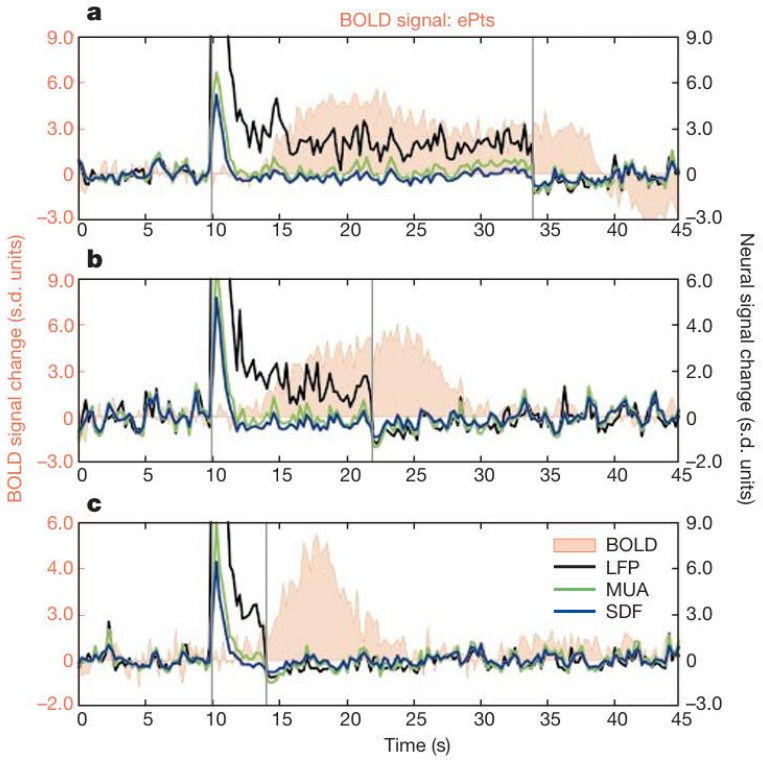

Figure 33. Simultaneous comparison of different neuronal and hemodynamic signals in visual cortex. Responses to visual stimuli of different durations are shown. Both SUA (spike density function) and MUA exhibit transient responses that decay after a few seconds, whereas LFPs remain sustained and correlate with the BOLD signal recorded by fMRI. These results demonstrate that each modality reflects distinct aspects of neuronal dynamics (adapted from Logothetis et al., 2001).

In clinical contexts, both types of signals have been highly valuable. SUA has played a central role in the study of epilepsy, movement disorders such as Parkinson's disease, and the mechanisms of general anesthesia, helping to identify specific neuronal patterns and guide deep brain stimulation surgeries (Cash & Hochberg, 2015). MUA, in turn, has been used as a stable source of information for the development of motor prostheses controlled by brain activity and for the study of neuronal network dynamics (**Figure 33**) (Stark & Abeles, 2007).

4.3. What is an ERP

There is a neurophysiological technique that enables the study of how the brain processes sensory, motor, or cognitive stimuli through electrical activity recorded at the scalp: event-related potentials, known as ERPs. ERPs are very small voltages extracted from the electroencephalogram by averaging techniques and are tightly time-locked to a specific stimulus or event. Their main strength lies in their high temporal resolution, as they can capture changes

in brain activity on the order of milliseconds, making them ideal tools for investigating cognitive processes such as attention, memory, language, and perception (Sur & Sinha, 2009a).

ERPs are divided into "exogenous" and "endogenous" components. Exogenous components appear within the first 100 milliseconds after a stimulus and depend mainly on its physical properties, such as the intensity or frequency of a sound. In contrast, endogenous components arise later and reflect how the subject evaluates and interprets the stimulus; they are therefore considered markers of internal cognitive processes. These components are usually labelled according to their latency and polarity, for example P50, N100, P200, N200, P300, or N400, each associated with different aspects of perception and information processing (Kutas & Federmeier, 2011; Sur & Sinha, 2009a).

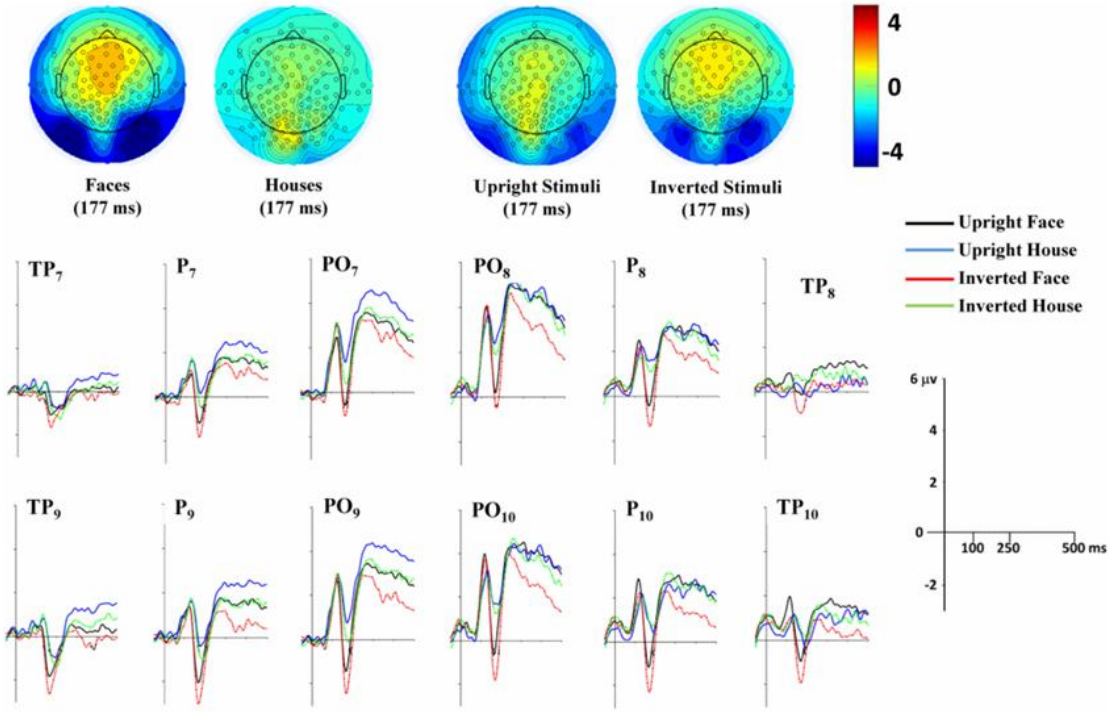

Figure 34. Representation of the N170 component in response to facial and non-facial stimuli. Top: topographic maps at the N170 peak (177 ms) for faces and houses, both in upright and inverted orientations. Bottom: average waveforms recorded at posterior electrodes, showing a larger negative peak (N170) for face stimuli compared with houses. This figure illustrates how the N170 serves as an early and sensitive marker of face processing (adapted from Gao et al., 2019).

In the perceptual domain, the N170 has been described as a marker sensitive to face perception, originating in the fusiform region. This component illustrates how ERPs can pinpoint the precise moment at which the brain recognizes a socially relevant category of stimuli such as faces (**Figure 34**) (Gao et al., 2019). Another example is mismatch negativity (MMN), an ERP that reflects a

pre-attentive mechanism for detecting changes in repetitive auditory sequences. It is generated primarily in auditory cortex and, to a lesser extent, in frontal regions (there is evidence for frontal involvement, though less consistent than temporal), demonstrating how the brain can detect irregularities even without conscious attention (Rosburg, 2005). A classic and extensively studied example is the N400, first described in 1980, which is elicited approximately 400 milliseconds after the presentation of an unexpected word in a sentence. Its amplitude reflects the difficulty of integrating the stimulus into a semantic context, and it is therefore directly associated with meaning processing. Thus, when a word fits poorly into a sentence, the N400 is larger, revealing how the brain detects semantic incongruities (Kutas & Federmeier, 2011).

The question arises as to whether an ERP can only be obtained from surface EEG or also from intracranial recordings. Available evidence shows that both are possible: an ERP can indeed be obtained from local field potential (LFP) recordings. In fact, intracranial LFPs are considered physiological analogues of ERPs measured at the scalp. Electrocorticography (ECoG) studies in epileptic patients show that intracranial potentials exhibit temporal and functional components equivalent to classical ERPs, but with higher spatial precision and less noise. These findings validate the interpretation of surface ERPs as projections of the local neuronal dynamics captured in LFPs (Llorens et al., 2011; Rosburg, 2005). Currently, some authors have even proposed a terminological distinction: to refer to ERPs measured intracortically as eLFPs (event-related Local Field Potentials), emphasizing that although they are conceptually equivalent, intracranial recordings provide an additional level of resolution and reliability in identifying the underlying neuronal processes (Caballero Tapia et al., 2025).

4.4. The monocular enucleation model in rodents

The monocular enucleation model in mice constitutes a key tool for investigating visual system plasticity and the consequences of extreme sensory deprivation. Unlike other deprivation methods, such as eyelid suture or dark rearing, which preserve some degree of spontaneous retinal activity, enucleation immediately and irreversibly eliminates both spontaneous and visually driven input from one eye. This makes it a robust paradigm of unilateral deafferentation, enabling precise analysis of the structural, functional, and molecular changes occurring in the central nervous system after the loss of half of the visual inputs.

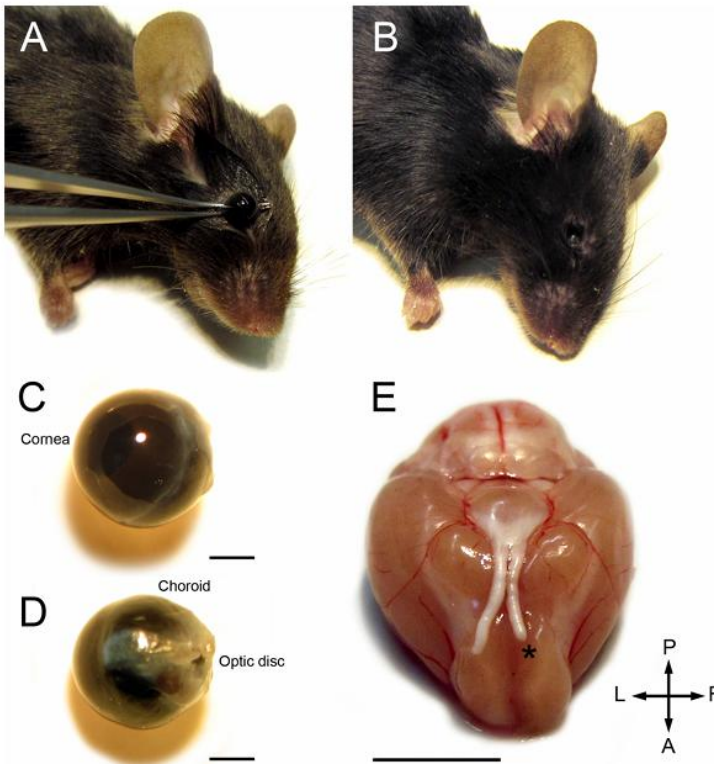

Figure 35. Representation of the monocular enucleation procedure in mice and postoperative condition. (A) Removal of the eyeball using curved forceps grasping the optic nerve. (B) Orbital cavity without signs of bleeding or apparent damage following the intervention. (C, D) Enucleated eye with intact cornea, choroid, and optic disc, reflecting preservation of globe integrity. (E) Ventral view of the brain showing a cleanly severed optic nerve (asterisk) and absence of damage to adjacent structures. This figure illustrates the technique described in the text and demonstrates the reproducibility and safety of the procedure in terms of animal welfare. Adapted from Aerts et al., 2014.

From a methodological perspective, highly reproducible protocols have been developed to perform enucleation in mice. One of the most widely adopted employs general anaesthesia with ketamine and medetomidine, followed by ocular disinfection. With the animal placed in a stable position, a curved serrated forceps is inserted behind the eye to grasp the optic nerve. Circular movements are then performed to constrict and sever the nerve, allowing the complete removal of the eyeball (**Figure 35**). This technique, validated in animals from 10-13 days of age after eye opening through adulthood, offers several advantages: minimal or no bleeding, rapid postoperative recovery, a relatively short learning curve for researchers, and preservation of

orbital tissues. One limitation is that it may cause some retinal damage, making it unsuitable for analyses focused on ocular tissues themselves, yet it is particularly well-suited for studies of central visual system plasticity (Aerts et al., 2014).

Experimentally, monocular enucleation (ME) has been employed both during early developmental stages and in adulthood. When performed at birth or shortly thereafter, it disrupts the normal maturation of visual pathways and triggers profound reorganization. In rodents, this includes rerouting of retinogeniculate and retinotectal projections to contralateral structures, as well as the recruitment of deafferented neurons to process input from the intact eye. These modifications are accompanied by morphological changes in the visual cortex, such as reduced neuropil volume, increased neuronal density, greater variability in dendritic orientation, and a decrease in dendritic spine number. Moreover, neonatal enucleation induces multimodal plasticity: visual cortical regions can become responsive to tactile stimuli, suggesting compensatory mechanisms of cross-modal reorganization (Nys et al., 2015).

The model has also been applied to humans, primarily in patients undergoing enucleation due to retinoblastoma or other ocular pathologies. These studies reveal degeneration in the optic chiasm and lateral geniculate nucleus, but also functional reorganization that helps maintain or even enhance certain visuospatial abilities, albeit at the expense of deficits in motion perception and stereopsis. Such findings underscore the translational relevance of the murine model for understanding brain plasticity following early visual loss (Kelly et al., 2014).

As for alternative experimental approaches, several less drastic methods of visual deprivation exist. Eyelid suture prevents visual stimulation while maintaining spontaneous retinal activity; dark rearing eliminates visual input but not intrinsic retinal activity. Intraocular injection of toxins such as TTX blocks activity transmission. Other models involve progressive degeneration of retinal ganglion cells, such as experimentally induced ocular hypertension. These strategies are useful for studying specific aspects of visual plasticity, including binocular competition or axonal degeneration processes, but they cannot substitute for the absolute and irreversible nature of monocular enucleation (ME) (Nys et al., 2015).


Objectives

Objectives

The general objective of this thesis is to determine whether three minimally invasive interventions with potential clinical use, transcranial direct current stimulation (tDCS), cholinergic enhancement via donepezil, and a structured visual stimulation protocol, are able to modulate the plasticity of the primary visual cortex (V1) following monocular loss of vision. To answer this question rigorously, the work is organised around a logical chain of objectives that encompasses, first, the neurophysiological characterisation of V1 under physiological conditions and, thereafter, a systematic comparison with the post-enucleation state, to finally assess the impact of each treatment, separately and in combination, on mesoscopic and temporal markers of cortical plasticity. This approach integrates electrophysiological recordings of local field potentials (LFPs) and unit activity in awake animals, with a cohort design that permits pre/post controls and comparisons between sensory stimulation modalities, ensuring that conclusions about plasticity rest on objective and reproducible measures of V1 function.

First, a specific objective is to characterise the physiological state of V1 as a basis for comparison. This entails describing the organisation of its responses to stimuli of different kinds (somatosensory, auditory, and visual) and establishing, in control animals, the profile of event-related oscillations and inter-trial synchronisation that defines its usual functioning. Characterisation will be carried out by means of multilayer LFP recordings and, where appropriate, unit activity (SUA/MUA) in awake, head-fixed animals on a running wheel, following standardised depth and duration protocols to ensure comparability across modalities and layers. This stage provides the physiological reference map upon which alterations attributable to monocular loss or to the interventions may be identified.

Second, an objective is defined to quantify how the V1 response changes after monocular vision loss in an experimental rodent model of enucleation. The comparison between the physiological state and the enucleated state will make it possible to describe, with frequency-band resolution, shifts in evoked spectral power and the reorganisation of phase coherence in response to the same somatosensory, auditory, and visual stimuli. This post-lesion evaluation will be conducted in cohorts specifically timed to capture windows of reorganisation and will include groups with early enucleation and cohorts with pre/post measures within the same animal, so that the acute effect can be dissociated from the temporal course of plasticity. The aim is to delimit whether the plasticity that emerges in V1 is predominantly intramodal (within vision) or intermodal (crossed from touch and hearing), thereby setting the question that will guide the intervention phase.

Third, it is proposed to evaluate the modulatory capacity of each intervention on V1 plasticity markers after enucleation, comparing tDCS, donepezil, and visual stimulation, both individually

and in combination. To this end, cohorts are designed in which, after a recovery period, treatments are applied according to parameterised and reproducible protocols: tDCS with a high-definition epicranial montage over V1; administration of donepezil in a regimen consistent with the literature on cholinergic enhancement; and a structured visual stimulation protocol in all treated animal groups which, in addition to its intrinsic interest, allows interactions with tDCS and/or donepezil to be explored. All treated groups are maintained in environmental enrichment to maximise plastic competence, in line with evidence that an enriched environment preserves or restores components of ocular plasticity in adulthood. With this design, the goal is to establish not only whether the interventions modulate V1, but in which direction they do so and with what specificity by sensory modality.

Fourth, an objective is set to develop and apply a suite of neurophysiological and inferential metrics to quantify plasticity. The spectral dimension will be analysed using time-frequency decomposition to extract event-related power by band (ERSP) and inter-trial phase coherence (ITC), as complementary indices of network reorganisation. In parallel, the latency of the band-specific coherence maximum will be measured as a sensitive estimator of response timing, allowing advances or delays associated with plasticity or with the treatments to be detected. These metrics will be summarised at the population level with robust procedures to compare distributions without assuming normality, strengthening the reproducibility and interpretability of changes induced by the lesion and by the interventions. The purpose of this objective is to equip the study with quantitative tools that serve as candidate biomarkers of plastic states in V1 and of their modulation.

The fifth objective is to compare systematically the effects of tDCS, donepezil, and their combination on the same indicators, with particular attention to possible synergies or "focusing" effects of plasticity when administered jointly. This cross-comparison will be carried out under the same recording time frame, identical stimulation parameters, and shared analysis protocols, with the aim of discerning whether there are differential modulatory profiles by sensory modality or by frequency band and, where applicable, of identifying combinations that optimise the sensory retraining of V1. The cohort structure (with arms of tDCS alone, donepezil alone, and the combination) guarantees causal inference regarding the intervention responsible for any observed change in the defined biomarkers.

Lastly, as a transversal objective with clinical projection, this thesis will seek to extract operational principles for visual rehabilitation: from the neurophysiological patterns that define the reorganisation of V1, the intention is to propose a set of markers and intervention rules that can guide future strategies of perceptual training and therapeutic interfaces, both in scenarios of partial loss and in contexts of restoration of visual input (e.g., prostheses, gene therapies). The

ambition is that indices derived from ERSP/ITC and response latency will serve as metrics for stratification and follow-up, and that intervention combinations defined in the preclinical model will translate into testable hypotheses in humans, under non-invasive protocols compatible with clinical practice.

Taken together, these objectives articulate an experimental programme that progresses from the physiological baseline to the state reorganised by visual loss, and thence towards the directed modulation of plasticity by means of tDCS, donepezil, and visual stimulation, all within a framework of quantitative analysis by frequency bands and response latencies and histological validation. The cohort design and the use of environmental enrichment to enhance plastic competence provide the study with an additional level of experimental control and lay the foundations for a responsible translation of the findings to human sensory-rehabilitation settings.


Materials
and
Methods

1. Material and methods

1.1 Experimental model

Sex was not considered as an experimental factor, as preliminary experiments conducted in the facility revealed no significant differences in eLFP measures between males and females (24 M | 16 F) under identical housing and recording conditions. Depending on the experiments conducted, animals were assigned to two housing cohorts. The first housing cohort was maintained under standard conditions (n = 23), and the second housing cohort was maintained in an enriched environment (n = 17). Unless otherwise indicated, analyses and comparisons were performed within-cohort.

In the first cohort, a total of 23 C57BL/6J mice (M|F), aged 2 to 6 months, were obtained from Charles River Laboratories. The animals were housed in a climate-controlled environment with a 12-hour light/dark cycle, in standard cages containing bedding, with food and water available ad libitum. The facility provided filtered air circulation and maintained a constant temperature of 20 °C. Each cage was additionally equipped with a running wheel, a mouse house placed under the wheel, and cardboard rolls to enrich the environment. Health status was specific pathogen-free. Ethical approval for the experimental procedures was granted by the Ethics Committee (CEBEA - Comité d'éthique et du bien-être animal) of the University of Mons, in accordance with Directive 2010/63/EU of the European Parliament and of the Council on the protection of animals used for scientific purposes, under protocol RI-013-01, carried out under the Neurosciences service authorization LA1500024.

The second cohort of 17 C57BL/6J mice (M|F; 2-6 months) was housed in enriched-environment cages with a maximum of five mice per cage. Each cage contained multiple running wheels (≥2 per cage), shelters and hideouts, cardboard tunnels/rolls, and assorted manipulanda (e.g., wooden toys) to promote sensorimotor stimulation. Bedding and paper nesting material were provided; food and water were available ad libitum. Rooms were maintained at 20 °C, on a 12:12 h light/dark cycle. Enrichment was identical across cages within this cohort, and animals were acclimated for at least 7 days before experiments. Health status was specific pathogen-free. All procedures were approved by the CEBEA of the University of Mons, in accordance with Directive 2010/63/EU of the European Parliament and of the Council on the protection of animals used for scientific purposes, under protocol RI-013-02, carried out under the Neurosciences service authorization LA1500024.

Animals were monitored postoperatively using both standardized pain scales and a specific pain scale. Cases of persistent or unrelieved distress triggered predefined humane endpoints and the animal was euthanized. Transient or procedure-related pain was managed with an approved analgesic regimen. If the head-fixation implant (head-post) showed loosening or impending detachment, the animal was anesthetised and repair or re-affixation was attempted; if repair proved infeasible or the device had already detached, the animal was euthanized.

1.1.1 Model Validation: reversible visual deprivation

At the beginning of the neuronal activity recordings, the question arose as to why visually evoked eLFPs in V1 appeared less "prototypical" than those elicited by somatosensory or auditory stimuli. We hypothesised that the functional state of the non-stimulated eye could modulate the gain and reliability of visual responses in V1, and that such modulation might account for the apparently reduced robustness of the waveform. To test this hypothesis, a reversible monocular inactivation paradigm was implemented in four C57BL/6J mice (n = 4), and V1 responses were recorded under contralateral and ipsilateral monocular visual stimulation, while the non-stimulated eye was manipulated either by optical occlusion (eye patch) or by retinal silencing (intraocular TTX injection). Given the contralateral dominance of projections to V1, it was anticipated that responses to contralateral stimulation would exceed those obtained with ipsilateral stimulation under all conditions.

The TTX injection protocol was adapted from Mikhail Y. Frenkel and Mark F. Bear (2004). Under 2-3% isoflurane inhalation anaesthesia and using a surgical microscope, the upper conjunctiva was exposed, and the globe stabilised with a 7-0 silk suture passed through the conjunctiva. Ophthalmic ointment was applied throughout the procedure to maintain ocular moisture. After conjunctival dissection, a fine needle was used to create a small puncture at the corneoscleral junction to access the vitreous chamber. A glass micropipette mounted on a stereotaxic holder, ensuring perpendicular alignment to the eye and precise depth control, was connected to a microinjection system (Picospritzer) and advanced to a depth of ≈0.7 mm. A volume of 1 µl of TTX (1 mM) was injected (saline in controls). The micropipette was left in place for 2 minutes before removal, after which the eye was rinsed repeatedly with sterile saline drops. Mydriasis occurred within ≤5 minutes and the pupillary light reflex was abolished in the treated eye. Retinal blockade following each injection lasted approximately 24 h.

Once vision loss in the eye of interest was confirmed, V1 activity was recorded in the left hemisphere while monocular visual stimuli were presented to either the contralateral or ipsilateral

eye relative to the recording site. The same recording and stimulation procedure was also performed with an eye patch instead of TTX, providing a non-pharmacological optical manipulation. This design allowed us to determine how occlusion versus silencing of the non-stimulated eye affected the amplitude of visually evoked eLFPs, and to verify across conditions the expected contralateral dominance over ipsilateral responses.

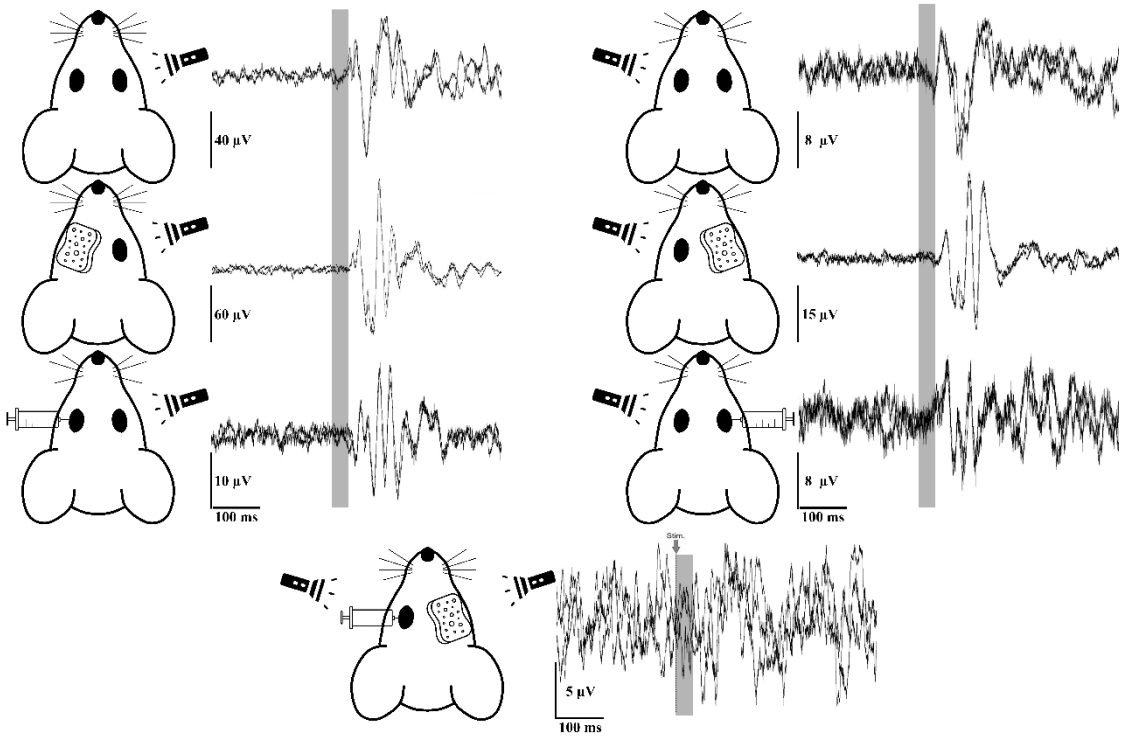

Figure 36. Visually evoked local field potential (eLFP) responses in V1 under monocular stimulation with manipulation of the non-stimulated eye. Left column: stimulation of the eye contralateral to the recording site. Right column: stimulation of the ipsilateral eye. Rows (top-bottom): control condition; occlusion of the non-stimulated eye (patch); retinal blockade of the non-stimulated eye with TTX. Bottom panel: bilateral inactivation (patch on one eye and TTX in the other). Two superimposed repetitions are shown per condition; the grey bar indicates the time of the flash. Amplitude scale bars and temporal interval (100 ms) are provided in each panel. Representative trace; n = 4 animals.

In the control condition, visual stimulation evoked a well-defined negative-positive complex that was time-locked to the stimulus, with a clear dominance of the contralateral eye over the ipsilateral one, as the eLFP amplitude was greater when stimulating contralaterally than ipsilaterally. When the non-stimulated eye was occluded with a patch, the response of the open eye was enhanced: peak-to-peak amplitude increased and the morphology of the complex became sharper, with no evident changes in latency. This effect may suggest the release of interocular

suppression and/or a rapid gain adjustment. In contrast, when the non-stimulated eye was silenced with TTX, the amplitude of the evoked component decreased, although the basic temporal profile and latency of the eLFP were preserved. This combination of "same shape, smaller amplitude, and reduced reliability" suggests that TTX does not alter the main afferent pathway of the stimulated eye (retina-thalamus-cortex), but instead affects the gain state of the shared circuit. By completely abolishing ganglion cell firing in the blocked eye, the binocular activity tone that normally maintains the excitability and synchronization of thalamocortical and intracortical circuits may be lost. This effect contrasts with that of eye patching, which does not suppress baseline retinal activity or the subcortical tone of the occluded eye and, in addition, reduces interocular competition, thereby enhancing the response of the open eye. Taken together, the results indicate that the state of the "non-stimulated" eye strongly modulates V1 gain: occlusion increases it, TTX blockade decreases it and reduces response robustness, and in all cases contralateral stimulation evokes greater amplitudes than ipsilateral stimulation (**Figure 36**).

1.1.2 Model Validation: stimulus-linked motor components latency

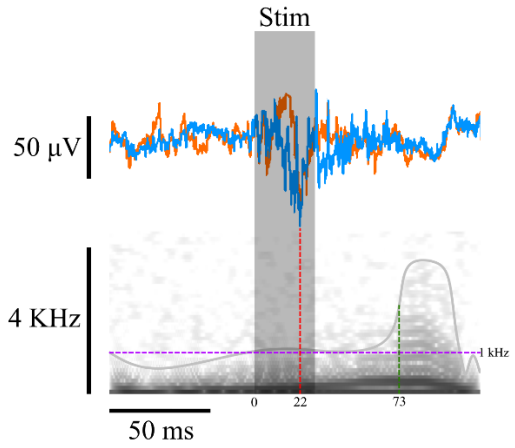

Figure 37. Cortical response (eLFP) and motor detection following stimulation. Top: two V1 eLFP traces (blue and orange) from the same recording, overlaid to show the coincidence of cortical latency; the grey band marks the stimulus window ("Stim"). The red dashed line indicates the eLFP latency (≈22 ms post-stimulus). Bottom: motor channel in sonogram mode (0-4 kHz); the purple dashed line denotes the detection threshold and the grey curve the energy envelope. The green dashed line marks the onset of the motor event (≈73 ms), occurring after the eLFP. Scale bars: 50 µV (vertical, top) and 50 ms (horizontal, bottom).

As an additional indirect validation, randomized analyses were conducted on recordings from distinct animal cohorts to compare the latency of the V1 response with that of the earliest

stimulus-linked motor components. Ten animals were randomly selected (two per cohort); for each animal, two complete recording sessions were chosen, and stimulation events across the three sensory modalities were identified in which a V1 response co-occurred with detectable motor-related activity.

To capture the onset of the vibrissal motor component, a small magnet was affixed to a bundle of left or right vibrissae, and a magnetic-field sensor was positioned a few millimetres away. Locomotion was detected with an instrumented wheel that registered movement using a laser sensor. Eyelid closure was monitored with an approach analogous to whisking: a small magnetised metal filament and the same magnetic-field detection system were used, and perturbations of the field were interpreted as blink events.

Motor signals were routed to the CED acquisition system for digitisation and displayed in the recording in Sonogram mode. For each stimulation event, a detection threshold was defined as twice the baseline activity; movement was deemed present when the signal exceeded this threshold within a predefined post-stimulus window (0-500 ms after stimulation) (**Figure 37**).

Latencies of motor activity were entered into a spreadsheet alongside the eLFP latency for the same event, a snapshot of the episode, the animal ID, the recording date, and the stimulus type. Median latencies were 97.9 ms for the motor component and 26 ms for the eLFP; the minimum values, in that order, were 70 ms and 14 ms.

1.2 Surgery

1.2.1 Head-fixation and craniotomy surgery

All animals underwent surgery to expose V1, with the monocular and binocular regions distinguished by two 1-mm diameter craniotomies above the left hemisphere, following the approach described by Van Brussel et al., (2009) and in collaboration with researchers from the Laboratory of Neuroplasticity and Neuroproteomics at Katholieke Universiteit Leuven, it was determined that differentiation between the monocular and binocular regions was required. Accordingly, the coordinates of both regions were adjusted to fit the recording protocol: monocular (AP = -3.8 mm; L = +2 mm; relative to bregma) and binocular (AP = -3.8 mm; L = +3 mm; relative to bregma).

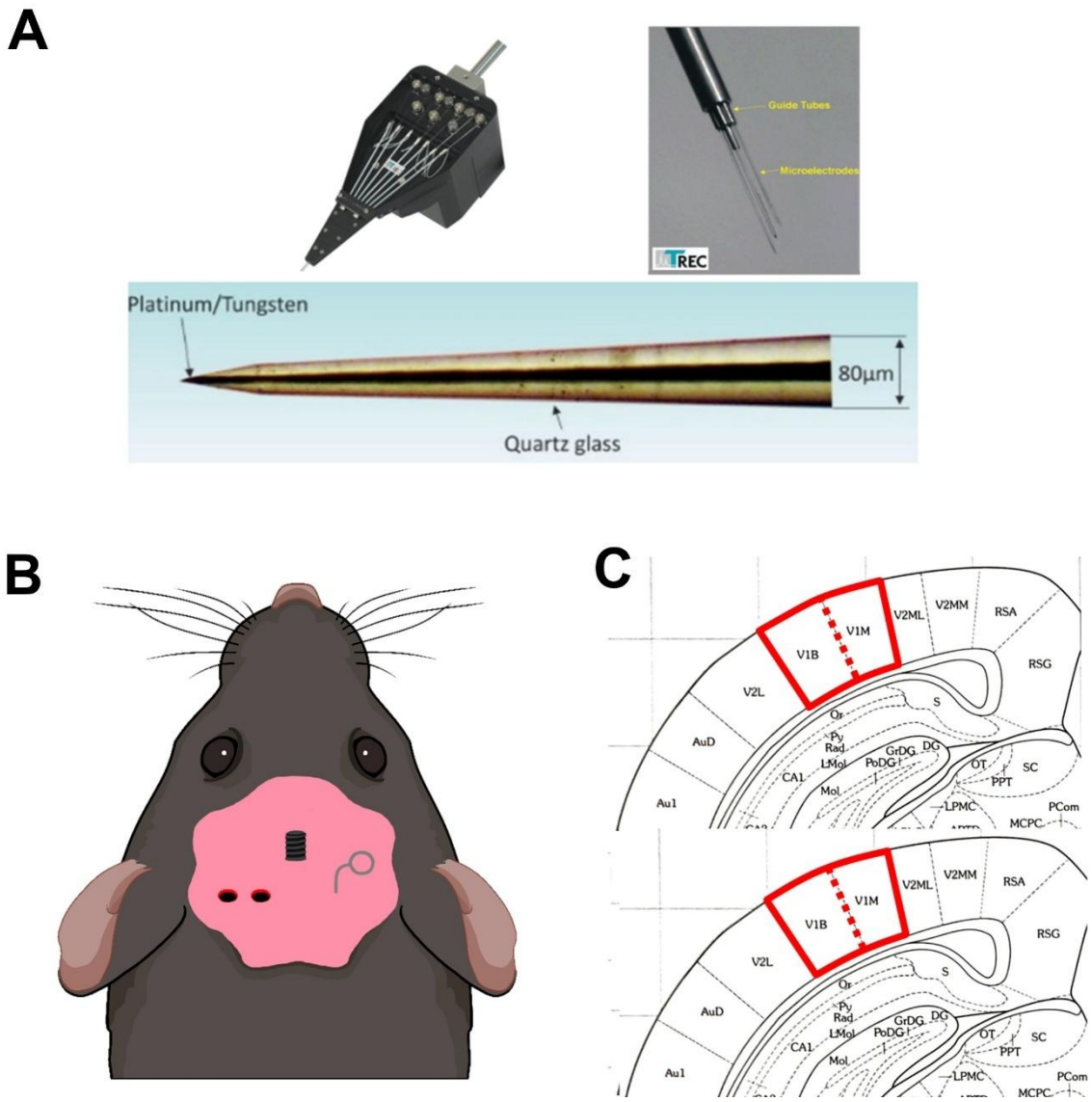

Figure 38. Overview of the technical and anatomical components of the experimental design. (A) Electrode setup used for neural recordings, including the electrode array, guide tubes, and a platinum/tungsten microelectrode encased in quartz glass with a tip diameter of 80 µm. (B) Schematic representation of a mouse with a cranial window and implanted electrode array, illustrating the positioning for neural recordings. (C) Recording sites overlaid on brain atlas sections of V1, showing electrode tracts within the binocular (V1B) and monocular (V1M) regions.

Prior to the surgical procedure, mice were anesthetised with an air/isoflurane mixture, using 3% for induction in a customised isoflurane chamber and 2-1% administered via a stereotaxic anaesthesia mask (mask kit for mice, 68601 RWD) during surgery (Iso-Vet, Piramal Critical Care B.V.). A silver wire electrode was positioned in the right hemisphere as a reference for the recording system. A head-holding system was then implanted, consisting of six bolts fixed to the skull and an additional bolt placed upside down over the midline and perpendicular to the frontal

plane to allow head fixation during the experiments. The holding system and the reference electrode were secured to the skull using dental cement (DuraLay, Ill., USA) (Sánchez-León, Campos, et al., 2025). Animals were placed in a mouse recovery box under a warm red light. As the animals regained consciousness, 0.25 mL of MELOXORAL® (0.5 mg/mL) was administered to minimise postoperative pain. Body weight was monitored daily for at least two days, and pain scales were assessed to determine the need for additional Meloxoral administration (0.1 mL). Animals were allowed to recover for at least seven days prior to neuronal recordings to reduce stress (**Figure 38**).

1.2.2 Monocular enucleation surgery

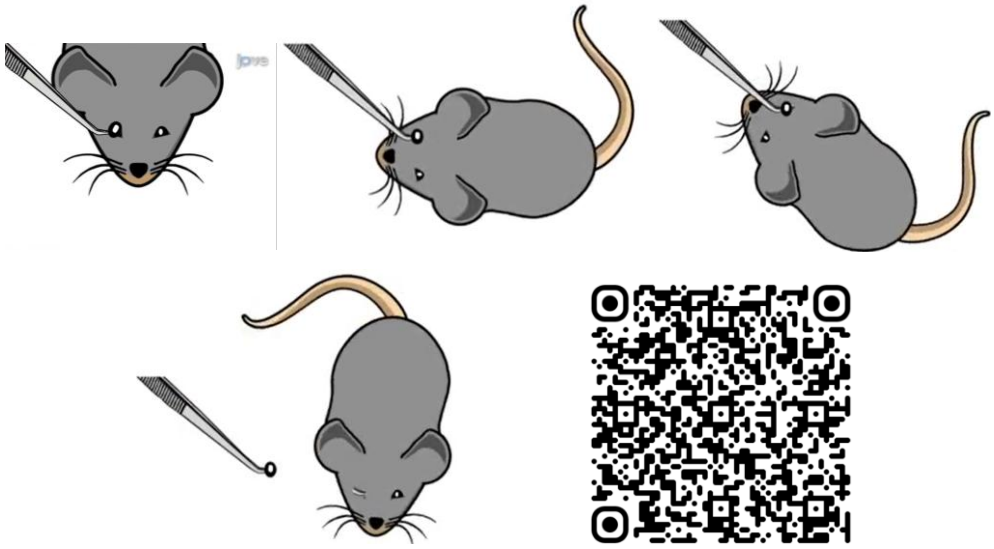

Figure 39. Schematic of the monocular enucleation procedure in the mouse. The drawings illustrate the basic phases of the intervention (animal restraint, exposure of the globe, and manipulation with instruments). The QR code links to a demonstration video of the protocol. The surgery was performed following the modified version of Aerts et al. (2014); details of anaesthesia, asepsis, and verification of anaesthetic depth are described in the Methodology section.

The monocular enucleation protocol was carried out following the modified procedure described by Aerts et al. (2014). Before to start the surgery procedure, mice were pre-anesthetised with an air/isoflurane mixture (3% for induction in a customised isoflurane chamber). Once loss of consciousness was observed, an intraperitoneal injection of rompun and ketamine (rompun 10 mg/kg + ketamine 100 mg/kg in saline solution) was administered. Anaesthetic depth was verified

by the absence of paw withdrawal reflex in response to toe pinch. The eyelids and periorbital area of the eye to be enucleated were disinfected with 70% ethanol.

The animals were positioned on a flat, dry, and smooth surface to optimise motion control during the procedure. A sterilised curved forceps with serrated tips (recommended tip size for mice: ≈0.5 × 0.4 mm) was used. Gentle pressure was applied with the forceps at the canthus to externalise the eyeball and expose the optic nerve. The forceps were then guided behind the globe to firmly clamp the optic nerve, ideally at the beginning of the curvature to encompass the entire nerve trunk. With the animal held in position, circular movements were performed in the direction of least resistance, gradually increasing the speed until constriction of the optic nerve and detachment of the globe were achieved (typically after 7-15 circular movements, ≈0.5-1 turn/s). The eyeball was removed with a clean cut of the nerve, preserving orbital tissues and without apparent damage to intracranial structures. In the rare event of bleeding, the orbit was filled with a viscous haemostatic agent (**Figure 39**).

After enucleation, animals were placed in a mouse recovery box under a warm red light. To prevent corneal desiccation of the contralateral eye, a lubricating ophthalmic ointment was applied. As the animals regained consciousness, 0.25 mL of MELOXORAL® (0.5 mg/mL) was administered to minimise postoperative pain. Body weight was monitored daily for at least two days, and pain scales were assessed to determine the need for additional meloxoral administration (0.1 mL). Animals were allowed to recover for at least seven days prior to neuronal recordings to reduce stress. This protocol is straightforward to learn and reproduce and is associated with minimal or no haemorrhage and rapid postoperative recovery in mice.

1.2.3 tDCS surgery

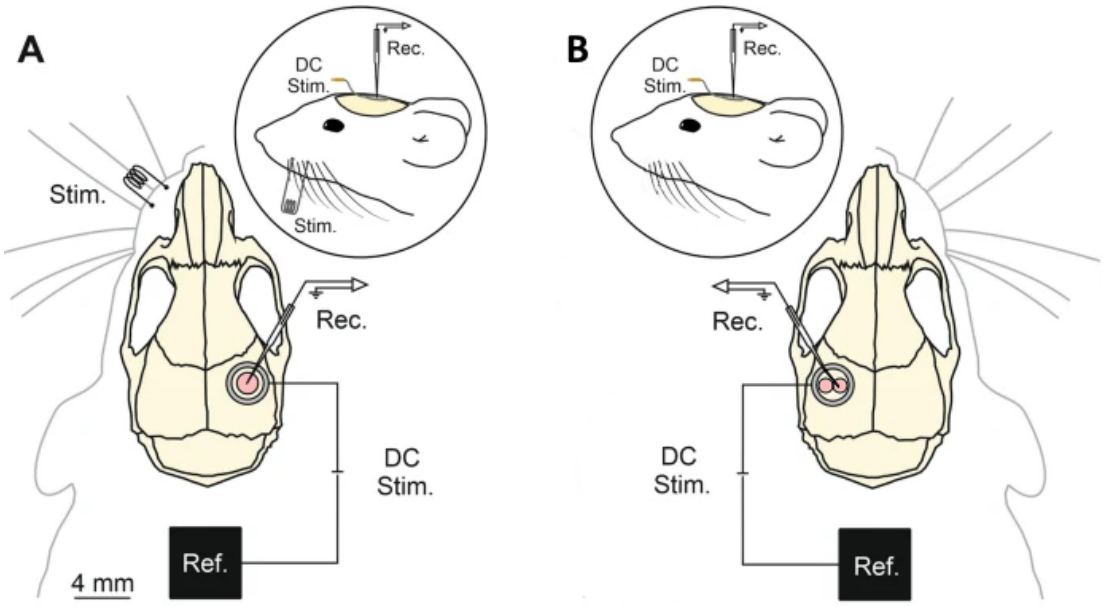

Figure 40. Schematic representation of the tDCS stimulation and recording setup. (A) Original configuration adapted from Sánchez-León et al., (2025) showing the positioning of the DC stimulation electrode, recording electrode, and reference electrode. (B) Modified configuration implemented in the present study, with the custom-made Ag/AgCl ring electrode placed over the primary visual cortex, aligned with the separation between the monocular and binocular craniotomy windows.

All animals in the tDCS stimulation cohort underwent surgery to implant a transcranial direct current stimulation (tDCS) ring electrode over the primary visual cortex, while all other procedures remained identical to those described above. Mice were anesthetised with an air/isoflurane mixture (3% for induction in a customised isoflurane chamber and 2-1% via a stereotaxic anaesthesia mask; mask kit for mice, 68601 RWD) during surgery (Iso-Vet, Piramal Critical Care B.V.). Once unconscious, the head was secured in the stereotaxic apparatus, and two craniotomies were performed at the coordinates described in section 1.2.1 (monocular: AP = -3.8 mm; L = +2 mm; relative to bregma; binocular: AP = -3.8 mm; L = +3 mm; relative to bregma).

In contrast to the other cohorts, and inspired by Sánchez-León et al., (2025) a custom-made chlorided silver (Ag/AgCl) ring electrode (inner Ø = 2.5 mm; outer Ø = 3.5 mm) was positioned such that its center coincided with the separation between the two craniotomy windows, which measured approximately 0.5 mm at its narrowest point. The ring was fixed to the skull with dental cement (DuraLay, Ill., USA) (**Figure 40**). All remaining steps followed the protocol described in section 1.2.1 of the methodology. Animals were placed in a mouse recovery box under a warm red light. As the animals regained consciousness, 0.25 mL of MELOXORAL® (0.5 mg/mL) was administered to minimise postoperative pain. Body weight was monitored daily for at least two days, and pain scales were assessed to determine the need for additional Meloxoral administration

(0.1 mL). Animals were allowed to recover for at least seven days prior to neuronal recordings to reduce stress.

1.3 Recording of LFP in awake animals

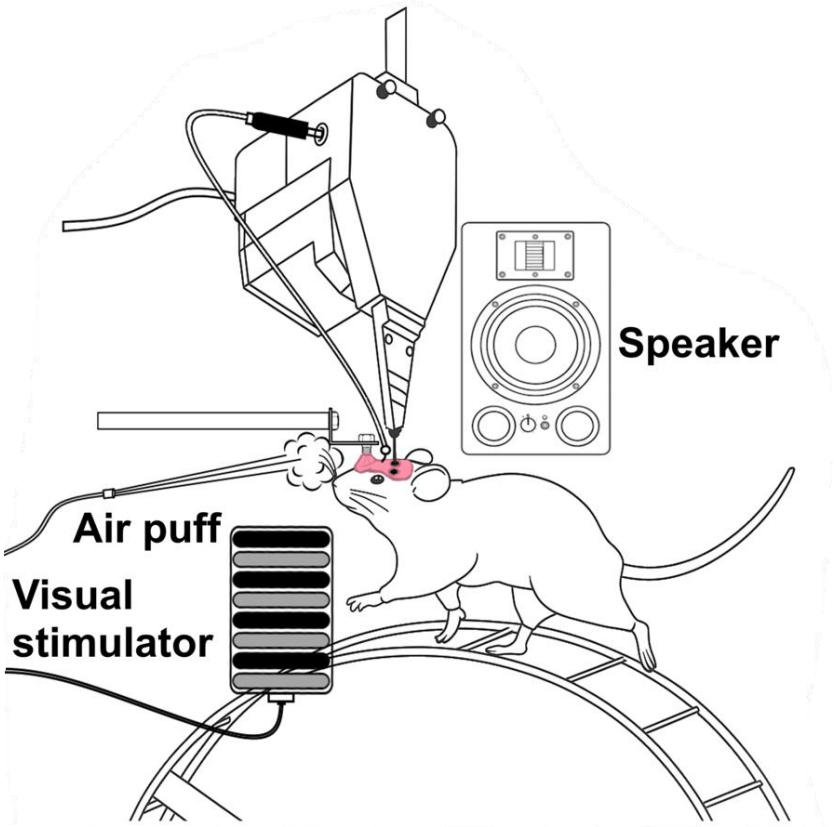

Figure 41. Schematic representation of the multisensory recording and stimulation setup in a head-fixed awake mouse. The animal walked on a running wheel while neuronal activity was recorded in the visual cortex using a microelectrode mounted on a seven-channel microdrive. Stimulators were positioned 14 cm from the animal: the visual stimulator delivered grid-pattern light flashes from the left side, perpendicular to the left eye (ipsilateral to the recorded hemisphere); the somatosensory stimulator delivered an air puff to the right whiskers (contralateral); and the auditory stimulator, a speaker placed on the right side of the animal (contralateral), emitted a 4 kHz sinusoidal tone at 60 dB. During sensory stimulation and neural recording, the animal was free to run or remain still, with head fixation being the only restriction.

Before the recording sessions, the animals underwent a 20-day habituation period in the animal facility to adapt to the new environment following arrival from Charles River Laboratories. They were further habituated to the recording setup for one week prior to electrophysiological recordings to ensure familiarity with the conditions before head fixation. Electrophysiological

activity was recorded using quartz-platinum/tungsten microelectrodes (0.5-0.8 MΩ) mounted in a circular seven-channel Eckhorn microdrive (Thomas Recordings©, Giessen, Germany) (**Figure 38** A). Power line noise at 50 Hz was removed with the Hum Bug Noise Eliminator (AM-Systems, USA).

At the beginning of each LFP recording session, animals were allowed 15 minutes of free movement within the designated area of the recording setup. Subsequently, the head was fixed while the animals were able to move freely on a running wheel, with the sole restriction being the lack of head movement. Once the animal was properly positioned and calm, the reference electrode was connected and the stimulators were placed approximately 14 cm away from the areas targeted for stimulation (Porciatti et al., 2002).

All stimulation protocols were defined and programmed using Spike2 CED software. Although several protocols are available to evoke responses, visual stimulation in this project was delivered through a flickering light flash at 1 Hz (Cambiaghi et al., 2011; Lopez et al., 2002) visual stimulation was delivered perpendicular to the left eye (ipsilateral to the recorded hemisphere) with a duration of 30 ms. In selected experimental cohorts, the contralateral eye was also stimulated; the corresponding procedures are detailed in Methods, Section 3. Light emission measured 100 lux at the source, 70 lux at 5 cm, and 15 lux at 50 cm through an eight-horizontal-grid system. Somatosensory stimulation consisted of a brief air puff to the right whiskers at 1 Hz (contralateral to the recording site), lasting 30 ms, with a delay of 9 ms between stimulation and contact with the animal. During the design and validation of the somatosensory stimulation system, acoustic and video assessments were performed to ensure that the air puff was directed focally to the vibrissae and did not provide cues through other sensory modalities. To characterise the acoustic emission of the whisker stimulator itself, sound-level measurements were performed in a quiet room of the animal facility. At the point of whisker contact, the device's peak sound pressure level did not exceed 30 dB. By contrast, during recording sessions the laboratory's ambient background (ventilation, equipment, furnishings) was 60-70 dB. Thus, in the experimental setting the stimulator's acoustic output lay well below the ambient noise floor; the 30 dB value refers to the stimulator's self-noise (measured in silence), not to the in-room level during recordings. Previous studies have reported that such somatosensory stimulation may also activate the auditory system; to minimise this cross-modal influence, some groups have adapted their setups to produce approximately 55 dB at the stimulator, while maintaining ambient noise around 70 dB during experiments (Galvez et al., 2007, 2009). These checks were performed several times per year, coinciding with routine equipment maintenance. The airflow trajectory was adjusted to avoid impinging on other facial regions, and video recordings did not reveal a consistent causal relationship between puff delivery and eyelid closure. It is acknowledged, however, that it is not entirely feasible to eliminate air turbulence noise or minor skin deflections,

and therefore a residual auditory or mechanoreceptive effect may persist. By documenting the acoustic limits, measurement frequency, and visual monitoring protocol, a reproducible methodology was established to ensure that the observed behavioural responses primarily reflected whisker deflection. Auditory stimulation was delivered through a speaker positioned to the right of the animal (with ears uncovered), emitting a 60 dB, 4 kHz sinusoidal wave lasting 30 ms (Taberner & Liberman, 2005) at 1 Hz.

Using the previously described device, the electrode was advanced through one of the craniotomy windows to a depth of 700 µm at a speed of 5 µm per second. After 30 seconds, it was retracted to 600 µm and a 2-minute interval was allowed before initiating the electrophysiological recording protocol. Neural activity was recorded at this depth for 300 s for each type of stimulus (visual, somatosensory, or auditory). The same protocol was repeated at depths of 400, and 200 µm in both the binocular and monocular regions. Upon completion of the recording session, or after a maximum duration of 2.5 hours, the craniotomy windows were cleaned and sealed with bone wax (**Figure 41**).

1.4 Unit activity recording in awake animals

The protocol was essentially identical to that used for LFP recordings. The same type of electrode was employed, namely quartz-platinum/tungsten microelectrodes, but with an impedance of 1-4 MΩ to facilitate single-unit recordings. Electrodes were mounted in a circular seven-channel Eckhorn microdrive (Thomas Recordings©, Giessen, Germany). A 100 Hz filter was applied to the raw signal, and 50 Hz noise was removed using the Hum Bug Noise Eliminator (AM-Systems, USA). Prior to the recording sessions, animals were allowed 15 minutes of free movement within the designated area of the recording setup. After this habituation period, the head was fixed while animals were free to move on a running wheel. Once the animal was properly positioned and calm, the reference electrode was connected and the stimulators were placed.

All preparatory procedures were identical to those described above. The method of lowering the electrode differed, as an active search for single-unit activity (SUA) was carried out in each cranial window, with both SUA and multi-unit activity (MUA) detected along V1. Once a clear signal was obtained, the recording protocol was initiated. Five stimuli of one type were presented for 15 seconds, after which the stimulus type was automatically switched, continuing until all three modalities had been delivered. This loop was repeated until 900 seconds of recording were completed. This procedure ensured that neuronal activity could be compared across the three types of stimulation while minimising the risk of losing the same SUA or MUA by interspersing

stimuli within the same session. Recordings lasting less than 800 seconds were excluded from further analysis.

1.5 Treatments

In this section, the three interventions used to modulate V1 plasticity following monocular deprivation (MD) are described: visual stimulation (1.5.3), transcranial direct-current stimulation (tDCS; 1.5.1), and donepezil injection (1.5.2). Only stimulation/drug protocols are detailed here; cohort composition is reported in Section 3 (Methods). To maximise the effectiveness of these plasticity-modulating interventions, all treated cohorts were maintained under environmental enrichment (EE). The literature indicates that EE preserves juvenile-like ocular-dominance plasticity into adulthood in animals reared in EE, and that even late transfer to EE reinstates MD-induced shifts in ocular dominance; in parallel, exposure to EE throughout development expands V1, broadens visual-field coverage, and reorganises cortical magnification, providing an anatomical-functional substrate that may potentiate the efficacy of these interventions (Bibollet-Bahena et al., 2023; Greifzu et al., 2014) . The EE protocol applied in this study was inspired by the cited studies but employed larger cages (86 × 86 × 25 cm) equipped with cardboard or wooden toys, shelters, nesting material, and at least two running wheels; objects were repositioned daily during transfer of the animals to the neural-recording area to maintain novelty.

1.5.1 tDCS

To modulate V1 plasticity, transcranial direct-current stimulation (tDCS) was delivered using a high-definition epicranial montage inspired by the chlorided-silver (Ag/AgCl) ring geometry described by Sánchez-León et al. (2025), 2.5 mm inner diameter and 3.5 mm outer diameter, affixed to the skull with dental cement, together with a 6 cm^2 rubber-pad return electrode on the shaved back, moistened with conductive gel, so that current density is concentrated at the active electrode and minimised at the return. tDCS was applied between the ring (active) and the dorsal pad (reference), following that configuration.

Polarity was set to anodal at the ring over V1, given that anodal stimulation increases excitability in the rodent visual cortex (Cambiaghi et al., 2011) and has shown functional efficacy in repeated protocols (200 μA, 20 min for 8 days) in an amblyopic rat model using an epicranial anode and

dorsal return. The 200 µA intensity from that study (Castaño-Castaño et al., 2017) was retained and transferred to the ring geometry, with the temporal treatment regimen adjusted accordingly.

Each session consisted of a constant current of 200 µA (Castaño-Castaño et al., 2017) for ≈15 min over two weeks to mirror the treatments described in the following sections. As a reference for current-density ranges in mouse V1, an epicranial electrode of 4.5 mm² yields 5.55 mA/cm² at 250 µA. For a ring-electrode area $A = \pi(r_{ext}^2 - r_{int}^2)$ with $r_{ext} = 0.175$ cm and $r_{int} = 0.125$ cm, $A = 0.0471$ cm²; with $I = 0.200$ mA, the current density at the active electrode was $J = \frac{I}{A} = \frac{0.200}{0.0471} = 4.24$ mA/cm²(Cambiaghi et al., 2011). At the 6 cm² return, the density was $J = \frac{I}{A} = \frac{0.200}{6} = 0.033$ mA/cm², some orders lower than at the cranial electrode.

An Isostim™ A320 stimulator was configured in EXT/DC mode to deliver direct current. The output was kept active by applying a constant +5 V to the EXT INPUT via a Power1401 (CED, Cambridge, UK). The intensity was set to 200 µA (Range ×1; Current = 0.2 mA) and the polarity to RED+ for anodal stimulation over the epicranial ring on V1; the black terminal was connected to the dorsal return electrode (6 cm² rubber pad). The duration of each session (≈15 min) was controlled from the Power1401.

1.5.2 Injection of Donepezil

Donepezil treatment has been widely used in rats, where doses of 1 mg/kg combined with visual training increase acetylcholine in the cortex, strengthen visual responses, and trigger an upregulation of cholinergic receptors that could support long-term plastic changes. This suggests that combining cholinergic potentiation with visual training could be useful for improving visual processing (Chamoun et al., 2016). In rats as well, but after optic nerve injury, i.e., partial bilateral crush, donepezil treatment improved brightness discrimination compared with serum-treated controls (Chamoun et al., 2017). In clinical trials in children and adults with anisometropic and/or strabismic amblyopia, daily oral donepezil was administered for 12 weeks with dose escalation according to age or patient improvement; participants under 18 years were patched for 2 h per day. The acuity of the amblyopic eye improved and was maintained even 10 weeks after discontinuing the drug, without changing the visual acuity of the fellow eye; that is, cholinergic potentiation even after the critical period could facilitate durable plasticity (Wu et al., 2023).

In this study, donepezil (DNPZ) (DPZ; Sigma-Aldrich, D6821-10MG) was dissolved in sterile 0.9% NaCl and administered intraperitoneally at 1 mg/kg, one injection per day for two weeks.

Following the protocol of Chamoun et al. (2016) , the injection was given 30 min before each visual-training session to coincide with the peak pharmacological effect.

Although in the original protocol stimulation was delivered for 10 min, the drug-accompanying visual treatment used there consisted of three monitors (one frontal and two lateral) at 21 cm with a luminance of 37 cd/m², whereas in the present study the stimulus subtended a smaller visual area; therefore, 5 min were added to the planned 10 min, yielding a final visual-stimulation duration of 15 min.

1.5.3 Visual stimulation

As mentioned in the previous section, donepezil treatment was administered together with visual stimulation to facilitate plasticity processes according to the literature. In this project, the same protocol used in that literature was to be adopted; however, given that non-invasive flickering light at beta or gamma frequencies reactivates plasticity in adult murine models in which such processes are no longer frequent or are linked to loss of plastic capacity, such as amblyopia, this line of stimulation was followed (Ma et al., 2025). Nevertheless, as will be shown later in the Results, in the control condition the frequency band with the highest peak power during visual stimulation is theta; therefore, this frequency was tested for visual stimulation while the other two types of treatment were carried out. Stimulation was delivered 30 minutes after the injection of donepezil or during tDCS, at 14 cm from the eye ipsilateral to the area where tDCS was applied, using the same visual stimulator that was used to evoke the V1 response at the time of recording, i.e., light flash (measured 100 lux at the source, 70 lux at 5 cm, and 15 lux at 50 cm) through an eight-horizontal-grid system. The animal was awake and could walk on the wheel, with the head fixed to ensure the angle of visual stimulation.

1.6 Histological confirmation of electrode position

At the end of the live animal experimentation period, a perfusion and tissue preservation protocol was carried out for the target brain regions. Animals were anesthetised in an isoflurane chamber (3% Iso-Vet), followed by a lethal intraperitoneal injection of ketamine (200 mg/kg). In selected cases, a needle adapted to the recording setup was inserted into both cranial windows to a depth of approximately 2 mm for coordinate verification. Prior to insertion, the tip was immersed in a

dye solution containing 2.5 mg/ml DiL (Tetramethylindocarbocyanine Perchlorate) (D282, Invitrogen™) in ethanol, according to the Lipophilic Tracers protocol.

To ensure accurate alignment with the targeted cortical regions, standard intracardiac perfusion with 4% paraformaldehyde (PFA) was performed. Brains were extracted, post-fixed in 4% PFA for 48 hours, and embedded in paraffin blocks. Coronal sections (≈15 µm) were obtained at the approximate coordinates of the cranial windows using a microtome and stained with Cresyl Violet. Fluorescence imaging was conducted with a Nikon Ti-E Fluorescence Phase Inverted Microscope PFS Lumencor (Nikon Corporation, Tokyo, Japan) using an excitation wavelength of 549 nm and an emission wavelength of 565 nm for DiL detection.

Electrode tracts were clearly visualised under fluorescence microscopy, with bright DiL signals marking the entire length of the tracks without evidence of tissue damage. These well-defined fluorescent bands were oriented perpendicularly to the cortical surface within both binocular and monocular zones, confirming accurate electrode placement in V1. The stable fluorescence of DiL enabled precise identification of electrode tracts with minimal lateral diffusion. This method, which required no additional tissue processing beyond standard perfusion and sectioning, preserved tissue integrity for further analyses. The use of DiL also facilitated the differentiation of closely spaced electrode tracts, ensuring that recordings were obtained from the intended cortical regions (DiCarlo et al., 1996). **Figure 45** illustrates the overlay of these sections with the Franklin and Paxinos atlas (2019), further validating electrode positioning within V1.

2. Data analysis and statistical methods

2.1 LFP recording analysis

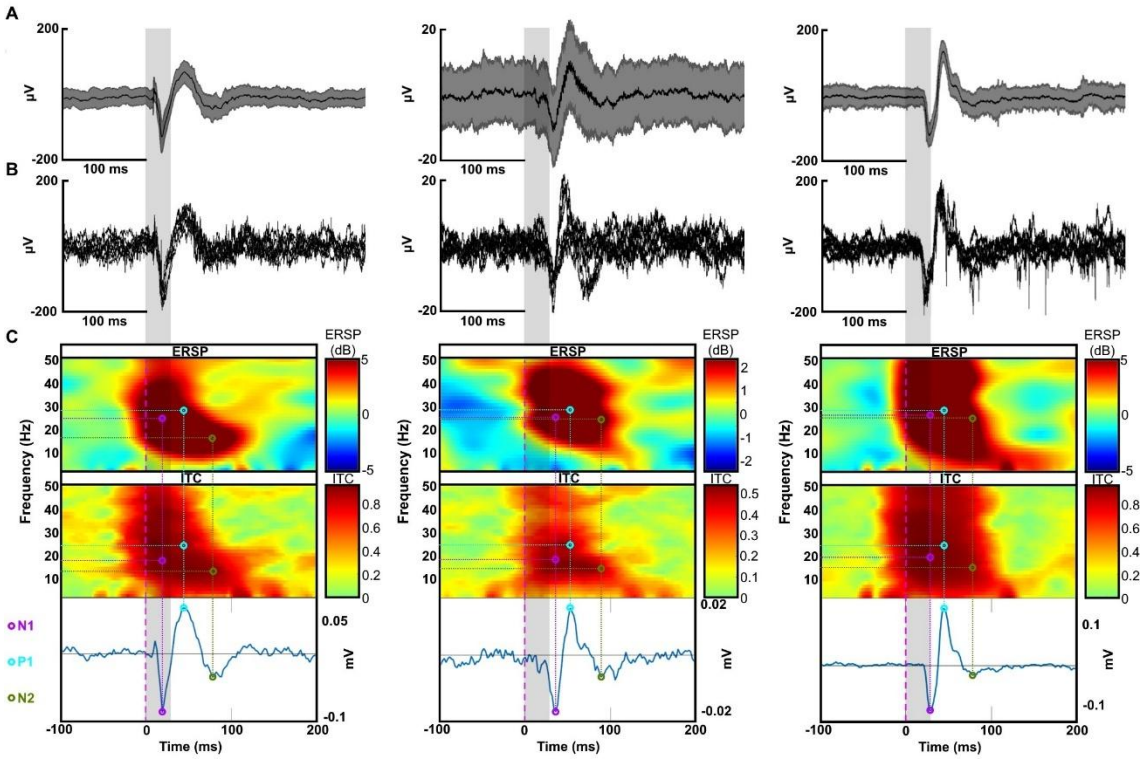

Figure 42. Signal processing and selection of ERSP/ITC values at ERP components. From left to right, the three columns correspond to somatosensory, auditory, and visual stimulation; the same processing pipeline is applied to each modality and panels (A-C) are shown for each.

(A) Grand-average of all stimulation events from a single recording session. The black central line represents the mean response, while the shaded grey area indicates the dispersion across trials.

(B) Superposition of eight individual stimulation events, showing how single-trial responses resemble the averaged waveform and its variability.

(C) ERSP and Inter-Trial Coherence (ITC) representations computed using EEGLAB. The upper heatmap shows ERSP values (dB), reflecting spectral power changes across time and frequency. The middle heatmap represents ITC, indicating phase alignment consistency across trials. The bottom panel depicts the corresponding event-related potential (ERP), where N1 (magenta), P1 (cyan), and N2 (green) mark the time points with the highest ERSP and ITC values. These key moments are highlighted by dashed lines in the ERSP and ITC maps, linking spectral features to specific ERP components.

Local field potential (LFP) signals were digitally stored following analogue-to-digital conversion using a Power1401 converter (CED, Cambridge, UK). Data were continuously digitised at a sampling rate of 25 kHz. Offline analyses and visualisations were performed with Spike2 (CED), Python, and EEGLAB (a MATLAB toolbox adapted for LFP analysis; **Figure 42**).

The evoked local field potential (eLFP) is a neurophysiological measure that reflects brain activity in response to specific stimuli, captured directly from intracortical recordings. eLFPs comprise a sequence of positive and negative deflections at characteristic latencies after stimulus onset. These features enable the identification of neuronal processing patterns, particularly the early components (N1, P1, and N2), which are critical for quantifying response latency and amplitude (Davies, 2010; Helfrich & Knight, 2019; Kaan, 2007; Rugg & Coles, 1996; Sur & Sinha, 2009b). The relative timing of N1 and P1 varied across trials, with N1 sometimes preceding P1 and, in other instances, following it (**Figure 42C**).

To assess the reliability of the neural responses, the grand-average LFP across all stimulation events was computed (**Figure 42A**). This representation provides an overview of the typical response pattern, in which the central black trace denotes the mean response and the shaded grey band reflects variability across trials. To further examine the consistency of individual responses, eight randomly selected stimulation events were overlaid on the same scale (**Figure 42B**). This visualisation indicates that single-trial waveforms generally follow the mean while exhibiting expected variability, supporting the stability of the evoked responses across trials.

A spectral analysis of V1-evoked responses was conducted using EEGLAB within MATLAB on data exported from Spike2. Event-related spectral perturbation (ERSP) and event-related potential (ERP) measures were quantified following the procedures described by Delorme and Makeig (2004). In this study, the ERP corresponds to the eLFP. An automated routine (Newtimef_VisionSpike_V1.m_DR) was implemented to detect positive and negative eLFP amplitude peaks, their latencies, and associated frequencies. For each eLFP recording, a time-frequency decomposition was applied over the 1-120 Hz range. At each time-frequency point, spectral power was normalized to the mean pre-stimulus baseline (-500 to 0 ms). The normalized values were then expressed in decibels using a 10*log10 transform (Grandchamp & Delorme, 2011) (**Figure 42C**, upper panel). In summary, for n trials, if $F_k(f, t)$ denotes the spectral estimate of trial k at frequency f and time t, then:

$$\mathrm{ERSP}(f,t) = \frac{1}{n}\sum_{k-1}^{n}|F_k(f,t)|^2$$

Inter-trial coherence (ITC), also referred to as the phase-locking factor, was used to quantify the consistency of oscillatory phase at a given latency and frequency across stimulus-locked LFP trials. In summary, for n trials, if $F_k(f,t)$ denotes the complex spectral estimate of trial k at frequency f and time t, then:

$$ITPC(f,t) = \left| \frac{1}{n} \sum_{k-1}^{n} \frac{F_k(f,t)}{|F_k(f,t)|} \right|$$

At each frequency and time point, software normalized the complex spectral estimate by dividing by its magnitude to isolate phase, averaged these unit-phase vectors across the n trials, and computed the length of the resulting vector yielding ITC values between 0 (no phase consistency) and 1 (perfect phase-locking) (**Figure 42C**, middle panel).

For each selected point in the eLFP signals, ERSP and ITC matrices were exported to Excel, and the peak values of ERP, ERSP, and ITC were recorded in separate worksheets for subsequent quantitative analysis. For each recording, the time points with the highest ERSP and ITC were identified and aligned with N1, P1, and N2 in the ERP (**Figure 42C**, bottom panel). These peaks were extracted automatically from the EEGLAB analysis and are indicated by dashed lines in the heat maps.

The extracted ERSP and ITC values were then analysed statistically. Normality was assessed with the Shapiro-Wilk test; as assumptions were not met, Kruskal-Wallis tests were used to evaluate group differences, and Dunn's post hoc tests were applied to determine pairwise differences between stimulation conditions. Data are reported as mean ± SEM, and statistical comparisons are displayed with boxplots.

2.2 Analysis of unit activity recordings

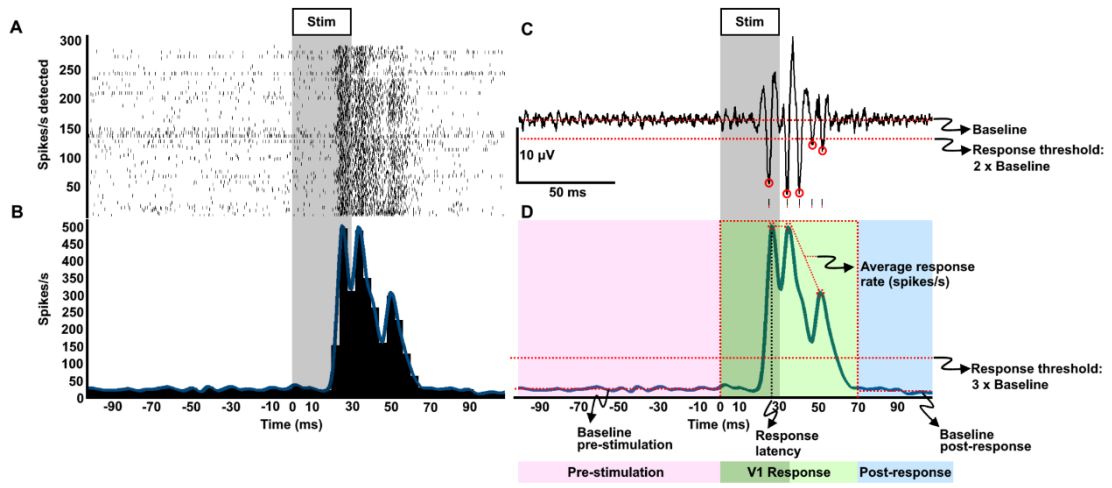

Figure 43. Process of extracting neural information from raw signals in response to visual stimulation in V1. (A) A raster plot displays detected units over time during the stimulation period (grey shaded area). Each dot represents a detected spike, and each row corresponds to a single trial. The highest spike density is observed shortly after stimulus onset.

(B) A peristimulus time histogram (PSTH) shows the firing rate (units per second) over time. A significant increase in firing activity is observed following stimulus onset, with two prominent peaks indicating strong neuronal responses in V1. The blue trace represents the smoothed average firing rate.

(C) A raw electrophysiological signal shows the multiunit activity detected in response to stimulation. Five small red marks indicate correctly identified spike events. The baseline activity is indicated by the lower dashed line, whereas the baseline threshold (set at 2× baseline) is indicated by the upper dashed line.

(D) A summary of response quantification illustrates different phases of neuronal activity: pre-stimulation baseline (pink), response latency period (green), and post-response phase (blue). The response latency is determined by the first significant increase in firing rate exceeding the 3× baseline threshold (red dashed line). Additionally, all peaks identified within the first 70 ms that surpass three times the baseline threshold are averaged to obtain the unit firing frequency during the response period. This allows for a precise estimation of V1 activation timing and response magnitude. The response latency is determined by the first peak that exceeds three times the baseline threshold within the response period.

Unit activity recordings were analyzed using Spike2 CED software (Cambridge, UK). For each recording session, three histograms, one per stimulation type, were generated to represent unit firing frequency 0.5 seconds before and 0.5 seconds after the stimulation. An example for contralateral visual stimulation is shown in **Figure 43 A,B**.

The initial raw electrophysiological signal is presented in **Figure 43 C** and corresponds to the unprocessed data recorded during a single visual stimulation in V1. Five small lines can be observed just below the peaks, indicating spikes correctly identified by the software.

Subsequently, a Python script was implemented to analyze all firing-rate graphs from all recordings. The script produced a report containing the average histograms for each stimulus type and an Excel file with the average frequency before, during, and after the stimulation event, as well as a value used to determine V1 response latency for different stimulation types. To obtain this value, the software selected an interval within the first 70 milliseconds after stimulus onset and identified the highest spike rate in the histogram within that interval. **Figure 43 D** visualises the detected multiunit events across an entire recording session, displaying the timing of events around the stimulation period and providing an overview of response consistency.

To visualize differences in responses across stimulation types, boxplots were generated. These plots characterized the distribution of unit firing frequencies for each stimulation type. A customized colour palette facilitated visual differentiation between time points. Statistical annotations were based on the Kruskal-Wallis test and Dunn's post hoc test to indicate differences between boxplots.

To determine V1 response latency to visual, auditory, and somatosensory stimulation, a representation methodology based on Levakova et al. (2015) was employed. Kernel density estimation (KDE) was used to obtain a continuous, smooth temporal distribution of unit activity, enabling identification of the density peak as the moment at which the highest frequency of active units is reached. This procedure provides a precise approximation of response latency, using values drawn from the interval automatically selected by the software within the first 70 ms after stimulus onset, where the highest spike rate was identified and exceeded at least three times the pre-stimulus baseline rate.

2.3 Ordinary least squares (OLS) model

In addition to presenting raw results, an additive OLS residualisation was applied, in line with the principle of Snoek et al., (2019) of controlling confounds to improve the interpretability of the analysis, removing variance attributable to Group and Modality prior to band-wise comparisons. This step is consistent with the central argument of Snoek et al. to disambiguate effects by removing alternative sources of information (confounds) that may distort interpretation; however, they caution that post hoc counterbalancing by subsampling can introduce positive bias (inflated performance), whereas whole-dataset confound regression (WDCR) can induce negative bias and even below-chance performance, and they therefore recommend performing confound regression within each cross-validation fold (CVCR). The present setting differs: no decoding or out-of-sample validation was performed, but rather band-wise inference on ERSP/ITC maxima across groups and modalities. Accordingly, the outcome variable y_i was residualised with an additive linear model including Group and Modality, and statistical tests were conducted on the residuals to separate global shifts from genuinely band-selective effects, while raw values (dB and ITC) were retained in parallel to communicate the real effect magnitudes.

The data were normalized to remove broad, across-the-board offsets attributable to experimental Group and recording Modality before performing band-wise comparisons. For each outcome type, ERSP (erSpMaxMax dB) and ITC (ITCMaxMax %), and separately for each sheet, an additive ordinary least squares (OLS) model with Group and Modality (the "Source File" field) as categorical predictors. Let y_i denote the observed measurement for observation i, $g(i)$ its group, and $m(i)$ its modality. The normalization model is

$$y_i = \mu + \alpha_{g(i)} + \gamma_{m(i)} + \varepsilon_i$$

Where μ is the intercept, α_g and γ_m are the main effects of Group and Modality, and ε_i is the error term. One level of each factor is used as the reference (baseline) for coding, often "visual"

for Modality when present, so the corresponding parameters are set to zero for identification (e.g., $\alpha_{control} = 0$, $\gamma_{visual} = 0$). This choice affects only how coefficients are reported; it does not affect fitted values or residuals.

For each observation, the fitted value was computed as

$$\hat{y}_i = \hat{\mu} + \hat{\alpha}_{g(i)} + \hat{\gamma}_{m(i)}$$

and defined the normalized value as the residual

$$r_i = y_i - \hat{y}_i$$

These residuals retain the original units and represent the portion of the measurement not explained by the additive main effects of Group and Modality. All downstream visualizations and tests were then performed either on r_i (normalized mode) or on y_i (raw mode), with the choice made explicitly at runtime.

Group differences within each band, stratified by Modality, were assessed using rank-based non-parametric statistics (Kruskal-Wallis and, where appropriate, Dunn's post hoc tests with optional Bonferroni/Holm correction). These tests do not assume normality and are compatible with residualised data. Conceptually, testing r_i evaluates whether groups differ within a band beyond what is explained by the additive global means of Group and Modality, focusing on band-selective effects.

Goodness of fit will be summarised by the correlation (R) between observed and fitted values, the coefficient of determination (R^2) and its adjusted version (adjusted R^2), together with the root mean square error (RMSE) in the original (natural) units; the overall significance of the model will be reported with the F-statistic and its p-value. The Akaike information criterion (AIC) and the Bayesian information criterion (BIC; Schwarz) will be reported for comparative reference across models, and the explained variance will be decomposed by means of type II analysis of variance (ANOVA). Assumptions will be evaluated on the residuals using the Jarque-Bera (normality) and Breusch-Pagan (homoscedasticity) tests, as well as the Durbin-Watson statistic (first-order autocorrelation); the influence of individual observations will be quantified with Cook's distance. In figures, means will be accompanied by the 95% confidence interval (95% CI), calculated as mean ± 1.96·standard error (SE); no t-tests will be performed on coefficients, since OLS is employed as a residualisation step prior to band inference and not as a basis for parametric inference on α_g or γ_m (**Appendix 1**).

2.4 Study of eLFP latency

For each recording session and for each modality, the maximum ITC in the time-frequency plane was located within a pre-defined post-stimulus window; from that maximum, two parameters were extracted: the latency (ms from stimulus onset) and the associated frequency (Hz), stratifying by bands (delta, theta, alpha, beta, gamma). This decision is grounded in the fact that ITC peak latencies are informative about change-detection dynamics: in audition, θ, α, and β take part in that process with differentiated roles, and β-ITC behaves as a faster indicator than α-ITC and N1 in the face of frequency transitions, as well as exhibiting temporal stability in the presence of concurrent neural activity. Likewise, stimuli with complex time-frequency structure (e.g., chirps or mid-trial changes) require longer latencies to achieve phase coherence, which justifies reporting the latency of the ITC peak as the primary marker of response time by band (Xia et al., 2023).

At the group level, the distributions of latencies (and, where appropriate, of peak frequencies) were described by Kernel Density Estimation (KDE) by band and condition (drugs vs. controls). KDE allows comparison of temporal shifts (advances/delays) between groups without assuming normality, offers high resolution, and enables analyses restricted to a priori hypotheses when one wishes to focus inference-properties demonstrated in validations specific to cognitive neuroscience. In replications and simulations with known properties, KDE detected true differences between conditions and kept few false alarms in null scenarios, in addition to distinguishing overlapping distributions with interpretable sensitivity; transferred to the one-dimensional case of latencies, this reinforces its suitability as a population summary and as a basis for between-group contrasts (Belyk et al., 2017).

Estimating one latency per recording and analysing it at the group level via distributions (KDE, shift functions, and bootstrap CIs) follows recent recommendations for characterising the temporal dynamics of early responses without assuming normality and with spatiotemporal control via permutations. In particular, it has been shown that extracting individual latencies and comparing them by robust/non-parametric methods yields reliable and reproducible estimates of onsets, provided that causal filters are applied to avoid temporal biases. This framework supports the procedure of (i) locating, per session and condition, the latency of the ITC maximum and (ii) comparing latency distributions between groups and bands to evaluate treatment-induced advances/delays (Bieniek et al., 2016).

Taken together, this methodological framework is supported both by empirical evidence linking ITC latencies to change detection (including the temporal advantage of β-ITC and the lengthening of latencies with more complex stimuli) and by specific validations of KDE for comparing distributions and resolving overlaps with a low false-positive rate. This set of decisions allows sensitive quantification of treatment-induced advances or delays in response time and their

documentation in a non-parametric and reproducible manner across frequency bands and sensory modalities.

3. Cohorts and timing

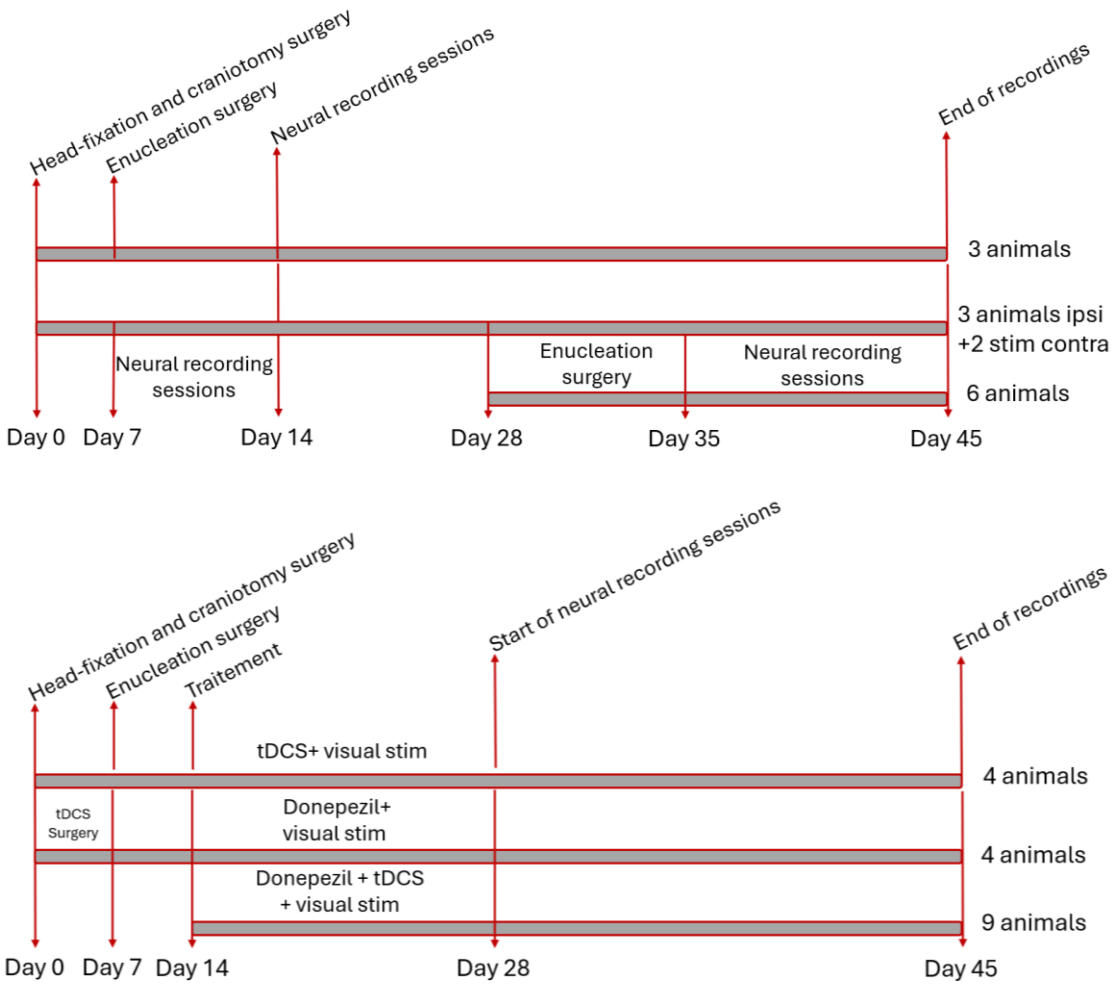

Figure 44. Cohort scheme and experimental timeline. The figure provides a synoptic overview of cohort organisation and the timing of surgeries, treatments and recordings. Top: timeline of untreated cohorts, controls (ipsilateral and contralateral visual stimulation) and monocular enucleation, including the control subgroup with deferred enucleation for pre/post comparison. Bottom: timeline of enucleated, treated cohorts (donepezil, tDCS, and donepezil + tDCS), highlighting that the tDCS surgery includes implantation of the ring. Temporal bars and markers indicate milestones (surgeries, start of treatments, recording windows and end of recordings).

Throughout the study, six cohorts of mice were organised, each with precise schedules for surgery, recovery, recording sessions and, where applicable, treatments. In addition to the six cohorts presented below, two further cohorts were included. The first consisted of five animals (n = 5) used for single- and multi-unit recordings. These animals followed the timeline of the control

group depicted in the upper panel of the **Figure 44**; however, in this case V1 responses to both contralateral and ipsilateral (defined relative to the recorded hemisphere) visual stimulation were recorded in all animals. The second cohort, not shown in the **Figure 44**, comprised four animals (n = 4) used for Model Validation via reversible visual deprivation, as described in Section 1.1.1 of the Methods.

Cohort 1 (Control - ipsilateral stimulation) comprised 3 animals. On Day 0, head-fixation and craniotomy were performed. Between Day 7 and Day 45, sessions were conducted to record the neural response to auditory, somatosensory and visual stimulation of the eye ipsilateral to the hemisphere where recordings were made. No enucleation was performed in this cohort.

Cohort 2 (Control - contralateral stimulation, right eye) included 3 animals. The same initial head-fixation and craniotomy were performed on Day 0. Between Day 7 and Day 45, sessions were carried out to record the V1 neural response to auditory, somatosensory and contralateral visual stimulation, that is, of the right eye, and the group remained as a control without enucleation.

Cohort 3 (Early monocular enucleation of the right eye, no treatment) had 3 animals. Head-fixation and craniotomy were performed on Day 0, followed by monocular enucleation of the right eye on Day 7. After one week of recovery, neural recording sessions began on Day 14 and continued until Day 45, when data acquisition ended.

Cohort 4 (Control with deferred enucleation: pre-/post-) consisted of 6 animals that started as controls. Head-fixation and craniotomy were first performed on Day 0, and between Day 7 and Day 28 sessions were carried out to record the neural response to auditory, somatosensory and visual stimulation of the eye ipsilateral to the hemisphere where recordings were made. On Day 28, enucleation of the right eye was performed. After one week of recovery, recordings were resumed on Day 35 and continued until Day 45. For this cohort, therefore, neural activity is available before and after enucleation.

The three remaining cohorts correspond to enucleated animals that, in addition, received treatments and visual stimulation according to the scheme of the second **Figure 44**. In all cases the same temporal framework was followed: Day 0 surgery, Day 7 enucleation, Day 14 start of treatment, and Day 28 start of recordings, ending on Day 45.

Cohort 5 (Enucleation + donepezil + visual stimulation) included 4 animals. After head-fixation and craniotomy on Day 0 and enucleation on Day 7, donepezil treatment began on Day 14 and was maintained together with visual stimulation. Neural recording sessions began on Day 28 and continued until Day 45.

Cohort 6 (tDCS intervention) grouped the animals with transcranial direct-current stimulation, whose surgical procedures were slightly different: in addition to head-fixation and craniotomy on

Day 0, a ring/coil for tDCS was implanted on the skull (tDCS surgery). After enucleation of the right eye on Day 7, tDCS began on Day 14 in combination with visual stimulation, and from Day 28 recordings were carried out until Day 45. Within this cohort there were two arms: tDCS only (4 animals) and tDCS + donepezil (9 animals), both following the same surgical and recording schedule; the only difference was the co-administration of donepezil in the combined arm.

In summary, the study included: ipsilateral controls (3) and contralateral/right-eye controls (3), early enucleation without treatment (3), control with deferred enucleation and pre-/post-recordings (6), enucleation + donepezil (4), and cohorts with tDCS, only (4) and combined with donepezil (9), with V1 responses to the three types of stimulation recorded during the recording phases in all cases. The key dates were common and are coded in the **Figure 44**: Day 0 (head-fixation and craniotomy; in tDCS, implantation of the ring in addition), Day 7 (right-eye enucleation for all enucleated groups), Day 14 (start of recordings for early enucleation and baseline recording window for controls; start of treatments in the pharmacological/electrical cohorts), Day 28 (deferred enucleation or start of recordings depending on cohort), Day 35 (restart of recordings post-enucleation in the deferred cohort) and Day 45 (end of recordings, according to the **Figure 44**). With this design, comparable data were obtained across control conditions, acute enucleation, deferred enucleation with pre-/post- measures, and enucleation combined with donepezil and/or tDCS.

4. Use of AI

In this work, generative artificial intelligence tools (e.g., ChatGPT, Gemini) were employed for a strictly instrumental purpose: to assist with translation and to support the development and debugging of code in Python and MATLAB. AI outputs were used as drafts or suggestions and were always reviewed, edited, and validated by the author. The tool did not make scientific decisions, nor did it replace the analysis, interpretation of results, or final writing.

For the linguistic component, AI was used to translate into British academic English and to propose improvements in fluency and style, while maintaining a glossary of technical terms to ensure terminological consistency. Each generated passage was checked manually, with meanings cross-verified and inappropriate literal renderings corrected before incorporation into the manuscript.

In programming, AI was employed to obtain examples of functions, code suggestions, and error localisation. All suggested code was rewritten and commented, and it was verified through tests with reference cases, checks of dimensions/units, and comparison of results with alternative methods where appropriate. Version control was maintained to ensure the traceability of changes.

To assure quality, any technical claim derived from the tool was cross-checked against the primary literature and the official documentation of the software libraries used. It is recognised that these systems may introduce errors or biases; responsibility for the accuracy of the content rests entirely with the author, who independently validated the results.

From an ethical and privacy perspective, no personal data, confidential information, or restricted datasets were shared with AI. Its use conformed to good academic practice: explicit disclosure of the use of these tools, human supervision at all stages, and preservation of intellectual authorship. Basic records of the queries/prompts and script versions were retained to support the reproducibility of the study.


Results

Results

1. Histological localization of electrodes in the primary visual cortex

Confirmation of electrode placement in the binocular and monocular regions of V1.

Before presenting the functional results, it was necessary to confirm the correct placement of the electrodes in the primary visual cortex (V1). This verification was essential, since V1 is not a homogeneous structure: at least two subregions with different functional properties can be distinguished. The binocular zone, located medially, receives afferents from both eyes and is specialized in stereoscopic integration, whereas the more lateral monocular zone receives input primarily from the contralateral eye. Because part of the analyses directly compared responses from these two areas, anatomical confirmation of electrode position was a critical step.

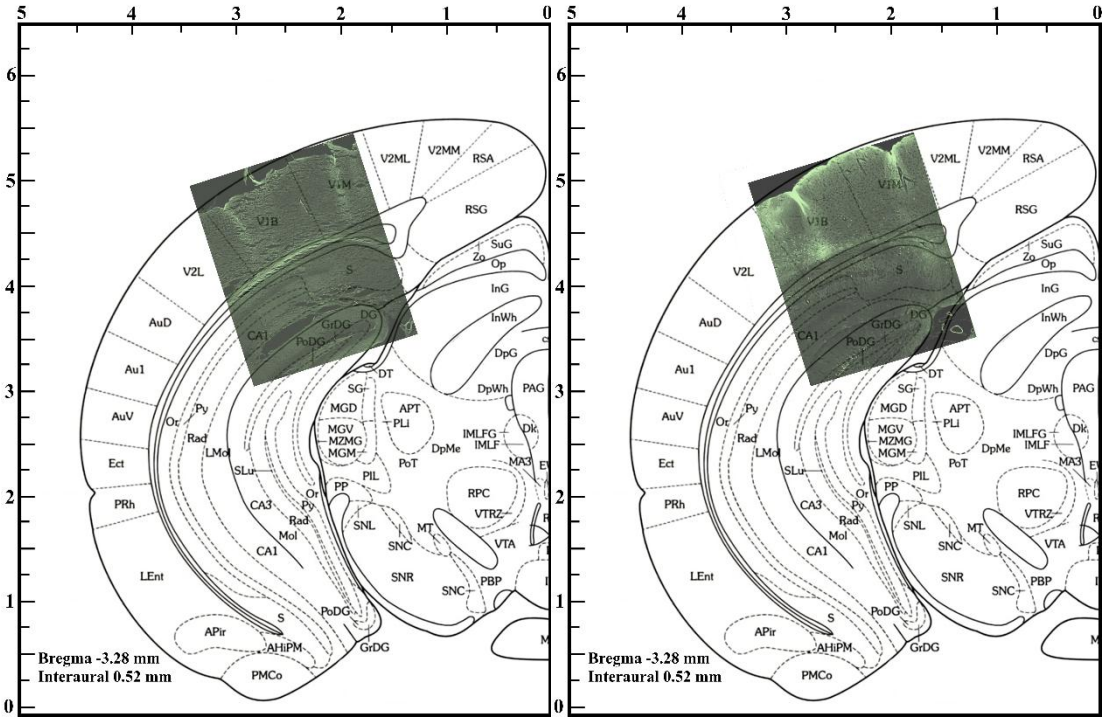

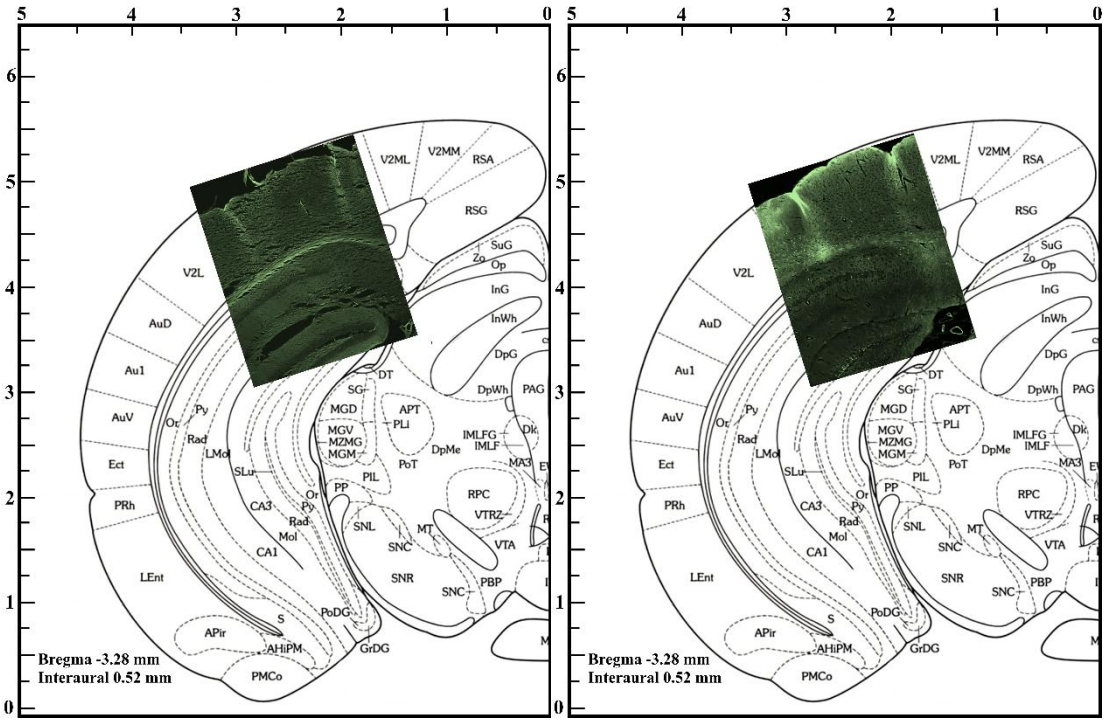

Figure 45. Histological sections overlaid on atlas images from Franklin and Paxinos (1997). This figure shows histological sections aligned with atlas images to confirm electrode tract positioning in the V1 region. The images demonstrate the overlap of electrode tracts within both the binocular and monocular zones of V1, validating the accurate targeting of these specific areas for neural recordings. Visible bands formed by DiL crystal deposits along the electrode tracts indicate the precise recording locations, ensuring reliable data collection from each region.

For this purpose, the lipophilic fluorescent tracer DiL was applied to the electrode tips. Following brain perfusion and tissue fixation, coronal sections were stained with Cresyl Violet and examined under fluorescence microscopy. DiL signals were clearly visualized along the electrode tracks, forming defined fluorescent bands perpendicular to the cortical surface, with no evidence of tissue damage.

The tracks confirmed precise electrode placement in both the binocular and monocular zones of V1, validating the correspondence between the neurophysiological recordings and the cortical regions of interest. Representative sections with electrode localization, superimposed on the Franklin and Paxinos (2019) atlas, are shown in **Figure 45**, ensuring the robustness of subsequent analyses.

2. V1 responds to multimodal stimuli with differential latency and frequency patterns

QUICK METHODS RECAP

V1 responses to three types of sensory stimulation were compared by assessing the maximum ERSP and ITC values across animal groups; intracortical LFPs were digitised at 25 kHz with a Power1401 and processed offline in Spike2/Python/EEGLAB. A 1-120 Hz decomposition was applied, and spectral power was normalised to the baseline (-500 to 0 ms), expressed in dB via 10·log10; ITC was computed as the mean phase-vector length (0-1). An automated routine detected peaks at time points coincident with N1, P1, and N2, and the maximum ERP/ERSP/ITC values were exported to spreadsheets for quantitative analysis. Stimulation was standardised at ≈14 cm: 30 ms visual flashes at 1 Hz (100 lux at the source; 70 at 5 cm; 15 at 50 cm), a 4 kHz pure tone at 60 dB, and a 30 ms somatosensory puff, with device self-noise (≤30 dB) documented against environmental noise (60-70 dB). Normality was evaluated (Shapiro-Wilk) and, as assumptions were not met, Kruskal-Wallis with Dunn's post-hoc tests were applied; results were presented as mean ± SEM and boxplots. Recordings were performed in both the monocular and binocular regions of V1. Here, 'monocular' and 'binocular' refer to cortical zones, not to the type of ocular stimulation.

2.1 Differences in ERSP and ITC across multimodal stimuli

The results presented below are an update of those reported in Caballero Tapia et al., (2025). Although the same data are used, the frequency-band classification system employed in this project has been updated and is based on that described by van Heusden et al., (2023): a classification of brain-wave distributions in mice as Delta (1-5 Hz), Theta (5-10 Hz), Alpha (10-13 Hz), Beta (13-30 Hz), and Gamma (30-120 Hz). For this reason, the figures do not coincide exactly with those in the publication, but, overall, the same pattern as described in the article is maintained.

ERSP dynamics

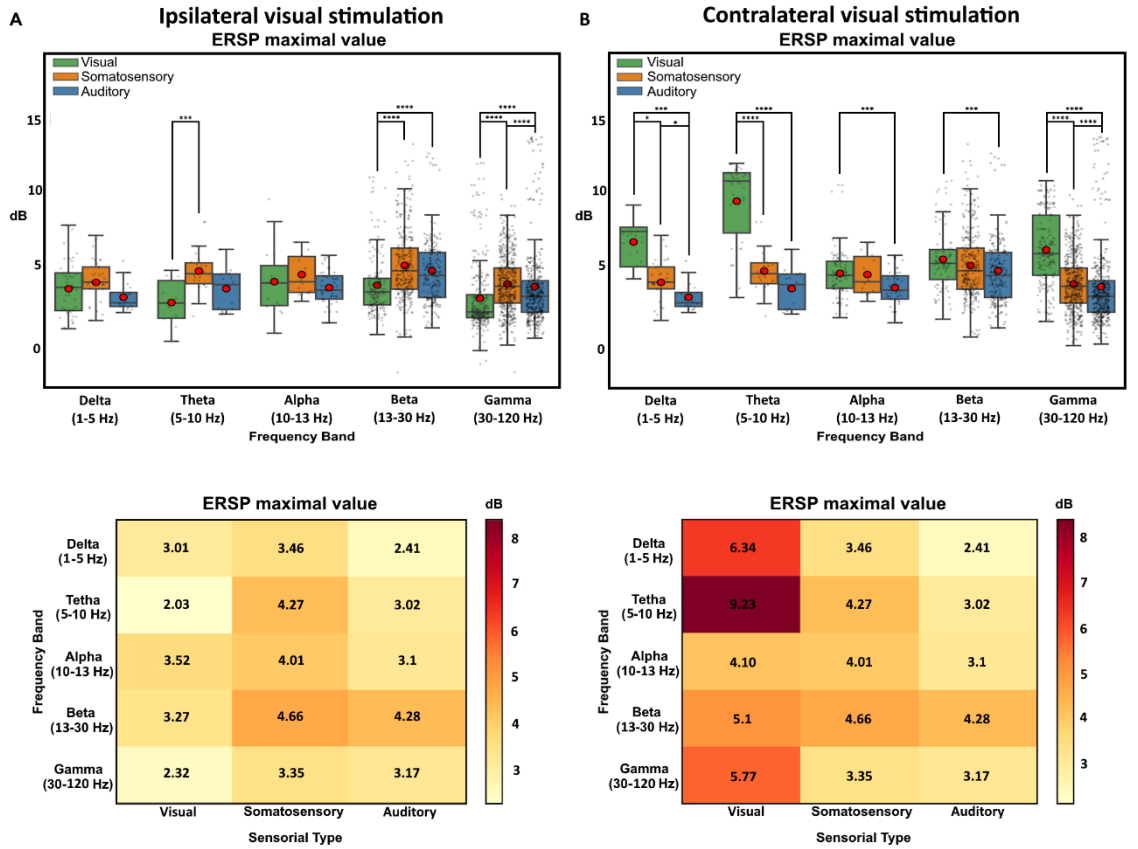

*Figure 46. Maximum ERSP values by frequency band and sensory modality. In (A) visual stimulation is applied ipsilateral to the recording site; in (B) it is contralateral. Somatosensory and auditory stimulations were always administered contralaterally and are therefore identical in (A) and (B). Upper panels: box plots showing the distribution of the maximum ERSP (dB) in five bands: delta (1-5 Hz), theta (5-10 Hz), alpha (10-13 Hz), beta (13-30 Hz), and gamma (30-120 Hz) for the visual (green), somatosensory (orange), and auditory (blue) modalities. Boxes show the median and IQR; points are individual values. Pairwise comparisons were performed using Dunn's test with Bonferroni correction; significance is marked as * p<0.05, ** p<0.01, *** p<0.001, **** p<0.0001. Lower panels: heatmaps with the mean values of the maximum ERSP (dB) by band (vertical axis) and modality (horizontal axis); the colour scale encodes the magnitude of the evoked power (lighter tones = lower; redder tones = higher).*

With ipsilateral visual stimulation (**Figure 46 A**), differences between the maximum values evoked by the three types of stimulation were confined to specific bands. In theta, the response to visual stimulation was lower than that evoked by somatosensory stimulation. In beta and gamma, the responses to somatosensory stimulation, and in gamma also to auditory stimulation, exceeded those evoked by visual stimulation. The heatmap averages confirm this pattern: for visual, maxima were in alpha ≈3.52 dB, followed by beta ≈3.27 dB and delta ≈3.01 dB, with lower values in theta ≈2.03 dB and gamma ≈2.32 dB. In contrast, somatosensory stimulation evoked high and consistent responses across all bands (Δ 3.46; θ 4.27; α 4.01; β 4.66; γ 3.35 dB), and auditory

stimulation reached a maximum in beta ≈4.28 dB (Δ 2.41; θ 3.02; α 3.10; γ 3.17 dB). Taken together, under ipsilateral conditions, beta was the most reactive band for somatosensory and auditory stimulation, whereas the response to visual stimulation remained moderate and was particularly low in theta and gamma.

By contrast, contralateral visual stimulation (**Figure 46 B**) evoked a generalized increase in ERSP compared to the other modalities, with significant differences relative to the values evoked by somatosensory and auditory stimulation in delta, theta, and gamma. The mean profile was clearly dominant in theta (≈9.23 dB) and also high in delta (≈6.34 dB), gamma (≈5.77 dB), and beta (≈5.10 dB); in alpha the increase was more modest (≈4.10 dB), comparable to somatosensory and slightly but significantly higher than auditory. As indicated in the legend, the values evoked by somatosensory and auditory stimulation are the same as in the ipsilateral condition (they were always applied contralaterally), thus maintaining their stable response pattern.

Whereas ipsilateral visual stimulation generates limited modulations (with somatosensory / auditory predominance in beta-gamma), contralateral visual stimulation triggers a broadband power increase in V1, with a prominent peak in theta and notable contributions in delta, beta, and gamma. This asymmetry highlights the strong hemispheric dependence of responses evoked by visual stimuli.

ITC dynamics

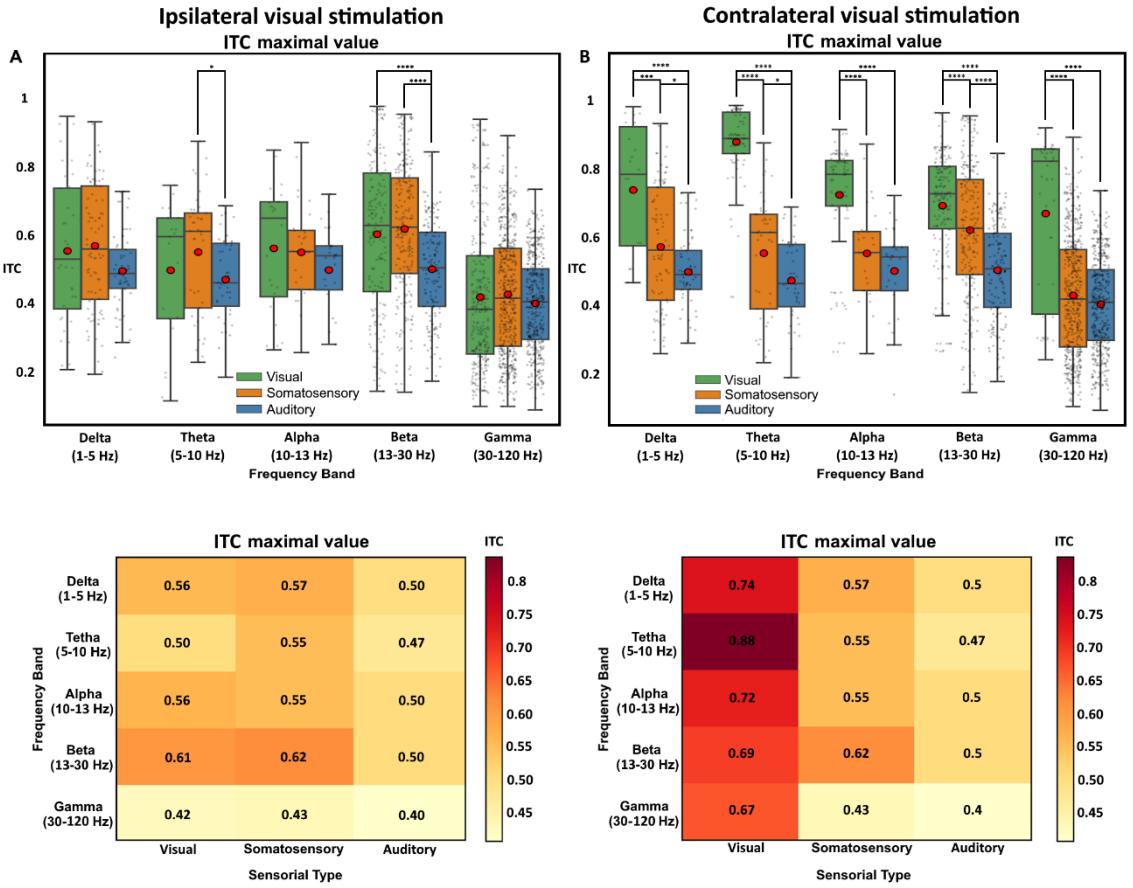

*Figure 47. Maximum ITC values by frequency band and sensory modality. In A, the visual stimulus is ipsilateral to the recording site, and in B it is contralateral. The other modalities (somatosensory and auditory) are presented contralaterally in both conditions. Upper panels: box plots showing the distribution of maximum ITC values evoked by visual (green), somatosensory (orange), and auditory (blue) stimulation in the delta (1-5 Hz), theta (5-10 Hz), alpha (10-13 Hz), beta (13-30 Hz), and gamma (30-120 Hz) bands. Each grey dot corresponds to an individual value, and the red dot indicates the mean. Comparisons were assessed with Dunn's post hoc test (Bonferroni correction). Significance levels: * $p < 0.05$; ** $p < 0.01$; *** $p < 0.001$; **** $p < 0.0001$. Lower panels: heatmaps with the mean maximum ITC values by band and stimulation modality (darker = higher ITC).*

Contralateral visual stimulation yields the highest ITC values across all bands, especially in delta, theta, and alpha, reaching a maximum of 0.88 in theta; under the ipsilateral condition, values remain moderate, and the main difference appears in beta, where visual and somatosensory exceed the auditory modality. The comparison of maximum inter-trial coherence (ITC) values showed a different pattern depending on the position of the visual stimulus relative to the recording site in V1. When visual stimulation was ipsilateral (**Figure 47 A**), ITC values remained moderate (~0.5-0.6 on average) and did not differ markedly from those obtained with somatosensory stimulation. In contrast, auditory stimulation consistently produced the lowest values across all bands. A more

subtle difference was also observed in theta (5-10 Hz) between the values evoked by auditory and somatosensory stimulation. Overall, during ipsilateral stimulation no ITC mean exceeded 0.7, with the highest values in beta (~0.61-0.62 for visual and somatosensory) and the lowest in gamma (30-120 Hz) (~0.42, 0.43, 0.40 for visual, somatosensory, and auditory).

With contralateral visual stimulation (**Figure 47 B**), the picture changed markedly: the visual stimulus generated ITC consistently greater than somatosensory and auditory across all bands, with significant differences in most comparisons. Mean ITC values for the visual modality were high not only in delta (1-5 Hz), theta, and alpha (10-13 Hz), but also in beta and gamma. The maximum was observed in theta (0.88), indicating particularly strong phase coupling in response to contralateral visual input. By contrast, the responses to somatosensory and auditory stimulation remained within ranges similar to those observed with ipsilateral stimulation, as they did not vary between the two studies, as indicated in the figure.

Taken together, the data indicate that only visual stimulation is strongly modulated by the hemifield of presentation: the contralateral stimulus enhances cortical phase synchrony in V1 across a broad frequency spectrum, with a peak in theta.

2.2 Influence of the type of stimulation on response latency and firing rate

QUICK METHODS RECAP

For the study of latency and firing rate (SUA/MUA), units were recorded with high-impedance electrodes following a loop that alternated 15 s blocks per stimulation modality until ≈900 s were completed (records <800 s were excluded). Latency was defined as the first increase in firing that exceeded 3× baseline within the 0-70 ms post-stimulus window; the firing rate was calculated as the average of spikes >3× baseline within that window. Temporal characterisation was represented with raster/PSTH and validated with kernel density estimation (KDE), complemented by boxplots to verify concordance between methods.

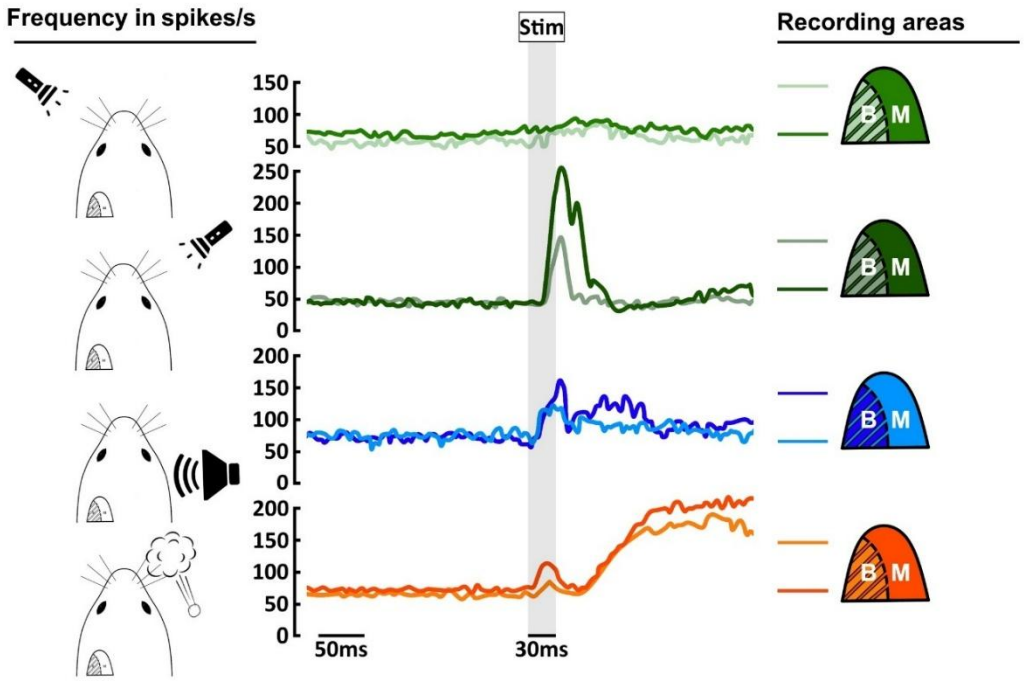

Figure 48. Analysis of single- and multi-unit frequency in V1 in response to different types of sensory stimulation. The plots show the grand average of firing rate (spikes/s) over time (ms) in response to visual (green), auditory (blue), and somatosensory (orange) stimuli. The shaded area marks the stimulation period. On the left side of the figure, the different stimulation conditions are illustrated. The first represents ipsilateral visual stimulation, the second contralateral visual stimulation, the third contralateral auditory stimulation, though without preventing the animal from perceiving the sound with the ipsilateral ear, and the last depicts somatosensory stimulation applied to the contralateral whiskers. The colour palette on the right indicates the origin of each activity represented. The first set (bright green) corresponds to ipsilateral visual stimulation, where the darker shade represents activity in the monocular zone and the lighter shade in the binocular zone. The second set (shaded green) represents contralateral visual stimulation, following the same convention: the darker green corresponds to the monocular zone, while the lighter green corresponds to the binocular zone (non-stimulated eye was not covered; however, the stimulus was positioned to minimize contralateral visibility). For auditory stimulation (third row), blue shades are used: the darker blue represents the binocular region, while the lighter blue represents the monocular region. Lastly, for somatosensory stimulation (fourth row), orange shades are applied: the darker orange corresponds to the monocular region and the lighter orange to the binocular region.

The recording of single-unit and multi-unit activity in V1 enabled analysis of both the per-second firing rate of these units and the response latency of V1 to the different types of stimulation. **Figure 48** illustrates the grand average of unit firing rates per second before and after stimulation. Ipsilateral stimulation evoked a small increase in V1 firing, whereas contralateral visual stimulation induced the most pronounced increase in firing among all types of stimulation tested,

affecting both monocular and binocular zones. V1 exhibited responses to different types of stimulation at the level of unit firing rate. Both auditory and somatosensory stimulation evoked firing-rate patterns more similar to those induced by contralateral visual stimulation than to those generated by ipsilateral stimulation. Approximately seventy milliseconds after stimulation, the activity recorded in V1 was associated with events beyond the direct sensory afference, such as motor or reflex responses. Somatosensory stimulation provided a example of this, eliciting a secondary increase in firing rate and suggesting the involvement of non-visual or non-sensorial influences in V1 neuronal activity.

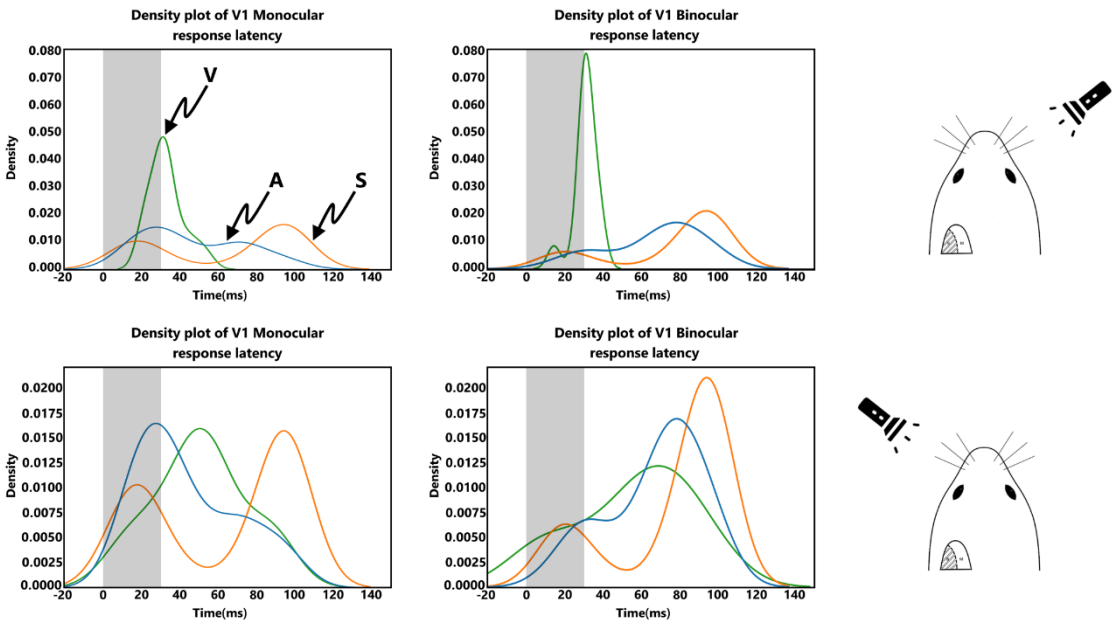

Figure 49. Kernel density plots of response latency in V1. Kernel density estimation (KDE) plots representing response latencies in the V1 region for different sensory stimuli. KDE is used to visualise the continuous distribution of response times, highlighting peaks and patterns in latency. The plots are divided into monocular (left) and binocular (right) response distributions. The x-axis represents time in milliseconds (ms), and the y-axis indicates density. Each plot includes three curves corresponding to different sensory modalities: green for visual stimuli (V), blue for auditory stimuli (A), and orange for somatosensory stimuli (S). The shaded area marks the stimulation period.

A first set of kernel density plots for the response latency values of V1 under different types of stimulation revealed clear differences depending on whether the visual stimulation was contralateral or ipsilateral and whether the recording area was in the binocular or monocular zone (**Figure 49**). The latency values showed a higher concentration around specific distributions, indicating distinct temporal processing characteristics for each condition. Contralateral visual stimulation evoked a response latency of 31 ms in both the monocular and binocular regions,

indicating a fast and synchronous activation across V1. Ipsilateral visual stimulation, however, resulted in longer latencies, with responses at 50 ms in the monocular zone and 68 ms in the binocular zone, suggesting weaker and delayed activation compared to contralateral input.

Somatosensory stimulation evoked an initial response at 18 ms in the monocular zone, slightly delayed to 20 ms in the binocular zone. A second latency peak appeared at 94 ms, identical in both monocular and binocular regions. Auditory stimulation elicited a response at 27 ms in the monocular zone and 33 ms in the binocular zone, following a latency pattern like early visual responses. A second response latency occurred at 71 ms in the monocular zone and 77 ms in the binocular zone (**Figure 49**).

These results indicate that somatosensory input elicits a faster response in V1 than visual input. In addition, the binocular zone showed slightly longer latencies than the monocular zone in general (except for contralateral visual input, for which the latency of the evoked response is practically the same in both zones), highlighting potential differences in the integration times of sensory inputs in V1.

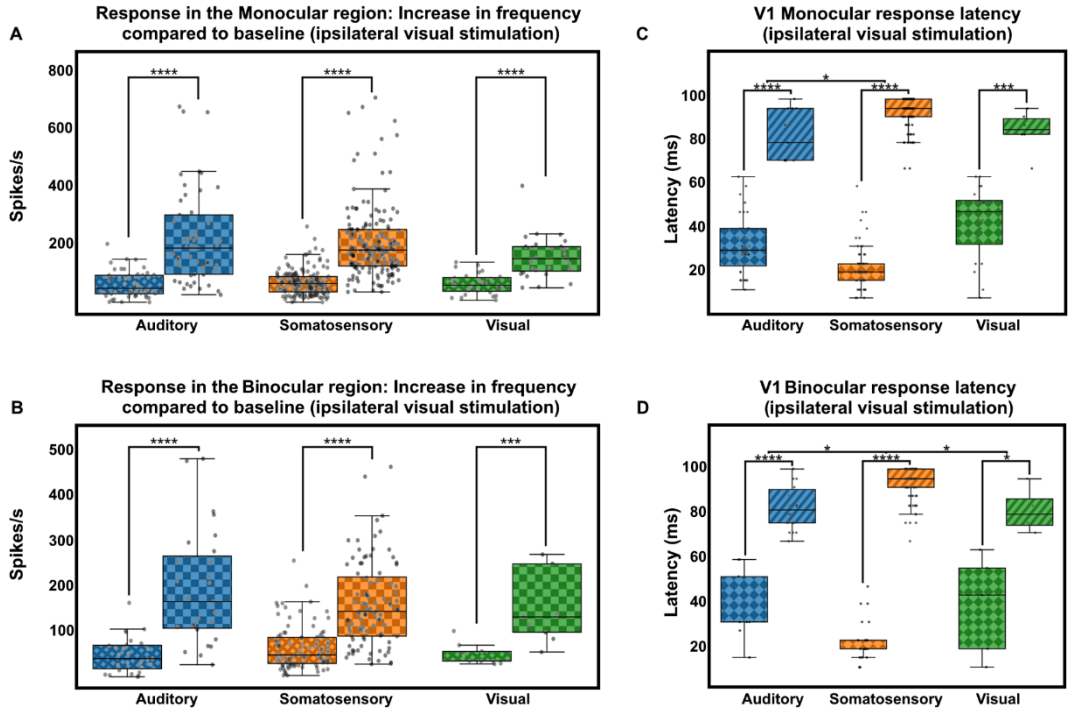

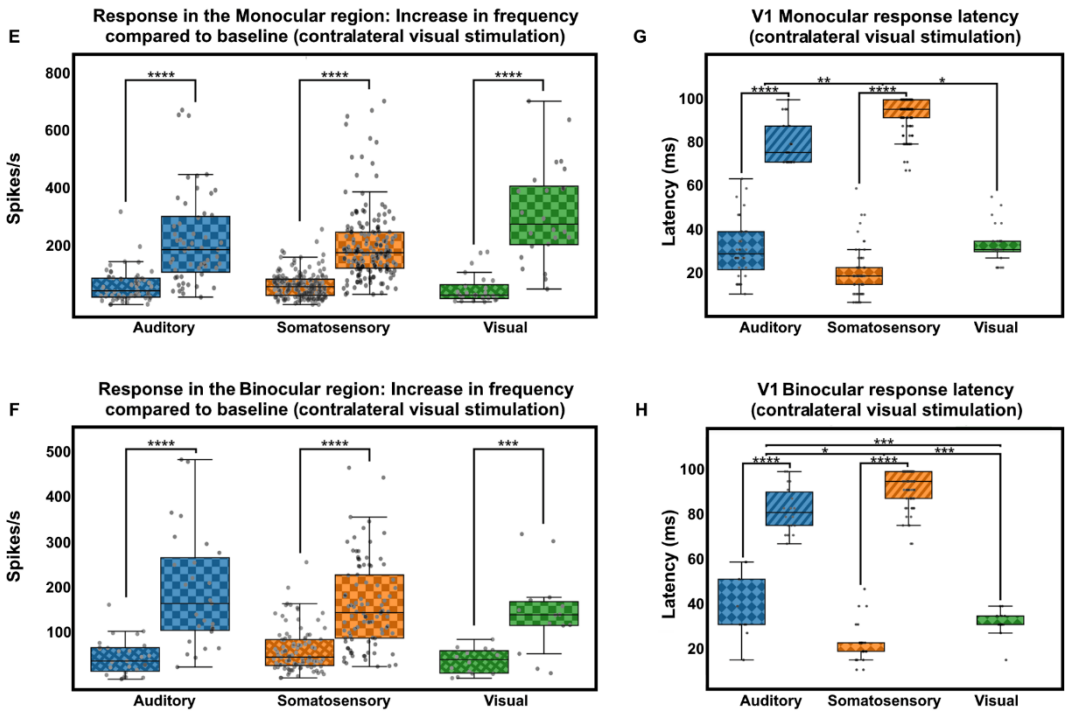

Figure 50. *Analysis of single- and multi-unit activity frequency and response latency in V1 following auditory, somatosensory, and visual stimulation. (A, B, E, F) Boxplots representing the increase in firing rate (spikes per second) compared to the baseline in the monocular (A, E) and binocular (B, F) regions of V1 in response to auditory (blue) and somatosensory (orange) stimulation. (A, B) correspond to ipsilateral visual stimulation (green), whereas (E, F) correspond to contralateral visual stimulation (green). The increase in firing rate was measured in the first 70 ms post-stimulus. Statistical significance levels are denoted by asterisks (* $p < 0.05$, ** $p < 0.01$, *** $p < 0.001$, **** $p < 0.0001$). (C, D, G, H) Boxplots showing the distribution of response latencies (ms) in the monocular (C, G) and binocular (D, H) regions of V1 for each sensory modality. (C, D) correspond to ipsilateral visual stimulation, whereas (G, H) correspond to contralateral visual stimulation. Depending on stimulus type and recording site, latency can be partitioned into two temporal components after stimulus: an early component up to 70 ms and a late component from 70 ms onward. The early component aligns with stimulus-evoked neuronal activity, whereas the late component likely reflects evoked motor activity or another higher-order process not investigated here.*

An alternative methodology for analysing response latency was based on boxplots (**Figure 50**), along with the calculation of median, mean, and standard deviation. This approach enabled direct visualisation of data distribution and facilitated trend identification across experimental conditions. Comparison of these results with the kernel density data from **Figure 49** showed strong concordance, reinforcing the robustness of both approaches and validating response time stability in V1.

Although minor differences in absolute values were observed, the general trend of monocular and binocular responses remained stable, reflecting consistent neuronal activation based on stimulation type (**Figure 50**). For contralateral visual stimulation, kernel density data showed a 31 ms latency in both monocular and binocular zones, indicating rapid, synchronised V1 activation. The median latency in boxplots was 30.29 ms for both conditions, closely aligning with the kernel density estimates. Slight variability in contralateral visual latency appeared in data dispersion, with standard deviations of 8.86 ms in the monocular zone and 5.81 ms in the binocular zone. This consistency across methodologies reinforced the reliability of early latency estimation in contralateral responses (**Figure 50 G, H**).

For ipsilateral visual stimulation, kernel density data indicated longer latency, with response times of 50 ms in the monocular zone and 68 ms in the binocular zone, suggesting delayed, less efficient activation compared to contralateral stimulation. Although the median latency in boxplots (42.3 ms in both conditions) remained close to kernel density estimates. Greater dispersion in these response times was reflected in the standard deviation (18.9 ms in the monocular zone and 24.6 ms in the binocular zone), suggesting neuronal response variability may explain part of the observed difference (**Figure 50 C, D**).

For somatosensory stimulation, kernel density data showed an initial latency of 18 ms in the monocular zone and 20 ms in the binocular zone, reflecting an early, efficient V1 response. The median values in boxplots were 18.2 ms in the monocular and 22.0 ms in the binocular zones, showing strong coherence with KDE (kernel density estimation) values. Kernel density data also revealed a second somatosensory latency at 94 ms, indicating late activation characteristic of this sensory modality. This second peak also appeared in boxplot values, with medians of 94.2 ms in both conditions. The standard deviation of approximately 8 ms in both conditions indicated low dispersion in this late latency, suggesting high stability in the somatosensory response (**Figure 50 C, D, G, H**).

For auditory stimulation, kernel density data showed a 27 ms latency in the monocular zone and 33 ms in the binocular zone, following an activation pattern like early visual responses. Boxplot values showed slight differences but maintained the trend, with medians of 28.3 ms and 30.2 ms, respectively. Similarly, kernel density estimates reported a second auditory latency at 71 ms in the monocular zone and 77 ms in the binocular zone, reflecting subsequent auditory stimulus processing. This pattern also appeared in boxplot values, with medians of 74.5 ms (monocular) and 80.32 ms (binocular). Data dispersion, reflected in standard deviations of 10-15 ms, may explain slight differences in absolute values (**Figure 50 C, D, G, H**).

The increase in firing rate was analysed by comparing the baseline, calculated as the mean over a 250 ms interval before stimulation, with the 70 ms post-stimulation window. Although the

baseline was not the same across all conditions studied here, it was confirmed that there were no significant differences between them. The response also showed substantial differences, reaching 145.7 Hz in ipsilateral (**Figure 50 A**) and 275.2 Hz in contralateral (**Figure 50 E**) stimulation, indicating contralateral visual stimulation elicited a higher spiking rate. In the binocular zone, the pattern was similar but less pronounced: the baseline was 31.5 Hz for ipsilateral (**Figure 50 B**) and 39.6 Hz for contralateral (**Figure 50 F**) stimulation, while the response reached 129.7 Hz in the ipsilateral (**Figure 50 B**) and 138.9 Hz in the contralateral condition (**Figure 50 F**), suggesting a smaller difference in this region.

For somatosensory stimulation, the baseline was 59.4 Hz in the monocular and 44.9 Hz in the binocular zone, while the response increased significantly to 175.7 Hz and 142.0 Hz, respectively, indicating strong activation. For auditory stimulation, baseline values were 42.7 Hz in the monocular and 36.6 Hz in the binocular zone, with the response reaching 182.4 Hz and 164.0 Hz, demonstrating a stable spike rate increase. While all sensory modalities increased neuronal activity relative to the baseline, contralateral visual stimulation in the monocular zone produced the highest unit rate increase, highlighting its role in V1 activation (**Figure 50 A, B, E, F**).

3. Enucleation alters synchronization and spectral power in V1

QUICK METHODS RECAP

To compare the neuronal activity of control versus enucleated animals, all followed the same experimental schedule (head-fixation and craniotomies; enucleation; baseline window or treatments; final recordings). Metrics were extracted in the same way as mentioned in the previous section when the V1 response to the three types of sensory stimulation under physiological conditions was described, obtaining ERSP (dB) and ITC (%) maxima by band (1-120 Hz, aggregated into δ, θ, α, β, and γ). Between-group comparisons were performed with non-parametric tests (Kruskal-Wallis and Dunn) on the maxima per frequency band × stimulation modality.

Prior to analyzing frequency-domain changes in power and coherence associated with monocular vision loss, we assessed event-related potential (ERP) amplitude in microvolts. No significant differences were detected between the physiological condition and monocular deprivation, and these results are therefore not reported further in this study.

3.1 Comparison of ERSP between controls and enucleated animals

In this study, the response of V1 was analyzed under three types of stimulation in five groups of animals with different physiological conditions (a control group, an enucleated group, an enucleated group treated with tDCS, an enucleated group treated with donepezil, and a final group treated with both tDCS and donepezil). This design yielded a total of 15 combinations. Using EEGLAB analysis, the maximal ERSP and ITC values were obtained across five frequency bands, resulting in 150 outcome combinations. These results were summarized using line charts with error bars, and the most relevant findings will be examined in greater detail. It should be noted that in this section only two groups of animals with different physiological conditions are considered: the control group and the vision-deprived group.

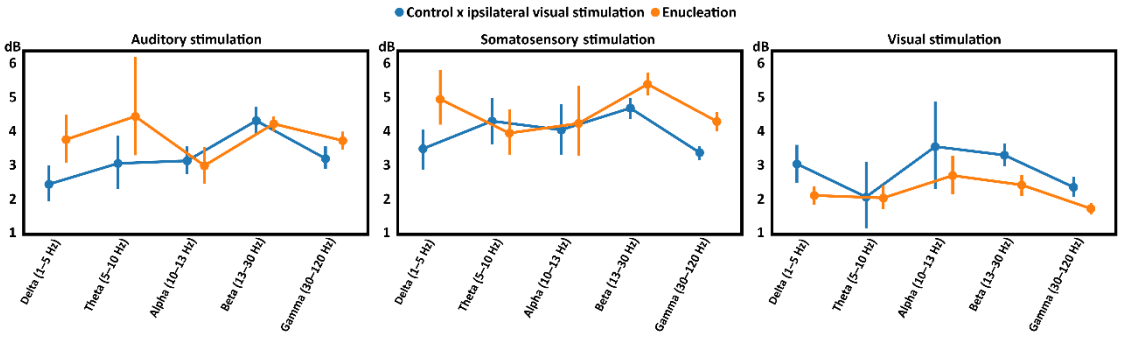

Figure 51. Maximum ERSP values across frequency bands (delta (1-5 Hz), theta (5-10 Hz), alpha (10-13 Hz), beta (13-30 Hz), and gamma (30-120 Hz)) were assessed during auditory, somatosensory, and visual stimulation. Error bars indicate the mean ± SEM for the control (blue) and enucleated (orange) groups. As the data are unnormalized, the figure enables direct comparison of spectral responses under different physiological conditions.

In response to auditory stimulation, the enucleated group exhibited higher ERSP values than controls in the delta and gamma bands. Visual stimulation consistently elicited stronger ERSP values in the control group across most frequency bands, with especially marked differences in the delta, beta and gamma bands. The theta band was an exception, where responses were comparable between groups. This pattern suggests a general reduction in visually evoked activity following enucleation.

Collectively, partial loss of visual input leads to diminished visually evoked power, while enhancing power in some frequency bands during auditory stimulation. A similar tendence in delta, beta, and gamma activity is also observed in response to somatosensory input (**Figure 51**).

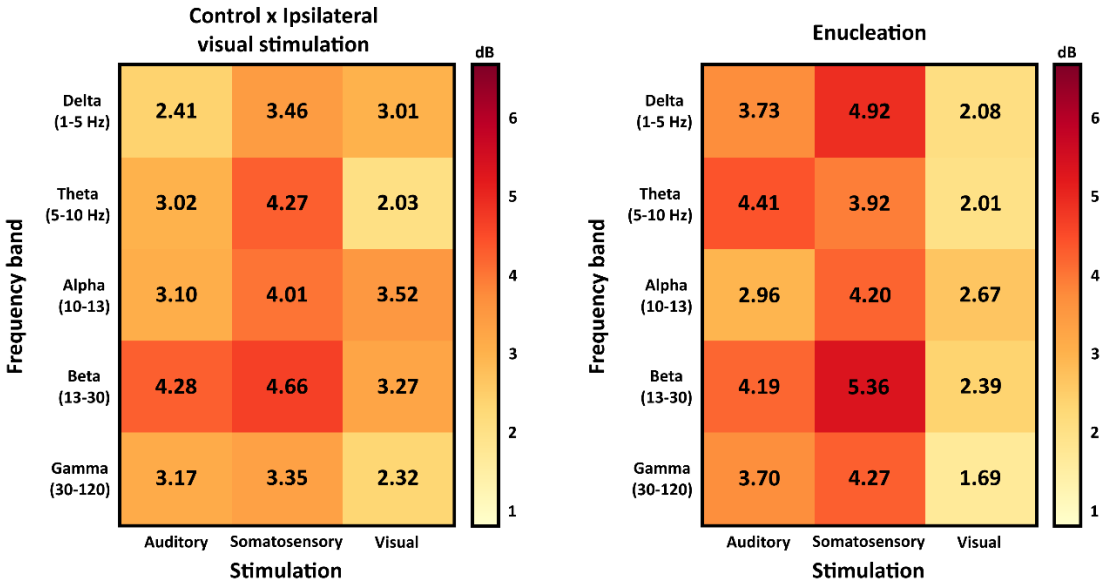

Figure 52. Heatmaps of ERSP values (dB) by frequency band, Delta (1-5 Hz), Theta (5-10 Hz), Alpha (10-13 Hz), Beta (13-30 Hz), and Gamma (30-120 Hz), and stimulation modality (Auditory, Somatosensory, Visual) for the control group with ipsilateral visual stimulation (left panel) and the enucleated group (right panel). Each cell represents the mean ERSP, with the colour bar indicating the dB scale. Relative to the control group, the enucleated group shows increased power in non-visual modalities, particularly in delta and somatosensory beta-gamma bands, and a generalized attenuation in response to visual stimulation.

Power (dB) was compared between control and enucleated groups across modalities and frequency bands using heatmaps, which provide a descriptive overview; between-group differences are treated as trends unless reported as statistically significant. During auditory stimulation, the enucleated group showed a increase in delta (+1.32 dB) and theta (+1.39 dB). Differences in alpha (-0.14 dB) and beta (-0.09 dB) were minimal, while a moderate increase was observed in gamma (+0.53 dB).

Somatosensory stimulation evoked higher values in delta (+1.46 dB), beta (+0.70 dB), and gamma (+0.92 dB). Alpha showed a small increase (+0.19 dB), whereas theta was reduced (-0.35 dB). Notably, the highest power value observed across all conditions corresponds to the somatosensory beta band in the enucleated group (5.36 dB).

Under visual stimulation, the pattern reversed: power was consistently lower in the enucleated group across all frequency bands. The most pronounced reductions were seen in delta (-0.93 dB), gamma (-0.63 dB), and beta (-0.88 dB), with minimal difference in theta (-0.02 dB) and a moderate decrease in alpha (-0.85 dB).

Taken together, these results suggest that monocular vision loss leads to enhanced power for non-visual sensory inputs, particularly in the delta and beta-gamma bands during somatosensory stimulation, accompanied by a systematic reduction in visually evoked activity (**Figure 52**).

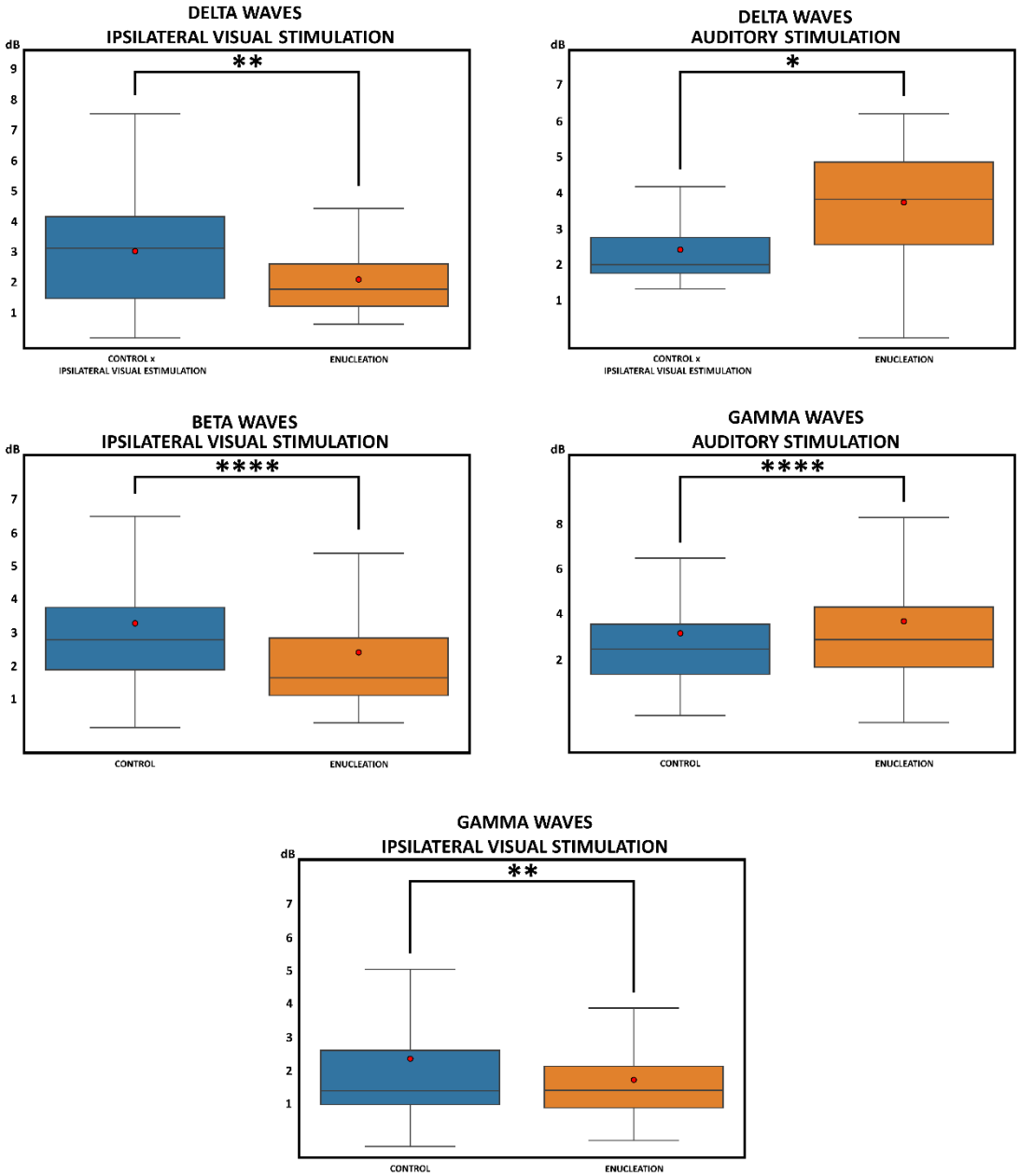

Figure 53. Boxplots of ERSP values across sensory modalities and frequency bands. Top left: visual-delta (1-5 Hz). Top right: auditory-delta (1-5 Hz). Middle left: visual-beta (13-30 Hz). Middle right: auditory-gamma (30-120 Hz). Bottom: visual-gamma (30-120 Hz). The groups shown are control (blue) and enucleated (orange). Boxes display the distribution of the original values; central lines indicate the median; whiskers show the range; and red points denote the group mean.

In delta band (1-5 Hz), a relative increase in ERSP values was observed in the enucleated group compared with controls during auditory stimulation, along with a significant decrease in response to visual stimulation. In contrast, no significant differences were found for somatosensory stimulation. When analysing the values, no significant differences in ERSP were observed in the theta band (5-10 Hz) and alpha band (10-13 Hz) between the control and enucleated groups, regardless of the stimulation modality (auditory, somatosensory, or visual). In beta band (13-30 Hz), a significant decrease in ERSP values was observed during visual stimulation in the enucleated group compared to the control group. By contrast, no significant differences were detected for the auditory or somatosensory modalities. Regarding the gamma band (30-120 Hz), significant increases in ERSP values were observed during auditory stimulation in the enucleated group. Moreover, a reduction in these values was detected during visual stimulation. Conversely, no significant differences were found for somatosensory stimulation.

Within the delta band (1-5 Hz), auditory ERSP mean values were higher in the enucleated group (3.73 dB) compared to the control group (2.41 dB). In contrast, visual stimulation produced a decrease in the enucleated group (2.08 dB) relative to the control group (3.02 dB). For the beta band (13-30 Hz), visual stimulation likewise showed a reduction in ERSP mean values in the enucleated group (2.59 dB) compared to the control (3.27 dB). Regarding the gamma band (30-120 Hz), an increase in auditory ERSP mean values was recorded in the enucleated group (4.29 dB) relative to the control (3.70 dB). Conversely, visual stimulation yielded a decrease in the enucleated group (1.69 dB) compared to the control (2.33 dB). No significant differences were found between groups for any of the somatosensory modalities (**Figure 53**).

3.2 Comparison of ITC between controls and enucleated animals

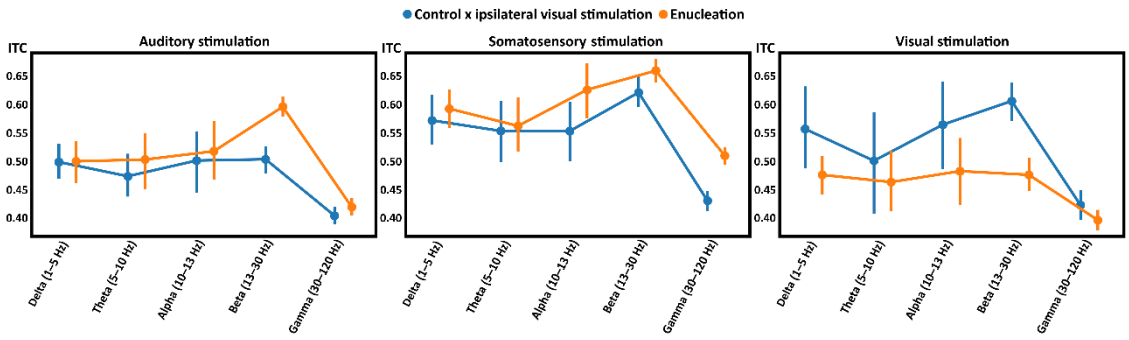

Figure 54. Maximum ITC values displayed as line plots with error bars for the auditory (left), somatosensory (center), and visual (right) modalities. Data correspond to the control (blue) and enucleated (orange) groups. Curves show mean ± SEM across frequency bands (delta, theta, alpha, beta, gamma).

Overall, enucleation is associated with increased coherence during auditory and somatosensory stimulation, whereas under ipsilateral visual stimulation a reduction in coherence is observed in enucleated animals.

The same analyses were conducted for the maximum ITC values. In this case, represent them in line charts with error bars is particularly informative, as the overall effect of enucleation generally results in increased ITC values across all frequency bands during auditory and somatosensory stimulation, whereas ipsilateral visual stimulation leads to reduced coherence values following enucleation (**Figure 54**).

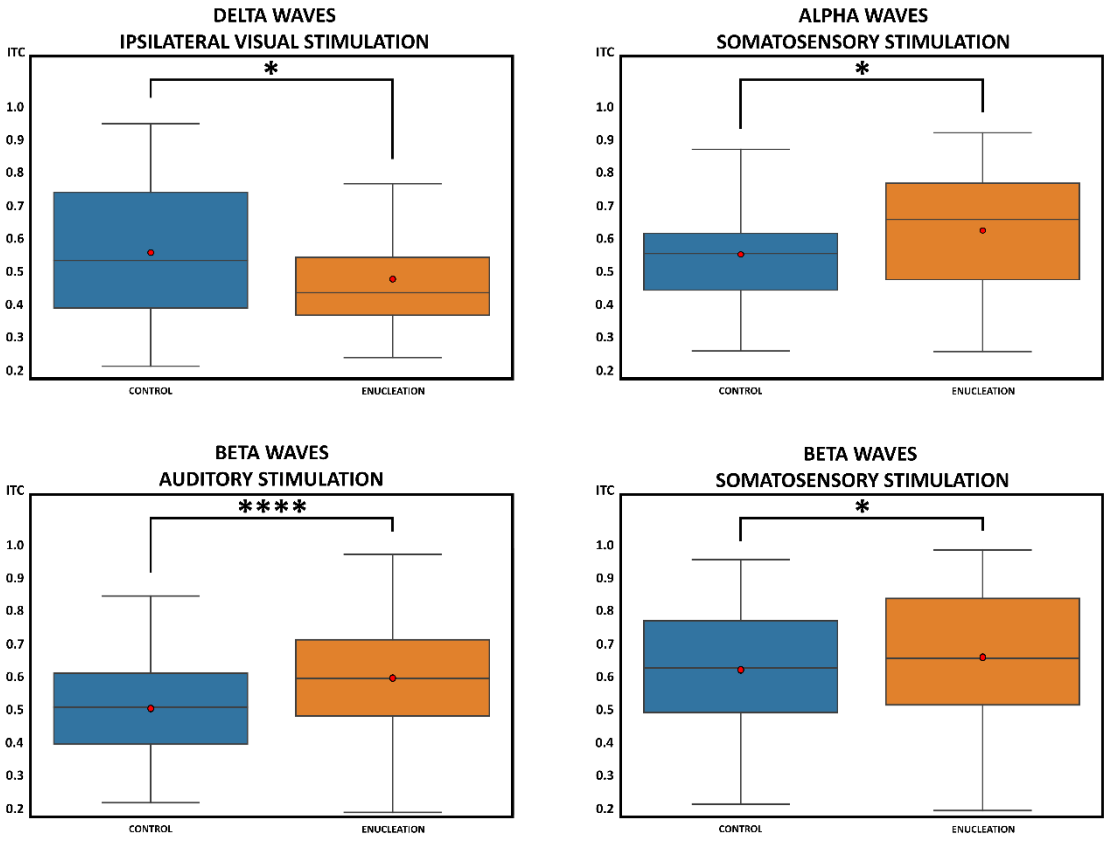

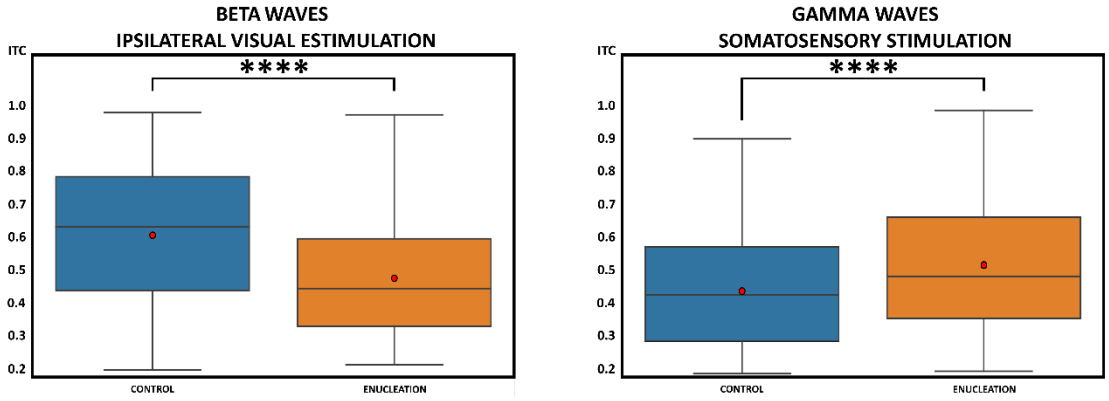

Figure 55. Boxplots of ITC values across sensory modalities and frequency bands. Top left: visual-delta (1-5 Hz). Top right: somatosensory-alpha (10-13 Hz). Middle left: auditory-beta (13-30 Hz). Middle right: somatosensory-beta (13-30 Hz). Bottom left: visual-beta (13-30 Hz). Bottom right: somatosensory-gamma (30-120 Hz). Boxes show the distribution of original values for the control (blue) and enucleated (orange) groups, with the central line indicating the median, whiskers representing the range, and the red point denoting the group mean.

In the delta band (1-5 Hz), no significant differences in phase coherence (ITC) were observed between the control and enucleated groups during auditory or somatosensory stimulation. However, a significant reduction in ITC values was evident during visual stimulation in the enucleated group compared to the control group.

Within the theta band (5-10 Hz), no significant differences in phase coherence (ITC) were observed between the control and enucleated groups across any stimulation modality (auditory, somatosensory, or visual). By contrast, in the alpha band (10-13 Hz), a significant increase in ITC values was detected during somatosensory stimulation in the enucleated group compared to the control group. No significant differences emerged for the auditory or visual modalities.

In the beta band (13-30 Hz), significant differences were found across all modalities. During visual stimulation, the control group exhibited higher ITC values than the enucleated group. In contrast, somatosensory stimulation was associated with increased ITC in the enucleated group relative to the control. For the gamma band (30-120 Hz), only somatosensory stimulation showed differences, with a significant increase in ITC following enucleation. The auditory and visual modalities did not exhibit significant changes (**Figure 55**).

4. tDCS and donepezil modulate cortical reorganization after enucleation

To evaluate the effects of tDCS, donepezil, and their combination on ERSP and ITC in the V1 response to the three types of stimulation, anodal tDCS was administered via an epicranial ring over V1 with a dorsal return, at 200 µA for ≈15 min per session over two weeks; donepezil was administered at 1 mg/kg i.p. for two weeks, 30 min before a visual training session with the same flash at ≈14 cm. In the same manner, the two treatments were combined to assess a possible synergy between them in modulating the V1 response.

4.1 Effects of tDCS, donepezil and both on ERSP

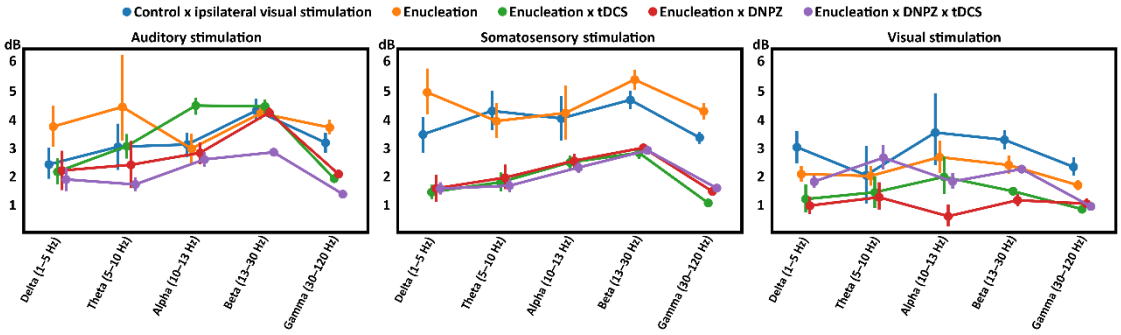

Figure 56. Maximum ERSP values by frequency band (delta 1-5 Hz, theta 5-10 Hz, alpha 10-13 Hz, beta 13-30 Hz, gamma 30-120 Hz) during auditory (left), somatosensory (center), and visual (right) stimulation. Curves show mean ± SEM for five groups: control (blue), enucleated (orange), tDCS (green), DNPZ (red), and tDCS+DNPZ (purple). Because the data are unnormalized, the figure permits direct comparison of spectral response magnitude across groups and modalities.

During auditory stimulation, slow-band (delta and theta) power tended to be higher in the enucleated group, without attaining statistical significance, than the control. The tDCS group closely matches control except for a selective increase in alpha and a decrease in gamma relative to both control and enucleated groups. Power in the DNPZ group is lower than in control and enucleated, and the combined treatment (tDCS+DNPZ) is lower still.

During somatosensory stimulation, larger power values were elicited in the control and enucleated groups than in the treated groups across the entire frequency range. Visual stimulation produced consistently higher values in the control group across nearly all bands, with a global attenuation in the enucleated group. Neither single treatment (tDCS or DNPZ) restored the visual response and, in most bands, further reduced it relative to enucleated. Visual stimulation elicited a slight theta increase in the tDCS+DNPZ condition relative to control.

Overall, the treatments weakened somatosensory responses and did not enhance high-frequency auditory activity; electrical stimulation selectively increased alpha power relative to control, and under visual stimulation the combined treatment may selectively favour theta.

When observing auditory stimulation in the beta band, the ERSP values obtained in almost all animal groups are very similar, which indicates that in this band the power remains stable. However, what is particularly noteworthy here is that when the two types of treatment are applied together, they have a suppressive effect on power, something that does not occur when the treatments are applied separately (**Figure 56**).

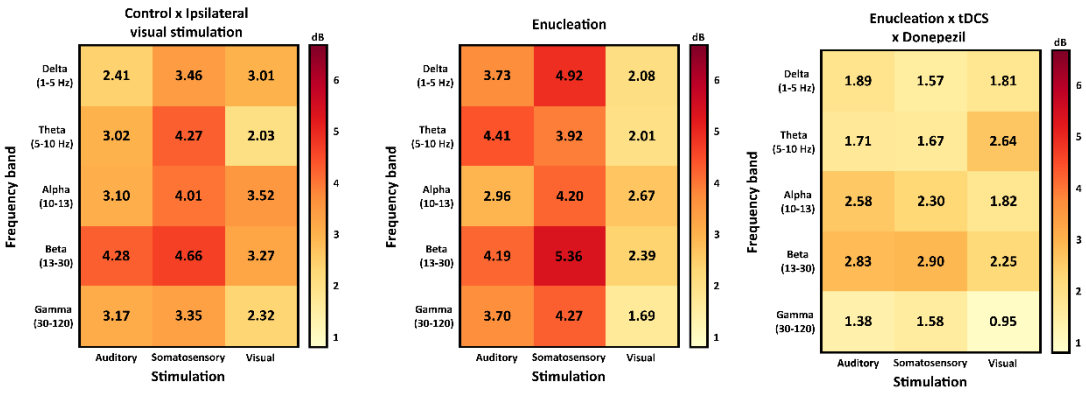

Figure 57. Heatmaps of maximum ERSP values (dB) by frequency band - delta 1-5 Hz, theta 5-10 Hz, alpha 10-13 Hz, beta 13-30 Hz, gamma 30-120 Hz - for three conditions: control with ipsilateral visual stimulation (left panel), enucleation (middle panel), and enucleation with combined tDCS + donepezil (right panel). Each cell represents the mean ERSP for a given stimulation modality (auditory, somatosensory, visual); the adjacent color bar indicates the dB scale. Because the data are unnormalized, the figure allows direct comparison of spectral response magnitudes across conditions and modalities.

Under auditory and somatosensory stimulation, the combined treatment appeared to be associated with an overall reduction of power across bands, with values generally lower than both control and enucleation, a pattern that could be consistent with a suppressive effect on non-visual activity. Under visual stimulation, the principal result was a theta increase to 2.64 dB, that nominally exceeded both control (2.03 dB) and enucleation (2.01 dB).

The combined treatment (tDCS+DNPZ) not only enhances theta-band power under visual stimulation but also exceeds control levels. This facilitation with the combined treatment is evident in the **Figure 57**, whereas administering tDCS or donepezil alone does not yield the same plastic facilitation effect.

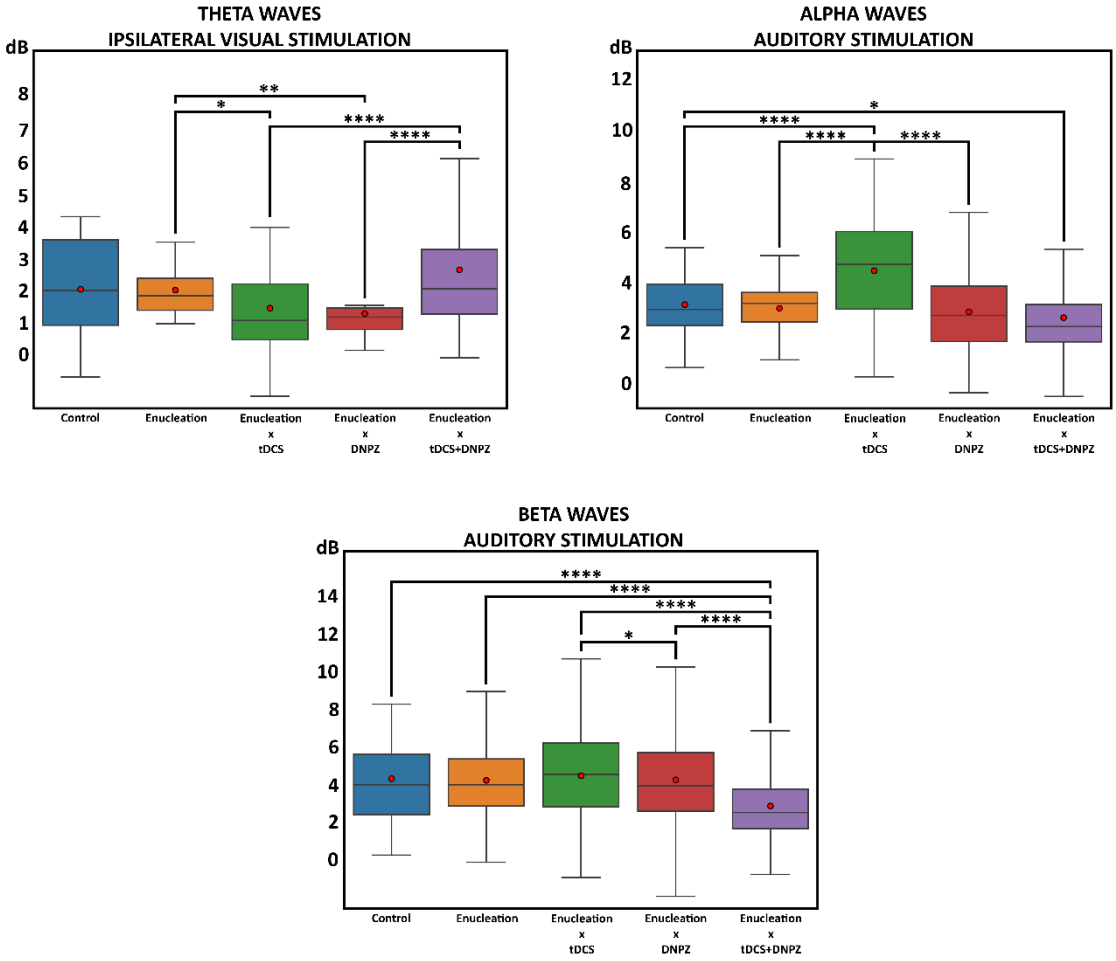

Figure 58. Distribution of ERSP power across experimental groups in selected modality × frequency band combinations. Boxplots are shown for three conditions. The upper left panel represents power values evoked by visual stimulation in the theta band (5-10 Hz); the upper right panel corresponds to auditory stimulation in the alpha band (10-13 Hz); and the lower panel displays auditory stimulation in the beta band (13-30 Hz). The groups compared are control, enucleated, tDCS (transcranial direct current stimulation), DNPZ (donepezil), and tDCS+DNPZ. In each boxplot, the central line indicates the median, the boxes represent the interquartile range (IQR), the whiskers extend up to 1.5 × IQR, and the dot denotes the mean.

These three graphs provide a more detailed view of the phenomena described above. In the group of animals treated with tDCS and DNPZ, visual stimulation produced power values comparable to those of the control group, which were significantly different from the values of the other two groups receiving the individual treatments. This may demonstrate that the treatments interact with each other, producing an effect opposite to that observed individually, thereby facilitating, to some extent, the increase of power in this frequency band.

Electrical treatment with tDCS evokes significantly higher power values in enucleated animals when auditory stimulation is used, indicating that this treatment alone facilitates intermodal plasticity toward the alpha frequency band. Another noteworthy effect of the treatments is the significant reduction of power in the beta band during auditory stimulation. The combined treatment induces inhibition of this frequency band in enucleated animals, whereas the individual treatments do not produce this reduction, since no significant differences were found between these treated groups and the control group (**Figure 58**).

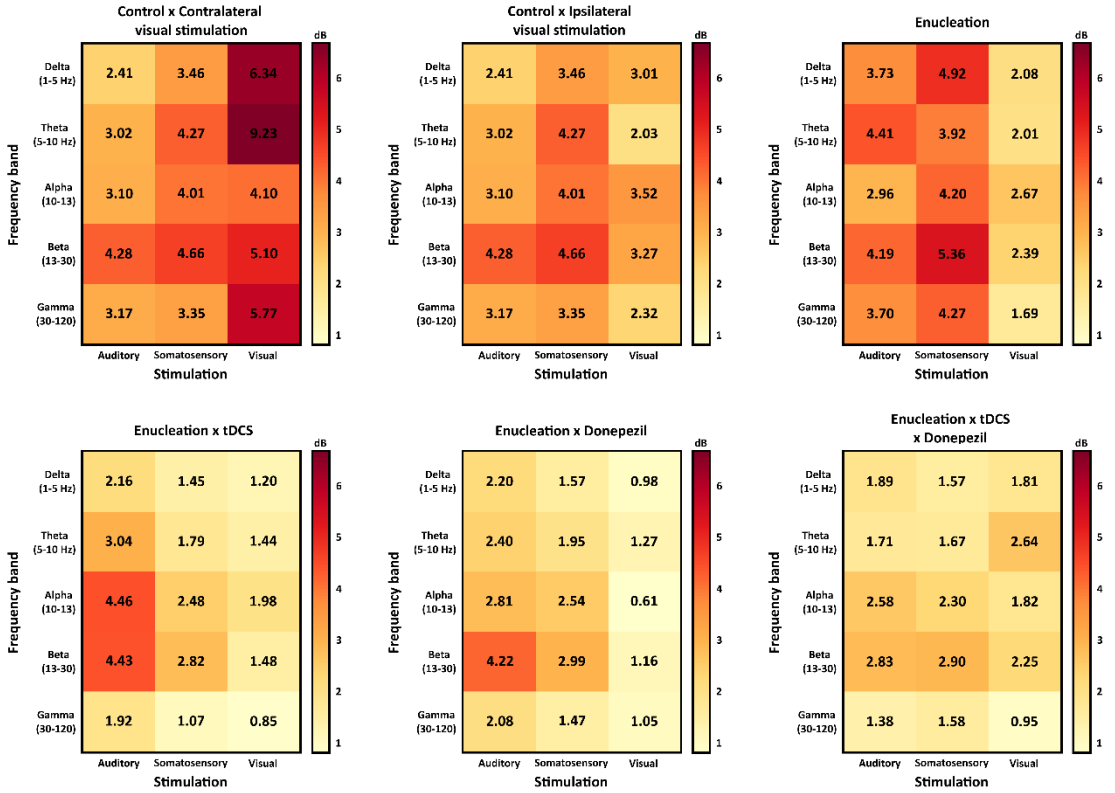

Figure 59. Heatmaps of maximum ERSP values (dB) by frequency band (Delta, Theta, Alpha, Beta, Gamma on the Y-axis) and sensory modality (auditory, somatosensory, visual on the X-axis). Top row: controls with contralateral visual stimulation (left), controls with ipsilateral visual stimulation (center), enucleated animals (right). Bottom row: enucleated animals treated with tDCS (left), with donepezil (center), and with combined tDCS + donepezil (right). Colors encode magnitude (yellow = lower; dark red = higher). Some values exceed the upper color-scale limit (6 dB) and appear saturated.

Under control conditions with contralateral visual stimulation, the visual column exhibits the highest maxima across several bands, with a marked theta peak (≈ 9.2 dB) and increases in delta and gamma; beta is elevated but less modality-selective. Auditory and somatosensory columns show intermediate responses, with similar alpha and beta values.

With ipsilateral visual stimulation, the power decrease consistently across bands, while auditory and somatosensory values remain as in the contralateral condition (they are the same as in the contralateral visual-stimulation panel).

Following enucleation, response to visual stimulation is attenuated across the spectrum ($\leq \approx 2.7$ dB), whereas power elicited by auditory and somatosensory stimulation increases, especially at the descriptive level in beta (somatosensory 5.36 dB) and, to a lesser extent, in delta, beta, and gamma, consistent with cross-modal potentiation of non-visual modalities.

In enucleated animals, tDCS induces a general suppression of somatosensory-elicited power across all bands but preserves the auditory-stimulation potentiation profile, with increases mainly in alpha (≈ 4.5 dB) and beta (≈ 4.4 dB) relative to enucleated mice without tDCS treatment. With combined tDCS + donepezil, attenuation is relatively uniform across modalities and bands, without prominent peaks, yielding moderate power values, nevertheless, the theta-band pattern is consistent with a facilitation of intramodal visual plasticity, with mean values nominally higher than both untreated enucleation and the control group, without reaching statistical significance. At a finer scale, the power pattern resembles that of the control group under contralateral stimulation but at generally lower absolute levels; a normalization-based analysis might make this similarity more evident.

Overall, the data support: (i) visual dominance with contralateral stimulation in controls, (ii) a selective reduction in power evoked by visual ipsilateral stimulation, (iii) auditory-somatosensory potentiation after enucleation, and (iv) treatment-dependent modulation, tDCS favouring the auditory modality in alpha, donepezil producing a more global reduction, when combined, the treatments were associated with a descriptive shift consistent with the facilitation of intramodal plasticity toward residual visual inputs (**Figure 59**).

4.2 Effects of tDCS, donepezil and both on ITC

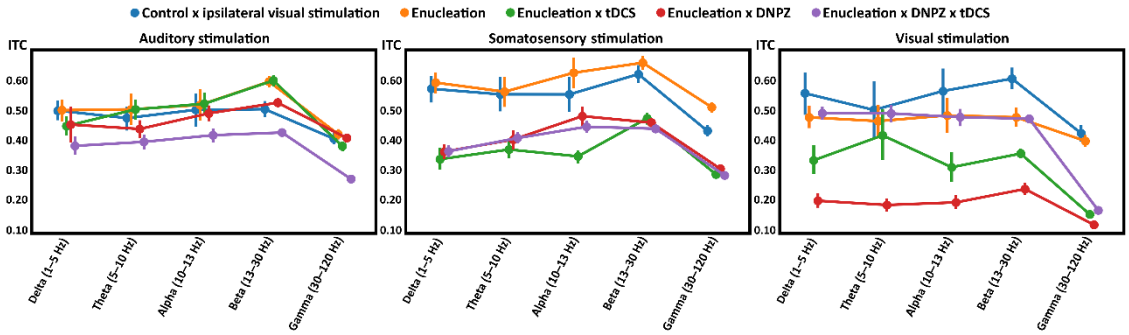

Figure 60. Line plots with error bars (mean ± SEM) of ITC values across frequency bands (delta 1-5 Hz, theta 5-10 Hz, alpha 10-13 Hz, beta 13-30 Hz, gamma 30-120 Hz) for three sensory modalities: auditory (left), somatosensory (middle), and visual (right). Experimental groups: control (blue), enucleated (orange), tDCS (green), DNPZ (red), and tDCS + DNPZ (purple).

During auditory stimulation, the group subjected to transcranial stimulation (tDCS) exhibits relatively high ITC values, exceeding those of the control group in the theta, alpha, and beta bands. This suggests that electrical stimulation may help maintain the temporal alignment of neuronal activity in response to auditory inputs within these mid-range frequencies. However, in the gamma band, all treated groups, and particularly the group receiving combined treatment (tDCS + DNPZ), show a decline in coherence, indicating reduced synchronization at higher frequencies, possibly as a consequence of the therapeutic intervention. The group treated solely with donepezil (DNPZ) displays a more pronounced response in the beta band, which may be linked to its action on cholinergic systems and its potential modulatory effect on neuronal synchrony at this frequency.

In the somatosensory modality, both the control and enucleated groups exhibit relatively high and consistent coherence across the theta, alpha, and beta bands, whereas the treated groups show lower values. This pattern suggests that electrical stimulation and pharmacological treatment, either alone or in combination, exert an attenuating effect on temporal coherence under conditions of non-visual stimulation. Such a reduction may reflect suppression of intermodal plasticity, possibly due to interference with adaptive mechanisms that would normally be activated in the absence of vision.

The most pronounced changes, however, are identified in the visual modality. The group receiving the combined tDCS and DNPZ treatment demonstrates a relative increase in ITC within the delta, theta, and alpha bands, reaching values comparable to those of the control group. This indicates that the combined intervention promotes reorganization of temporal coherence within the visual modality, particularly at lower frequencies associated with attentional processes and visual information processing. In contrast, the group treated exclusively with donepezil shows

markedly reduced ITC across all bands, reinforcing the notion that pharmacological treatment alone is insufficient to restore neuronal synchrony in the primary visual cortex. The tDCS-only group also exhibits low coherence values, suggesting that electrical stimulation by itself is not enough to effectively reestablish synchrony patterns (**Figure 60**).

Overall, these findings suggest that the combination of treatments enhances intramodal neuronal coherence in the visual cortex, especially within the theta and alpha bands, which are linked to sensory integration and cortical plasticity. This effect may be associated with the prior administration of theta-rhythm visual stimulation and tDCS together of the remaining eye, pointing toward a possible induction of rhythmic entrainment in cortical activity. By contrast, the application of either treatment in isolation or combination appears to exert a suppressive effect on coherence in non-visual modalities, with the exception of the tDCS group under auditory stimulation.

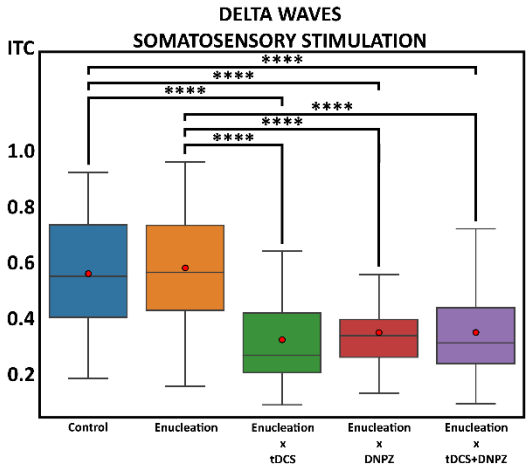

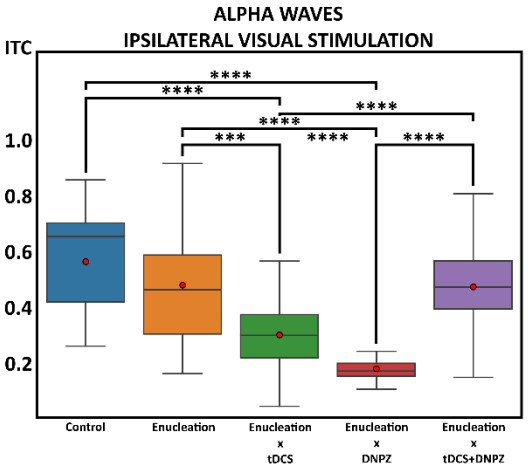

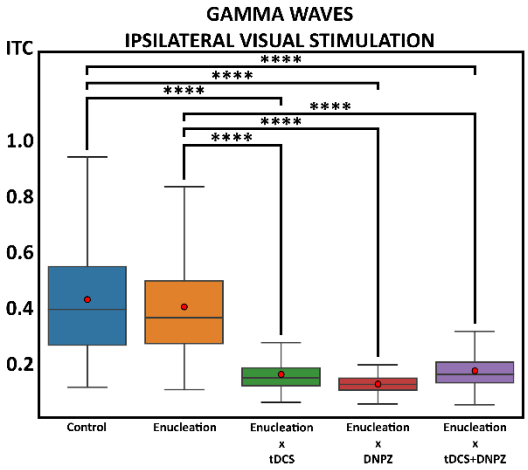

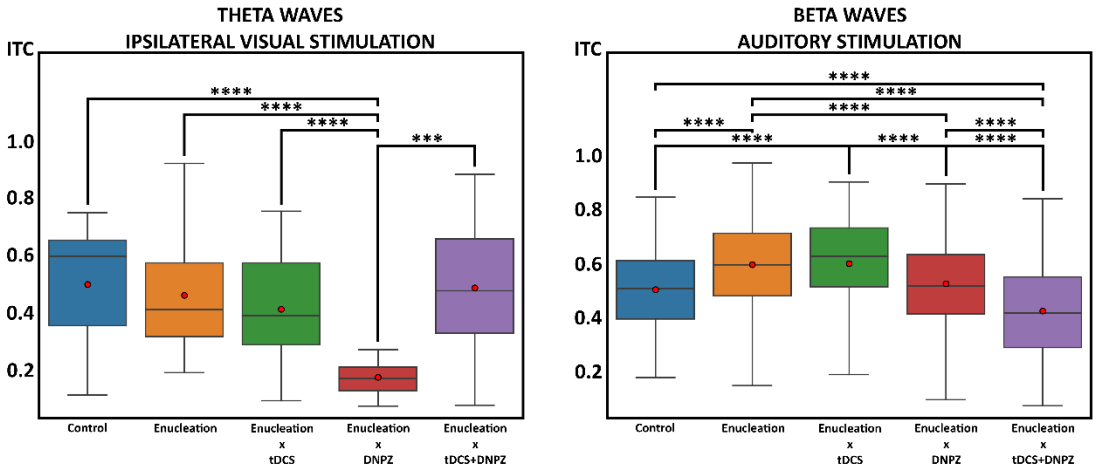

Figure 61. Boxplots of ITC values across sensory modalities and frequency bands. Top panel: somatosensory-delta (1-5 Hz). Middle left: visual-alpha (10-13 Hz). Middle right: visual-gamma (30-120 Hz). Bottom left: visual-theta (5-10 Hz). Bottom right: auditory-beta (13-30 Hz). Boxes represent the distribution of the original values for each experimental group: control (blue), enucleated (orange), tDCS (green), DNPZ (red), and tDCS + DNPZ (purple). Central lines indicate the median; whiskers reflect the range; red points denote the group mean.

These five boxplots provide a more detailed view of the effects of treatment on trial-to-trial temporal coherence across different sensory modalities. In the somatosensory modality, ITC values in the delta band show a significant reduction compared with the control and enucleated groups in all treated groups relative to the untreated animals. Strikingly, the combined treatment (tDCS + DNPZ) fails in reversing this reduction, remaining significantly lower than the values observed in the non-treated animals. This supports the hypothesis that the interventions, whether applied individually or in combination, exert an inhibitory effect on intermodal plasticity toward somatosensory inputs.

Under visual stimulation, ITC values in the alpha band are notably higher in the group treated with tDCS + DNPZ, reaching levels close to those of the control group and differing from the groups treated individually. Statistically, the combined treatment group displayed significant differences compared to both the DNPZ-only and the tDCS-only groups, indicating a synergistic effect of the combined treatment in restoring temporal coherence at this frequency. This result supports the idea that both treatments interact to counteract the suppressive effects observed when they are applied independently. By contrast, the DNPZ-only group exhibited the lowest coherence values, with statistically significant differences compared to the tDCS group, suggesting that the pharmacological intervention alone may even hinder phase alignment in this band. In gamma band, coherence is consistently reduced in all treated groups compared with the control and enucleated groups. Importantly, the combined treatment does not achieve a significant

improvement in coherence, suggesting that none of the interventions, either individually or together, can restore synchrony in high-frequency activity associated with visual processing. This may indicate that gamma synchronization is particularly vulnerable to treatment approaches maybe visual theta stimulation inhibits gamma response.

In the theta band under visual stimulation, a distinctive pattern emerges among the groups. ITC under combined tDCS+DNPZ was similar in magnitude to control and enucleation, with no consistent elevation, which may suggest an effective potentiation of phase synchronization at low frequencies. Statistically, the combined treatment group shows significant differences compared to the DNPZ group. Nevertheless, the suppressive effect on phase coherence induced by the drug does not overshadow the contribution of electrical stimulation in maintaining coherence levels comparable to those of the other groups. The DNPZ-only group displays the lowest ITC values, with significant differences compared to all other groups. This finding reinforces the idea that pharmacological intervention is not only ineffective but may actively contribute to a reduction in temporal coherence within this band. As noted earlier, electrical stimulation was administered, and the animals were also exposed to visual stimulation at theta rhythm, which may account for an induced entrainment of activity within this frequency band that persists over time (at least up to two weeks after treatment).

Using auditory stimulation, coherence in the beta band shows a unique profile: the tDCS group presents the highest values, significantly exceeding the control group, the DNPZ group, and the combined treatment group. This finding suggests that tDCS alone facilitates intermodal plasticity for auditory information within this frequency band. Interestingly, neither pharmacological treatment nor the combined intervention reproduces this effect, suggesting that cholinergic modulation may counteract or mask the facilitatory impact of electrical stimulation in this context (**Figure 61**).

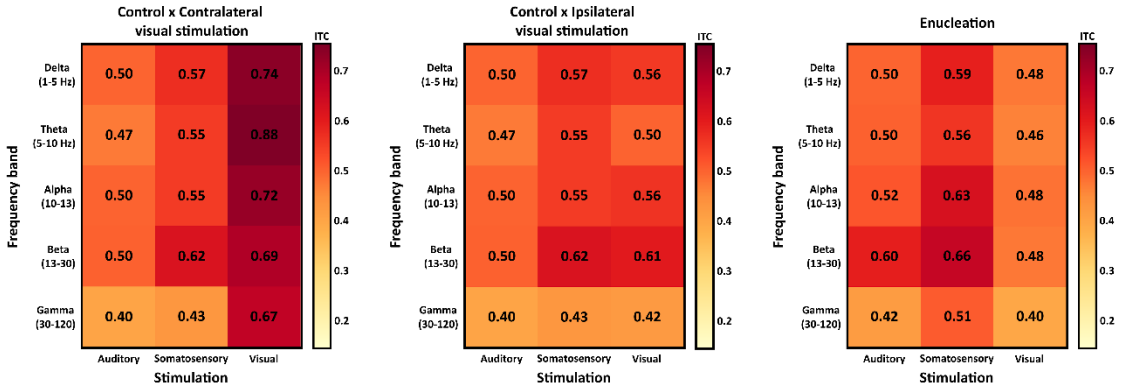

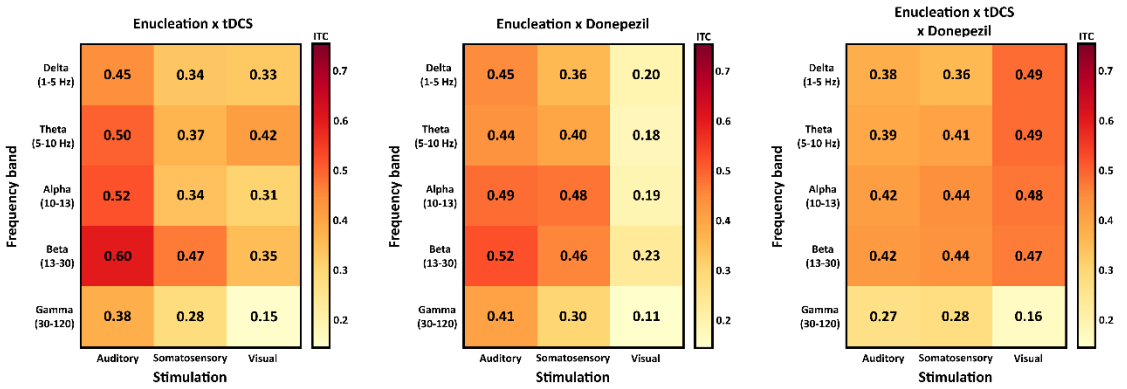

Figure 62. Heatmaps of maximum coherence values (ITC) by frequency band (Delta, Theta, Alpha, Beta, Gamma; Y-axis) and sensory modality (auditory, somatosensory, visual; X-axis) under six conditions: controls with contralateral visual stimulation (top-left), controls with ipsilateral visual stimulation (top-center), enucleated animals (top-right), enucleated + tDCS (bottom-left), enucleated + donepezil (bottom-center), and enucleated + tDCS + donepezil (bottom-right). The numbers in each cell indicate the maximum ITC, and the colour scale represents its magnitude (warm tones = higher coherence). Note: some values approach or exceed the upper limit indicated on the colour bar (≈ 0.70), so they appear chromatically saturated.

With contralateral visual stimulation in controls, a predominance in phase coherence evoked by visual input is observed across all bands, with a peak in theta (0.88) and very high values in delta (0.74), alpha (0.72), beta (0.69), and gamma (0.67). Auditory and somatosensory stimulation elicit lower, relatively flat responses (≈ 0.40-0.62), confirming a robust bias toward contralateral visual input.

In controls with ipsilateral visual stimulation, the high coherence values evoked by visual input was attenuated and the pattern becomes more balanced. In this case, coherence values elicited by somatosensory stimulation lead several bands, while the visual modality yields very similar values in beta, alpha, and delta. Gamma remains low and homogeneous across all stimulation modalities (≈ 0.40-0.43).

After enucleation, the balance consistently shifts toward non-visual inputs. The somatosensory modality reaches the highest ITC across all bands (alpha = 0.63; beta = 0.66; delta = 0.59; theta = 0.56; gamma = 0.51), and the auditory modality also increases (e.g., beta = 0.60). The coherence evoked by visual modality remains lower (≈ 0.40-0.48). This pattern suggests cross-modal potentiation of coherence for non-visual stimuli.

Treatments reconfigure this scenario in differential ways. With tDCS, there is a general coherence suppression of somatosensory- and visual-evoked responses (e.g., somatosensory-γ = 0.28; visual-γ = 0.15), while the coherence values evoked by auditory stimulation preserves relatively

high values, especially in beta (0.60) and alpha (0.52). Coherence in Gamma decreases markedly across all three stimulus modalities.

With donepezil, the reduction is more global, and visually evoked coherence values drop to minima across the spectrum ($\delta = 0.20$; $\theta = 0.18$; $\alpha = 0.19$; $\beta = 0.23$; $\gamma = 0.11$). The combination of tDCS + donepezil generates a characteristic pattern: gamma coherence remains low across modalities (≤ 0.28; visual = 0.16), but visual stimulation again places coherence above that elicited by non-visual stimuli from delta through beta ($\delta = 0.49$; $\theta = 0.49$; $\alpha = 0.48$; $\beta = 0.47$). Coherence elicited by auditory and somatosensory stimulation was lower and similar to each other. Taken together, this constitutes a partial "restoration" of the contralateral vision-dominated profile, although at absolute levels lower than in that condition.

(i) contralateral vision maximizes stimulus-locked phase coupling across all bands, especially theta; (ii) ipsilateral stimulation reduces that dominance and redistributes coherence toward the somatosensory stimulation modality; (iii) enucleation shifts dominance to non-visual stimuli; (iv) tDCS selectively favours the auditory modality (α/β) and depresses γ; (v) donepezil acts as a global suppressor with a pronounced impact on the visual modality; and (vi) the tDCS + donepezil combination rebalances the system toward a visually dominant profile but with lower overall amplitude (**Figure 62**).

4.3 Alternative OLS modelling of frequency data

QUICK METHODS RECAP

For the alternative OLS-based analysis to unmask possible patterns in the modulation of the V1 response to the three sensory stimuli, in addition to the raw results in dB for ERSP and % for ITC, an additive residualisation was applied: from each observation the mean effects of group (control animals, enucleation without treatment, enucleation with tDCS, enucleation with DNPZ, and enucleation with tDCS + DNPZ) and stimulation modality were subtracted before the contrasts by frequency band. This approach was used to isolate band-selective effects as opposed to global shifts and was interpreted jointly with the raw results within the 1-120 Hz range.

Having described the raw ERSP (dB) and ITC (%) values, it becomes apparent that a common band × modality pattern may be present across groups, accompanied by a global shift (overall attenuation) in some of them. To disambiguate whether the differences reflect this uniform offset or genuinely band-selective effects, the additive OLS residual normalisation described in Methods

(Section 2.3) was applied. Normalised results by band and modality (contrasts on r_i) are presented below, shown in parallel with the raw values to document the actual magnitude of the measurements.

4.3.1 Alternative OLS modelling of maximum ERSP

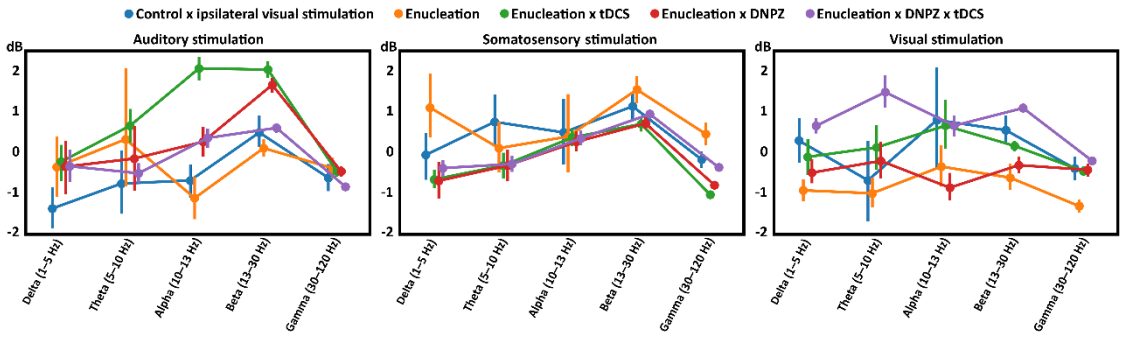

Figure 63. Line plots with error bars showing normalized ERSP values across frequency bands for three sensory modalities. Left panel: auditory stimulation. Middle panel: somatosensory stimulation. Right panel: visual stimulation. The five experimental groups are included: control (blue), enucleated (orange), tDCS (green), DNPZ (red), and tDCS + DNPZ (purple). The curves depict the progression of the normalized value across the frequency bands (delta, theta, alpha, beta, gamma).

Representing maximum ERSP values using OLS normalization under auditory stimulation facilitates visualization of the following pattern: the tDCS group (green) attains the highest values in the mid-frequency bands, with marked peaks in alpha and beta. In these two bands, this group exceeds the control group (blue) and the other groups, and it also exhibits an ascending trajectory from theta through beta before declining in gamma. The group treated with DNPZ (red) likewise shows higher ERSP values than the controls, with its maximum in the beta band. The enucleated group (orange) displays a different profile: in delta and theta its values resemble those of the treated animals; however, there is a drop in alpha, and in beta it remains below the control group. The combined tDCS+DNPZ group (purple) falls within an intermediate range: it does not reach the tDCS peaks in alpha and beta, but it surpasses the enucleation group and, at some points, approaches the control. A notable feature is that in gamma all groups converge toward negative values or values close to zero, with none sustaining the high levels observed in beta.

Under somatosensory stimulation, the overall pattern changes visibly. In delta, the enucleated group (orange) presents the highest power values and again leads in beta, with a maximum in that band that exceeds the control (blue) and the treated groups. Overall, the control group exhibits

higher power than the treated animals. All treated groups show lower maximum ERSP values than the control and enucleation groups, as already evident in the raw data; however, there is a convergence of the treated groups toward the control and enucleation values, indicating that the raw measurements were substantially affected by gain.

The effect of this model under visual stimulation shows even sharper contrasts, especially in theta. The combined tDCS+DNPZ treatment (purple) exhibits a distinct peak in theta that exceeds all other groups. This group also maintains relatively high values in beta, again above the control and the others animal groups. The fact that the untreated visually deprived group shows the lowest power values, except in the alpha band, where it exceeds the donepezil-treated group, suggests that the treatments reinforce intramodal plasticity and may even potentiate it, as seen with the dual intervention, since animals receiving both treatments exhibit higher power than the other groups, including the controls. In the tDCS group (green), visually evoked power remains very similar to that of the controls; in contrast, the pharmacological treatment appears to depress this intramodal plasticity, as evoked values remain below those of the controls and, as noted above, can even fall below the untreated enucleation group. This makes the facilitatory effect of the dual treatment on intramodal plasticity particularly noteworthy, given that the pharmacological intervention alone exerts the opposite effect and the outcome cannot be explained by a mere compensatory action of tDCS, since the dual-treatment values exceed those obtained with tDCS alone. Moreover, while tDCS by itself facilitates cross-modal plasticity for auditory input, this facilitatory effect disappears when it is combined with the drug (**Figure 63**).

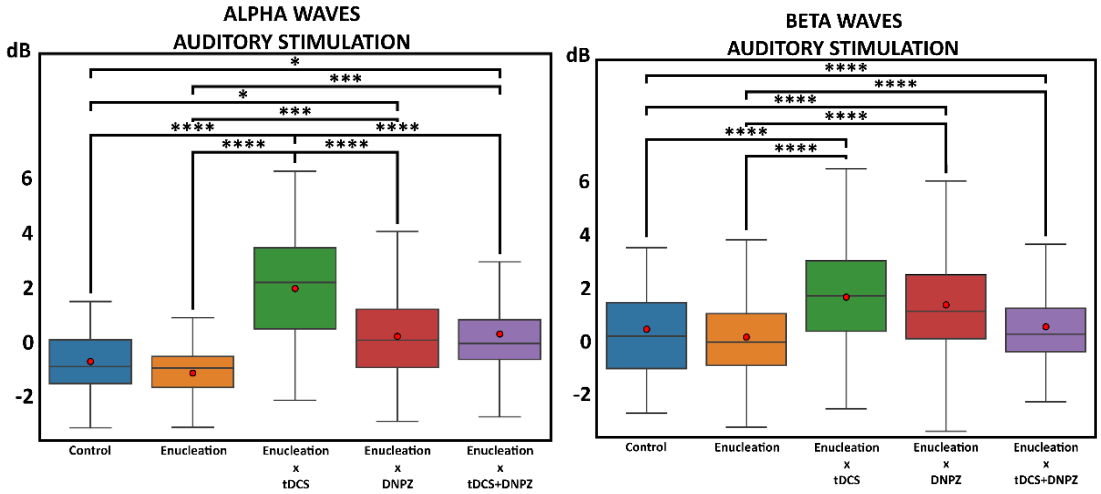

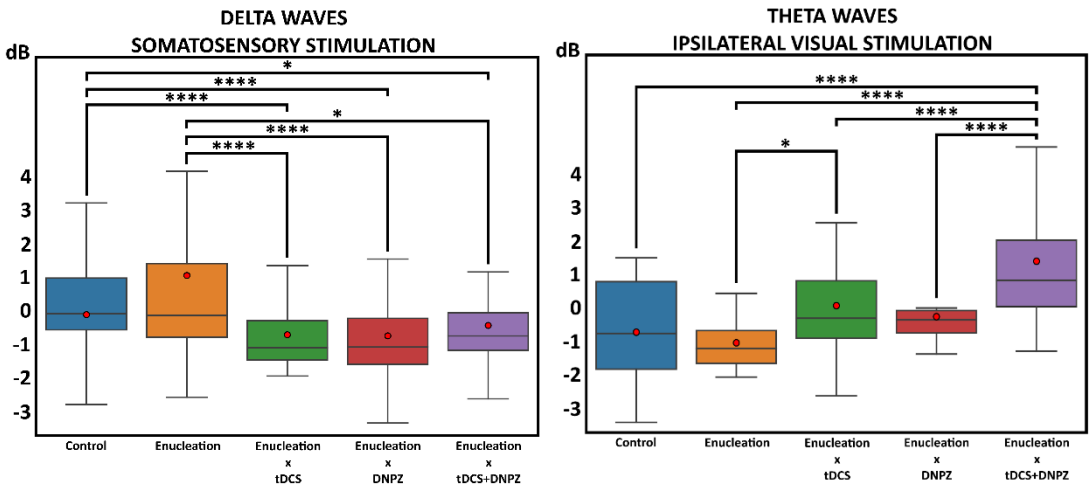

Figure 64. Boxplots of normalized ERSP values across sensory modalities and frequency bands. Top left: auditory stimulation, alpha band (10-13 Hz). Top right: auditory stimulation, beta band (13-30 Hz). Bottom left: somatosensory stimulation, delta band (1-5 Hz). Bottom right: visual stimulation, theta band (5-10 Hz). The five experimental groups are shown: control (blue), enucleated (orange), tDCS (green), DNPZ (red), and tDCS + DNPZ (purple). Boxes indicate each group's distribution of normalized values; red points denote the mean.

Delving further into the analysis, auditory stimulation in the alpha band evokes distinct patterns of maximum values across animal groups. The tDCS-treated group attains the highest values among all groups; its distribution lies consistently above the others. The DNPZ and tDCS+DNPZ groups occupy an intermediate range: both fall below tDCS yet remain above the non-pharmacological groups (control and enucleation).

The same pattern holds in the beta band. Evoked values in the electrically treated animals remain much higher than those in the control and enucleated groups. The double-treatment and the pharmacological-only groups remain in an intermediate zone and still exceed the untreated animals significantly.

By contrast, somatosensory inputs evoke greater power in the control and enucleation groups, whereas the treatments, whether administered individually or in combination, do not facilitate convergence of power values toward those of the untreated animals. As already indicated by the raw data, each proposed intervention adversely affects cross-modal plasticity for somatosensory inputs.

Under visual stimulation, for example in the theta band, the group receiving the combined treatment exhibits the highest evoked power, exceeding all other groups, including the control. Electrical treatment alone also yields a significant improvement relative to the untreated enucleated group. In contrast, the DNPZ-treated group does not show power values significantly

higher than those of either the control or the enucleation group. However, when the drug is administered together with the electrical treatment, a potentiating interaction is observed, producing an outcome different from that obtained when the two interventions are applied separately (**Figure 64**).

4.3.2 Alternative OLS modeling of maximum ITC

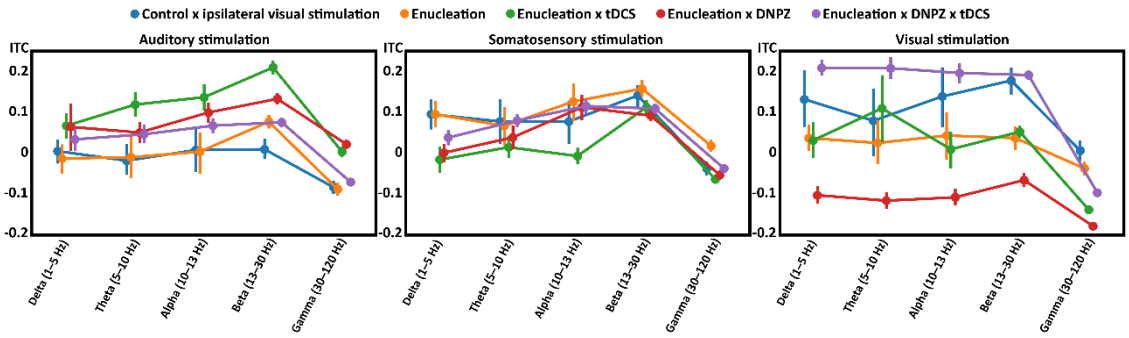

Figure 65. Line plots with error bars showing normalized ITC values across frequency bands for three sensory modalities. Left panel: auditory stimulation. Middle panel: somatosensory stimulation. Right panel: visual stimulation. Experimental groups are shown control (blue), enucleated (orange), tDCS (green), DNPZ (red), and tDCS + DNPZ (purple).

The tDCS-treated group (green) systematically exhibits the highest coherence in the mid-frequency ranges, with peaks in alpha and beta. In these bands, this group exceeds the control (blue) and the remaining groups, showing an ascending progression from theta through beta, followed by a decline in gamma. The DNPZ-treated group (red) likewise shows elevated coherence relative to the control, with a maximum in the beta band. In contrast, the enucleated group (orange) displays a flatter profile: its values in delta and theta are comparable to those of the treated groups, but coherence drops in alpha and remains below the control in beta. The combined-treatment group (tDCS + DNPZ, purple) occupies an intermediate position: it does not reach the phase alignment observed with tDCS alone, yet it surpasses the enucleated animals and approaches the control values in certain bands. A salient feature common to all groups is the convergence toward low or near-zero coherence in gamma, suggesting a general loss or reduction of phase consistency at higher frequencies under auditory stimulation.

The use of somatosensory stimulation shifts the overall pattern; the enucleated group (orange) shows the highest levels of inter-trial coherence, with a peak in beta and elevated values from delta through beta. The control animals (blue) likewise exhibit high phase consistency,

particularly in beta. By contrast, the tDCS (green), DNPZ (red), and combined (purple) groups display lower coherence values across almost the entire spectrum, remaining below both the enucleated and control groups. Nevertheless, an exception arises with the pharmacological intervention: the dual-treatment group reaches coherence values in theta and alpha that approximate those of the control and enucleation groups, and the DNPZ-only group also attains alpha-band coherence comparable to the untreated animals. Thus, in this case, the intervention that appears to interfere with the coherence of the response to somatosensory stimulation is the electrical treatment rather than the pharmacological one.

Under visual stimulation, the combined-treatment group (purple) exhibits a peak in theta, surpassing all other groups, and maintains elevated coherence values in delta, theta, alpha, and beta. This group's strong phase alignment across bands, particularly in beta, exceeds even that of the control group (blue), indicating a marked enhancement of stimulus-locked synchronization. The tDCS group (green) displays a profile that closely follows the control in the lower bands, but its values decline more sharply at higher frequencies. By contrast, the DNPZ-treated group (red) shows the lowest coherence across nearly all bands, especially in theta and gamma, suggesting a suppression of phase consistency induced by the pharmacological intervention. The enucleated group (orange) again shows an intermediate profile, above the DNPZ group but below the control. Notably, the combined-treatment group achieves higher coherence values than those obtained with tDCS alone, indicating a synergistic effect in promoting intramodal synchronization. This is particularly noteworthy given that DNPZ by itself appears to diminish phase alignment; thus, its combination with tDCS yields a facilitatory outcome that cannot be explained solely as compensation (**Figure 65**).

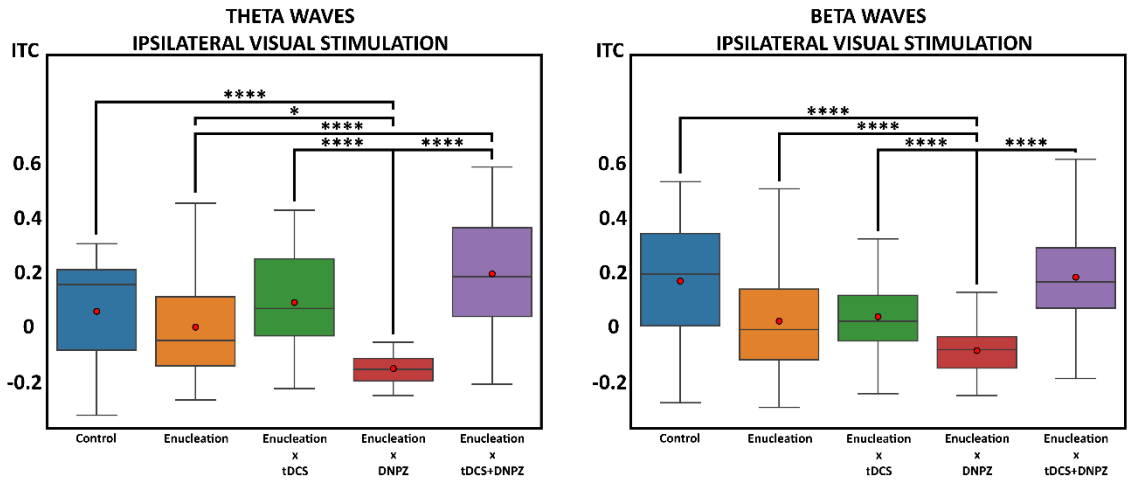

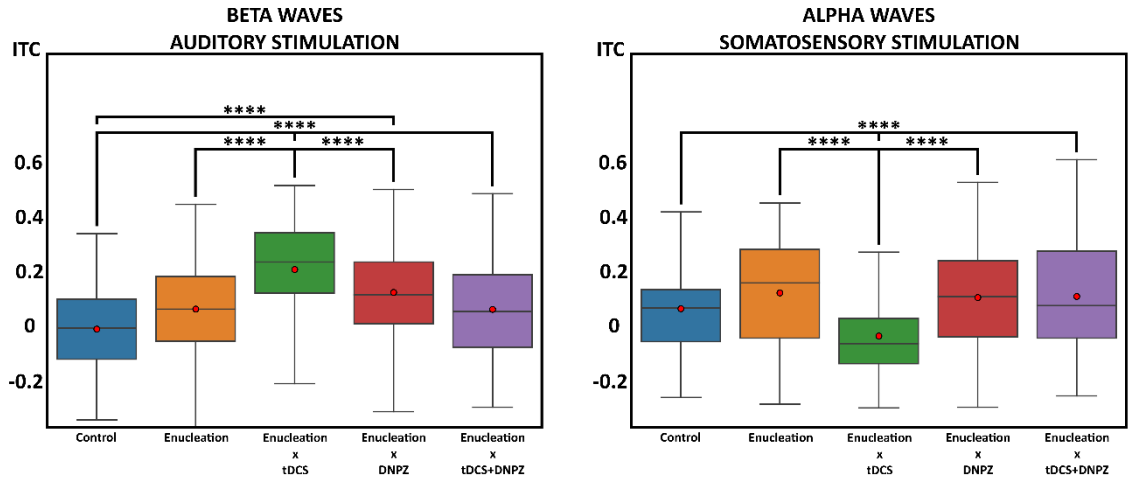

Figure 66. Boxplots of normalized ITC (residual) values across modalities and frequency bands. Top left: visual stimulation, theta band (5-10 Hz). Top right: visual stimulation, beta band (13-30 Hz). Bottom left: auditory stimulation, beta band (13-30 Hz). Bottom right: somatosensory stimulation, alpha band (10-13 Hz). Each panel shows the distribution for the experimental groups: control (blue), enucleated (orange), tDCS (green), DNPZ (red), and tDCS + DNPZ (purple). Red points indicate the group mean. Differential effects are observed as a function of modality and frequency.

Under visual stimulation, in the theta band, the group receiving the combined tDCS + DNPZ treatment exhibits the highest coherence values; however, differences between this group, the tDCS-only group, and the control group are not significant. By contrast, the differences relative to the DNPZ-treated group and the enucleated group are significant. In the DNPZ-only group, intramodal plasticity appears inhibited, as this group shows by far the lowest coherence values. In the beta band, the same pattern persists during visual stimulation: the tDCS + DNPZ group again reaches the highest coherence values. Although the difference from the control group is less pronounced than in theta and remains nonsignificant, the elevated values reinforce the notion of a sustained facilitatory effect of the dual treatment. The tDCS-only group, by contrast, shows more moderate values, not differing significantly from the enucleated group, suggesting that this intervention may be more effective at lower frequencies, whereas its combination with DNPZ extends the benefits to mid-frequency bands such as beta. The DNPZ group replicates the theta-band pattern, presenting the lowest coherence values, which supports the idea of a generalized inhibitory effect on visual synchronization. Taken together, these results confirm that the dual treatment not only increases power but also improves phase alignment at low frequencies.

By contrast, under auditory stimulation in the beta band, a different profile emerges. Here, the tDCS-only group shows the greatest coherence, surpassing the control and all other groups. The median is high and the dispersion low, indicating a consistent effect. The DNPZ-treated group also exhibits elevated coherence; although the increase appears less striking than that of tDCS on

inspection, it is nevertheless significant. The enucleated and tDCS + DNPZ groups fall in an intermediate range, with moderate values. Notably, the control group presents the lowest coherence in this condition, reinforcing the specific facilitatory effect of tDCS on auditory temporal synchronization in the beta band. These data suggest that tDCS alone is sufficient to promote cross-modal plasticity toward temporally precise auditory inputs. The absence of an additional improvement with the dual treatment suggests that the combination does not confer extra benefits in facilitating plasticity in this case.

Finally, under somatosensory stimulation in the alpha band, the enucleated group shows the highest coherence values, exceeding even the control, albeit not significantly. The groups treated with DNPZ or with the combined tDCS + DNPZ show values similar to the control, without notable differences, which may reflect a relative resistance of the somatosensory system to external intervention or a possible ceiling effect in coherence that precludes further improvement. In contrast, the tDCS-only group shows the lowest coherence in this band, at odds with its facilitatory effects in the auditory and visual modalities. This apparent modality-specific interference suggests that tDCS may disrupt intrinsic somatosensory rhythms, particularly those in the alpha band. The fact that neither donepezil nor the combined treatment reverses this decrease reinforces the notion of a particular vulnerability of the somatosensory system to electrical modulation (**Figure 66**).

Overall, these results show that the effects of tDCS, donepezil, and their combination on inter-trial coherence are strongly modulated by sensory modality and frequency band. The most robust facilitatory effect is observed in visual theta coherence with the dual treatment, supporting the hypothesis of enhanced intramodal plasticity via synergistic neuromodulation. In the auditory domain, tDCS alone is effective, especially in beta, whereas in the somatosensory system, enucleation leads to a unique compensatory potentiation in alpha that is not replicated by any intervention. The findings obtained with the OLS model clarify significant differences that would not be visible in the raw data, likely due to gain bias arising from various factors.

4.4 The total population size of the conducted records.

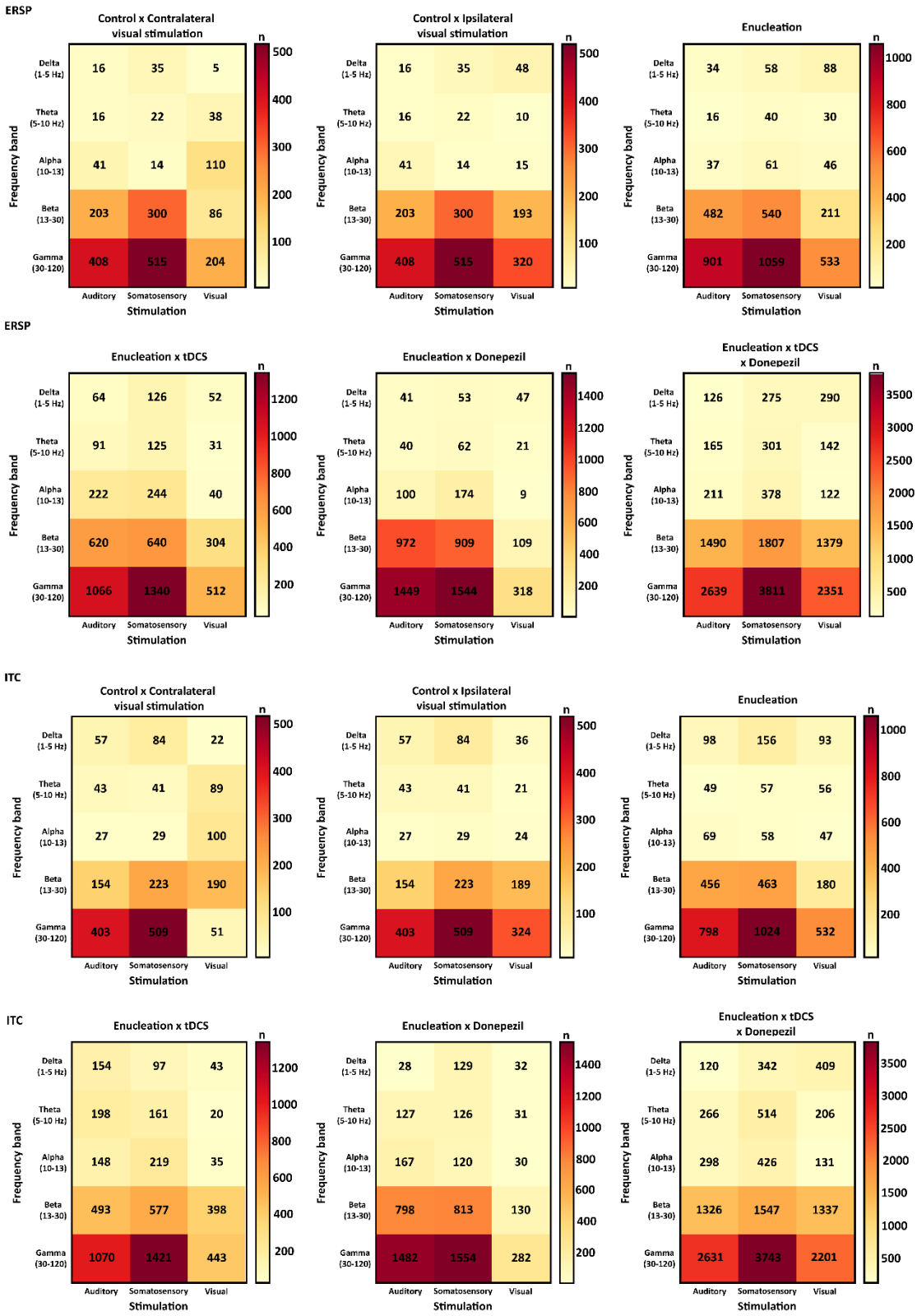

Figure 67. Heatmaps illustrating the count of peak occurrences (N) for ERSP (event-related spectral perturbation) across six animal groups: contralateral visual stimulation in control, ipsilateral visual stimulation in control, enucleation, enucleation x tDCS, enucleation x DNPZ, and enucleation x both treatments (tDCS + DNPZ). Each heatmap shows the number of ERSP peaks by frequency band (Y-axis:

delta, theta, alpha, beta, gamma) and sensory stimulation type (X-axis: auditory, somatosensory, visual), with color intensity and overlaid values reflecting the frequency of peak responses. Corresponding heatmaps illustrating the count of peak occurrences (N) for ITC (inter-trial coherence) for the same groups in the same order.

The heterogeneity in sample size was assessed using five heatmaps, each corresponding to one of the five animal groups analyzed. These heatmaps illustrate the count of records by frequency band and type of sensory stimulation. The results reveal an uneven distribution of observations across experimental conditions. Notably, the beta and gamma frequency bands exhibit a higher volume of data, with a marked predominance in somatosensory stimulation, where in some instances up to nearly ten times more records are observed compared to other conditions. This trend is consistently observed in both ERSP and ITC measurements, suggesting a potential influence of sensory modality and frequency band on the density of the collected data. This variability should be considered when interpreting the statistical analyses presented earlier (**Figure 67**).

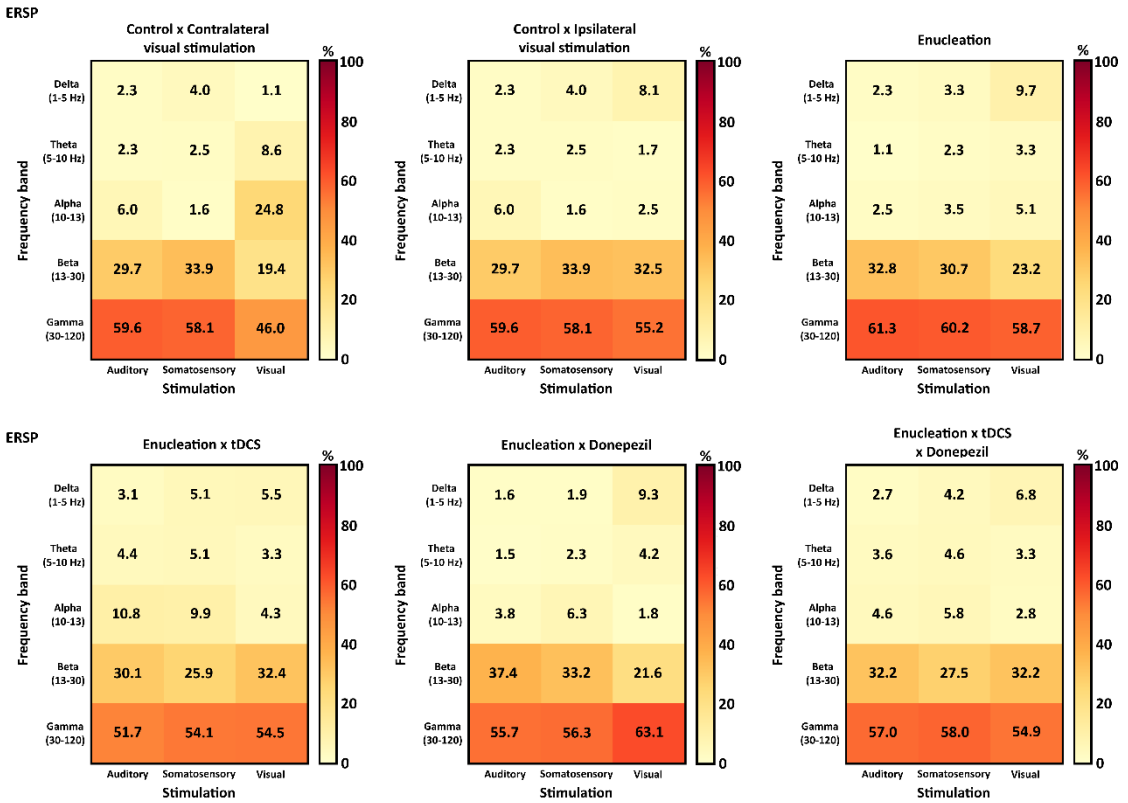

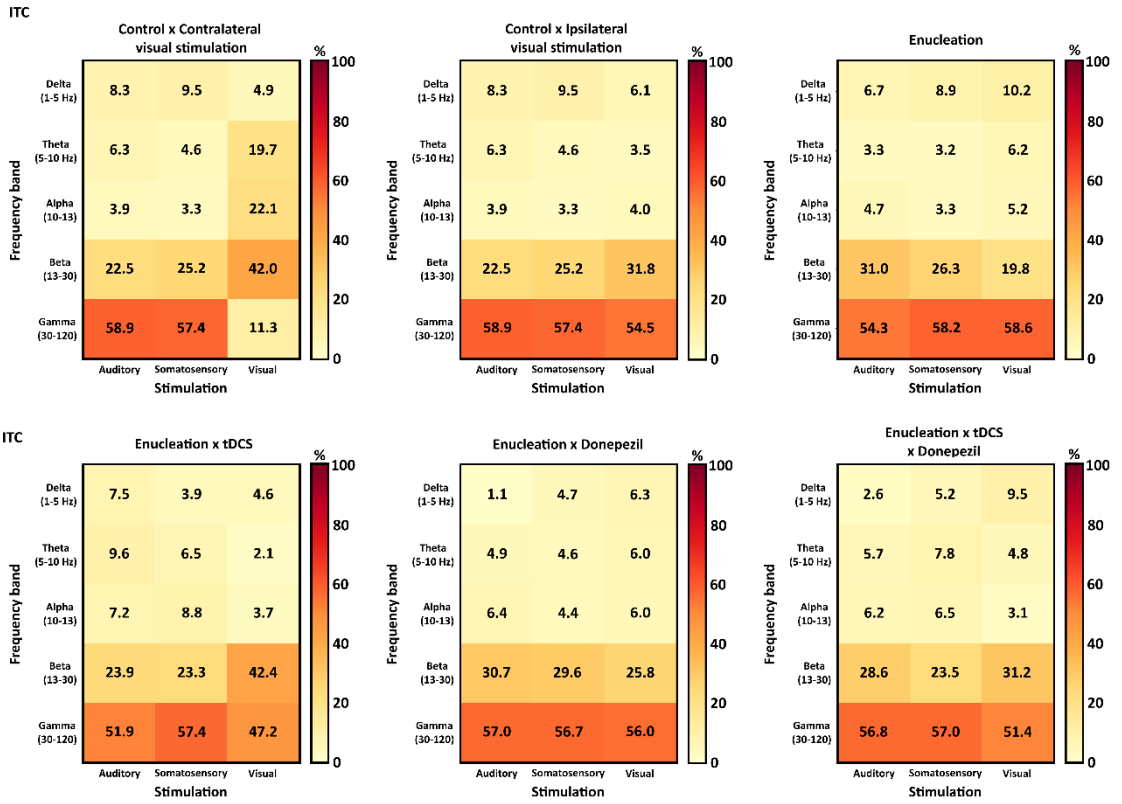

Figure 68. Distribution of data across frequency bands and stimulation modalities for ERSP and ITC. Each heatmap represents the percentage of values per stimulation modality (auditory, somatosensory, or visual).

The total number of data points analyzed in this study was 70,272, raising the reasonable question of whether the predominance of values in the beta and gamma bands is procedural. To address this, data from control animals subjected to contralateral visual stimulation were examined. The results are displayed in the heatmaps above which represent the percentage of data per stimulation modality across all experimental groups, for both ERSP values and maximum ITC. Interestingly, the distribution shows not only a concentration of values in the beta and gamma frequency bands, but also a notable contribution of the alpha band, which exceeds beta in terms of the number of maximum ERSP values. In the case of ITC, however, the gamma band carries less weight, accounting for only 11% of the data. These findings suggest a potential pattern whereby non-optimal sensory information for V1 tends to engage higher-frequency bands, whereas optimal contralateral visual input to V1 recruits a broader portion of the sub-gamma spectrum and, in particular, evokes or relies on beta rhythms (42% of n), given the higher likelihood of obtaining maximum ITC values in that frequency range (**Figure 68**).

4.5 Effect of treatments on response latency

QUICK METHODS RECAP

To study the influence of the treatments and of enucleation on the latency of the ITC peak in the V1 response to the three types of sensory stimulation, for each session and modality the ITC maximum was located within a predefined post-stimulus window, and the latency (ms) and associated frequency were extracted, stratifying by bands within the 1-120 Hz range. At the group level, latency distributions were described with KDE by band and condition (Control, Enucleation, and enucleation x tDCS, DNPZ, tDCS+DNPZ) to visualise advances/delays and shape changes without assuming normality.

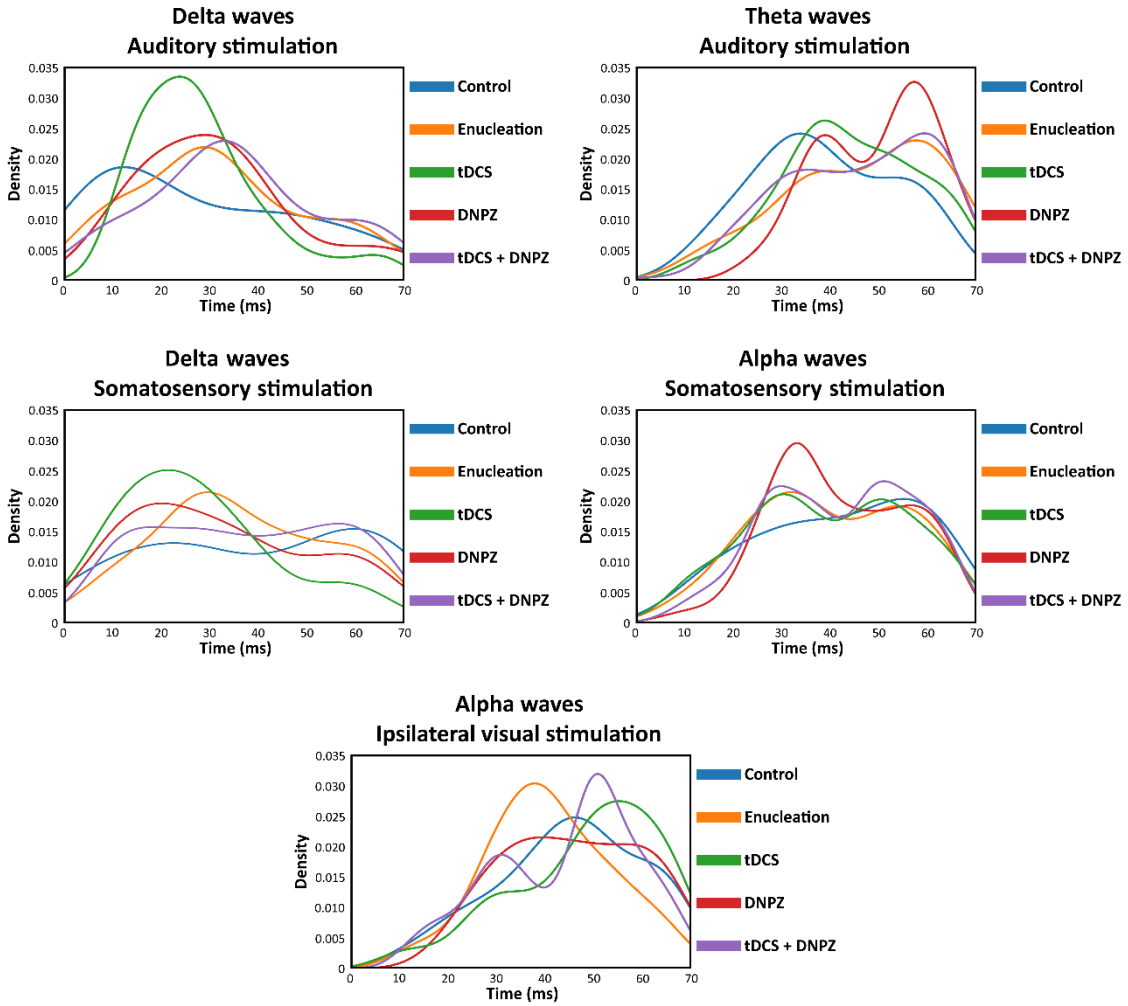

Figure 69*. Latency distributions of the phase-locking coherence (ITC) peak estimated via Kernel Density Estimation (KDE) by band and modality. Curves by condition: Control (blue), Enucleation (orange), tDCS (green), DNPZ (red), and tDCS+DNPZ (purple). X-axis: time from stimulus onset (ms); Y-axis: density.*

The curves allow visualising advances/delays and changes in shape (width, bimodality) between conditions without assuming normality.

The latency distributions of the ITC peak reveal systematic modulations by treatment, frequency band, and sensory modality. Taken together, coherence peaks in delta concentrate within early windows (≈10-40 ms), whereas those in theta and alpha are organised within middle and late windows (≈30-60 ms). Against this backdrop, the treatments produce differentiated temporal shifts and changes in the shape of the distributions (width and bimodality), which allow the interpretation of advances or delays of the phase response at the population level.

Using auditory stimulation, in the delta band, the probability of the coherence peak is around ≈15-20 ms in controls, but following enucleation this probability is delayed towards ≈30-35 ms; neither donepezil (DNPZ) nor the combined treatment (tDCS+DNPZ) restores the early latency of the control group (both remain around ≈30-35 ms). In contrast, tDCS concentrates the density at shorter latencies (≈18-22 ms) and with greater height, indicating an advance and greater temporal consistency. Continuing with auditory stimulation but in the theta band, a similar yet later pattern is observed: controls show a maximum in the middle window (≈35-40 ms), whereas in the enucleated animal groups without treatment and with DNPZ and tDCS+DNPZ the probability of the peak is shifted towards late times (≈55-60 ms), with the DNPZ effect being the most pronounced (highest density and latest peak). tDCS attenuates this delay by recovering an early component at ≈38-45 ms.

With somatosensory stimulation in delta, both in the control group and in the group of enucleated animals treated with tDCS + donepezil the probability of the ITC peak is distributed over time such that temporally the maximal coherence may appear at any moment, but in the enucleated groups without treatment and with tDCS and donepezil administered separately, the probability of the frequency maximum is found around 20 ms for the treated enucleated groups and around 30 ms for the untreated enucleated animals; thus, in this case the effect of enucleation is associated with an increase in the probability of coherence at early latencies after somatosensory stimulation, potentially evidencing a cross-modal plasticity process towards somatosensory information.

Also with somatosensory stimulation, but in alpha, the probability of the maximum coherence peak in the control group is distributed over time with a slight increase between 50 and 60 ms, whereas in the other animal groups there are two preferred windows (≈30-35 ms and ≈50-60 ms), but they differ in their relative weight. In the group of enucleated animals treated with DNPZ the probability of the ITC peak shows a sharp peak at ≈32-35 ms; in the enucleated group without treatment, the group treated with tDCS, and the group treated with the combination of tDCS + donepezil, a more moderate advance occurs with a less sharp profile.

Finally, in alpha with ipsilateral visual stimulation a double dissociation is observed: enucleation markedly advances the peak (maximum at ≈35-40 ms versus ≈45-50 ms in controls), tDCS delays it (≈55-60 ms), and the combination generates a narrow peak centred at ≈50 ms (intermediate between control and tDCS). DNPZ maintains an intermediate profile, with a broad plateau where the probability of maximal coherence lies between ≈30 and ≈65 ms (**Figure 69**).

In summary, the results show (i) auditory delays with untreated enucleation and DNPZ, especially in theta; (ii) advances induced by tDCS in delta (auditory and somatosensory) and moderate advances in alpha using somatosensory stimulation; and (iii) treatment×modality interactions: the tDCS+DNPZ combination aligns with DNPZ (delay) in auditory bands.


Discussion

Discussion

1. Physiological response of V1 to stimuli of differing nature

The physiological interpretation of the two metrics that have been used on LFP, which, although they have classically been employed in the field of electroencephalography, which can be considered a particularly more filtered version of the same synaptic generators that are recorded with intracortical LFP, is that ERSP quantifies, with respect to a baseline, increases (ERS) or decreases (ERD) in power in specific bands; therefore it acts as an index of amplitude modulation of local oscillations derived from transient changes in synaptic input, in the excitation-inhibition balance, and in population recruitment/synchrony (Buzsáki et al., 2012; Delorme & Makeig, 2004; Pfurtscheller & Lopes Da Silva, 1999), whereas ITC (also termed phase-locking factor) captures phase consistency across trials at a given time-frequency point and is therefore a direct index of the temporal synchronisation of ongoing oscillations with the event (Lachaux et al., 1999; Tallon-Baudry, 1999; Tallon-Baudry et al., 1996). These metrics are not redundant because they measure orthogonal dimensions of the signal, an increase in ITC can exist without notable changes in ERSP when a stimulus readjusts the phase of ongoing activity (phase-reset hypothesis), generating stable evoked components even with constant amplitude (Makeig et al., 2002; Tallon-Baudry, 1999), and an increase in power can occur without an increase in ITC when the event modulates the gain/amplitude of neuronal activity without aligning its phase across trials (Pfurtscheller & Lopes Da Silva, 1999). In the local field potential, where synaptic transmembrane currents dominate the extracellular potential and the contribution is more local than in EEG, this dissociation is particularly informative (Buzsáki et al., 2012); thus, when subtracting the evoked potential as a separation of evoked vs induced, strictly phase-locked effects decrease to a greater extent than induced power changes (Tallon-Baudry, 1999); on the other hand, introducing jitter into the latencies or shuffling the trials markedly reduces measures based on inter-trial phase consistency (Lachaux et al., 1999). The pre-stimulus phase predicts both perceptual performance and the amplitude of the evoked response, providing evidence for a functional role of temporal synchrony beyond power (Busch et al., 2009; Jensen & Mazaheri, 2010). Taken together, in this work ITC has been interpreted as a marker of temporal alignment and therefore of mechanisms that coordinate the arrival of information, such as phase reset and thalamo-cortical or cortico-cortical couplings, whereas ERSP would reflect amplitude modulations linked to changes in excitability/gain and in global synaptic recruitment; when both measures co-appear in the same band, concurrent mechanisms are suggested (phase readjustment

and gain change), which can be dissociated and moreover generate manipulable predictions with rhythmic stimulation.

Taken together, the present findings confirm that V1 is driven predominantly by contralateral visual input but can also be modulated by auditory and somatosensory stimuli, with notable differences in response latency and firing rate. These observations support a growing body of literature that challenges the traditional view that multisensory integration occurs exclusively at higher cortical stages following extensive processing in separate sensory areas. Recent electrophysiological and anatomical studies in humans and primates have demonstrated that early cortical regions, classically considered unisensory, can integrate information from multiple sensory modalities at very early phases of cortical processing (J. J. Foxe & Schroeder, 2005; Schroeder & Foxe, 2005). These studies have revealed direct anatomical connections between primary auditory and visual cortices, as well as neuronal responses with characteristic feedforward processing profiles, indicating that direct and rapid mechanisms could underlie the multisensory responses observed in the present study.

Contralateral visual stimulation served primarily as a control measure to verify the precise placement of the recordings within the mouse visual cortex. As expected, this type of stimulation evoked the most characteristic response in V1, confirming the correct localisation of the electrodes. A direct comparison between contralateral and ipsilateral visual stimulation revealed a dominance of contralateral input, with shorter response latencies and higher firing rates in both the monocular and binocular regions of V1.

However, what was particularly striking in the results was that both auditory and somatosensory stimulation evoked responses in V1 with shorter latencies than ipsilateral visual stimulation. This unexpected finding suggests that non-visual sensory modalities may activate V1 not only via distinct pathways, but also through possibly faster processing. These results accord with evidence from human studies suggesting that visual processing entails rapid and widespread activation across cortical areas; for example, Foxe and Simpson (2002) demonstrated that activity propagates from early visual cortex to frontal regions in approximately 30 ms from stimulus onset, underscoring the existence of fast and distributed processing pathways in the human brain. The rapid activation following somatosensory and auditory stimulation raises interesting questions about the extent of intermodal integration in V1, given that the visual cortex is traditionally thought to be specialised for processing visual inputs. Although this was not directly investigated here, it is essential to explore whether specific oscillatory dynamics, particularly in the beta band, contribute to the sensory integration observed in V1. Beta oscillations have been implicated in sensory processing across multiple cortical regions, suggesting a possible role in modulating visual perception and interactions between modalities.

The results indicate that theta-band activity in V1 exhibits not only the highest spectral power but also the highest inter-trial coherence in response to repetitive contralateral visual stimulation. Notably, ipsilateral stimulation did not evoke a theta response in V1 with comparable power or coherence. This suggests that continuous exposure to visual patterns in the contralateral field may have induced plasticity in V1, in line with the findings of Zold and Shuler (2015), who reported that theta oscillations in V1 emerge with experience and can encode temporal information about relevant visual events.

An alternative explanation is that the theta activity observed in V1 was not generated exclusively locally, but was modulated by hippocampal theta oscillations. Fournier et al. (2020) demonstrated that activity in V1 can be phase-coupled to theta oscillations recorded in CA1, suggesting an interaction between the hippocampus and the visual cortex during spatial tasks. Although the present experiment did not involve active navigation, the animals moved on a running wheel, which may have influenced theta dynamics. Rhythmic locomotion is associated with hippocampal theta oscillations, and it is possible that this movement contributed to the modulation of V1 activity, potentially reflecting hippocampal activity.

Other studies have investigated the role of beta-band oscillations across different cortices. For example, in the sensorimotor cortex, this frequency band serves a role in both sensory and motor integration, subserving higher-order functions such as postural control (Baker, 2007; Lalo et al., 2007). Therefore, in V1 this band could have a similar role in sensory integration to enhance perception of the environment. In humans, a link between beta-band oscillations and sensory gating has been described. It has been proposed that the first stimulus generates a transient signal within a local neuronal assembly, modifying responses to subsequent stimuli and allowing inhibitory conditioning to occur (Hong et al., 2008). In the murine model employed here, ipsilateral visual stimulation and contralateral somatosensory stimulation evoked an increase in beta phase coherence, in a manner similar to that observed with somatosensory stimulation in humans (Cheron et al., 2007), in line with the present results. Beta-band oscillations have been associated with improvements in concentration and visual perception during post-stroke rehabilitation, as demonstrated by Cho et al. (2015). These oscillations appear to lower the threshold for the transmission of visual information, thereby facilitating the processing of visual stimuli during attentional states. Consequently, the increase in beta activity observed here could play a global role in modulating visual perception at different levels of the visual system (Dubey et al., 2023; Wróbel, 2000). Except in the case of somatosensory stimulation, alpha event-related synchronisation was the weakest, which is consistent with the literature indicating that alpha activity tends to be suppressed during eyes-open states or in active tasks (Toscani et al., 2010). Vanneau et al. (2024) showed that switching modality reduces alpha-band coherence in the sensory cortices and increases frontal theta activity, reflecting less efficient processing and greater

cognitive effort. Although V1 was not examined, these effects suggest that attentional reconfiguration alters cortical synchrony. The observed increase in theta coherence during repeated contralateral visual stimulation could indicate a similar mechanism in V1. The authors' priming-expectancy model supports this, as repeated inputs can increase preparation and neuronal synchronisation, whereas intermodal switching disrupts these anticipatory dynamics.

In general, auditory stimulation evokes lower power and phase coherence compared with other modalities. A concern might be raised that the animals did not perceive the frequency band used for stimulation. However, it was noted from the outset that C57BL/6J mice develop high-frequency hearing loss from 2-3 months of age. Heffner et al. (2001) showed that this loss begins above ≈18 kHz and progressively worsens to ≥30 kHz, without affecting the mid-low range (≤10 kHz). Accordingly, stimuli were set entirely within that mid-low range, so the high-frequency hypoacusis of C57BL/6J mice should not have influenced the behavioural results or temporal processing. It could be argued that the somatosensory stimulus employed (air puff) also generates incidental auditory cues or subtle mechanical stimulation of the eyelid or the eyeball, either of which could masquerade as a "visual" response in V1. Nevertheless, as detailed in the Methods, sound-level measurements confirmed that the air puff never exceeded 30 dB against a background noise of 60-70 dB, and video did not reveal systematic eyelid closures during delivery of the stimulus. Thus, any intermodal noise or tactile artefact was minimised. Moreover, the observed latency following the air puff, brief in character, is consistent both with rapid transmission from somatosensory to visual cortex and with a subsomatosensory pathway (non-vibrissal). Consequently, minor auditory or oculomechanoreceptive contributions cannot be completely excluded; however, these controls and the temporal signature leave open the possibility that V1 activation genuinely reflects input from the somatosensory system.

Somatosensory stimulation produces a generalised elevation in both parameters (ERSP and ITC), potentially due to the proximity of the primary somatosensory area and to a greater sensitivity of beta activity to this type of stimulus (Kisley & Cornwell, 2006). V1 exerts a significant influence on S1 activity in mice of the same strain as those used here, but this influence has not been observed to be fully reciprocal, from S1 towards V1 (Dinh et al., 2024). The capacity of the visual cortex to respond actively to somatosensory stimulation could be explained by such connectivity (Massé et al., 2016). It is noteworthy that early somatosensory evoked potentials (frontal N30 components) in humans increase when somatosensory stimulation is accompanied by visual observation of the stimulated hand, likely involving modulation in the beta band and a reorganisation of ongoing oscillations (Cebolla & Cheron, 2015; Rossi et al., 2002).

The beta frequency band serves as a gateway to multisensory plasticity. Evidence suggests that beta oscillation plays a role in the primary visual cortex and can be evoked by any of the sensory

stimulations tested, as reflected in both power and phase coherence. Cortical beta waves in awake primates are linked to phase-dependent short-term synaptic plasticity (Zanos et al., 2018), which could account for the role of oscillations in attention, learning, and cortical reorganisation. Womelsdorf and Hoffman (2018) describe that synaptic plasticity (the strengthening or weakening of neuronal connections) depends on the synchronisation of electrical stimulation with the phases of beta oscillation in the brain. Stimulation during the beta depolarisation phase increases neuronal sensitivity to incoming signals, promoting short-term changes in synaptic strength via calcium-dependent mechanisms. These changes persist beyond the oscillations themselves, demonstrating that phase synchronisation can influence synaptic plasticity. This finding could explain why this frequency band is present regardless of the type of stimulation (Mongillo et al., 2008; Singer, 2017).

Studies show that V1 neurons respond to visual stimuli and encode decision-making and rewards, indicating that V1 is a multisensory area that integrates non-visual information (Zhang & Zador, 2023). This multisensory integration may be related to the increased V1 response to non-visual inputs. Similarly, the integration of auditory and somatosensory stimuli in V1, as suggested by the present findings, could require a higher firing rate owing to the complexity of interactions between sensory modalities. For example, Meijer et al. (2017) observed that V1 neurons modulate their firing rates as a function of the temporal congruence of visual and auditory stimuli. Congruent stimuli increase firing rates, evidencing efficient integration, whereas incongruent stimuli suppress them, underscoring the role of temporal synchronisation in proper multisensory integration, as observed in monkeys (Wang et al., 2008). It is noteworthy that non-visual stimuli, such as auditory and somatosensory inputs, elicit faster responses in V1 than visual ones. Early multisensory integration is supported by a wide variety of anatomical routes (ascending, descending, and lateral) and occurs at multiple hierarchical levels, creating an extremely flexible and complex substrate for representing sensory information. Although it remains unclear to what extent feedforward convergence at lower hierarchical levels contributes to conscious perception, it may nevertheless improve the speed and accuracy of responses even without voluntary involvement. This diversity in space (which areas are connected), in time (very short or longer latencies), and in magnitude (signal strength) implies that the classic hierarchical model of "process first separately and then integrate" should be expanded to include anatomical and temporal dimensions, recognising that even the most "basic" sensory cortices participate in higher-order functions (J. J. Foxe & Schroeder, 2005). Research commonly finds that auditory stimuli evoke earlier responses than visual ones. For example, Oude Lohuis et al. (2024) found that V1 responds more rapidly to auditory stimuli (latency ≈ 27 ms) than to visual stimuli (≈40 ms), in line with the observation here of shorter latencies for non-visual inputs. This may suggest an optimisation of V1 to integrate non-visual stimuli efficiently, which is essential for navigation

and rapid responses to the environment in mice. Moreover, somatosensory stimulation elicited rapid responses in S1, within 10 ms, which could explain why V1 responds to somatosensory inputs at ≈18 ms (Ahissar et al., 2000). Other brain areas, such as the auditory cortex, also show modulation of firing rate in response to sensory modalities. Bizley et al. (2007) found that approximately 15% of neurons in the primary auditory cortex of ferrets are influenced by visual signals, a figure that increases to almost 50% in higher-level auditory areas. This underlines the impact of visual stimuli on neuronal activity beyond V1, suggesting that multisensory integration is not limited to a single cortical region. Similarly, visual stimuli in mouse S1 modulate tactile processing via theta and gamma oscillations, improving tactile processing under visual control. Inactivation of V1 with lidocaine reveals that V1-S1 connections are vital for oscillatory modulation, although tactile responses do not disappear, implying that subcortical circuits contribute to visuo-tactile integration (Sieben et al., 2013). Fu et al. (2003) observed, in the caudomedial region of the auditory cortex in monkeys, that 72% of neurons responded to somatosensory stimuli, highlighting the capacity of the auditory cortex for somatosensory integration.

Multisensory integration may be linked to locomotion-facilitated neuronal plasticity, given that locomotion increases the firing rates of V1 neurons and improves the encoding of visual stimuli by reducing noise and response times. This suggests that, during locomotion, V1 is better adapted to process multisensory inputs efficiently. Although subjects were free to move, recordings were obtained only when they were immobile, to ensure a measurement of multisensory integration in the absence of movement. This locomotion-enhanced plasticity could extend to auditory and somatosensory integration, supporting the view that V1 is a highly adaptable cortical region (Dadarlat & Stryker, 2017; Stryker, 2014).

Adaptations and perspectives on multisensory integration in V1 have deepened the understanding that it is not limited to visual processing, but responds to a variety of sensory stimuli, including auditory and somatosensory stimuli. Research on firing rates and response latencies in V1 suggests that it plays a key role in the efficient integration of different sensory modalities, especially in contexts of rapid adaptation and processing. This knowledge opens promising prospects for the therapeutic modulation of oscillations in situations of sensory impairment.

The present results position the primary visual cortex not merely as a passive recipient of visual inputs, but as a dynamic multisensory hub whose rapid intermodal engagement fundamentally shapes perceptual and behavioural outcomes. The fact that auditory and somatosensory signals reach V1 more rapidly than contralateral visual input highlights a fast environmental surveillance mechanism, whereas modality-specific oscillatory patterns, particularly in the beta band, suggest intrinsic temporal frameworks that regulate the flow of information, facilitate short-term synaptic

plasticity, and optimise stimulus discrimination under varying attentional demands. Functionally, this implies that V1 contributes directly to sensorimotor coordination and expectation-driven processing, integrating disparate sensory streams to enhance the speed and accuracy of responses. Moreover, the ubiquitous beta-band coherence across modalities points to a potential target for neuromodulation strategies in sensory rehabilitation and compels a reappraisal of hierarchical models to recognise the role of V1 in higher-order functions such as predictive coding and intermodal learning.

2. Effect of monocular deprivation on V1 responses to stimuli of different modalities

Monocular enucleation did not alter ERP amplitudes, but it systematically reorganised V1 activity in the frequency domain; some authors, through histological studies, have documented that ME induces the reactivation of V1 with a multimodal component (auditory and somatosensory influence) at 3-7 weeks post-enucleation, via pre-existing V1-S1 connections (Van Brussel et al., 2011). Following monocular vision loss, the V1 response to auditory stimulation showed increased maximum power in the delta and theta bands, with no differences in alpha and beta, and an upward trend in gamma; by contrast, the V1 response to somatosensory stimulation exhibited increases in delta, beta, and gamma, especially in beta; however, the response to visual stimulation was markedly affected, as maximum power values were greatly reduced across the entire frequency range, except in the theta band.

Significantly, an increase was observed in the delta and gamma bands under auditory stimulation, and this gamma increase has previously been described following monocular deprivation specifically, in the non-deprived eye during audio-visual processing (≈65-75 Hz, 160-260 ms), accompanied by a gamma increase during unisensory auditory stimulation (≈50-60 Hz, 100-300 ms), consistent with auditory 'up-weighting'; by contrast, the deprived eye group shows an early alpha reduction to visual stimuli (Federici et al., 2023). By contrast, the opposite was observed with visual stimulation, where maximum power values decreased in the delta, beta, and gamma bands. Julku et al. (2021) reported decreases in oscillatory power with stimulation of the amblyopic eye, markedly affecting the 2-10 Hz frequency range and exhibiting broadband suppression, and these decreases are associated with loss of visual acuity; evoked responses also diminish. They concluded that the correlation with acuity arises primarily at low frequencies.

With respect to phase coherence, the effect was similar, as a decrease in coherence in the delta and beta bands was observed when visual stimulation was delivered following monocular vision

loss. In one study, following dichoptic "push-pull" (polarised) stimulation in anisometropic/amblyopic patients (n = 36), significant changes were reported in the beta band over the occipital and mid-temporal regions, with no change in controls (n = 33), and it was proposed that beta-band activity in the dorsal pathway during stimulation may serve as an acute marker of the effect of dichoptic training (Shi et al., 2020). It is noteworthy that visual deprivation led to a significant increase in beta coherence under auditory stimulation. Moreover, many authors use phase coherence in the theta, alpha, and beta bands for auditory change detection, which may constitute an indirect indication that an intermodal plasticity process is underway and that beta activity is being potentiated to detect auditory changes in V1 (Xia et al., 2023).

In contrast with the maximum power values, where no significant differences were observed between the control group and the monocular deprivation group, the maximum coherence values showed significant increases in the alpha, beta, and gamma frequency bands following monocular vision loss. It is not uncommon for no changes to be reported in spectral power while changes are observed in coherence; for example, Leclerc et al. (2005) likewise did not report differences in overall EEG power in any frequency range. However, EEG coherence was significantly increased in blind subjects compared with sighted subjects in the theta, alpha, and beta frequency bands.

Monocular vision loss elicited a decrease in both spectral power and coherence across the frequency spectrum in V1's response to visual stimulation, which is the opposite of what occurs under auditory and somatosensory stimulation; therefore, an intermodal plasticity process towards auditory and somatosensory inputs is suggested. In cat models of strabismic amblyopia, intracortical recordings and correlogram analyses have documented a decrease in synchrony between V1 neurons dominated by the amblyopic eye; the effect is particularly marked with high spatial frequency gratings, whereas the mean firing rate is barely reduced, suggesting that the principal deficit lies in temporal/oscillatory coordination rather than in response amplitude (Roelfsema et al., 1994). In congenitally blind individuals, using MEG (magnetoencephalography), auditory stimulation not only activates primary auditory cortex but also generates gamma activity in the visual cortex, accompanied by a trial-by-trial correlation between gamma power in A1 and V1, that is, a specific functional coupling between the two areas during auditory processing (Schepers et al., 2012). Complementarily, somatosensory-visual connectivity has been tested in humans with rTMS and PET: in early-onset blind individuals, focal rTMS over S1 increases regional cerebral blood flow in early occipital cortex (areas 17/18), a macroscopic marker of intermodal recruitment of V1 that does not appear in sighted individuals, reinforcing the idea of functional S1→occipital pathways emerging after visual deprivation (Wittenberg et al., 2004). In the same vein, during Braille reading, fMRI shows activation of V1 and of classical visual areas in blind individuals, providing a direct example of crossmodal plasticity whereby occipital cortex participates in complex tactile operations (Sadato et al., 1996).

Lastly, the resting-state oscillatory organisation of the visual cortex in blind individuals evidences a rhythmic reconfiguration characterised by increased interactions/correlations in slow (delta) and fast (gamma) bands together with a decrease in alpha power (8-12 Hz), which fits with a shift in the balance of intrinsic inhibitory and coupling mechanisms of the visual system deprived of retinal input (Hawellek et al., 2013).

The significant increase in response coherence to somatosensory, rather than auditory, stimulation, without a significant increase in power, suggests that V1 is specialised in synchronising a response to this sensory input, since an increase in phase coherence (ITC), i.e., the reordering of the phase of oscillations, without a concomitant increase in power in the human auditory cortex, is associated with better performance in an auditory task when there has been prior stimulation with a visual flash that precedes the sound; that is, an increase in ITC but not in power improves the speed of response to auditory sensory input (Thorne et al., 2011); and possibly, owing to the nature of the animal species used, that is, in the murine model employed, whisker-based somatosensation plays a key role because it allows one to follow, with circuit-level precision, how touch progresses from local signals (encoded in space and time in vS1/vS2) to explicit representations that are useful for deciding and acting; that is, tactile cognition. Moreover, in mice touch not only detects but also integrates, links across time, combines with other modalities, and guides planned actions (Diamond & Toso, 2023); hence, after the loss of monocular vision there is a generalised increase in phase coherence but not in power when somatosensory stimulation is delivered, since it is justified to posit that a process of crossmodal plasticity has occurred or is under way and that the neuronal populations of V1 are being used for somatosensory processing.

3. Effects of the treatments on the V1 response in enucleated animals

Each treatment generated in V1 a differentiated neurophysiological profile, demonstrable both in the stimulus-induced event-related spectral perturbations (ERSP), in the inter-trial phase coherence (ITC), and in the latency of the responses to somatosensory, auditory, and visual stimuli presented ipsilateral to the recording site.

3.1 Effects of tDCS

Taken together, transcranial direct current stimulation (tDCS) acts selectively, markedly enhancing audition in mid-frequency bands and attenuating somatosensory plasticity, whilst on its own it fails in restoring the visual organisation lost following enucleation.

Electrical stimulation significantly elevates alpha power relative to the control group and to the enucleated group without treatment, indicating a possible facilitatory effect on intermodal plasticity towards visual inputs in that frequency band; moreover, there is an increase in the maximum phase coherence across all the treatments and even the controls in the beta band when auditory stimulation is applied. As described earlier in the introduction, there is a strong relation between audition and vision, each being capable of modulating the response of the other, as in the McGurk effect, where vision modifies what is heard; by applying weak electrical currents to the head it is possible to 'turn up or down the volume' of the illusion, that is, tDCS is capable of altering the connection between vision and audition (L. M. Marques et al., 2014). On the other hand, another group tested that tDCS can increase or decrease the excitability of regions of the brain in order to modulate a multisensory illusion (sound-induced flash illusion (SIFI)), in which auditory information is what modifies visual perception, and they succeeded in modulating the excitability of visual and temporal areas by modifying the SIFI effect (Bolognini et al., 2011); and in this project the anodal tDCS treatment plus visual stimulation may have served to strengthen that visual-auditory connection and to facilitate crossmodal plasticity after the loss of monocular vision. Multiple studies report direct electrophysiological evidence that tACS is associated with increases in alpha-band power, particularly under continuous stimulation, and occasionally beyond the alpha range, whilst computational modelling indicates that any after-effects may arise via spike-timing-dependent plasticity (STDP) like mechanisms (De Koninck et al., 2023; Zaehle et al., 2010).

The effect of the tDCS treatment, when somatosensory stimulation was presented, was the opposite; that is, it produced an inhibition of the power of the V1 response to somatosensory stimulation across the entire frequency band, both for power and for coherence. It is known that when whiskers are stimulated in mice, the visually evoked activity in the primary visual cortex is suppressed. That suppression is mediated by local fast-spiking interneurons in layer 2/3, which receive direct inputs from the primary somatosensory cortex for whiskers (SSp-bfd), chiefly from layer-6 excitatory neurones (Weiler et al., 2024); therefore, anodal tDCS stimulation may potentiate that suppression, resulting in an inhibition of power and coherence in the V1 response to somatosensory stimulation. Although it has not been added to this study, in a control animal the effect of tDCS on the response to somatosensory stimulation was tested, and, although it is not representative, the same inhibitory effect on the V1 response as that of the enucleated animals was observed.

Some authors have described benefits of tDCS in accelerating the learning of a compensatory audiovisual training (AVT) and, with an occipital montage, achieving a sustained improvement in detection in the blind field; beyond that, it does not add improvements in visual search, but the variability of the results was very large. It may be that the facilitation by tDCS is directed more towards auditory inputs than towards the visual inputs of the remaining eye (Diana et al., 2025).

3.2 Effects of Donepezil

The results of this project show that administering donepezil for 15 days decreases (has a depressant effect on) the power and phase coherence of the V1 response to visual, somatosensory, and auditory stimulation, as measured under the conditions and analyses used in this study, that is, with this protocol, donepezil reduces the strength and synchrony of the primary visual cortex response to those stimuli.

Enucleation abruptly eliminates the retinothalamic drive and triggers early changes in visual structures. In the mouse, after neonatal bilateral enucleation (P0), an early reduction in dLGN size is observed; between P1 and P4, the position of thalamocortical afferents is not dramatically altered despite that reduction. At P4, ephrin-A5 expression in visual cortex is significantly decreased relative to controls. These changes occur before natural eye opening and constitute indicators of early plasticity, without by themselves demonstrating a topographic “readjustment” of maps (Kozanian et al., 2015).

In parallel, visual deprivation during the critical period increases GABAergic inhibition in L2/3 of V1: the number of inhibitory synapses increases, the presynaptic release probability from PV and SOM interneurons increases, and overall, the excitation/inhibition (E/I) ratio in pyramidal neurones declines (Kannan et al., 2016).

Then, on this substrate, it is plausible that, after losing the retinothalamic input, V1 comes to rely relatively more on intracortical circuitry (recurrent/callosal) and, under the E/I shift, donepezil-induced cholinergic elevation could potentiate inhibitory circuits and curtail recurrent/lateral propagation, with a net decrease in the V1 response; however, this is only a hypothesis.

3.3 Effects of tDCS + Donepezil

The combined treatment of donepezil and occipital anodal tDCS for 14 days could explain a dual pattern in V1: on the one hand, a decrease in the V1 response to auditory stimuli; on the other, an

increase in theta power (and, in general, in excitability) in response to visual stimulation. The suppression of visual responses by auditory stimuli in V1 (via local inhibitory circuits) has been demonstrated in the mouse; a "noise burst" activates the auditory cortex and, through corticocortical projections, recruits local inhibitory circuits in V1 (especially translaminar ones connecting infra- with supragranular layers) that reduce synaptic and spiking responses to visual stimuli during bimodal stimulation; moreover, blocking GABA in V1 reverses that suppression, indicating GABAergic inhibition as a key mechanism (Iurilli et al., 2012).

To this intermodal inhibitory bias would be added the cholinergic effect of donepezil. In primates, acetylcholine frequently suppresses visual responses outside layer 4c of V1 through an increase in GABA inhibition (the effect disappears with gabazine), whereas in 4c it may increase gain; taken together, ACh adjusts the network response without broadening the tuning (Disney et al., 2012). Consistent with this, it has been described in visual cortex that ACh reduces the intracortical propagation of excitation (that is, it depresses recurrent transmission), with effects that depend on the source of input, which helps to "confine" activity to relevant synapses and to limit horizontal spread (Kimura et al., 1999).

In contrast to that cholinergic filtering, anodal tDCS over V1 tends to elevate visual excitability: with 15 min, increases are observed in the amplitude of the N70 component of the VEP with low-contrast stimuli, and reductions in phosphene threshold, canonical indicators of greater V1 excitability (Antal et al., 2004). When applied repeatedly over several days, this anodal facilitation is also associated with improvements in visual perceptual learning (e.g., orientation discrimination), together with decreases in phosphene threshold and paired-VEP changes compatible with greater cortical excitability (Sczesny-Kaiser et al., 2016).

Moreover, enhancing cholinergic tone with donepezil increases the magnitude of perceptual learning and makes the improvement more specific to the trained direction of motion and location, which suggests greater neuronal selectivity in populations that encode the relevant feature (Rokem & Silver, 2010).

By analogy with the motor cortex, where an AChE inhibitor (rivastigmine) "focuses" plasticity: it blocks the global facilitation induced by anodal tDCS but enhances and prolongs the specific synaptic plasticity induced by PAS, also consolidating inhibitory effects when stimulation is asynchronous, it can be proposed that cholinergic enhancement biases the direction and magnitude of the plasticity brought about by tDCS (Kuo et al., 2007). This "focusing effect" strengthens relevant connections and dampens diffuse changes. In the same vein, recent reviews emphasise that tDCS interacts with neurotransmitter systems, including acetylcholine, and can shift the excitation/inhibition balance, providing a neurochemical basis for this modulation of plasticity (Yamada & Sumiyoshi, 2021).

Therefore, the GABAergic inhibition in V1 triggered by auditory inputs via A1, the cholinergic suppression of visual responses and of intracortical transmission, and the increase in excitability/visual learning by anodal tDCS and the cholinergic "focusing" of plasticity, could bias the plasticity induced by tDCS and donepezil in V1 towards the strengthening of residual visual circuits (e.g., of the remaining eye ipsilateral to the recording) and, at the same time, "switch off" (via GABA) non-visual inputs such as auditory ones, favouring a pro-visual intermodal plasticity and discouraging crossmodal plasticity towards the input of auditory information.

4. Differences between the results and those obtained with the Ordinary Least Squares (OLS) model

OLS normalisation subtracts from each measurement the mean effect of Treatment (animal groups: control, enucleation without treatment, enucleation + tDCS, …) and of Stimulation Modality in order to "remove" global shifts before comparing by bands (Ding, 2021). This helps to reveal fine patterns, but it brings several limitations. The most important, in this context, is that part of the expected physiological baseline is also eliminated: in V1 the visual modality and, in particular, the Control group should respond more. By subtracting those averages, the comparisons cease to be on an "absolute" scale (dB, %) and move to a scale relative to the model's re-centring. Therefore, expressions such as "above control" after OLS do not necessarily mean that the value is greater than the raw control, but that it is greater than an adjusted mean after removing those offsets. In other words, the model changes what is being measured: it is no longer "how much there is" in absolute terms, but "how much remains" once what the model attributes to Treatment and Modality has been discounted.

Moreover, the OLS model used is additive: it assumes that the effects of Treatment and Modality add without interacting. If, in reality, a treatment changes how each modality responds (or this varies by band), part of that variation may end up split between what the model removes and what it leaves in the residuals. That "allocation" can alter the shape of the results relative to the raw values (for example, giving more prominence to some bands and less to others) without the physiology necessarily having changed, but rather the model's assignment of variance. Added to this is that the procedure is two-step (first fit, then test on residuals) (Freckleton, 2002): the uncertainty of the fit is not propagated to the subsequent statistical contrast, so the p-values of the raw results and those of OLS are not directly comparable and may be calibrated differently.

Lastly, there are practical assumptions that condition the reading. OLS assumes independence and similar variances across groups and modalities; if there are repeated measures per individual,

differences in variance, or outlying observations, the fit and the residuals can be distorted. The use of peaks (ERSP/ITC maxima) introduces a selection bias that normalisation does not correct and that can amplify or attenuate differences depending on the search domain (Kriegeskorte et al., 2009). Band-by-band comparison generates many tests that are correlated; normalisation can concentrate or disperse the signal across bands and change which contrasts become "significant" for statistical reasons (Luck & Gaspelin, 2017). And if there is imbalance (Treatment×Modality cells with few cases), the adjusted means become unstable, and the residuals become sensitive to small sample fluctuations.

In sum, the results after OLS should be read as differences that remain after removing the global averages of Treatment and Modality (Ding, 2021); Raw results show absolute magnitudes. That certain conclusions change between Raw and OLS does not invalidate the findings, but it does delimit the scope of what can be stated: part of those differences depends on the modelling decision (what is removed and what is retained) and on the assumptions of additivity, independence, and homogeneity of variances, as well as on the use of peaks and the multiplicity of band-wise tests.

The comparison between raw data and the residual deviations after removing the means of Treatment and Modality in results via OLS should be read on two different scales. Remembering that raw results show absolute magnitudes (dB, %), whereas the residual deviations after removing the treatment and modality means in results via OLS (hereafter called OLS results) reflect band-selective deviations that remain after subtracting the mean effects of Treatment (Control, Enucleated, tDCS, DNPZ, tDCS+DNPZ) and Modality (visual, auditory, somatosensory). With this caveat, the two analyses trace a coherent pattern: enucleation shifts the dynamics of V1 towards non-visual modalities and the treatments modulate that reorganisation with band selectivity; normalisation helps to distinguish which differences are scale-dependent and which appear as selective effects once global offsets have been discounted.

In theta under visual stimulation, the maximum ERSP values indicate that the tDCS+DNPZ combination facilitates power to levels comparable to Control and distinct from each treatment separately, even descriptively exceeding the Control average. On the OLS scale, that indication translates into a selective positive deviation for the combination relative to the additive pattern, whereas tDCS shows residual improvement relative to Enucleated, and DNPZ does not exhibit residual differences relative to Control or Enucleated. That is, what in the raw results suggests "recovery up to Control", in the OLS results is expressed as a selective enhancement in theta for the combination after removing global offsets (without here interpreting absolute superiority over Control).

In alpha under auditory stimulation, the raw values of maximum power already showed that tDCS significantly elevates power. The OLS results reproduce that profile as a positive residual deviation for tDCS and, in addition, detect positive deviations for DNPZ and for the combination relative to the untreated (always in residual terms). In other words, normalisation strengthens the evidence for auditory facilitation and broadens the set of groups that show a selective excess over the additive pattern.

In beta under auditory stimulation, the ERSP results suggest a specific inhibition with the combination (significant reduction) that does not appear with the treatments separately. But with the OLS results the pattern changes: tDCS shows a positive residual deviation relative to Control and Enucleated, and both DNPZ and the combination also show residual excesses relative to the untreated. Thus, what in the raw results appeared as an "inhibition" is revealed as an effect of global gain: once the offset is removed, a selective facilitation emerges in alpha/beta that the raw values masked.

With somatosensory stimulation, the raw maximum power values pointed to a broad attenuation with all treatments relative to Control and Enucleated. The OLS results make that reading more precise: in delta, all treated groups show negative residual deviations, with convergence of the curves after removing the scale bias. Here normalisation does not change the direction of the effect, but circumscribes it to the bands where it is most stable. In gamma under visual stimulation, both approaches coincide: there is no recovery with any treatment; in the OLS results, the residual trajectories cluster at low or negative values, reinforcing that visually driven gamma remains depressed.

Now, in the raw coherence results during visual stimulation in theta, tDCS+DNPZ occupies the highest position, with no differences relative to Control but above DNPZ and Enucleated without treatment; DNPZ is the lowest, and the OLS results confirm that profile in residual terms: the combination presents a selective excess relative to DNPZ and Enucleated without treatment, while residual differences with Control and with tDCS remain not evident. Continuing with vision but in alpha, the OLS results do not add further evidence relative to the raw values; the synergy is expressed more evident in theta and beta. In beta, the OLS results bring to light a residual benefit of the combination relative to DNPZ, with no residual differences relative to Control.

The most robust and concordant result in ITC is under auditory stimulation in beta, with tDCS occupying first position both in the raw values and in the OLS results, and with DNPZ also above Control on both scales. The combination of treatments remains in an intermediate range in both analyses, suggesting that the cholinergic component does not add, in this domain, a temporal benefit beyond that conferred by stimulation. At the somatosensory extreme, the suppressions persist after normalisation, with one nuance: in the raw values a significant reduction in delta is

observed in all treated groups; with the OLS results, the focus of interference shifts towards alpha, where tDCS shows a negative residual deviation, while DNPZ and the combination approach the adjusted pattern of Control. The OLS results, therefore, do not contradict the "somatosensory attenuation", but locate it more precisely (delta in power; alpha in coherence for tDCS).

Taken together, the raw-vs-OLS reading allows stable conclusions to be separated from scale-dependent conclusions. Maintained are the auditory facilitation by tDCS in alpha/beta (ERSP and ITC), the visual synergy of the combination in theta coherence relative to DNPZ and Enucleated without treatment, and the persistent depression of visual gamma (power and coherence). Two key readings change with the OLS results: in visual theta (ERSP), what in the raw results looked like "recovery up to Control" is expressed in the OLS results as a selective residual excess of the combination after removing global offsets; and in beta with auditory stimulation, the "inhibition" in the raw results becomes a positive residual deviation for the treated groups, revealing that the previous pattern was modulated by gain. Somatosensory attenuation persists, but OLS relocates its most stable band; and the lack of recovery of gamma is confirmed by both approaches.

5. Baseline Beta Dominance and Treatment-Robust High-Frequency Shifts of Maxima in V1

In general, maximum power values concentrate preferentially in gamma and beta, with alpha at an intermediate level; theta and delta appear less frequently; and the same holds for the maxima of phase coherence. Relative to that reference pattern, when the input is not optimal for V1 (e.g., auditory, somatosensory, ipsilateral visual, or after deprivation), the choice of the band containing the maximum shifts towards higher frequencies. The treatments do not overturn this baseline rule; however, in the control group with contralateral visual stimulation the values appear to be more distributed across the frequency bands, yet with beta being more dominant in terms of phase coherence and gamma in maximum power values, making evident which sensory input is dominant in V1; moreover, there is ample scientific evidence supporting the relation between the beta/gamma frequency bands and visual information in V1. Thus, it becomes evident that a congruent/efficient input tends to recruit and couple sub-gamma rhythms, with beta coordination standing out for inter-areal integration; by contrast, a mismatched input increases gamma associated with prediction error/surprise, transiently shifting processing towards higher-frequency modes. In Michalareas *et al.*, (2016), directed influences between human visual areas were analysed with MEG and compared with laminar patterns of feedforward/feedback connectivity described in the macaque, resulting in feedforward influences predominating in gamma, while feedback influences do so in alpha-beta; in the macaque, Kerkoerle et al., (2014)

recorded across the layers of V1 and simultaneously in V4, and used microstimulation to "probe" causal directions, finding that gamma originated in layer 4 and propagated feedforward, whereas alpha travelled in the feedback direction; moreover, blocking NMDA (linked to feedback) suppressed alpha and enhanced gamma; in humans, during LFP recordings in auditory cortex it has been demonstrated that surprise/violation is encoded in gamma, changes in prediction in beta, and the precision (confidence) of the prediction relates to alpha (Sedley et al., 2016); another group proposed a predictive routing framework: predictions selectively prepare/inhibit the expected pathways via alpha/beta, so that when the input violates the prediction, gamma and feedforward increase because that pathway was not inhibited (Bastos et al., 2020).

6. Differences in the latency of the appearance of phase-coherence maxima under different conditions

The latency of the ITC peak is greatly altered by the treatment that has been applied and by the condition of the animal, only the most notable differences being highlighted here, such as that tDCS accelerates phase coherence in a general manner across the frequency spectrum; studies in Parkinson's disease have shown that, after two weeks of tDCS stimulation over the prefrontal cortex, the P300 appeared earlier, that is, with a shorter latency, and power increased in alpha and beta, therefore electrical treatment may improve processing efficiency and tune oscillatory networks (Fabio et al., 2024); other authors have used tACS as a treatment and, in visual tasks, have been able to bring forward ERP components such as P300 by means of this electrical stimulation (Jaušovec & Jaušovec, 2014; Pahor & Jaušovec, 2018), and, more modestly but significantly, tDCS in vascular dementia succeeded in shortening P300 latency. On the other hand, donepezil acts as a brake on ITC coherence when auditory stimulation is used, but with somatosensory stimulation it makes the latency of the ITC peak more robust; some authors have not reported significant differences in latency with and without donepezil treatment, but what did change were the ITC patterns in delta, theta, alpha, and beta (Gurtubay-Antolin et al., 2023).

The combined tDCS+DNPZ treatment produces an effect similar to that of donepezil, but, in general, it causes ITC peaks to be more spread out over time than with DNPZ, although a study has been conducted in China in which patients with stroke sequelae were given combined donepezil and tDCS treatment, and it resulted in an improvement in memory and cognition tasks, as well as a significant reduction in P300 latency, the limitation of the study being that the experimental group was small, but it is quite promising (Hu et al., 2023). Enucleation causes delays in ITC coherence in general for auditory and somatosensory stimulation, with the exception of the alpha band, where the ITC peaks are distributed over time in the physiological

condition but, after enucleation, are more likely to be found in two specific time intervals, that is, it may be a reflection of intermodal plasticity; in alpha, enucleation advances the ITC peak latency with respect to controls, and tDCS delays it. There is precedent showing that, in adults with age-related hearing loss, somatosensory stimulation shows significantly shorter latencies in temporal regions than in normal-hearing controls, which is indicative of cross-modal organisation (Cardon & Sharma, 2018).


Conclusion

Conclusion

In this project it has been demonstrated that, under physiological conditions, V1 does not act as a passive recipient of retinothalamic input, but as a dynamic multisensory node. In response to auditory and somatosensory stimuli, its activity emerges with relatively short latencies and with a characteristic oscillatory profile in which the beta band plays a central role as a temporal scaffold for integration and for short-term plasticity. Inter-trial phase coherence, broad and consistent, suggests intrinsic rhythmic frameworks that coordinate the flow of information and discrimination under different attentional demands. This could be the basis (in power and in phase coherence) that serves as a reference for comparing reorganised neurological states.

Monocular enucleation does not produce robust alterations in the amplitude of ERP components, but it does produce a systematic reconfiguration in the spectral domain, yielding a decrease in power and in inter-trial phase coherence evoked by visual stimulation, and selective increases (according to frequency band) under auditory and somatosensory stimulation. The redistribution confirms an intermodal readjustment in V1 in which the residual visual signal is weakened and the non-visual signal gains weight, with the beta band (and delta to a lesser extent) as a sensitive axis of the new sensory coordination. The resultant plasticity is predominantly intermodal in spectro-temporal terms.

The interventions proposed in this study (which are minimally invasive in humans for possible clinical applications) reveal differential profiles. Anodal tDCS over V1 shows selectivity (it favours alpha power during auditory stimulation with respect to the control group and to the enucleated group without treatments, and, in parallel, it attenuates the somatosensory response across the spectrum). Treatment with donepezil exerts an overall depressant effect on power and coherence in V1 under the applied protocol, although there is slight maintenance of power and of phase coherence with auditory stimulation, especially in beta. The tDCS+donepezil combination does not operate as a non-specific amplifier ; rather, it tends to focus plasticity, with indications consistent with a facilitation of theta-band power and phase coherence during visual stimulation with respect to the enucleation-without-treatment group and of a reduction in auditory and somatosensory interference, which points to a potential modulation of cross-modal plasticity towards intramodal plasticity for the residual visual information. Even so, tDCS by itself did not restore the lost visual organisation in absolute terms.

Plasticity after monocular vision loss is not an epiphenomenon, but a structured and steerable process. V1 integrates and rebalances inputs and can be guided by rational combinations of electrical neuromodulation and cholinergic potentiation, relying on spectral biomarkers, with emphasis on beta for non-visual inputs and theta for visual inputs, and on phase, or on the latency

of inter-trial phase coherence, to monitor the direction and magnitude of change. This framework provides operational principles for sensory retraining in visual rehabilitation or restoration.

In the short and medium term, the work opens concrete avenues. A reduced set of oscillatory and coherence biomarkers could be validated and standardised as criteria for stratification and monitoring of patients with partial vision loss or undergoing restoration (prostheses, gene or pharmacological therapies, training), given the sensitivity of V1 to intermodal plasticity shown in this study and in others cited here. Likewise, tDCS could be combined with task-specific perceptual training and the cholinergic timing (dose and moment relative to the session) optimised to enhance the "focusing" effect and the specificity of plasticity, avoiding diffuse modulations; ideally, with closed-loop protocols that couple stimulation to beta/alpha windows relevant to each sensory modality. A study at the level of cortical circuits and layers would be a good complement to this project, for example, laminar and connectivity approaches (optogenetics, multilayer recordings, calcium imaging) that identify which interneurons and corticocortical projections support auditory-somatosensory reweighting and its modulation by ACh and tDCS.

In addition, the biological spectrum could be broadened, comparing ages and deprivation windows, as well as reversible/bilateral deprivations, in order to delimit the dependence on "system state" and on the developmental timetable so as to complete what is described in this project. In a larger study, physiology could be anchored to behavioural/ecological outcomes (detection, localisation, navigation), integrating performance measures with neurophysiological markers, in line with person-centred rehabilitation; or, in animals, behavioural experiments could be carried out while recording in vivo activity so as to associate the neurological changes in the states studied here with tasks and to examine how the treatments can modulate behavioural responses alongside neural ones, these experiments potentially being conducted in virtual-reality environments, and even applying recording techniques that yield more information, such as Neuropixels.

Finally, if vision-recovery techniques are effective and standardised, this work may lay the foundations, with the markers used here, for studying possible treatments that modulate plasticity and for facilitating the task of V1 in once again interpreting visual information.

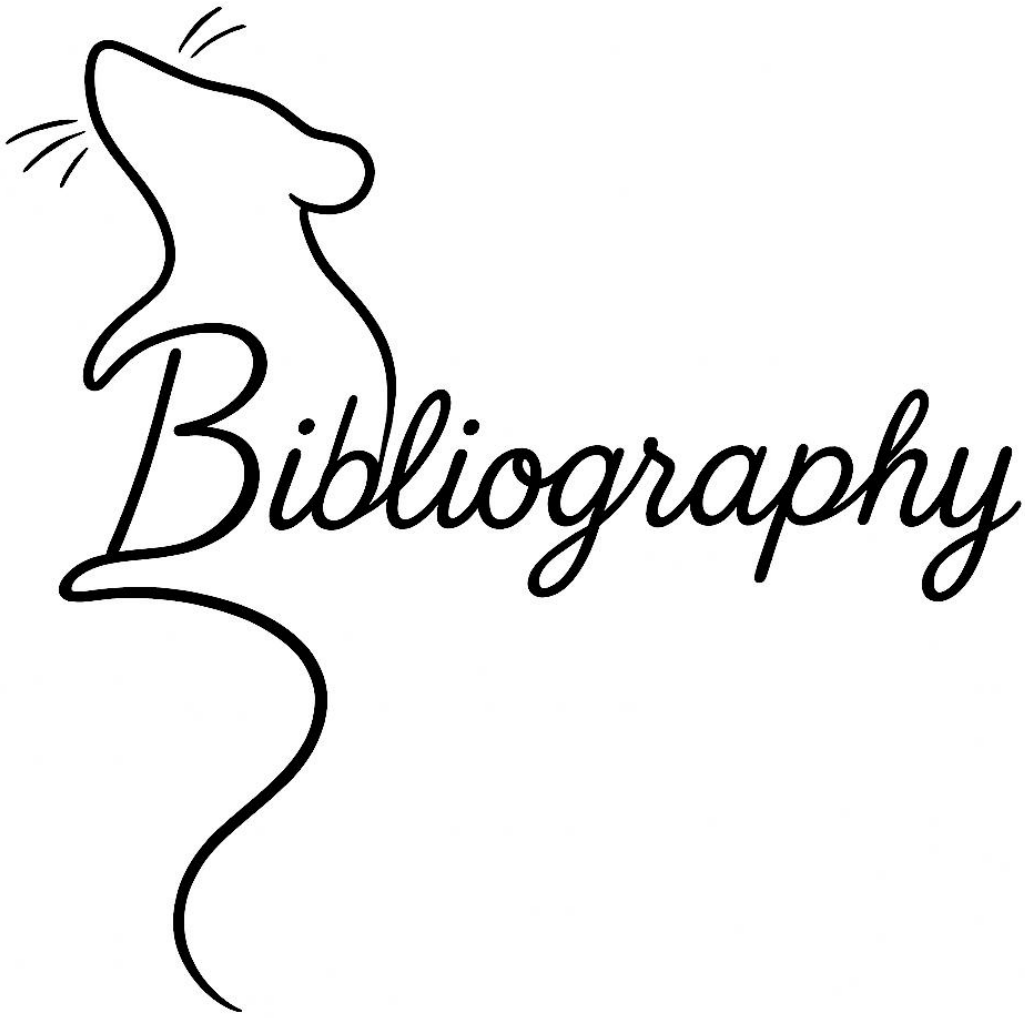
Bibliography

Bibliography

Aerts, J., Nys, J., & Arckens, L. (2014). A Highly Reproducible and Straightforward Method to Perform In Vivo Ocular Enucleation in the Mouse after Eye Opening. *Journal of Visualized Experiments*, *92*, 51936. https://doi.org/10.3791/51936

Ahissar, E., Sosnik, R., & Haidarliu, S. (2000). Transformation from temporal to rate coding in a somatosensory thalamocortical pathway. *Nature*, *406*(6793), 302–306. https://doi.org/10.1038/35018568

Ahmadi, N., Constandinou, T. G., & Bouganis, C.-S. (2021). Inferring entire spiking activity from local field potentials. *Scientific Reports*, *11*(1), 19045. https://doi.org/10.1038/s41598-021-98021-9

Alshahrani, M., Al-Jabbar, M., Senan, E. M., Ahmed, I. A., & Saif, J. A. M. (2023). Hybrid Methods for Fundus Image Analysis for Diagnosis of Diabetic Retinopathy Development Stages Based on Fusion Features. *Diagnostics*, *13*(17), 2783. https://doi.org/10.3390/diagnostics13172783

Alwashmi, K., Meyer, G., Rowe, F., & Ward, R. (2024). Enhancing learning outcomes through multisensory integration: A fMRI study of audio-visual training in virtual reality. *NeuroImage*, *285*, 120483. https://doi.org/10.1016/j.neuroimage.2023.120483

Amedi, A., Stern, W. M., Camprodon, J. A., Bermpohl, F., Merabet, L., Rotman, S., Hemond, C., Meijer, P., & Pascual-Leone, A. (2007). Shape conveyed by visual-to-auditory sensory substitution activates the lateral occipital complex. *Nature Neuroscience*, *10*(6), 687–689. https://doi.org/10.1038/nn1912

Antal, A., Kincses, T. Z., Nitsche, M. A., Bartfai, O., & Paulus, W. (2004). Excitability Changes Induced in the Human Primary Visual Cortex by Transcranial Direct Current Stimulation: Direct Electrophysiological Evidence. *Investigative Opthalmology & Visual Science*, *45*(2), 702. https://doi.org/10.1167/iovs.03-0688

Apte, R. S. (2021). Age-Related Macular Degeneration. *New England Journal of Medicine*, *385*(6), 539–547. https://doi.org/10.1056/NEJMcp2102061

Assi, L., Chamseddine, F., Ibrahim, P., Sabbagh, H., Rosman, L., Congdon, N., Evans, J., Ramke, J., Kuper, H., Burton, M. J., Ehrlich, J. R., & Swenor, B. K. (2021). A Global Assessment of Eye Health and Quality of Life: A Systematic Review of Systematic Reviews. *JAMA Ophthalmology*, *139*(5), 526. https://doi.org/10.1001/jamaophthalmol.2021.0146

Baker, S. N. (2007). Oscillatory interactions between sensorimotor cortex and the periphery. *Current Opinion in Neurobiology*, *17*(6), 649–655. https://doi.org/10.1016/j.conb.2008.01.007

Basole, A., White, L. E., & Fitzpatrick, D. (2003). Mapping multiple features in the population response of visual cortex. *Nature*, *423*(6943), 986–990. https://doi.org/10.1038/nature01721

Bastos, A. M., Lundqvist, M., Waite, A. S., Kopell, N., & Miller, E. K. (2020). Layer and rhythm specificity for predictive routing. *Proceedings of the National Academy of Sciences*, *117*(49), 31459–31469. https://doi.org/10.1073/pnas.2014868117

Beer, A. L., Plank, T., & Greenlee, M. W. (2011). Diffusion tensor imaging shows white matter tracts between human auditory and visual cortex. *Experimental Brain Research*, *213*(2–3), 299–308. https://doi.org/10.1007/s00221-011-2715-y

Belyk, M., Brown, S., & Kotz, S. A. (2017). Demonstration and validation of Kernel Density Estimation for spatial meta-analyses in cognitive neuroscience using simulated data. *Data in Brief*, *13*, 346–352. https://doi.org/10.1016/j.dib.2017.06.003

Bennett, M. (2020). An Attempt at a Unified Theory of the Neocortical Microcircuit in Sensory Cortex. *Frontiers in Neural Circuits*, *14*, 40. https://doi.org/10.3389/fncir.2020.00040

Bertonati, G., Amadeo, M. B., Campus, C., & Gori, M. (2023). Task-dependent spatial processing in the visual cortex. *Human Brain Mapping*, *44*(17), 5972–5981. https://doi.org/10.1002/hbm.26489

Bibollet-Bahena, O., Tissier, S., Ho-Tran, S., Rojewski, A., & Casanova, C. (2023). Enriched environment exposure during development positively impacts the structure and function of the visual cortex in mice. *Scientific Reports*, *13*(1), 7020. https://doi.org/10.1038/s41598-023-33951-0

Bieniek, M. M., Bennett, P. J., Sekuler, A. B., & Rousselet, G. A. (2016). A robust and representative lower bound on object processing speed in humans. *European Journal of Neuroscience*, *44*(2), 1804–1814. https://doi.org/10.1111/ejn.13100

Bizley, J. K., Nodal, F. R., Bajo, V. M., Nelken, I., & King, A. J. (2007). Physiological and Anatomical Evidence for Multisensory Interactions in Auditory Cortex. *Cerebral Cortex*, *17*(9), 2172–2189. https://doi.org/10.1093/cercor/bhl128

Bolognini, N., Rossetti, A., Casati, C., Mancini, F., & Vallar, G. (2011). Neuromodulation of multisensory perception: A tDCS study of the sound-induced flash illusion. *Neuropsychologia*, *49*(2), 231–237. https://doi.org/10.1016/j.neuropsychologia.2010.11.015

Bourne, R. R. A., Jonas, J. B., Bron, A. M., Cicinelli, M. V., Das, A., Flaxman, S. R., Friedman, D. S., Keeffe, J. E., Kempen, J. H., Leasher, J., Limburg, H., Naidoo, K., Pesudovs, K., Peto, T., Saadine, J., Silvester, A. J., Tahhan, N., Taylor, H. R., Varma, R., … Resnikoff, S. (2018). Prevalence and causes of vision loss in high-income countries and in Eastern and Central Europe in 2015: Magnitude, temporal trends and projections. *British Journal of Ophthalmology*, *102*(5), 575–585. https://doi.org/10.1136/bjophthalmol-2017-311258

Bourne, R., Steinmetz, J., Flaxman, S., & Vision Loss Expert Group (VLEG). (2020). *Magnitude of Global Vision Loss* (IAPB Evidence Series). International Agency for the Prevention of Blindness (IAPB). https://www.iapb.org/learn/vision-atlas/

Brigo, F., Study Group for the History of Neurology of the Italian Neurological Society; Epilepsy Study Group of the Italian Neurological Society, Benna, P., Di Gennaro, G., Labate, A., Lorusso, L., Mecarelli, O., Reale, G., & Volpe, E. (2025). A century of EEG: Unveiling the electrical nature of epilepsy. *Neurological Sciences*, *46*(4), 1911–1913. https://doi.org/10.1007/s10072-024-07919-5

Brown, D. M., Nguyen, Q. D., Marcus, D. M., Boyer, D. S., Patel, S., Feiner, L., Schlottmann, P. G., Rundle, A. C., Zhang, J., Rubio, R. G., Adamis, A. P., Ehrlich, J. S., & Hopkins, J. J. (2013). Long-term Outcomes of Ranibizumab Therapy for Diabetic Macular Edema: The

36-Month Results from Two Phase III Trials. *Ophthalmology*, *120*(10), 2013–2022. https://doi.org/10.1016/j.ophtha.2013.02.034

Brown, D. M., Schmidt-Erfurth, U., Do, D. V., Holz, F. G., Boyer, D. S., Midena, E., Heier, J. S., Terasaki, H., Kaiser, P. K., Marcus, D. M., Nguyen, Q. D., Jaffe, G. J., Slakter, J. S., Simader, C., Soo, Y., Schmelter, T., Yancopoulos, G. D., Stahl, N., Vitti, R., … Korobelnik, J.-F. (2015). Intravitreal Aflibercept for Diabetic Macular Edema. *Ophthalmology*, *122*(10), 2044–2052. https://doi.org/10.1016/j.ophtha.2015.06.017

Bruninx, R., & Lepièce, G. (2020). L'image du mois. La rétinite pigmentaire [Retinitis pigmentosa]. *Revue médicale de Liège*, *75*(2), 73–74.

Burns, S. P., Xing, D., & Shapley, R. M. (2010). Comparisons of the Dynamics of Local Field Potential and Multiunit Activity Signals in Macaque Visual Cortex. *The Journal of Neuroscience*, *30*(41), 13739–13749. https://doi.org/10.1523/JNEUROSCI.0743-10.2010

Busch, N. A., Dubois, J., & VanRullen, R. (2009). The Phase of Ongoing EEG Oscillations Predicts Visual Perception. *Journal of Neuroscience*, *29*(24), 7869–7876. https://doi.org/10.1523/JNEUROSCI.0113-09.2009

Buzsáki, G., Anastassiou, C. A., & Koch, C. (2012). The origin of extracellular fields and currents—EEG, ECoG, LFP and spikes. *Nature Reviews Neuroscience*, *13*(6), 407–420. https://doi.org/10.1038/nrn3241

Caballero Tapia, A., Cheron, G., Ristori, D., Arckens, L., & Ris, L. (2025). Beyond Vision: Response of the Mouse Visual Cortex to Multimodal Stimulation. *European Journal of Neuroscience*, *62*(3), e70225. https://doi.org/10.1111/ejn.70225

Calvert, G. A., Bullmore, E. T., Brammer, M. J., Campbell, R., Williams, S. C., McGuire, P. K., Woodruff, P. W., Iversen, S. D., & David, A. S. (1997). Activation of auditory cortex during silent lipreading. *Science*, *276*(5312), 593–596.

Cambiaghi, M., Teneud, L., Velikova, S., Gonzalez-Rosa, J. J., Cursi, M., Comi, G., & Leocani, L. (2011). Flash visual evoked potentials in mice can be modulated by transcranial direct

current stimulation. *Neuroscience*, *185*, 161–165. https://doi.org/10.1016/j.neuroscience.2011.04.022

Cang, J., Fu, J., & Tanabe, S. (2023). Neural circuits for binocular vision: Ocular dominance, interocular matching, and disparity selectivity. *Frontiers in Neural Circuits*, *17*, 1084027. https://doi.org/10.3389/fncir.2023.1084027

Cardon, G., & Sharma, A. (2018). Somatosensory Cross-Modal Reorganization in Adults With Age-Related, Early-Stage Hearing Loss. *Frontiers in Human Neuroscience*, *12*, 172. https://doi.org/10.3389/fnhum.2018.00172

Cash, S. S., & Hochberg, L. R. (2015). The Emergence of Single Neurons in Clinical Neurology. *Neuron*, *86*(1), 79–91. https://doi.org/10.1016/j.neuron.2015.03.058

Castaño-Castaño, S., Garcia-Moll, A., Morales-Navas, M., Fernandez, E., Sanchez-Santed, F., & Nieto-Escamez, F. (2017). Transcranial direct current stimulation improves visual acuity in amblyopic Long-Evans rats. *Brain Research*, *1657*, 340–346. https://doi.org/10.1016/j.brainres.2017.01.003

Cebolla, A. M., & Cheron, G. (2015). Sensorimotor and cognitive involvement of the beta–gamma oscillation in the frontal N30 component of somatosensory evoked potentials. *Neuropsychologia*, *79*, 215–222. https://doi.org/10.1016/j.neuropsychologia.2015.04.033

Chamoun, M., Groleau, M., Bhat, M., & Vaucher, E. (2016). Dose-dependent effect of donepezil administration on long-term enhancement of visually evoked potentials and cholinergic receptor overexpression in rat visual cortex. *Journal of Physiology-Paris*, *110*(1–2), 65–74. https://doi.org/10.1016/j.jphysparis.2016.11.010

Chamoun, M., Sergeeva, E. G., Henrich-Noack, P., Jia, S., Grigartzik, L., Ma, J., You, Q., Huppé-Gourgues, F., Sabel, B. A., & Vaucher, E. (2017). Cholinergic Potentiation of Restoration of Visual Function after Optic Nerve Damage in Rats. *Neural Plasticity*, *2017*, 1–10. https://doi.org/10.1155/2017/6928489

Chen, J., Yang, C., Zheng, W., Li, Z., Huang, Y., Yao, S., Chen, X., Chen, X., Xie, R., Luo, R., Zhang, Y., Ye, G., Shen, X., Xiao, Y., Zhu, Y., & Huang, W. (2024). Global, Regional,

and National Epidemiology of Visual Impairment in Working-Age Individuals, 1990-2019. *JAMA Ophthalmology*, *142*(1), 25. https://doi.org/10.1001/jamaophthalmol.2023.5617

Cheron, G., Cebolla, A. M., De Saedeleer, C., Bengoetxea, A., Leurs, F., Leroy, A., & Dan, B. (2007). Pure phase-locking of beta/gamma oscillation contributes to the N30 frontal component of somatosensory evoked potentials. *BMC Neuroscience*, *8*(1), 75. https://doi.org/10.1186/1471-2202-8-75

Chino, Y. M., Kaas, J. H., Smith, E. L., Langston, A. L., & Cheng, H. (1992). Rapid reorganization of cortical maps in adult cats following restricted deafferentation in retina. *Vision Research*, *32*(5), 789–796. https://doi.org/10.1016/0042-6989(92)90021-A

Cho, H.-Y., Kim, K., Lee, B., & Jung, J. (2015). The effect of neurofeedback on a brain wave and visual perception in stroke: A randomized control trial. *Journal of Physical Therapy Science*, *27*(3), 673–676. https://doi.org/10.1589/jpts.27.673

Christ, S. L., Zheng, D. D., Swenor, B. K., Lam, B. L., West, S. K., Tannenbaum, S. L., Muñoz, B. E., & Lee, D. J. (2014). Longitudinal Relationships Among Visual Acuity, Daily Functional Status, and Mortality: The Salisbury Eye Evaluation Study. *JAMA Ophthalmology*, *132*(12), 1400. https://doi.org/10.1001/jamaophthalmol.2014.2847

Chuvarayan, Y., Finger, R. P., & Köberlein-Neu, J. (2020). Economic burden of blindness and visual impairment in Germany from a societal perspective: A cost-of-illness study. *The European Journal of Health Economics*, *21*(1), 115–127. https://doi.org/10.1007/s10198-019-01115-5

Cui, S., Lee, D., & Wen, D. (2024). Toward brain-inspired foundation model for EEG signal processing: Our opinion. *Frontiers in Neuroscience*, *18*, 1507654. https://doi.org/10.3389/fnins.2024.1507654

Dadarlat, M. C., & Stryker, M. P. (2017). Locomotion Enhances Neural Encoding of Visual Stimuli in Mouse V1. *The Journal of Neuroscience*, *37*(14), 3764–3775. https://doi.org/10.1523/JNEUROSCI.2728-16.2017

Darian-Smith, C., & Gilbert, C. (1995). Topographic reorganization in the striate cortex of the adult cat and monkey is cortically mediated. *The Journal of Neuroscience*, *15*(3), 1631–1647. https://doi.org/10.1523/JNEUROSCI.15-03-01631.1995

Davies, P. L. (2010). Middle and late latency ERP components discriminate between adults, typical children, and children with sensory processing disorders. *Frontiers in Integrative Neuroscience*, *4*. https://doi.org/10.3389/fnint.2010.00016

De Koninck, B. P., Brazeau, D., Guay, S., Herrero Babiloni, A., & De Beaumont, L. (2023). Transcranial Alternating Current Stimulation to Modulate Alpha Activity: A Systematic Review. *Neuromodulation: Technology at the Neural Interface*, *26*(8), 1549–1584. https://doi.org/10.1016/j.neurom.2022.12.007

Delorme, A., & Makeig, S. (2004). EEGLAB: An open source toolbox for analysis of single-trial EEG dynamics including independent component analysis. *Journal of Neuroscience Methods*, *134*(1), 9–21. https://doi.org/10.1016/j.jneumeth.2003.10.009

Diamond, M. E., & Toso, A. (2023). Tactile cognition in rodents. *Neuroscience & Biobehavioral Reviews*, *149*, 105161. https://doi.org/10.1016/j.neubiorev.2023.105161

Diana, L., Casati, C., Melzi, L., Marzoli, S. B., & Bolognini, N. (2025). Enhancing multisensory rehabilitation of visual field defects with transcranial direct current stimulation: A randomized clinical trial. *European Journal of Neurology*, *32*(1), e16559. https://doi.org/10.1111/ene.16559

DiCarlo, J. J., Lane, J. W., Hsiao, S. S., & Johnson, K. O. (1996). Marking microelectrode penetrations with fluorescent dyes. *Journal of Neuroscience Methods*, *64*(1), 75–81. https://doi.org/10.1016/0165-0270(95)00113-1

Ding, P. (2021). The Frisch–Waugh–Lovell theorem for standard errors. *Statistics & Probability Letters*, *168*, 108945. https://doi.org/10.1016/j.spl.2020.108945

Dinh, T. N. A., Moon, H. S., & Kim, S.-G. (2024). Separation of bimodal fMRI responses in mouse somatosensory areas into V1 and non-V1 contributions. *Scientific Reports*, *14*(1), 6302. https://doi.org/10.1038/s41598-024-56305-w

Disney, A. A., Aoki, C., & Hawken, M. J. (2012). Cholinergic suppression of visual responses in primate V1 is mediated by GABAergic inhibition. *Journal of Neurophysiology*, *108*(7), 1907–1923. https://doi.org/10.1152/jn.00188.2012

Douglas, R. J., & Martin, K. A. C. (2004). NEURONAL CIRCUITS OF THE NEOCORTEX. *Annual Review of Neuroscience*, *27*(1), 419–451. https://doi.org/10.1146/annurev.neuro.27.070203.144152

Dubey, A., Markowitz, D. A., & Pesaran, B. (2023). Top-down control of exogenous attentional selection is mediated by beta coherence in prefrontal cortex. *bioRxiv*. https://doi.org/10.1101/2023.01.11.523664

Edwards, T. L., Cottriall, C. L., Xue, K., Simunovic, M. P., Ramsden, J. D., Zrenner, E., & MacLaren, R. E. (2018). Assessment of the Electronic Retinal Implant Alpha AMS in Restoring Vision to Blind Patients with End-Stage Retinitis Pigmentosa. *Ophthalmology*, *125*(3), 432–443. https://doi.org/10.1016/j.ophtha.2017.09.019

Einevoll, G. T., Kayser, C., Logothetis, N. K., & Panzeri, S. (2013). Modelling and analysis of local field potentials for studying the function of cortical circuits. *Nature Reviews Neuroscience*, *14*(11), 770–785. https://doi.org/10.1038/nrn3599

Fabio, R. A., Suriano, R., & Gangemi, A. (2024). Effects of Transcranial Direct Current Stimulation on Potential P300-Related Events and Alpha and Beta EEG Band Rhythms in Parkinson's Disease. *Journal of Integrative Neuroscience*, *23*(2), 25. https://doi.org/10.31083/j.jin2302025

Federici, A., Bernardi, G., Senna, I., Fantoni, M., Ernst, M. O., Ricciardi, E., & Bottari, D. (2023). Crossmodal plasticity following short-term monocular deprivation. *NeuroImage*, *274*, 120141. https://doi.org/10.1016/j.neuroimage.2023.120141

Fink, J. J., Delaney-Busch, N., Dawes, R., Nanou, E., Folts, C., Harikrishnan, K., Hempel, C., Upadhyay, H., Nguyen, T., Shroff, H., Stoppel, D., Ryan, S. J., Jacques, J., Grooms, J., Berry-Kravis, E., Bear, M. F., Williams, L. A., Gerber, D., Bunnage, M., … Dempsey, G. T. (2024). Deep functional measurements of Fragile X syndrome human neurons

reveal multiparametric electrophysiological disease phenotype. *Communications Biology*, *7*(1), 1447. https://doi.org/10.1038/s42003-024-07120-6

Fitzpatrick, D., Lund, J. S., Schmechel, D. E., & Towles, A. C. (1987). Distribution of GABAergic neurons and axon terminals in the macaque striate cortex. *Journal of Comparative Neurology*, *264*(1), 73–91. https://doi.org/10.1002/cne.902640107

Fong, D. S., Aiello, L., GARDNER, T. W., KING, G. L., BLANKENSHIP, G., CAVALLERANO, J. D., FERRIS, F. L., & KLEIN, R. (2004, January). Retinopathy in Diabetes. *Diabetes Care*, *27*(Supplement 1), S84–S87.

Fournier, J., Saleem, A. B., Diamanti, E. M., Wells, M. J., Harris, K. D., & Carandini, M. (2020). Mouse Visual Cortex Is Modulated by Distance Traveled and by Theta Oscillations. *Current Biology*, *30*(19), 3811-3817.e6. https://doi.org/10.1016/j.cub.2020.07.006

Foxe, J. J., & Schroeder, C. E. (2005). The case for feedforward multisensory convergence during early cortical processing: *NeuroReport*, *16*(5), 419–423. https://doi.org/10.1097/00001756-200504040-00001

Foxe, J., & Simpson, G. (2002). Flow of activation from V1 to frontal cortex in humans. *Experimental Brain Research*, *142*(1), 139–150. https://doi.org/10.1007/s00221-001-0906-7

Franklin, K.B.J. & Paxinos, G. (2019). *Paxinos and Franklin's the Mouse Brain in Stereotaxic Coordinates, Compact: The Coronal Plates and Diagrams*. Elsevier Science. https://books.google.ie/books?id=IdoTugEACAAJ

Frasnelli, J., Collignon, O., Voss, P., & Lepore, F. (2011). Crossmodal plasticity in sensory loss. In *Progress in Brain Research* (Vol. 191, pp. 233–249). Elsevier. https://doi.org/10.1016/B978-0-444-53752-2.00002-3

Freckleton, R. P. (2002). On the misuse of residuals in ecology: Regression of residuals vs. multiple regression. *Journal of Animal Ecology*, *71*(3), 542–545. https://doi.org/10.1046/j.1365-2656.2002.00618.x

Frenkel, M. Y., & Bear, M. F. (2004). How Monocular Deprivation Shifts Ocular Dominance in Visual Cortex of Young Mice. *Neuron*, *44*(6), 917–923. https://doi.org/10.1016/j.neuron.2004.12.003

Fu, K.-M. G., Johnston, T. A., Shah, A. S., Arnold, L., Smiley, J., Hackett, T. A., Garraghty, P. E., & Schroeder, C. E. (2003). Auditory Cortical Neurons Respond to Somatosensory Stimulation. *The Journal of Neuroscience*, *23*(20), 7510–7515. https://doi.org/10.1523/JNEUROSCI.23-20-07510.2003

Fu, Y., Kaneko, M., Tang, Y., Alvarez-Buylla, A., & Stryker, M. P. (2015). A cortical disinhibitory circuit for enhancing adult plasticity. *eLife*, *4*, e05558. https://doi.org/10.7554/eLife.05558

Galindo-Camacho, R. M., Blanco-Llamero, C., Da Ana, R., Fuertes, M. A., Señoráns, F. J., Silva, A. M., García, M. L., & Souto, E. B. (2022). Therapeutic Approaches for Age-Related Macular Degeneration. *International Journal of Molecular Sciences*, *23*(19), 11769. https://doi.org/10.3390/ijms231911769

Galvez, R., Weible, A. P., & Disterhoft, J. F. (2007). Cortical barrel lesions impair whisker-CS trace eyeblink conditioning. *Learning & Memory*, *14*(1–2), 94–100. https://doi.org/10.1101/lm.418407

Galvez, R., Weiss, C., Cua, S., & Disterhoft, J. (2009). A novel method for precisely timed stimulation of mouse whiskers in a freely moving preparation: Application for delivery of the conditioned stimulus in trace eyeblink conditioning. *Journal of Neuroscience Methods*, *177*(2), 434–439. https://doi.org/10.1016/j.jneumeth.2008.11.002

Gao, C., Conte, S., Richards, J. E., Xie, W., & Hanayik, T. (2019). The neural sources of N170: Understanding timing of activation in face-selective areas. *Psychophysiology*, *56*(6), e13336. https://doi.org/10.1111/psyp.13336

Ghazanfar, A., & Schroeder, C. (2006). Is neocortex essentially multisensory? *Trends in Cognitive Sciences*, *10*(6), 278–285. https://doi.org/10.1016/j.tics.2006.04.008

Gómez-Ulla de Irazazábal, F., & Ondategui-Parra, S. (2012). *Informe sobre la ceguera en España* (p. 129) [Informe Técnico]. Retinaplus, Ernst & Young, SL. https://www.esvision.es/wp-content/uploads/2019/11/Informe_Ceguera.pdf

Grandchamp, R., & Delorme, A. (2011). Single-Trial Normalization for Event-Related Spectral Decomposition Reduces Sensitivity to Noisy Trials. *Frontiers in Psychology*, *2*. https://doi.org/10.3389/fpsyg.2011.00236

Greifzu, F., Pielecka-Fortuna, J., Kalogeraki, E., Krempler, K., Favaro, P. D., Schlüter, O. M., & Löwel, S. (2014). Environmental enrichment extends ocular dominance plasticity into adulthood and protects from stroke-induced impairments of plasticity. *Proceedings of the National Academy of Sciences*, *111*(3), 1150–1155. https://doi.org/10.1073/pnas.1313385111

Gupta, A., Lam, J., Custis, P., Munz, S., Fong, D., & Koster, M. (2018). Implantable miniature telescope (IMT) for vision loss due to end-stage age-related macular degeneration. *Cochrane Database of Systematic Reviews*, *2018*(5). https://doi.org/10.1002/14651858.CD011140.pub2

Gurtubay-Antolin, A., Bruña, R., Collignon, O., & Rodríguez-Fornells, A. (2023). Tactile expectancy modulates occipital alpha oscillations in early blindness. *NeuroImage*, *265*, 119790. https://doi.org/10.1016/j.neuroimage.2022.119790

Guy, J., & Staiger, J. F. (2017). The Functioning of a Cortex without Layers. *Frontiers in Neuroanatomy*, *11*, 54. https://doi.org/10.3389/fnana.2017.00054

Harris, K. D., & Shepherd, G. M. G. (2015). The neocortical circuit: Themes and variations. *Nature Neuroscience*, *18*(2), 170–181. https://doi.org/10.1038/nn.3917

Hawellek, D. J., Schepers, I. M., Roeder, B., Engel, A. K., Siegel, M., & Hipp, J. F. (2013). Altered Intrinsic Neuronal Interactions in the Visual Cortex of the Blind. *The Journal of Neuroscience*, *33*(43), 17072–17080. https://doi.org/10.1523/JNEUROSCI.1625-13.2013

Heffner, R. S., Koay, G., & Heffner, H. E. (2001). Focus: Sound-Localization Acuity Changes with Age in C57BL/6J Mice. In *Handbook of Mouse Auditory Research* (pp. 45–50). CRC Press eBooks. https://doi.org/10.1201/9781420038736-7

Heier, J. S., Brown, D. M., Chong, V., Korobelnik, J.-F., Kaiser, P. K., Nguyen, Q. D., Kirchhof, B., Ho, A., Ogura, Y., Yancopoulos, G. D., Stahl, N., Vitti, R., Berliner, A. J., Soo, Y., Anderesi, M., Groetzbach, G., Sommerauer, B., Sandbrink, R., Simader, C., & Schmidt-Erfurth, U. (2012). Intravitreal Aflibercept (VEGF Trap-Eye) in Wet Age-related Macular Degeneration. *Ophthalmology*, *119*(12), 2537–2548. https://doi.org/10.1016/j.ophtha.2012.09.006

Heier, J. S., Cohen, M. N., Chao, D. L., Pepio, A., Shiraga, Y., Capuano, G., Rogers, A., Ackert, J., Sen, H. N., & Csaky, K. (2024). Phase 1 Study of JNJ-81201887 Gene Therapy in Geographic Atrophy Secondary to Age-Related Macular Degeneration. *Ophthalmology*, *131*(12), 1377–1388. https://doi.org/10.1016/j.ophtha.2024.06.013

Heinen, S. J., & Skavenski, A. A. (1991). Recovery of visual responses in foveal V1 neurons following bilateral foveal lesions in adult monkey. *Experimental Brain Research*, *83*(3). https://doi.org/10.1007/BF00229845

Helfrich, R. F., & Knight, R. T. (2019). Cognitive neurophysiology: Event-related potentials. In *Handbook of Clinical Neurology* (Vol. 160, pp. 543–558). Elsevier. https://doi.org/10.1016/B978-0-444-64032-1.00036-9

Herreras, O. (2016). Local Field Potentials: Myths and Misunderstandings. *Frontiers in Neural Circuits*, *10*. https://doi.org/10.3389/fncir.2016.00101

Hoffmann, F., & La Roche Ltd. (2022, January 31). *FDA approves Roche's Vabysmo, the first bispecific antibody for the eye, to treat two leading causes of vision loss*.

Hölig, C., Guerreiro, M. J. S., Lingareddy, S., Kekunnaya, R., & Röder, B. (2023). Sight restoration in congenitally blind humans does not restore visual brain structure. *Cerebral Cortex*, *33*(5), 2152–2161. https://doi.org/10.1093/cercor/bhac197

Holladay, J. T. & FACS MSEE. (2004). Visual Acuity Measurements. *Journal of Cataract and Refractive Surgery*.

Holloway, V. (2000). The reorganization of sensorimotor function in children after hemispherectomy: A functional MRI and somatosensory evoked potential study. *Brain*, *123*(12), 2432–2444. https://doi.org/10.1093/brain/123.12.2432

Hong, L. E., Buchanan, R. W., Thaker, G. K., Shepard, P. D., & Summerfelt, A. (2008). Beta (~16 Hz) frequency neural oscillations mediate auditory sensory gating in humans. *Psychophysiology*, *45*(2), 197–204. https://doi.org/10.1111/j.1469-8986.2007.00624.x

Horton, J. C., & Adams, D. L. (2005). The cortical column: A structure without a function. *Philosophical Transactions of the Royal Society B: Biological Sciences*, *360*(1456), 837–862. https://doi.org/10.1098/rstb.2005.1623

Hsu, P.-C., Chen, P.-Y., Chung, Y.-S., Lin, T.-C., Hwang, D.-K., Chen, S.-J., & Kao, C.-L. (2019). First implantation of retinal prosthesis in a patient with high myopia after surgery and rehabilitation program in Taiwan. *Journal of the Chinese Medical Association*, *82*(7), 599–602. https://doi.org/10.1097/JCMA.0000000000000091

Hu, W., Wang, X., Li, X., & Wang, Q. (2023). Effect of Transcranial Direct Current Stimulation Combined with Donepezil on stroke patients with memory impairment. *Pakistan Journal of Medical Sciences*, *39*(3). https://doi.org/10.12669/pjms.39.3.6822

Hubel, D. H., & Wiesel, T. N. (1959). Receptive fields of single neurones in the cat's striate cortex. *The Journal of Physiology*, *148*(3), 574.

Iurilli, G., Ghezzi, D., Olcese, U., Lassi, G., Nazzaro, C., Tonini, R., Tucci, V., Benfenati, F., & Medini, P. (2012). Sound-Driven Synaptic Inhibition in Primary Visual Cortex. *Neuron*, *73*(4), 814–828. https://doi.org/10.1016/j.neuron.2011.12.026

Jaušovec, N., & Jaušovec, K. (2014). Increasing working memory capacity with theta transcranial alternating current stimulation (tACS). *Biological Psychology*, *96*, 42–47. https://doi.org/10.1016/j.biopsycho.2013.11.006

Jensen, O., & Mazaheri, A. (2010). Shaping Functional Architecture by Oscillatory Alpha Activity: Gating by Inhibition. *Frontiers in Human Neuroscience*, *4*. https://doi.org/10.3389/fnhum.2010.00186

Jorstad, N. L., Close, J., Johansen, N., Yanny, A. M., Barkan, E. R., Travaglini, K. J., Bertagnolli, D., Campos, J., Casper, T., Crichton, K., Dee, N., Ding, S.-L., Gelfand, E., Goldy, J., Hirschstein, D., Kiick, K., Kroll, M., Kunst, M., Lathia, K., … Lein, E. S. (2023). Transcriptomic cytoarchitecture reveals principles of human neocortex organization. *Science*, *382*(6667), eadf6812. https://doi.org/10.1126/science.adf6812

Julku, H., Rouhinen, S., Huttunen, H. J., Lindberg, L., Liinamaa, J., Saarela, V., Karvonen, E., Booms, S., Mäkelä, J. P., Uusitalo, H., Castrén, E., Palva, J. M., & Palva, S. (2021). Reduced evoked activity and cortical oscillations are correlated with anisometric amblyopia and impairment of visual acuity. *Scientific Reports*, *11*(1), 8310. https://doi.org/10.1038/s41598-021-87545-9

Kaan, E. (2007). Event-Related Potentials and Language Processing: A Brief Overview. *Language and Linguistics Compass*, *1*(6), 571–591. https://doi.org/10.1111/j.1749-818X.2007.00037.x

Kajikawa, Y., & Schroeder, C. E. (2011). How Local Is the Local Field Potential? *Neuron*, *72*(5), 847–858. https://doi.org/10.1016/j.neuron.2011.09.029

Kalia, A., Lesmes, L. A., Dorr, M., Gandhi, T., Chatterjee, G., Ganesh, S., Bex, P. J., & Sinha, P. (2014). Development of pattern vision following early and extended blindness. *Proceedings of the National Academy of Sciences*, *111*(5), 2035–2039. https://doi.org/10.1073/pnas.1311041111

Kannan, M., Gross, G. G., Arnold, D. B., & Higley, M. J. (2016). Visual Deprivation During the Critical Period Enhances Layer 2/3 GABAergic Inhibition in Mouse V1. *The Journal of Neuroscience*, *36*(22), 5914–5919. https://doi.org/10.1523/JNEUROSCI.0051-16.2016

Kashani, A. H., Lebkowski, J. S., Rahhal, F. M., Avery, R. L., Salehi-Had, H., Dang, W., Lin, C.-M., Mitra, D., Zhu, D., Thomas, B. B., Hikita, S. T., Pennington, B. O., Johnson, L. V., Clegg, D. O., Hinton, D. R., & Humayun, M. S. (2018). A bioengineered retinal pigment epithelial monolayer for advanced, dry age-related macular degeneration. *Science Translational Medicine*, *10*(435), eaao4097. https://doi.org/10.1126/scitranslmed.aao4097

Kataoka, S. Y., Lois, N., Kawano, S., Kataoka, Y., Inoue, K., & Watanabe, N. (2023). Fenofibrate for diabetic retinopathy. *Cochrane Database of Systematic Reviews*, *2023*(6). https://doi.org/10.1002/14651858.CD013318.pub2

Kayser, C., & Logothetis, N. K. (2007). Do early sensory cortices integrate cross-modal information? *Brain Structure and Function*, *212*(2), 121–132. https://doi.org/10.1007/s00429-007-0154-0

Kelly, K. R., McKetton, L., Schneider, K. A., Gallie, B. L., & Steeves, J. K. E. (2014). Altered anterior visual system development following early monocular enucleation. *NeuroImage: Clinical*, *4*, 72–81. https://doi.org/10.1016/j.nicl.2013.10.014

Khattab, A. A. A., Ahmed, M. M., & Hammed, A. H. (2022). Pars plana vitrectomy for tractional diabetic macular edema with or without internal limiting membrane peeling. *Medical Hypothesis Discovery and Innovation in Ophthalmology*, *11*(3), 110–118. https://doi.org/10.51329/mehdiophthal1454

Kimura, F., Fukuda, M., & Tsumoto, T. (1999). Acetylcholine suppresses the spread of excitation in the visual cortex revealed by optical recording: Possible differential effect depending on the source of input. *European Journal of Neuroscience*, *11*(10), 3597–3609. https://doi.org/10.1046/j.1460-9568.1999.00779.x

Kisley, M. A., & Cornwell, Z. M. (2006). Gamma and beta neural activity evoked during a sensory gating paradigm: Effects of auditory, somatosensory and cross-modal stimulation. *Clinical Neurophysiology*, *117*(11), 2549–2563. https://doi.org/10.1016/j.clinph.2006.08.003

Kozanian, O. O., Abbott, C. W., & Huffman, K. J. (2015). Correction: Rapid Changes in Cortical and Subcortical Brain Regions after Early Bilateral Enucleation in the Mouse. *PLOS ONE*, *10*(11), e0142461. https://doi.org/10.1371/journal.pone.0142461

Kriegeskorte, N., Simmons, W. K., Bellgowan, P. S. F., & Baker, C. I. (2009). Circular analysis in systems neuroscience: The dangers of double dipping. *Nature Neuroscience*, *12*(5), 535–540. https://doi.org/10.1038/nn.2303

Kulmala, J., Era, P., Pärssinen, O., Sakari, R., Sipilä, S., Rantanen, T., & Heikkinen, E. (2008). Lowered vision as a risk factor for injurious accidents in older people. *Aging Clinical and Experimental Research*, *20*(1), 25–30. https://doi.org/10.1007/BF03324744

Kuo, M.-F., Grosch, J., Fregni, F., Paulus, W., & Nitsche, M. A. (2007). Focusing Effect of Acetylcholine on Neuroplasticity in the Human Motor Cortex. *The Journal of Neuroscience*, *27*(52), 14442–14447. https://doi.org/10.1523/JNEUROSCI.4104-07.2007

Kutas, M., & Federmeier, K. D. (2011). Thirty Years and Counting: Finding Meaning in the N400 Component of the Event-Related Brain Potential (ERP). *Annual Review of Psychology*, *62*(1), 621–647. https://doi.org/10.1146/annurev.psych.093008.131123

Lachaux, J.-P., Rodriguez, E., Martinerie, J., & Varela, F. J. (1999). Measuring phase synchrony in brain signals. *Human Brain Mapping*, *8*(4), 194–208. https://doi.org/10.1002/(SICI)1097-0193(1999)8:4%253C194::AID-HBM4%253E3.0.CO;2-C

Lalo, E., Gilbertson, T., Doyle, L., Lazzaro, V. D., Cioni, B., & Brown, P. (2007). Phasic increases in cortical beta activity are associated with alterations in sensory processing in the human. *Experimental Brain Research*, *177*(1), 137–145. https://doi.org/10.1007/s00221-006-0655-8

Lam, B. L. (2008). Reported Visual Impairment and Risk of Suicide: The 1986-1996 National Health Interview Surveys. *Archives of Ophthalmology*, *126*(7), 975. https://doi.org/10.1001/archopht.126.7.975

Lambert, S. R. (2023). What we have learned from the Infant Aphakia Treatment Study: The 49th Annual Frank D. Costenbader Lecture. *Journal of American Association for Pediatric Ophthalmology and Strabismus*, *27*(5), 253–258. https://doi.org/10.1016/j.jaapos.2023.08.001

Leclerc, C., Segalowitz, S. J., Desjardins, J., Lassonde, M., & Lepore, F. (2005). EEG coherence in early-blind humans during sound localization. *Neuroscience Letters*, *376*(3), 154–159. https://doi.org/10.1016/j.neulet.2004.11.046

Lee, H.-K. (2023). Metaplasticity framework for cross-modal synaptic plasticity in adults. *Frontiers in Synaptic Neuroscience*, *14*, 1087042. https://doi.org/10.3389/fnsyn.2022.1087042

Lennie, P., & Van Hemel, S. B. (Eds) (with National Research Council (US) Committee on Disability Determination for Individuals with Visual Impairments). (2002). *Visual Impairments: Determining Eligibility for Social Security Benefits*. National Academies Press (US). doi: 10.17226/10320.

Levakova, M., Tamborrino, M., Ditlevsen, S., & Lansky, P. (2015). A review of the methods for neuronal response latency estimation. *Biosystems*, *136*, 23–34. https://doi.org/10.1016/j.biosystems.2015.04.008

Ligue Braille, La Lumière, & Œuvre Nationale des Aveugles. (2020). *Fiche 1: La déficience visuelle*. AVIQ – Agence pour une Vie de Qualité. https://www.aviq.be/handicap

Lim, J. I., Kim, S. J., Bailey, S. T., Kovach, J. L., Vemulakonda, G. A., Ying, G., & Flaxel, C. J. (2025). Diabetic Retinopathy Preferred Practice Pattern®. *American Academy of Ophthalmology*, *132*(4), P75–P162. https://doi.org/10.1016/j.ophtha.2024.12.020

Llorens, A., Trébuchon, A., Liégeois-Chauvel, C., & Alario, F.-X. (2011). Intra-Cranial Recordings of Brain Activity During Language Production. *Frontiers in Psychology*, *2*. https://doi.org/10.3389/fpsyg.2011.00375

Lopez, L., Brusa, A., Fadda, A., Loizzo, S., Martinangeli, A., Sannita, W. G., & Loizzo, A. (2002). Modulation of flash stimulation intensity and frequency: Effects on visual evoked potentials and oscillatory potentials recorded in awake, freely moving mice. *Behavioural Brain Research*, *131*(1–2), 105–114. https://doi.org/10.1016/S0166-4328(01)00351-5

Luck, S. J., & Gaspelin, N. (2017). How to get statistically significant effects in any ERP experiment (and why you shouldn't). *Psychophysiology*, *54*(1), 146–157. https://doi.org/10.1111/psyp.12639

Ma, C., Wang, Z., Wu, W., Ma, X., Wang, L., Zhang, X., Chen, W., Kuang, X., Li, Y., Miao, Y., Xue, T., Jiang, B., & Yang, Y. (2025). Non-invasive light flickering reinstates visual

plasticity in adult mice via lipocalin 2. *BMC Biology*, *23*(1), 237. https://doi.org/10.1186/s12915-025-02360-2

Maffei, A., Lambo, M. E., & Turrigiano, G. G. (2010). Critical Period for Inhibitory Plasticity in RodentBinocular V1. *The Journal of Neuroscience*, *30*(9), 3304–3309. https://doi.org/10.1523/JNEUROSCI.5340-09.2010

Maidenbaum, S., Abboud, S., & Amedi, A. (2014). Sensory substitution: Closing the gap between basic research and widespread practical visual rehabilitation. *Neuroscience & Biobehavioral Reviews*, *41*, 3–15. https://doi.org/10.1016/j.neubiorev.2013.11.007

Makeig, S., Westerfield, M., Jung, T.-P., Enghoff, S., Townsend, J., Courchesne, E., & Sejnowski, T. J. (2002). Dynamic Brain Sources of Visual Evoked Responses. *Science*, *295*(5555), 690–694. https://doi.org/10.1126/science.1066168

Marques, A. P., Macedo, A. F., Lima Ramos, P., Moreno, L. H., Butt, T., Rubin, G., & Santana, R. (2019). Productivity Losses and Their Explanatory Factors Amongst People with Impaired Vision. *Ophthalmic Epidemiology*, *26*(6), 378–392. https://doi.org/10.1080/09286586.2019.1632904

Marques, L. M., Lapenta, O. M., Merabet, L. B., Bolognini, N., & Boggio, P. S. (2014). Tuning and disrupting the brainâ€"modulating the McGurk illusion with electrical stimulation. *Frontiers in Human Neuroscience*, *8*. https://doi.org/10.3389/fnhum.2014.00533

Marshall, L. H. (1987). Instruments, Techniques, and Social Units in American Neurophysiology, 1870–1950. In G. L. Geison (Ed.), *Physiology in the American Context 1850–1940* (pp. 351–369). Springer New York. https://doi.org/10.1007/978-1-4614-7528-6_16

Massé, I. O., Ross, S., Bronchti, G., & Boire, D. (2016). Asymmetric Direct Reciprocal Connections Between Primary Visual and Somatosensory Cortices of the Mouse. *Cerebral Cortex*, cercor;bhw239v1. https://doi.org/10.1093/cercor/bhw239

Massimino, S. (2025). Interview with Prof. Giacomo Rizzolatti. *Preliminary Reports and Negative Results in Life Science and Humanities*, *Vol 2*, V-XI Pages. https://doi.org/10.13129/3035-062X/PRNR-4978

McCullough, P., Mohite, A., Virgili, G., & Lois, N. (2023). Outcomes and Complications of Pars Plana Vitrectomy for Tractional Retinal Detachment in People With Diabetes: A Systematic Review and Meta-analysis. *JAMA Ophthalmology*, *141*(2), 186. https://doi.org/10.1001/jamaophthalmol.2022.5817

Mehta, S. (2015). Age-Related Macular Degeneration. *Primary Care: Clinics in Office Practice*, *42*(3), 377–391. https://doi.org/10.1016/j.pop.2015.05.009

Meijer, G. T., Mertens, P. E. C., Pennartz, C. M. A., Olcese, U., & Lansink, C. S. (2019). The circuit architecture of cortical multisensory processing: Distinct functions jointly operating within a common anatomical network. *Progress in Neurobiology*, *174*, 1–15. https://doi.org/10.1016/j.pneurobio.2019.01.004

Meijer, G. T., Montijn, J. S., Pennartz, C. M. A., & Lansink, C. S. (2017). Audiovisual Modulation in Mouse Primary Visual Cortex Depends on Cross-Modal Stimulus Configuration and Congruency. *The Journal of Neuroscience*, *37*(36), 8783–8796. https://doi.org/10.1523/JNEUROSCI.0468-17.2017

Merabet, L. B., & Pascual-Leone, A. (2010). Neural reorganization following sensory loss: The opportunity of change. *Nature Reviews Neuroscience*, *11*(1), 44–52. https://doi.org/10.1038/nrn2758

Mesik, L., Ma, W., Li, L., Ibrahim, L. A., Huang, Z. J., Zhang, L. I., & Tao, H. W. (2015). Functional response properties of VIP-expressing inhibitory neurons in mouse visual and auditory cortex. *Frontiers in Neural Circuits*, *09*. https://doi.org/10.3389/fncir.2015.00022

Michaelides, M., Besirli, C. G., Yang, Y., De Guimaraes, T. A. C., Wong, S. C., Huckfeldt, R. M., Comander, J. I., Sahel, J.-A., Shah, S. M., Tee, J. J. L., Kumaran, N., Georgiadis, A., Minnick, P., Zeldin, R., Naylor, S., Xu, J., Clark, M., Anglade, E., Wong, P., … Bainbridge, J. (2024). Phase 1/2 AAV5-hRKp.RPGR (Botaretigene Sparoparvovec) Gene Therapy: Safety and Efficacy in RPGR-Associated X-Linked Retinitis Pigmentosa. *American Journal of Ophthalmology*, *267*, 122–134. https://doi.org/10.1016/j.ajo.2024.05.034

Michalareas, G., Vezoli, J., van Pelt, S., Schoffelen, J.-M., Kennedy, H., & Fries, P. (2016). Alpha-Beta and Gamma Rhythms Subserve Feedback and Feedforward Influences among Human Visual Cortical Areas. *Neuron*, *89*(2), 384–397. https://doi.org/10.1016/j.neuron.2015.12.018

Micheli, A. (2011). En torno a los primeros estudios de electrofisiología. *Archivos de Cardiología de México*, *81*, 337–342.

Mojon-Azzi, S. M., Sousa-Poza, A., & Mojon, D. S. (2010). Impact of Low Vision on Employment. *Ophthalmologica*, *224*(6), 381–388. https://doi.org/10.1159/000316688

Mongillo, G., Barak, O., & Tsodyks, M. (2008). Synaptic Theory of Working Memory. *Science*, *319*(5869), 1543–1546. https://doi.org/10.1126/science.1150769

Montero-Odasso, M., Van Der Velde, N., Alexander, N. B., Becker, C., Blain, H., Camicioli, R., Close, J., Duan, L., Duque, G., Ganz, D. A., Gómez, F., Hausdorff, J. M., Hogan, D. B., Jauregui, J. R., Kenny, R. A., Lipsitz, L. A., Logan, P. A., Lord, S. R., Mallet, L., … the Task Force on Global Guidelines for Falls in Older Adults. (2021). New horizons in falls prevention and management for older adults: A global initiative. *Age and Ageing*, *50*(5), 1499–1507. https://doi.org/10.1093/ageing/afab076

Mountcastle, V. B. (1957). MODALITY AND TOPOGRAPHIC PROPERTIES OF SINGLE NEURONS OF CAT'S SOMATIC SENSORY CORTEX. *Journal of Neurophysiology*, *20*(4), 408–434. https://doi.org/10.1152/jn.1957.20.4.408

Murray, M. M., Thelen, A., Thut, G., Romei, V., Martuzzi, R., & Matusz, P. J. (2016). The multisensory function of the human primary visual cortex. *Neuropsychologia*, *83*, 161–169. https://doi.org/10.1016/j.neuropsychologia.2015.08.011

Nys, J., Aerts, J., Ytebrouck, E., Vreysen, S., Laeremans, A., & Arckens, L. (2014). The cross-modal aspect of mouse visual cortex plasticity induced by monocular enucleation is age dependent. *Journal of Comparative Neurology*, *522*(4), 950–970. https://doi.org/10.1002/cne.23455

Nys, J., Scheyltjens, I., & Arckens, L. (2015). Visual system plasticity in mammals: The story of monocular enucleation-induced vision loss. *Frontiers in Systems Neuroscience*, *9*. https://doi.org/10.3389/fnsys.2015.00060

O'Connor, J. P. (2003). Thomas Willis and the background to Cerebri Anatome. *Journal of the Royal Society of Medicine*, *96*(3), 139–143.

O'Kusky, J., & Colonnier, M. (1982). A laminar analysis of the number of neurons, glia, and synapses in the visual cortex (area 17) of adult macaque monkeys. *Journal of Comparative Neurology*, *210*(3), 278–290. https://doi.org/10.1002/cne.902100307

Openshaw, A., Branham, K., & Heckenlively, J. (2008). *Understanding Retinitis Pigmentosa*. Kellogg Eye Center, University of Michigan.

Orphanet. (2024). *Stargardt disease*. INSERM – Institut National de la Santé et de la Recherche Médicale. https://www.orpha.net/en/disease/detail/827

Osaba, M., Doro, J., Liberal, M., Lagunas, J., Kuo, I. C., & Reviglio, V. E. (2019). Relationship Between Legal Blindness and Depression. *Med Hypothesis Discov Innov Ophthalmol*, *8*(4), 306–311.

Ostrovsky, Y., Andalman, A., & Sinha, P. (2006). Vision Following Extended Congenital Blindness. *Psychological Science*, *17*(12), 1009–1014. https://doi.org/10.1111/j.1467-9280.2006.01827.x

Oude Lohuis, M. N., Marchesi, P., Olcese, U., & Pennartz, C. M. A. (2024). Triple dissociation of visual, auditory and motor processing in mouse primary visual cortex. *Nature Neuroscience*, *27*(4), 758–771. https://doi.org/10.1038/s41593-023-01564-5

Pahor, A., & Jaušovec, N. (2018). The Effects of Theta and Gamma tACS on Working Memory and Electrophysiology. *Frontiers in Human Neuroscience*, *11*, 651. https://doi.org/10.3389/fnhum.2017.00651

Palanker, D., Le Mer, Y., Mohand-Said, S., Muqit, M., & Sahel, J. A. (2020). Photovoltaic Restoration of Central Vision in Atrophic Age-Related Macular Degeneration. *Ophthalmology*, *127*(8), 1097–1104. https://doi.org/10.1016/j.ophtha.2020.02.024

Parker, M. A., Erker, L. R., Audo, I., Choi, D., Mohand-Said, S., Sestakauskas, K., Benoit, P., Appelqvist, T., Krahmer, M., Ségaut-Prévost, C., Lujan, B. J., Faridi, A., Chegarnov, E. N., Steinkamp, P. N., Ku, C., Da Palma, M. M., Barale, P.-O., Ayelo-Scheer, S., Lauer, A., … Yang, P. (2022). Three-Year Safety Results of SAR422459 (EIAV-ABCA4) Gene Therapy in Patients With ABCA4-Associated Stargardt Disease: An Open-Label Dose-Escalation Phase I/IIa Clinical Trial, Cohorts 1-5. *American Journal of Ophthalmology*, *240*, 285–301. https://doi.org/10.1016/j.ajo.2022.02.013

Patino, C. M., McKean-Cowdin, R., Azen, S. P., Allison, J. C., Choudhury, F., & Varma, R. (2010). Central and Peripheral Visual Impairment and the Risk of Falls and Falls with Injury. *Ophthalmology*, *117*(2), 199-206.e1. https://doi.org/10.1016/j.ophtha.2009.06.063

Pesaran, B., Vinck, M., Einevoll, G. T., Sirota, A., Fries, P., Siegel, M., Truccolo, W., Schroeder, C. E., & Srinivasan, R. (2018). Investigating large-scale brain dynamics using field potential recordings: Analysis and interpretation. *Nature Neuroscience*, *21*(7), 903–919. https://doi.org/10.1038/s41593-018-0171-8

Peters, A., & Sethares, C. (1991). Organization of pyramidal neurons in area 17 of monkey visual cortex. *Journal of Comparative Neurology*, *306*(1), 1–23. https://doi.org/10.1002/cne.903060102

Pfurtscheller, G., & Lopes Da Silva, F. H. (1999). Event-related EEG/MEG synchronization and desynchronization: Basic principles. *Clinical Neurophysiology*, *110*(11), 1842–1857. https://doi.org/10.1016/S1388-2457(99)00141-8

Porciatti, V., Pizzorusso, T., & Maffei, L. (2002). Electrophysiology of the postreceptoral visual pathway in mice. *Documenta Ophthalmologica. Advances in Ophthalmology*, *104*(1), 69–82. https://doi.org/10.1023/a:1014463212001

Purola, P. K. M., Nättinen, J. E., Ojamo, M. U. I., Koskinen, S. V. P., Rissanen, H. A., Sainio, P. R. J., & Uusitalo, H. M. T. (2021). Prevalence and 11-year incidence of common eye diseases and their relation to health-related quality of life, mental health, and visual

impairment. *Quality of Life Research*, *30*(8), 2311–2327. https://doi.org/10.1007/s11136-021-02817-1

Que, L., Zhu, Q., Jiang, C., & Lu, Q. (2025). An analysis of the global, regional, and national burden of blindness and vision loss between 1990 and 2021: The findings of the Global Burden of Disease Study 2021. *Frontiers in Public Health*, *13*, 1560449. https://doi.org/10.3389/fpubh.2025.1560449

Rey, H. G., Pedreira, C., & Quian Quiroga, R. (2015). Past, present and future of spike sorting techniques. *Brain Research Bulletin*, *119*, 106–117. https://doi.org/10.1016/j.brainresbull.2015.04.007

Rizzi, M. (2011). Historia de los implantes cocleares. *Federación Argentina de Sociedades de Otorrinolaringología*, *5*, 8–11.

Rodríguez, G., Chakraborty, D., Schrode, K. M., Saha, R., Uribe, I., Lauer, A. M., & Lee, H.-K. (2018). Cross-Modal Reinstatement of Thalamocortical Plasticity Accelerates Ocular Dominance Plasticity in Adult Mice. *Cell Reports*, *24*(13), 3433-3440.e4. https://doi.org/10.1016/j.celrep.2018.08.072

Roelfsema, P. R., König, P., Engel, A. K., Sireteanu, R., & Singer, W. (1994). Reduced Synchronization in the Visual Cortex of Cats with Strabismic Amblyopia. *European Journal of Neuroscience*, *6*(11), 1645–1655. https://doi.org/10.1111/j.1460-9568.1994.tb00556.x

Rokem, A., & Silver, M. A. (2010). Cholinergic Enhancement Augments Magnitude and Specificity of Visual Perceptual Learning in Healthy Humans. *Current Biology*, *20*(19), 1723–1728. https://doi.org/10.1016/j.cub.2010.08.027

Rosburg, T. (2005). Subdural recordings of the mismatch negativity (MMN) in patients with focal epilepsy. *Brain*, *128*(4), 819–828. https://doi.org/10.1093/brain/awh442

Rosenfeld, P. J., Brown, D. M., Heier, J. S., Boyer, D. S., Kaiser, P. K., Chung, C. Y., & Kim, R. Y. (2006). Ranibizumab for Neovascular Age-Related Macular Degeneration. *The New England Journal of Medicine*, *355*(14), 1419–1431.

Rossi, S., Tecchio, F., Pasqualetti, P., Ulivelli, M., Pizzella, V., Romani, G. L., Passero, S., Battistini, N., & Rossini, P. M. (2002). Somatosensory processing during movement observation in humans. *Clinical Neurophysiology*, *113*(1), 16–24. https://doi.org/10.1016/S1388-2457(01)00725-8

Rossi Sebastiano, A., Poles, K., Gualtiero, S., Romeo, M., Galigani, M., Bruno, V., Fossataro, C., & Garbarini, F. (2024). Balancing the Senses: Electrophysiological Responses Reveal the Interplay between Somatosensory and Visual Processing During Body-Related Multisensory Conflict. *The Journal of Neuroscience*, *44*(19), e1397232024. https://doi.org/10.1523/JNEUROSCI.1397-23.2024

Rozo, J. A., Martínez-Gallego, I., & Rodríguez-Moreno, A. (2024). Cajal, the neuronal theory and the idea of brain plasticity. *Frontiers in Neuroanatomy*, *18*, 1331666. https://doi.org/10.3389/fnana.2024.1331666

Rugg, M. D., & Coles, M. G. H. (1996). *Electrophysiology of Mind*. Oxford University Press. https://doi.org/10.1093/acprof:oso/9780198524168.001.0001

Russell, S., Bennett, J., Wellman, J. A., Chung, D. C., Yu, Z.-F., Tillman, A., Wittes, J., Pappas, J., Elci, O., McCague, S., Cross, D., Marshall, K. A., Walshire, J., Kehoe, T. L., Reichert, H., Davis, M., Raffini, L., George, L. A., Hudson, F. P., … Maguire, A. M. (2017). Efficacy and safety of voretigene neparvovec (AAV2-hRPE65v2) in patients with RPE65 -mediated inherited retinal dystrophy: A randomised, controlled, open-label, phase 3 trial. *The Lancet*, *390*(10097), 849–860. https://doi.org/10.1016/S0140-6736(17)31868-8

Sadato, N., Pascual-Leone, A., Grafman, J., Ibañez, V., Deiber, M.-P., Dold, G., & Hallett, M. (1996). Activation of the primary visual cortex by Braille reading in blind subjects. *Nature*, *380*(6574), 526–528. https://doi.org/10.1038/380526a0

Sahel, J.-A., Boulanger-Scemama, E., Pagot, C., Arleo, A., Galluppi, F., Martel, J. N., Esposti, S. D., Delaux, A., De Saint Aubert, J.-B., De Montleau, C., Gutman, E., Audo, I., Duebel, J., Picaud, S., Dalkara, D., Blouin, L., Taiel, M., & Roska, B. (2021). Partial recovery of visual function in a blind patient after optogenetic therapy. *Nature Medicine*, *27*(7), 1223–1229. https://doi.org/10.1038/s41591-021-01351-4

Sahel, J.-A., Marazova, K., & Audo, I. (2015). Clinical Characteristics and Current Therapies for Inherited Retinal Degenerations. *Cold Spring Harbor Perspectives in Medicine*, *5*(2), a017111–a017111. https://doi.org/10.1101/cshperspect.a017111

Sánchez-León, C. A., Campos, G. S.-G., Fernández, M., Medina, J. F., & Márquez-Ruiz, J. (2025). Somatodendritic orientation determines tDCS-induced neuromodulation of Purkinje cell activity in awake mice. *bioRxiv*. https://doi.org/10.1101/2023.02.18.529047

Sánchez-León, C. A., Sánchez-Garrido Campos, G., Fernández, M., Sánchez-López, Á., Medina, J. F., & Márquez-Ruiz, J. (2025). Somatodendritic orientation determines tDCS-induced neuromodulation of Purkinje cell activity in awake mice. *eLife*, *13*, RP100941. https://doi.org/10.7554/eLife.100941

Schepers, I. M., Hipp, J. F., Schneider, T. R., Röder, B., & Engel, A. K. (2012). Functionally specific oscillatory activity correlates between visual and auditory cortex in the blind. *Brain*, *135*(3), 922–934. https://doi.org/10.1093/brain/aws014

Schmolesky, M. (2005). The Primary Visual Cortex. *Webvision: The Organization of the Retina and Visual System [Internet]*, 1089–1122.

Schroeder, C. E., & Foxe, J. (2005). Multisensory contributions to low-level, 'unisensory' processing. *Current Opinion in Neurobiology*, *15*(4), 454–458. https://doi.org/10.1016/j.conb.2005.06.008

Schwartz, S. D., Regillo, C. D., Lam, B. L., Eliott, D., Rosenfeld, P. J., Gregori, N. Z., Hubschman, J.-P., Davis, J. L., Heilwell, G., Spirn, M., Maguire, J., Gay, R., Bateman, J., Ostrick, R. M., Morris, D., Vincent, M., Anglade, E., Del Priore, L. V., & Lanza, R. (2015). Human embryonic stem cell-derived retinal pigment epithelium in patients with age-related macular degeneration and Stargardt's macular dystrophy: Follow-up of two open-label phase 1/2 studies. *The Lancet*, *385*(9967), 509–516. https://doi.org/10.1016/S0140-6736(14)61376-3

Schwiening, C. J. (2012). A brief historical perspective: Hodgkin and Huxley. *The Journal of Physiology*, *590*(11), 2571–2575. https://doi.org/10.1113/jphysiol.2012.230458

Sczesny-Kaiser, M., Beckhaus, K., Dinse, H. R., Schwenkreis, P., Tegenthoff, M., & Höffken, O. (2016). Repetitive Transcranial Direct Current Stimulation Induced Excitability Changes of Primary Visual Cortex and Visual Learning Effects—A Pilot Study. *Frontiers in Behavioral Neuroscience*, *10*. https://doi.org/10.3389/fnbeh.2016.00116

Sedley, W., Gander, P. E., Kumar, S., Kovach, C. K., Oya, H., Kawasaki, H., Howard, M. A., & Griffiths, T. D. (2016). Neural signatures of perceptual inference. *eLife*, *5*, e11476. https://doi.org/10.7554/eLife.11476

Shaikh, N., Kumar, V., Ramachandran, A., Venkatesh, R., Tekchandani, U., Tyagi, M., Jayadev, C., Dogra, M., & Chawla, R. (2024). Vitrectomy for cases of diabetic retinopathy. *Indian Journal of Ophthalmology*, *72*(12), 1704–1713. https://doi.org/10.4103/IJO.IJO_30_24

Shi, W., He, L., Lv, B., Li, L., & Wu, T. (2020). Evaluating the Acute Effect of Stereoscopic Recovery by Dichoptic Stimulation Using Electroencephalogram. *Computational and Mathematical Methods in Medicine*, *2020*, 1–7. https://doi.org/10.1155/2020/9497369

Sieben, K., Röder, B., & Hanganu-Opatz, I. L. (2013). Oscillatory Entrainment of Primary Somatosensory Cortex Encodes Visual Control of Tactile Processing. *The Journal of Neuroscience*, *33*(13), 5736–5749. https://doi.org/10.1523/JNEUROSCI.4432-12.2013

Singer, W. (2017). Synchronous Oscillations and Memory Formation ☆. In *Learning and Memory: A Comprehensive Reference* (pp. 591–597). Elsevier. https://doi.org/10.1016/B978-0-12-809324-5.21027-4

Siu, C., & Murphy, K. (2018). The development of human visual cortex and clinical implications. *Eye and Brain*, *Volume 10*, 25–36. https://doi.org/10.2147/EB.S130893

Snoek, L., Miletić, S., & Scholte, H. S. (2019). How to control for confounds in decoding analyses of neuroimaging data. *NeuroImage*, *184*, 741–760. https://doi.org/10.1016/j.neuroimage.2018.09.074

Stargardt, K. (1909). Über familiäre, progressive Degeneration in der Maculagegend des Auges. *Graefe's Archiv für Ophthalmologie*, *LXXI*(3), 534–550. https://doi.org/10.1007/bf01961301

Stark, E., & Abeles, M. (2007). Predicting Movement from Multiunit Activity. *The Journal of Neuroscience*, *27*(31), 8387–8394. https://doi.org/10.1523/JNEUROSCI.1321-07.2007

Stein, B. E., & Stanford, T. R. (2008). Multisensory integration: Current issues from the perspective of the single neuron. *Nature Reviews Neuroscience*, *9*(4), 255–266. https://doi.org/10.1038/nrn2331

Stevenson, R. A., Ghose, D., Fister, J. K., Sarko, D. K., Altieri, N. A., Nidiffer, A. R., Kurela, L. R., Siemann, J. K., James, T. W., & Wallace, M. T. (2014). Identifying and Quantifying Multisensory Integration: A Tutorial Review. *Brain Topography*, *27*(6), 707–730. https://doi.org/10.1007/s10548-014-0365-7

Striem-Amit, E., Cohen, L., Dehaene, S., & Amedi, A. (2012). Reading with Sounds: Sensory Substitution Selectively Activates the Visual Word Form Area in the Blind. *Neuron*, *76*(3), 640–652. https://doi.org/10.1016/j.neuron.2012.08.026

Stryker, M. P. (2014). A Neural Circuit That Controls Cortical State, Plasticity, and the Gain of Sensory Responses in Mouse. *Cold Spring Harbor Symposia on Quantitative Biology*, *79*, 1–9. https://doi.org/10.1101/sqb.2014.79.024927

Sur, S., & Sinha, V. (2009a). Event-related potential: An overview. *Industrial Psychiatry Journal*, *18*(1), 70. https://doi.org/10.4103/0972-6748.57865

Sur, S., & Sinha, V. (2009b). Event-related potential: An overview. *Industrial Psychiatry Journal*, *18*(1), 70. https://doi.org/10.4103/0972-6748.57865

Taberner, A. M., & Liberman, M. C. (2005). Response Properties of Single Auditory Nerve Fibers in the Mouse. *Journal of Neurophysiology*, *93*(1), 557–569. https://doi.org/10.1152/jn.00574.2004

Tallon-Baudry, C. (1999). Oscillatory gamma activity in humans and its role in object representation. *Trends in Cognitive Sciences*, *3*(4), 151–162. https://doi.org/10.1016/S1364-6613(99)01299-1

Tallon-Baudry, C., Bertrand, O., Delpuech, C., & Pernier, J. (1996). Stimulus Specificity of Phase-Locked and Non-Phase-Locked 40 Hz Visual Responses in Human. *The Journal*

of Neuroscience, *16*(13), 4240–4249. https://doi.org/10.1523/JNEUROSCI.16-13-04240.1996

Teichert, M., Isstas, M., Liebmann, L., Hübner, C. A., Wieske, F., Winter, C., Lehmann, K., & Bolz, J. (2019). Visual deprivation independent shift of ocular dominance induced by cross-modal plasticity. *PLOS ONE*, *14*(3), e0213616. https://doi.org/10.1371/journal.pone.0213616

Teleńczuk, B., Dehghani, N., Le Van Quyen, M., Cash, S. S., Halgren, E., Hatsopoulos, N. G., & Destexhe, A. (2017). Local field potentials primarily reflect inhibitory neuron activity in human and monkey cortex. *Scientific Reports*, *7*(1), 40211. https://doi.org/10.1038/srep40211

The Diabetic Retinopathy Vitrectomy Study Research Group. (1985). Early Vitrectomy for Severe Vitreous Hemorrhage in Diabetic Retinopathy: Two-Year Results of a Randomized Trial Diabetic Retinopathy Vitrectomy Study Report 2. *Archives of Ophthalmology*, *103*(11), 1644–1652. https://doi.org/10.1001/archopht.1985.01050110038020

Thorne, J. D., De Vos, M., Viola, F. C., & Debener, S. (2011). Cross-Modal Phase Reset Predicts Auditory Task Performance in Humans. *The Journal of Neuroscience*, *31*(10), 3853–3861. https://doi.org/10.1523/JNEUROSCI.6176-10.2011

Toscani, M., Marzi, T., Righi, S., Viggiano, M. P., & Baldassi, S. (2010). Alpha waves: A neural signature of visual suppression. *Experimental Brain Research*, *207*(3–4), 213–219. https://doi.org/10.1007/s00221-010-2444-7

Triarhou, L. C. (2021). Pre-Brodmann pioneers of cortical cytoarchitectonics I: Theodor Meynert, Vladimir Betz and William Bevan-Lewis. *Brain Structure and Function*, *226*(1), 49–67. https://doi.org/10.1007/s00429-020-02168-6

Tseng, V. L., Yu, F., Lum, F., & Coleman, A. L. (2016). Cataract Surgery and Mortality in the United States Medicare Population. *Ophthalmology*, *123*(5), 1019–1026. https://doi.org/10.1016/j.ophtha.2015.12.033

Van Brussel, L., Gerits, A., & Arckens, L. (2009). Identification and localization of functional subdivisions in the visual cortex of the adult mouse. *Journal of Comparative Neurology*, *514*(1), 107–116. https://doi.org/10.1002/cne.21994

Van Brussel, L., Gerits, A., & Arckens, L. (2011). Evidence for Cross-Modal Plasticity in Adult Mouse Visual Cortex Following Monocular Enucleation. *Cerebral Cortex*, *21*(9), 2133–2146. https://doi.org/10.1093/cercor/bhq286

Van Heusden, F. C., Van Nifterick, A. M., Souza, B. C., França, A. S. C., Nauta, I. M., Stam, C. J., Scheltens, P., Smit, A. B., Gouw, A. A., & Van Kesteren, R. E. (2023). Neurophysiological alterations in mice and humans carrying mutations in APP and PSEN1 genes. *Alzheimer's Research & Therapy*, *15*(1), 142. https://doi.org/10.1186/s13195-023-01287-6

Van Kerkoerle, T., Self, M. W., Dagnino, B., Gariel-Mathis, M.-A., Poort, J., Van Der Togt, C., & Roelfsema, P. R. (2014). Alpha and gamma oscillations characterize feedback and feedforward processing in monkey visual cortex. *Proceedings of the National Academy of Sciences*, *111*(40), 14332–14341. https://doi.org/10.1073/pnas.1402773111

Van Middendorp, J. J., Sanchez, G. M., & Burridge, A. L. (2010). The Edwin Smith papyrus: A clinical reappraisal of the oldest known document on spinal injuries. *European Spine Journal*, *19*(11), 1815–1823. https://doi.org/10.1007/s00586-010-1523-6

Van Munster, E. P. J., Van Der Aa, H. P. A., Verstraten, P., & Van Nispen, R. M. A. (2021). Barriers and facilitators to recognize and discuss depression and anxiety experienced by adults with vision impairment or blindness: A qualitative study. *BMC Health Services Research*, *21*(1), 749. https://doi.org/10.1186/s12913-021-06682-z

van Atteveldt, N., Murray, M. M., Thut, G., & Schroeder, C. E. (2014). Multisensory Integration: Flexible Use of General Operations. *Neuron*, *81*(6), 1240–1253. https://doi.org/10.1016/j.neuron.2014.02.044

Vanneau, T., Quiquempoix, M., Foxe, J. J., & Molholm, S. (2024). *Neural Mechanisms of Intersensory Switching: Evidence for Delayed Sensory Processing and Increased Cognitive Effort*. Neuroscience. https://doi.org/10.1101/2024.11.26.625211

Vasalauskaite, A., Morgan, J. E., & Sengpiel, F. (2019). Plasticity in Adult Mouse Visual Cortex Following Optic Nerve Injury. *Cerebral Cortex*, *29*(4), 1767–1777. https://doi.org/10.1093/cercor/bhy347

Verkhratsky, A., Krishtal, O. A., & Petersen, O. H. (2006). From Galvani to patch clamp: The development of electrophysiology. *Pflügers Archiv - European Journal of Physiology*, *453*(3), 233–247. https://doi.org/10.1007/s00424-006-0169-z

Vision Loss Expert Group of the Global Burden of Disease Study, Bourne, R. R. A., Jonas, J. B., Friedman, D., Nangia, V., Bron, A., Tapply, I., Fernandes, A. G., Cicinelli, M. V., Arrigo, A., Leveziel, N., Resnikoff, S., Taylor, H. R., Sedighi, T., Bikbov, M. M., Braithwaite, T., Cheng, C.-Y., Congdon, N., Del Monte, M. A., … Steinmetz, J. D. (2024). Global estimates on the number of people blind or visually impaired by glaucoma: A meta-analysis from 2000 to 2020. *Eye*, *38*(11), 2036–2046. https://doi.org/10.1038/s41433-024-02995-5

Vision Loss Expert Group of the Global Burden of Disease Study, Curran, K., Peto, T., Jonas, J. B., Friedman, D., Kim, J. E., Leasher, J., Tapply, I., Fernandes, A. G., Cicinelli, M. V., Arrigo, A., Leveziel, N., Resnikoff, S., Taylor, H. R., Sedighi, T., Flaxman, S., Bikbov, M. M., Braithwaite, T., Bron, A., … Zheng, P. (2024). Global estimates on the number of people blind or visually impaired by diabetic retinopathy: A meta-analysis from 2000 to 2020. *Eye*, *38*(11), 2047–2057. https://doi.org/10.1038/s41433-024-03101-5

Vision Loss Expert Group of the Global Burden of Disease Study, Furtado, J. M., Jonas, J. B., Tapply, I., Fernandes, A. G., Cicinelli, M. V., Arrigo, A., Leveziel, N., Resnikoff, S., Taylor, H. R., Sedighi, T., Flaxman, S., Battaglia Parodi, M., Bikbov, M. M., Braithwaite, T., Bron, A., Cheng, C.-Y., Congdon, N., Del Monte, M. A., … Bourne, R. R. A. (2024). Global estimates on the number of people blind or visually impaired by age-related macular degeneration: A meta-analysis from 2000 to 2020. *Eye*, *38*(11), 2070–2082. https://doi.org/10.1038/s41433-024-03050-z

Vision Loss Expert Group of the Global Burden of Disease Study, Little, J.-A., Congdon, N. G., Resnikoff, S., Braithwaite, T., Leasher, J., Naidoo, K., Fricke, T., Tapply, I., Fernandes,

A. G., Cicinelli, M. V., Arrigo, A., Leveziel, N., Taylor, H. R., Sedighi, T., Flaxman, S., Parodi, M. B., Bikbov, M. M., Bron, A., … Bourne, R. (2024). Global estimates on the number of people blind or visually impaired by Uncorrected Refractive Error: A meta-analysis from 2000 to 2020. *Eye*, *38*(11), 2083–2101. https://doi.org/10.1038/s41433-024-03106-0

Vision Loss Expert Group of the Global Burden of Disease Study & the GBD 2019 Blindness and Vision Impairment Collaborators. (2025). Prevalence of Vision Loss in High-Income Countries and in Eastern and Central Europe in 2020: Magnitude and Temporal Trends. *Ophthalmic Epidemiology*, 1–14. https://doi.org/10.1080/09286586.2025.2486461

Wai Wong, C., Yeo, I., & Cheung, G. (2018, February 1). Management of Submacular Hemorrhage. *EyeNet Magazine*, *Ophthalmic pearls*, 35–37.

Wang, Y., Celebrini, S., Trotter, Y., & Barone, P. (2008). Visuo-auditory interactions in the primary visual cortex of the behaving monkey: Electrophysiological evidence. *BMC Neuroscience*, *9*(1), 79. https://doi.org/10.1186/1471-2202-9-79

Weiler, S., Rahmati, V., Isstas, M., Wutke, J., Stark, A. W., Franke, C., Graf, J., Geis, C., Witte, O. W., Hübener, M., Bolz, J., Margrie, T. W., Holthoff, K., & Teichert, M. (2024). A primary sensory cortical interareal feedforward inhibitory circuit for tacto-visual integration. *Nature Communications*, *15*(1), 3081. https://doi.org/10.1038/s41467-024-47459-2

Welp, A., Woodbury, R., & McCoy, M. (2016). Chapter 3: The Impact of Vision Loss. In *Making Eye Health a Population Health Imperative: Vision for Tomorrow* (pp. 135–154). https://www.ncbi.nlm.nih.gov/books/NBK385157/ doi: 10.17226/23471

Werth, R. (2006). Visual functions without the occipital lobe or after cerebral hemispherectomy in infancy. *European Journal of Neuroscience*, *24*(10), 2932–2944. https://doi.org/10.1111/j.1460-9568.2006.05171.x

Wittenberg, G. F., Werhahn, K. J., Wassermann, E. M., Herscovitch, P., & Cohen, L. G. (2004). Functional connectivity between somatosensory and visual cortex in early blind humans.

European Journal of Neuroscience, *20*(7), 1923–1927. https://doi.org/10.1111/j.1460-9568.2004.03630.x

Womelsdorf, T., & Hoffman, K. (2018). Latent Connectivity: Neuronal Oscillations Can Be Leveraged for Transient Plasticity. *Current Biology*, *28*(16), R879–R882. https://doi.org/10.1016/j.cub.2018.06.073

Womelsdorf, T., Valiante, T. A., Sahin, N. T., Miller, K. J., & Tiesinga, P. (2014). Dynamic circuit motifs underlying rhythmic gain control, gating and integration. *Nature Neuroscience*, *17*(8), 1031–1039. https://doi.org/10.1038/nn.3764

World Health Organization. (2019). *World report on vision*. World Health Organization. https://iris.who.int/handle/10665/328717

Wróbel, A. (2000). Beta activity: A carrier for visual attention. *Acta Neurobiologiae Experimentalis*, *60*(2), 247–260. https://doi.org/10.55782/ane-2000-1344

Wu, C., Gaier, E. D., Nihalani, B. R., Whitecross, S., Hensch, T. K., & Hunter, D. G. (2023). Durable recovery from amblyopia with donepezil. *Scientific Reports*, *13*(1), 10161. https://doi.org/10.1038/s41598-023-34891-5

Wundari, B. G., Fujita, I., & Ban, H. (2025). Human and artificial visual systems share a computational principle for transforming binocular disparity into depth representation. *Communications Biology*, *8*(1), 1042. https://doi.org/10.1038/s42003-025-08474-1

Xia, C., Li, J., Yan, R., Su, W., & Liu, Y. (2023). Contribution of inter-trial phase coherence at theta, alpha, and beta frequencies in auditory change detection. *Frontiers in Neuroscience*, *17*, 1224479. https://doi.org/10.3389/fnins.2023.1224479

Xu, X., Hanganu-Opatz, I. L., & Bieler, M. (2020). Cross-Talk of Low-Level Sensory and High-Level Cognitive Processing: Development, Mechanisms, and Relevance for Cross-Modal Abilities of the Brain. *Frontiers in Neurorobotics*, *14*, 7. https://doi.org/10.3389/fnbot.2020.00007

Yamada, Y., & Sumiyoshi, T. (2021). Neurobiological Mechanisms of Transcranial Direct Current Stimulation for Psychiatric Disorders; Neurophysiological, Chemical, and

Anatomical Considerations. *Frontiers in Human Neuroscience*, *15*, 631838. https://doi.org/10.3389/fnhum.2021.631838

Zaehle, T., Rach, S., & Herrmann, C. S. (2010). Transcranial Alternating Current Stimulation Enhances Individual Alpha Activity in Human EEG. *PLoS ONE*, *5*(11), e13766. https://doi.org/10.1371/journal.pone.0013766

Zampieri, F., ElMaghawry, M., Zanatta, A., & Thiene, G. (2015). Andreas Vesalius: Celebrating 500 years of dissecting nature. *Global Cardiology Science and Practice*, *2015*(5), 66. https://doi.org/10.5339/gcsp.2015.66

Zanos, S., Rembado, I., Chen, D., & Fetz, E. E. (2018). Phase-Locked Stimulation during Cortical Beta Oscillations Produces Bidirectional Synaptic Plasticity in Awake Monkeys. *Current Biology*, *28*(16), 2515-2526.e4. https://doi.org/10.1016/j.cub.2018.07.009

Zhang, A., & Zador, A. M. (2023). Neurons in the primary visual cortex of freely moving rats encode both sensory and non-sensory task variables. *PLOS Biology*, *21*(12), e3002384. https://doi.org/10.1371/journal.pbio.3002384

Zilles, K. (2018). Brodmann: A pioneer of human brain mapping—his impact on concepts of cortical organization. *Brain*, *141*(11), 3262–3278. https://doi.org/10.1093/brain/awy273

Zold, C. L., & Hussain Shuler, M. G. (2015). Theta Oscillations in Visual Cortex Emerge with Experience to Convey Expected Reward Time and Experienced Reward Rate. *Journal of Neuroscience*, *35*(26), 9603–9614. https://doi.org/10.1523/JNEUROSCI.0296-15.2015

Appendix 1

Field	Value		Value	
Method	Least squares (additive OLS)		Least squares (additive OLS)	
Dependent variable	ITC (normalized units)		ERSP (dB, normalized)	
Mode	NORMALIZADO		NORMALIZADO	
Parameters	Group: control; Stimulation: visual		Group: control; Stimulation: visual	
Parameter				
Intercept (μ̂)	0,567927		2,86454	
Group: control (α̂_control)	0		0	
Group: dnpz (α̂_dnpz)	-0,039069		-1,21185	
Group: enuclea (α̂_enuclea)	0,0243459		0,302984	
Group: tdcs (α̂_tdcs)	-0,0296586		-1,38866	
Group: tdcs + dnpz (α̂_tdcs+dnpz)	-0,0627235		-1,56633	
Stimulation: auditory (γ̂_auditory)	-0,0287562		0,886131	
Stimulation: somatosensory (γ̂_somatosensory)	-0,0236336		0,648789	
Stimulation: visual (γ̂_visual)	0		0	
Model statistics				
Statistic				
R	0,244		0,359	
R^2	0,06		0,129	
Adjusted R^2	0,059		0,129	
F-statistic	189,98		743,798	
p-value (F-stat)	2,96E-274		0	
RMSE	0,1514		2,174	
Akaike (AIC)	-19694,84		154284,66	
Schwarz (BIC)	-19631,22		154352,4	
ANOVA (Type II)				
Term	**sum_sq**	**PR(>F)**	**sum_sq**	**PR(>F)**
Group (Type II)	28,009715	1,1284E-254	20594,66566	0
Stimulation (Type II)	2,033754	5,88674E-20	3671,895087	1,4045E-167
Residual	481,184464		166028,1983	

Table A1. OLS summary with two columns (ITC and ERSP), including metadata (method, dependent variable, mode); parameters (intercept and group/stimulation-modality effects); model references (Control group for Group and Visual stimulation for Stimulation type); and, finally, model statistics (R, R^2, adjusted R^2, F, p(F), RMSE, AIC, BIC) and Type II ANOVA results with sum_sq and PR(>F) for Group, Stimulation, and Residual.

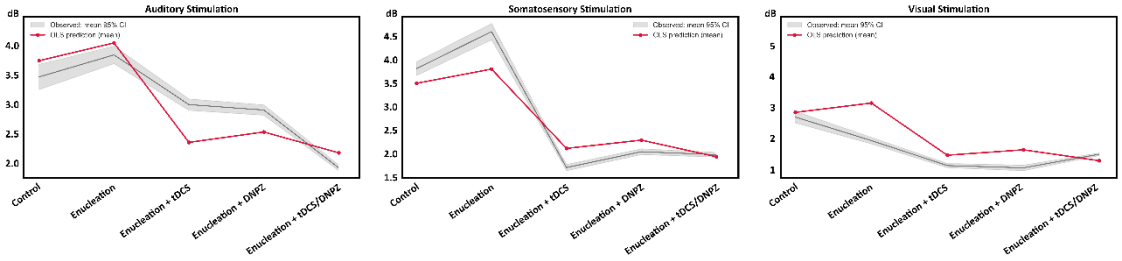

https://bit.ly/49BZK4C

Figure A1. Comparison by modality (panels: Auditory, Somatosensory, Visual) between the mean ERSP observed per group (grey band: mean ± 95% CI) and the prediction of the OLS additive model (red line; mean). Axes: X = groups (in the order: Control, Enucleation, Enucleation + tDCS, Enucleation + DNPZ,

Enucleation + tDCS/DNPZ); Y = dB. Model references: Group = Control; Stimulation = Visual. Below, a link and a QR code are included to view the 3D representation of this data.

For ERSP values, the global fit holds, as the F-test yielded F = 743.798 with p ≈ 0, so the set of main effects of Group and Stimulation Modality explains variation relative to the null model. The overall explanatory power is moderate (R = 0.359, R^2 = 0.129; adjusted R^2 = 0.129), indicating that the additive component captures an appreciable, though not dominant, fraction of the variability across conditions.

The prediction error is RMSE = 2.174 dB. Given that several Group coefficients are of the order of 0.6-1.6 dB in magnitude, the error is comparable to the effect size of some levels; therefore, the additive fit is useful for removing global offsets but leaves a substantial remainder that justifies analysing the residuals by band.

The coefficients describe clear average shifts: relative to control × ipsilateral visual stimulation ($\hat{\mu}$= 2.8645 dB), the pattern by Group is enucleation > control > enucleation + dnpz > enucleation + tdcs > enucleation + tdcs/dnpz, and by Modality there is an increase with auditory (+0.8861 dB) and somatosensory (+0.6488 dB) relative to visual; in conclusion, there are systematic Group and Stimulation Modality offsets in ERSP.

Type II ANOVA confirms that both factors contribute significantly (Group: SS = 20594.67, p = 0; Modality: SS = 3671.90, p = 1.40 × 10^−167). In terms of proportion of the total sum of squares, Group explains ≈10.8%, Modality ≈1.93%, and the Residual ≈87.25%. Thus, the principal weight within the additive effects is provided by Group; Modality also contributes, but to a lesser extent.

With respect to assumptions, prior diagnostics showed non-normality (significant Jarque-Bera) and heteroscedasticity (significant Breusch-Pagan), and positive autocorrelation (Durbin-Watson = 0.54 < 2); therefore, the classical assumptions are not fully met. However, since OLS is employed here for residualisation rather than for t-tests on coefficients, these violations do not invalidate its use as a pre-adjustment.

With regard to the ERSP values, the additive model fits significantly and captures offsets of moderate size (especially by Group); the substantive remainder left in the residuals supports non-parametric band-wise comparisons.

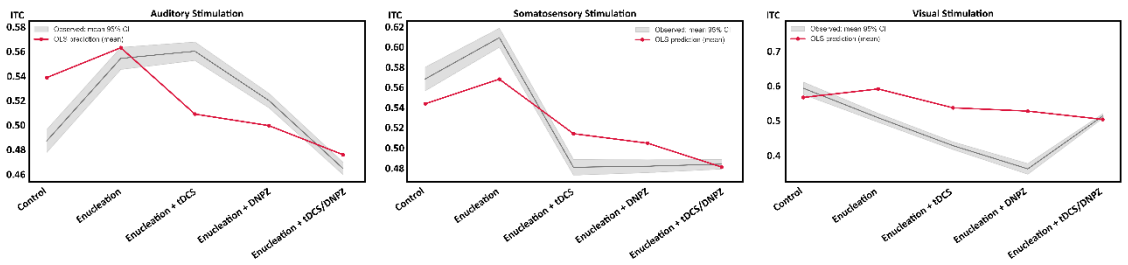

https://bit.ly/4ouxRQO

Figure A2. Comparison by modality (panels: Auditory, Somatosensory, Visual) between the mean ITC observed per group (grey band: mean ± 95% CI) and the prediction of the OLS additive model (red line; mean). Axes: X = groups (in the order: Control, Enucleation, Enucleation + tDCS, Enucleation + DNPZ, Enucleation + tDCS/DNPZ); Y = dB. Model references: Group = Control; Stimulation = Visual. Below, a link and a QR code are included to view the 3D representation of this data.

By contrast, for the ITC values, the global fit also holds. The F-test yielded F = 189.980 with p = 2.96 × 10^−274, so the main effects explain variation relative to the null. The overall explanatory power is low (R = 0.244, R^2 = 0.060; adjusted R^2 = 0.059), indicating that the additive component captures only a small part of the variation in ITC.

The prediction error is RMSE = 0.1514. Most of the Group and Modality coefficients have magnitudes below that value, so the residual noise is larger than many estimated additive effects. Thus, the additive fit in ITC is useful as an offset control, but the additive signal is weak; most of the relevant structure remains in the residuals.

In terms of coefficients, relative to control × visual stimulation ($\hat{\mu}$ = 0.5679), the shifts by Group are small (maximum absolute ≈ 0.063) and by Modality are negative for auditory stimulation (−0.0288) and somatosensory stimulation (−0.0236) relative to visual stimulation. Conclusion: there are small offsets, with the opposite sign to those observed in ERSP for the stimulation modalities.

Type II ANOVA shows that Group (SS = 28.0097, p = 1.13 × 10^−254) and Modality (SS = 2.0338, p = 5.89 × 10^−20) are significant. In proportion, Group explains ≈5.48%, Modality ≈0.40%, and the Residual ≈94.12% of the total. Conclusion: although both factors are statistically detectable, their explanatory weight is small in ITC.

Regarding assumptions, prior diagnostics indicate non-normality and heteroscedasticity (significant Jarque-Bera and Breusch-Pagan) and positive autocorrelation (Durbin-Watson = 0.69 < 2); therefore, the classical assumptions are not met; as in ERSP, this does not invalidate the use of OLS as a residualisation stage.

In conclusion for the ITC values, the additive model fits (significant F), but its explanatory capacity is low; it functions as a control, leaving most of the variation for band-wise analysis on residuals.

Appendix 2

Comportement de l'animal		
	Observation(s)	**Recommandation(s)**
0	Normal	NA
1	Changements mineurs, faible réduction de la réponse ou réponse excessive	Faites un suivi quotidien et contactez le vétérinaire si aucune amélioration n'est constatée dans les 3 à 4 jours.
2	Réactions anormales, mobilité anormale et réduite, vigilance réduite, inactivité	Faites un suivi quotidien et contactez le vétérinaire si aucune amélioration n'est constatée dans les 2 jours
3	Vocalisations spontanées, auto-mutilation très agité ou immobile, réactions violentes ou pas de réactions au toucher	Point limite adapté

Paramètre pertinent en fonction des procédures expérimentales prévues : Chirurgie d'énucleation monoculaire		
	Observation(s)	**Recommandation(s)**
0	Normal	NA
1	Hémorragie légère ou perte de sang minime	NA
2	Signes de douleur modérée, perte de sang modérée ou hémorragie modérée.	Surveillance au cours des premières heures après la chirurgie pour exclure ce point ou augmenter à un score supérieur
3	Signes de douleur sévère, hémorragie continue ou perte de sang importante	Point limite adapté

Paramètre pertinent en fonction des procédures expérimentales prévues : Chirurgie pour exposer V1 et placer le dispositif de fixation de la tête de l'animal		
	Observation(s)	**Recommandation(s)**
0	Normal	NA
1	Hémorragie légère ou perte de sang minime	NA
2	Signes de douleur modérée, perte de sang modérée, hémorragie modérée ou inflammation de la zone de la chirurgie ou de la peau adjacente à la chirurgie	Surveillance au cours des premières heures après la chirurgie pour exclure ce point ou augmenter à un score supérieur
3	Signes de douleur sévère, hémorragie continue ou perte de sang importante, inflammation de la zone de la chirurgie ou de la peau adjacente à la chirurgie importante.	Point limite adapté
4	Lésions corticales irréversibles pendant la chirurgie	Point limite adapté

SCORE TOTAL

En cas de score total ≥ 5 ou de score de 3 dans n'importe quelle variable, l'euthanasie de l'animal sera réalisée

Appendix 3

European Journal of Neuroscience

WILEY | EJN European Journal of Neuroscience FENS

RESEARCH REPORT

Beyond Vision: Response of the Mouse Visual Cortex to Multimodal Stimulation

Antonio Caballero Tapia[1] | Guy Cheron[2] | Dominique Ristori[2] | Lutgarde Arckens[3] | Laurence Ris[1]

[1]Neurosciences Laboratory, University of Mons (UMONS), Mons, Belgium | [2]Laboratory of Neurophysiology and Movement Biomechanics (LNMB), Université libre de Bruxelles (ULB), Brussels, Belgium | [3]Research group of Neuroplasticity and Neuroproteomics, KU Leuven, Leuven, Belgium

Correspondence: Antonio Caballero Tapia (antonio.caballerotapia@umons.ac.be)

Received: 13 May 2025 | **Revised:** 3 July 2025 | **Accepted:** 26 July 2025

Associate Editor: John Foxe.

Funding: This work was supported by Chaire Les Amis des Aveugles.

Keywords: event-related oscillations | in vivo electrophysiology | stimulation | visual cortex | visual evoked potentials

ABSTRACT

Sensory perception emerges from the integration of multiple inputs from different sensory modalities, a process previously attributed to higher-order cortices. However, increasing evidence suggests that the primary visual cortex also processes nonvisual stimuli. Here, we investigated the response of the primary visual cortex to visual, auditory and somatosensory stimuli in awake, head-fixed mice using evoked local field potentials, multi- and single-unit recordings. Our results demonstrate that the primary visual cortex responds to auditory and somatosensory inputs with distinct frequency band modulations and firing rate patterns across monocular and binocular regions. Notably, somatosensory stimuli elicited the fastest response latencies, suggesting a privileged role in murine sensory processing. Auditory and somatosensory stimuli modulated the primary visual cortex activity similarly to contralateral visual inputs, whereas ipsilateral visual stimulation resulted in weaker responses. These findings indicate that the primary visual cortex is not solely dedicated to vision but also responds to auditory and somatosensory stimuli, supporting a potential role in multisensory processing.

1. Introduction

1.1. Multisensory integration in environmental perception

Perceiving the environment is not a simple task. Even though we are exposed to stimuli from various modalities throughout our lives, such as vision, hearing, and touch, multisensory input is required to recreate reality in the brain. Moreover, the most crucial aspect of creating a coherent and accurate perception involves the combination of sensory inputs. This process has been extensively studied primarily at the mesoscopic level using techniques such as EEG (electroencephalography) (Bertonati *et al.*, 2023; Rossi Sebastiano *et al.*, 2024) and fMRI (functional magnetic resonance imaging) (Alwashmi *et al.*, 2024) in human subjects. Studies in primates, which also investigate sensory integration, conclude that possibly the entire neocortex is in some way multisensory, implying that the senses do not function independently during the cognitive process of reconstructing reality in the brain (Ghazanfar & Schroeder, 2006; Kayser & Logothetis, 2007). Other research in rodents suggests that the mechanism behind sensory integration resides in different neuronal microcircuits that operate in parallel and are flexibly recruited based on factors such as the stimulus characteristics and behavioural constraints (Meijer *et al.*, 2019; Xu *et al.*, 2020; Oude Lohuis *et al.*, 2024).

1.2. Redefining the primary visual cortex: more than just visual

The traditional view of sensory organisation was that multisensory integration was restricted to higher-order brain regions, occurring only after substantial preprocessing of information in the sensory-specific lower-level cortices. Consequently, regions like primary visual cortex (V1) were considered to perform exclusively visual functions. However, recent multisensory studies indicate a new trend in brain organisation and perception, showing that multisensory convergence and integration in lower-level cortices is the rule rather than the exception (Murray *et al.*, 2016). Other studies have demonstrated the existence of direct heteromodal cortical connections between the primary auditory cortex and V1 using enucleated mice as a model. These studies identified the A1-V2L-V1 indirect pathway as crucial for multisensory processing, highlighting its role in the integration of auditory and visual information in the absence of visual inputs (Laramée *et al.*, 2011). In the same line, other studies have highlighted that visuotactile motion congruence increases gamma-band activity in V1, suggesting its role in multisensory integration. These findings demonstrate that V1 not only processes visual information but also integrates somatosensory inputs (Krebber *et al.*, 2015).

1.3. Recording of V1 activity

LFP (local field potential) measures the combined electrical activity within a neural tissue volume. In V1, LFP signals evoked by visual stimuli have been widely investigated, though debate exists on whether these signals reflect a small, localised neuron population or a larger, distributed one.

Recent studies suggest that LFP signals originate within approximately 250 μm of the recording electrode in V1 (Katzner *et al.*, 2009). Neuronal processes appear in the rhythmic oscillations from LFPs, where Fourier transforms help identify characteristic frequencies and provide quantitative information about various frequency bands (Masimore *et al.*, 2004). In cats, multisensory processing in the extrastriate visual cortex (PLLS) has been studied by examining single units, showing that neurons respond to auditory stimuli and that visual response may be modulated by concurrent auditory input (Allman & Meredith, 2007). In mice, Meijer et al., (2017) used two-photon calcium imaging on large V1 populations in awake animals with single-cell resolution to explore the tuning properties of V1 neurons to visual and auditory stimuli, finding that auditory modulation of V1 responses depends on visual contrast and sound composition and timing.

1.4. Study of the V1 response to auditory, somatosensory and visual stimulation

In this study, we explored the visual cortex's response to visual, auditory, and somatosensory stimulation in awake, head-fixed mice. Our goal was to record evoked potentials, a well-known technique for studying visual systems in different species (Lopez *et al.*, 2002; Marenna *et al.*, 2019; Hayden *et al.*, 2023). We used two recording methods, LFP and unit activity recordings, to assess the visual cortex's response to the three types of sensory input. By averaging LFP activity, we obtained evoked local field potentials (eLFPs), which reflect intracortical electrical responses to stimuli. Unlike traditional Event-Related Potentials (ERPs) derived from surface recordings such as EEG (electroencephalogram) or electrocorticogram, eLFPs provide a measure of cortical processing at the local network level, capturing deeper, intracortical responses with greater spatial specificity.

We also utilised neuro-oscillatory responses analysed in the time-frequency (TF) domain, a computationally intensive but precise method for studying brain activity across frequency bands (Javitt *et al.*, 2020). LFP signal analysis was conducted using EEGLAB in MATLAB to extract Event-Related Spectral Perturbation (ERSP) and Inter-Trial Coherence (ITC) across relevant frequency bands (0.5-100 Hz (Hertz)) (Makeig *et al.*, 2002; Cheron *et al.*, 2007; Chen *et al.*, 2015; Bastos *et al.*, 2023).

In this study, our unit activity recordings showed changes in V1 neuron firing rates depending on the type of sensory input, revealing V1's response latency to stimuli and differences between monocular and binocular V1 regions. These findings contribute to our understanding of sensory processing and may suggest integrative processes in V1.

2. Material and methods

2.1. Experimental model

We used 14 C57BL/6J mice (M|F) aged 2 to 6 months from Charles River Laboratories. The mice were accommodated in a climate-controlled environment with a 12-hour light/dark cycle, placed in regular cages containing bedding, water, and food available without restrictions. The facility maintained filtered air circulation and maintained a constant temperature at 20°C. The cages were additionally equipped with a running wheel, a mouse house under the wheel, and cardboard rolls to enhance the mice's environment. Ethical approval for the experimental procedures was obtained from the ethics committee (CEBEA - *Comité d'éthique et du bien-être animal*) of the University of Mons and conform for the Directive 2010/63/EU of the European Parliament and of the Council on the protection of animals used for scientific purposes.

2.2. Surgery

All animals underwent surgery to expose V1, distinguishing the monocular from the binocular region through two 1 mm ø craniotomies above the left hemisphere. Referring to the study by Van Brussel et al., (2009) and with the collaboration of the authors from the Laboratory of Neuroplasticity and Neuroproteomics, Katholieke Universiteit Leuven, we determined that it was necessary to differentiate between the monocular and binocular regions. Therefore, we adjusted the coordinates of both regions to align with our recording protocol: monocular (AP = − 3.8 mm; L = +2 mm; relative to bregma) and binocular (AP = − 3.8 mm; L = +3 mm; relative to bregma) (Figure 1C).

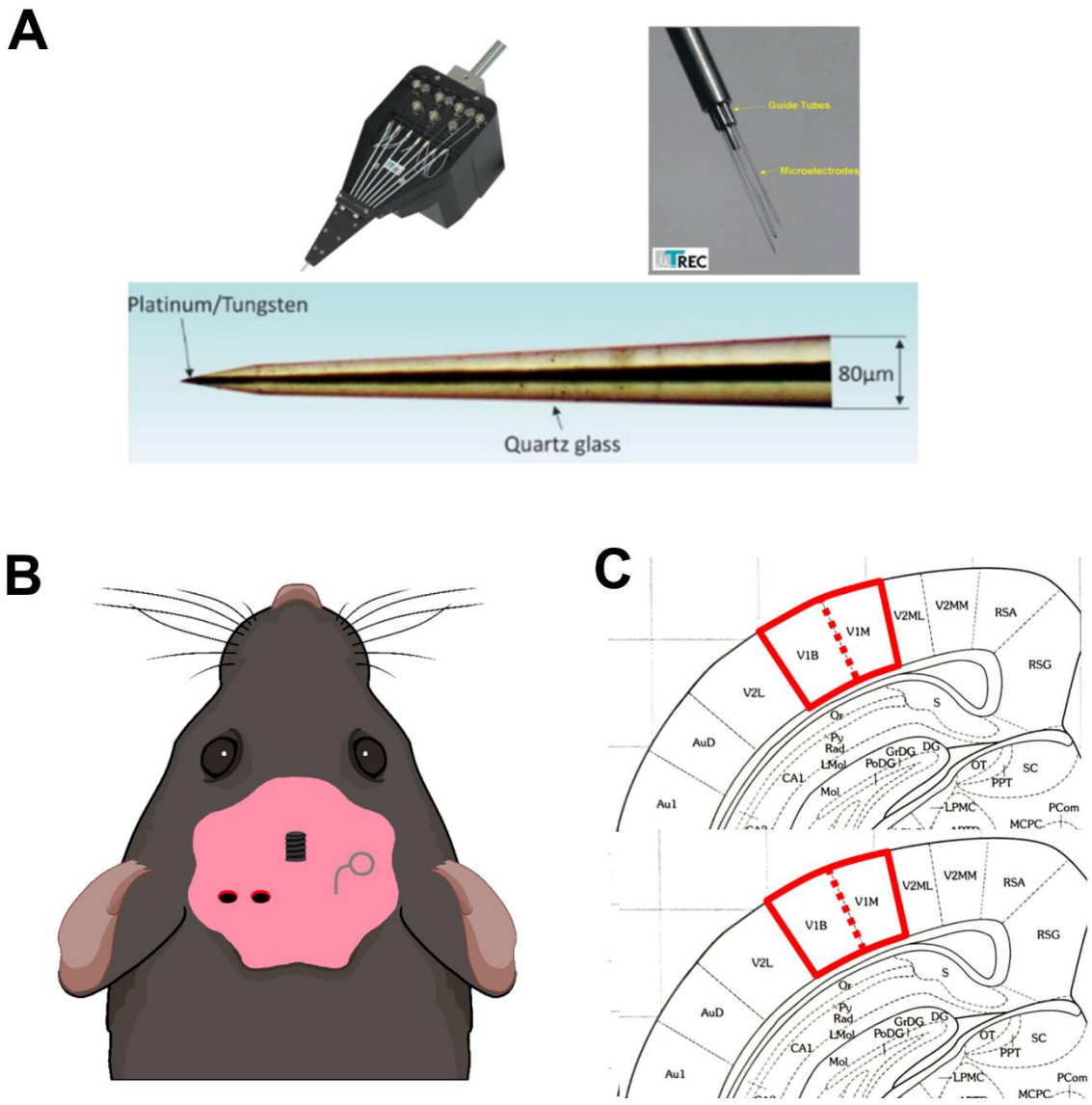

Figure 1. Experimental setup for neural recordings in mice.

This figure provides an overview of the technical and anatomical components of the experimental design. (A) Illustration of the electrode setup used for recording neural activity, including a close-up of the electrode array, guide tubes, and a microelectrode made of platinum/tungsten encased in quartz glass, with a tip diameter of 80 µm. (B) Diagram of a mouse with a cranial window and implanted electrode array, indicating the positioning for neural recordings. (C) Overlay of recording sites on brain atlas images from V1, showing the electrode tracts positioned within the binocular (V1B) and monocular (V1M) areas.

Before initiating the surgical procedure, the mice were anesthetised with an air/isoflurane mixture, 3% for induction in a customised isoflurane chamber and 2-1% through a mask (stereotaxic anaesthesia mask kit mice 68601 RWD) during surgery (Iso-Vet, Piramal Critical Care B.V.). In the right hemisphere, we positioned a silver wire electrode as the reference to the recording

system. Finally, a head-holding system was implanted, consisting of six bolts screwed to the skull and a bolt placed over the middle skull upside down and perpendicular to the frontal plane to allow for head fixation during the experiments. The holding system and the reference electrode were cemented to the skull (DuraLay, Ill., USA) (Figure 1B) (Sánchez-León *et al.*, 2025).

The animals were allowed to recover on a heating pad with warm light until they had fully recovered from the surgery.

2.3. Recording of LFP in awake animals

Before the recording sessions, animals underwent a habituation period of 20 days in the animal facility to adapt to their new environment after arrival from Charles River Laboratories. Additionally, they were habituated to the recording setup for one week prior to the electrophysiological recordings, ensuring they were familiar with the conditions before head fixation. For the recording of electrophysiological activity, we used quartz-platinum/tungsten microelectrodes (0.5 to 0.8 MΩ) in a circular seven-channel Eckhorn microdrive (Thomas Recordings©, Giessen, Germany) (Figure 1A). 50 Hz noise was removed using the Hum Bug Noise Eliminator (AM-Systems, U.S.A.). At the beginning of the LFP recording sessions, the animals were allowed 15 minutes of free movement in the designated area, which is located within the same recording setup. Subsequently, the animal's head was fixed in the recording setup, where it could make all desired movements on a mouse wheel, with the only restriction being on head movement. Once the animal was correctly positioned and calm, the reference electrode was connected, and the stimulators were placed approximately 14 cm away from the areas of the animal to be stimulated (Porciatti *et al.*, 2002).

All stimulation protocols were defined and programmed using Spike 2 CED software (CED©). Several protocols exist to evoke the response, but for this project, visual stimulation was performed using a flickering light flash at 1 Hz (Lopez *et al.*, 2002; Cambiaghi *et al.*, 2011) perpendicular to the left eye (ipsilateral to the recorded hemisphere) with a 30 ms (miliseconds) duration. The emission was 100 lux at the source, 70 lux at 5 cm, and 15 lux at 50 cm through an 8-horizontal-grid system. Somatosensory stimulation involved a brief air puff to the animal's right whiskers (contralateral to brain recording) lasting 30 ms (there was a delay of 9 ms from stimulation to the stimulus reaching the animal). During the design and commissioning of our somatosensory stimulation system, we performed acoustic and video assessments to ensure that the air-puff was delivered focally to the vibrissae and did not provide cues via other sensory channels. Using a sound level meter, we confirmed that the peak sound pressure at the point of contact with the whiskers did not exceed 30 dB SPL (sound pressure level), while the laboratory background noise (from ventilation, machinery and furnishings) was maintained consistently between 60 - 70 dB SPL. Other investigators have noted that such somatosensory stimulation can

also engage the auditory system and, to minimise this cross-modal influence, adapt their set-ups by ensuring their stimulator generates approximately 55 dB SPL while the animal experiences 70 dB SPL of ambient noise during experiments (Galvez *et al.*, 2007, 2009). These checks are repeated several times per year, coinciding with routine equipment maintenance. The airflow trajectory was adjusted to avoid impinging on other facial regions and based on video recordings, we cannot confirm a causal relationship between puff delivery and eyelid closure. We acknowledge, however, that it is not feasible to eliminate entirely the noise of air turbulence or minor skin deflections, and thus a residual auditory or mechanoreceptive effect may remain. By documenting our acoustic limits, the frequency of measurements and our visual monitoring protocol, we provide a reproducible methodology that ensures the observed behavioural responses arise principally from whiskers deflection. Auditory stimulation was achieved using a speaker positioned to the right of the animal (no ears were covered) emitting a 60 dB (decibels) 4 kHz sinusoidal wave for 30 ms (Taberner & Liberman, 2005).

Using the previously mentioned device, we lowered the electrode through one of the windows to a depth of 700 µm (micrometers) (lowering and raising the electrode at a speed of 5 µm per second). After 30 seconds, we raised the electrode to 600 µm and waited for 2 minutes before initiating the electrophysiological recording protocol. Electrophysiological activity was recorded at the same depth for 300 s per type of stimulus (visual, somatosensory, or auditory). The same protocol was repeated for each depth (600, 400 & 200 µm) and in each window (binocular and monocular area). Once the recording was completed, or after exceeding 2.5 hours, the windows were sealed with bone wax after cleaning the area.

2.4. Unit activity recording in awake animals

The protocol is essentially the same as that used for LFP recording. We used the same type of electrode, quartz-platinum/tungsten microelectrodes, but in this case, to facilitate single-unit recording, the electrode impedance was 1 to 4 MΩ in a circular seven-channel Eckhorn microdrive (Thomas Recordings©, Giessen, Germany). A 100 Hz filter was applied to the raw signal. Before initiating the recording sessions, the animals were allowed 15 minutes of free movement in the designated area, which is located within the same recording setup. 50 Hz noise was removed using the Hum Bug Noise Eliminator (AM-Systems, U.S.A.). After the free movement period, the animal's head was fixed in the recording setup, where it could make all desired movements on a mouse wheel. Once the animal was correctly positioned and calm, the reference electrode was connected, and the stimulators were placed.

All necessary preparatory protocols were as detailed above. In this case, the method of lowering the electrode was different. To conduct this recording, we performed an active search for single-unit activity (SUA) in each cranial window, but we found both SUA and multi-unit activity

(MUA) along V1. Once a clear signal was found, the protocol was initiated, interchanging five stimuli for 15 seconds of one type of stimulation. After these seconds, the type of stimulus was automatically changed, and then again for the remaining stimulus type. This loop continued until 900 seconds of recording were completed. This approach allowed us to observe how the neural activity varied with the three types of stimulation, reducing the risk of not recording the same SUA or MUA, as the stimuli were interspersed during the same recording session. If the duration of the session did not exceed 800 seconds, it was not considered for the posterior analysis.

2.5. Histological confirmation of electrode position

At the end of the live animal experimentation period, we conducted a perfusion and tissue preservation protocol for the target brain tissue. The animals were anesthetized using an isoflurane chamber (3% Iso-Vet), followed by a lethal intraperitoneal injection of ketamine (200 mg/kg). In some cases, a needle adapted to the recording setup was introduced into both cranial windows to a depth of approximately 2 mm for coordinate verification. Before insertion, the tip was immersed in a dye solution containing 2.5 mg/ml of DiI (Tetramethylindocarbocyanine Perchlorate) (D282) (Invitrogen™) in ethanol, following the Lipophilic Tracers protocol.

To ensure accurate alignment with the targeted cortical regions, we performed a standard intracardiac perfusion using 4% paraformaldehyde (PFA). The brain was extracted, post-fixed in 4% PFA for 48 hours, and embedded in a paraffin block. Coronal sections (~15 µm) were obtained at the approximate coordinates of the cranial windows using a microtome and stained with Cresyl Violet. Fluorescent imaging was performed with a Nikon Ti-E Fluorescence Phase Inverted Microscope PFS Lumencor (Nikon Corporation, Tokyo, Japan) using an excitation wavelength of 549 nm and an emission wavelength of 565 nm for DiI detection.

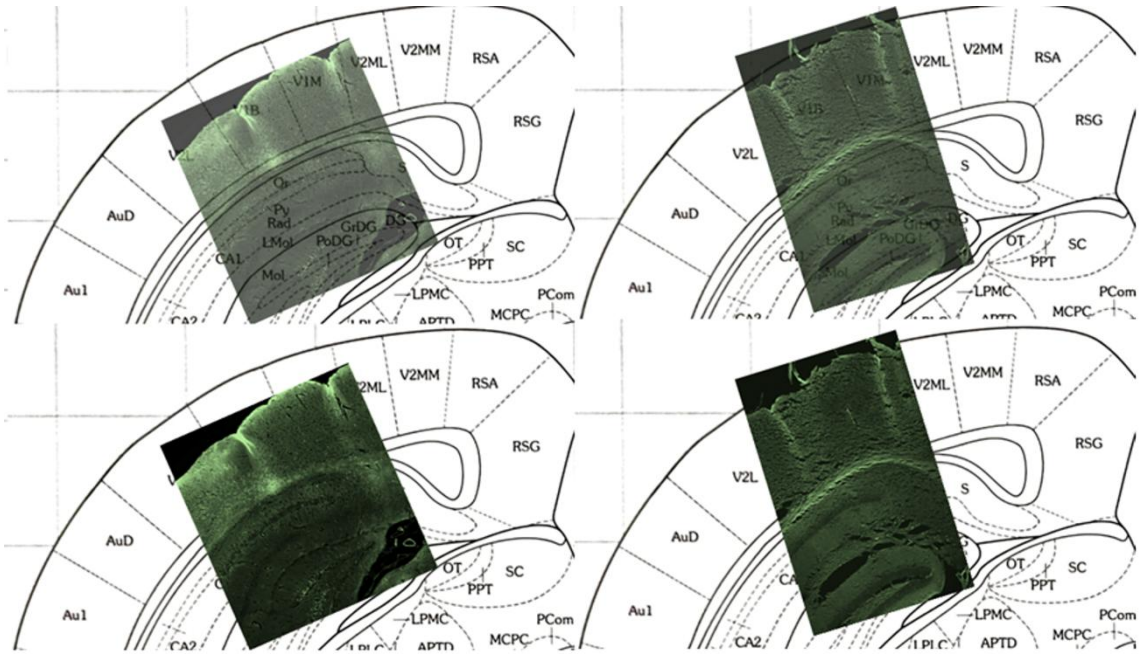

Figure 2. Histological sections overlaid on atlas images from Franklin and Paxinos (1997).

This figure shows histological sections aligned with atlas images to confirm electrode tract positioning in the V1 region. The images demonstrate the overlap of electrode tracts within both the binocular and monocular zones of V1, validating the accurate targeting of these specific areas for neural recordings. Visible bands formed by DiI crystal deposits along the electrode tracts indicate the precise recording locations, ensuring reliable data collection from each region.

The electrode tracts were clearly visualized under fluorescence microscopy, revealing bright DiI traces that effectively marked the entire length of the track without detectable tissue damage. These well-defined fluorescent bands were perpendicular to the cortex within both binocular and monocular zones, confirming accurate electrode placement in V1. The stable fluorescence of DiI allowed for precise identification of electrode tracts with minimal lateral diffusion. This method, which does not require extensive tissue processing beyond standard perfusion and sectioning, helped preserve tissue integrity for further analyses. The use of DiI also enabled differentiation of closely spaced electrode tracts, ensuring that recordings were conducted from the intended cortical areas (DiCarlo *et al.*, 1996). Figure 2 illustrates the overlay of these sections with the Franklin and Paxinos atlas (2019), further validating electrode positioning within V1.

3. Data analysis and statistical methods

3.1. LFP recording analysis

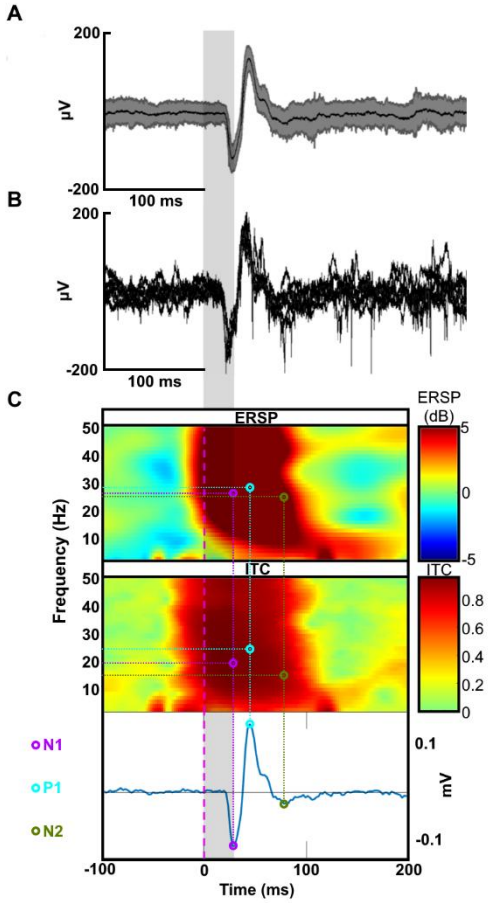

Figure 3. Signal processing and selection of ERSP/ITC values at ERP components.

(A) Grand-average of all stimulation events from a single recording session. The black central line represents the mean response, while the shaded grey area indicates the dispersion across trials.

(B) Superposition of eight individual stimulation events, showing how single-trial responses resemble the averaged waveform and its variability.

(C) ERSP and Inter-Trial Coherence (ITC) representations computed using EEGLAB. The upper heatmap shows ERSP values (dB), reflecting spectral power changes across time and frequency. The middle heatmap represents ITC, indicating phase alignment consistency across trials. The bottom panel depicts the corresponding event-related potential (ERP), where N1 (magenta), P1 (cyan), and N2 (green) mark the time points with the highest ERSP and ITC values. These key moments are highlighted by dashed lines in the ERSP and ITC maps, linking spectral features to specific ERP components.

LFP were digitally stored on a computer following analogue-to-digital conversion with a Power 1401 analogue-digital converter (CED©, Cambridge, UK). The recorded data were continuously digitised at a rate of 25 kHz. Offline analysis and visual representations were performed using Spike 2 CED software (CED©), Python, and EEGLAB (a MATLAB toolbox adapted for LFP analysis) (Figure 3).

The eLFP is a neurophysiological measure that reflects brain activity in response to specific stimuli, captured directly from intracortical recordings. eLFPs consist of a series of positive and negative peaks occurring at characteristic moments after stimulus presentation. These peaks allow for the identification of neuronal processing patterns, particularly early components (N1, P1, and N2), which are crucial for analysing response latency and amplitude (Rugg & Coles, 1996; Kaan, 2007; Sur & Sinha, 2009; Davies, 2010; Helfrich & Knight, 2019). In our recordings, the polarity of N1 and P1 varied between trials, with N1 sometimes preceding P1 and vice versa (Figure 3C).

To ensure the reliability of the recorded neural responses, we first computed the grand-average LFP across all stimulation events (Figure 3A). This representation provides an overall view of the typical response pattern, where the black central line denotes the mean response and the shaded grey area reflects the variability across trials. To further examine the consistency of individual responses, we plotted eight randomly selected stimulation events superimposed on the same scale (Figure 3B). This visualisation confirms that single-trial responses generally follow the mean waveform while exhibiting natural variability, reinforcing the stability of evoked responses across trials.

We performed a spectral analysis of V1-evoked responses using the MATLAB toolbox EEGLAB applied to Spike2 (*spike 2 Mathlab_DR*). We quantified ERSP and the event-related potential (ERP) following the procedure of Delorme and Makeig (2004). The ERP corresponds here to the eLFP. An automatic procedure (*Newtimef_VisionSpike_V1.m_DR*) was developed to detect positive and negative eLFP amplitude peaks, latencies and related frequencies. For each eLFP recording, we applied a time-frequency decomposition over the 1-80 Hz range. At each frequency and time point, we normalized spectral power by dividing it by the mean power in the pre-stimulus baseline (-500 to 0 ms). We then converted these normalized values to decibels via a $\log_{10}$ transform (Grandchamp & Delorme, 2011) (Figure 3C, upper panel). In summary, for n trials, if $F_k(f, t)$ denotes the spectral estimate of trial k at frequency f and time t, then:

$$\mathrm{ERSP}(f,t) = \frac{1}{n}\sum_{k-1}^{n} |F_k(f,t)|^2$$

We also performed ITC, or phase-locking factor, analysis a measure of the consistency of oscillatory phase at a given latency and frequency across stimulus-locked LFP trials. In summary, for n trials, if $F_k(f,t)$ denotes the complex spectral estimate of trial k at frequency f and time t, then:

$$ITPC(f,t) = \left|\frac{1}{n}\sum_{k-1}^{n} \frac{F_k(f,t)}{|F_k(f,t)|}\right|$$

At each frequency and time point, we normalized the complex spectral estimate by dividing by its magnitude to isolate phase, averaged these unit-phase vectors across the n trials, and computed the length of the resulting vector yielding ITC values between 0 (no phase consistency) and 1 (perfect phase-locking) (Figure 3C, middle panel).

Finally, for each selected point in the eLFP signals we exported ERSP and ITC matrices to Excel and recorded the peak values of ERP, ERSP, and ITC in separate worksheets for subsequent quantitative analysis.

For each recording, we identified the time points with the highest ERSP and ITC values, corresponding to N1, P1, and N2 in the ERP (Figure 3C, bottom panel). These peak values were extracted automatically from the EEG analysis and are indicated by dashed lines in the heatmaps.

The extracted ERSP and ITC values were then analysed statistically. Since the data did not meet normality assumptions (Shapiro-Wilk test), we used a Kruskal-Wallis test to assess the differences between the frequency bands. Dunn's post hoc test was applied to determine significant differences between the stimulation conditions. Data are presented as mean ± SEM (standard error of the mean), with statistical comparisons represented in boxplots.

3.2. Analysis of unit activity recordings

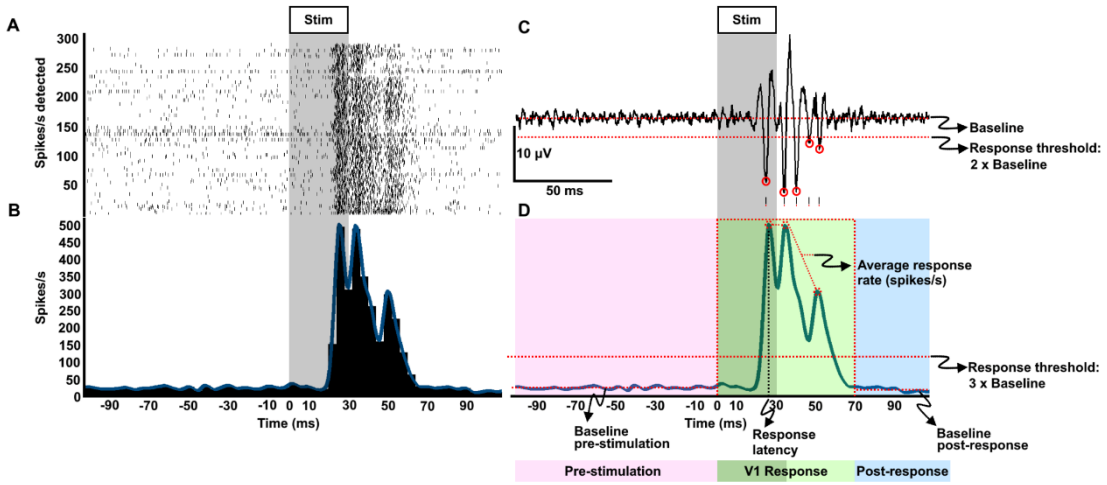

Figure 4. Process of extracting neural information from raw signals in response to visual stimulation in V1.

(A) Raster plot displaying detected units over time during the stimulation period (grey shaded area). Each dot represents a detected spike, and each row corresponds to a single trial. The highest spike density is observed shortly after the stimulus onset. (B) Peristimulus time histogram (PSTH) showing the firing rate (units per second) over time. A significant increase in firing activity is observed following the stimulus onset, with two prominent peaks indicating strong neuronal responses in V1. The blue trace represents the

smoothed average firing rate. (C) Raw electrophysiological signal showing the multiunit activity detected in response to the stimulation. The four small red marks highlight correctly identified spike events, confirming accurate event detection by the software. The baseline firing rate is represented by the lower dashed line, while the response threshold (2× baseline) is indicated by the upper dashed line. (D) Summary of response quantification. The plot illustrates different phases of neuronal activity: pre-stimulation baseline (pink), response latency period (green), and post-response phase (blue). The response latency is determined by the first significant increase in firing rate exceeding the 3× baseline threshold (red dashed line). Additionally, all peaks identified within the first 70 ms that surpass three times the baseline threshold are averaged to obtain the unit firing frequency during the response period. This allows for a precise estimation of V1 activation timing and response magnitude. The response latency is determined by the first peak that exceeds three times the baseline threshold within the response period. Additionally, all peaks within the first 70 ms that surpass three times the baseline are averaged to obtain the unit firing frequency during the response period.

To analyse the unit activity recordings, we used Spike 2 CED software (CED©) and generated three histograms for each recording session, one for each type of stimulation, representing the unit frequency 0.5 seconds before and after the stimulation. A good example for contralateral visual stimulation is shown in Figure 4A, B.

The initial raw electrophysiological signal is illustrated in Figure 4C, which shows the unprocessed data recorded during one visual stimulation in V1. Just below the peaks, five small lines can be observed, representing the correct identification of spikes by the software.

Following this, we coded a Python script to analyse all the firing rate graphs from all the recordings. This script returned a document with the average histograms for each type of stimulus and an Excel document with the average frequency before, during, and after the stimulation event, as well as a value that helps determine the V1 response latency to different types of stimulation. To obtain this value, the software selected an interval within the first 70 milliseconds after the onset of stimulation, identifying the highest spike rate in the histogram within this interval. The plot in Figure 4D visualises the detected multiunit events across an entire recording session, displaying the timing of multiunit events around the stimulation period and providing a comprehensive overview of response consistency.

To visualise the differences in the response to different types of stimulation, boxplots were generated. These plots allowed us to determine the distribution of unit firing frequencies for each type of stimulation. The customised colour palette facilitated visual differentiation between time points. Statistical annotations on these plots were based on the Kruskal-Wallis test and Dunn's post hoc test to show the differences between the boxplots.

To determine the response latency of V1 to different types of sensory stimulation (visual, auditory, and somatosensory), we employed a representation methodology based on Levakova et al. (2015). Using kernel density estimation, we achieved a continuous and smooth temporal distribution, allowing us to identify, through the density peak, the moment when the highest frequency of active units is reached. This approach provides a precise approximation of the response latency, based on values derived from the interval selected by our software within the first 70 milliseconds after the onset of stimulation, where the highest spike rate was identified, exceeding at least three times the baseline rate recorded before stimulation.

4. Results

4.1. Dynamics of ERSP values in V1 response to trimodal stimulation

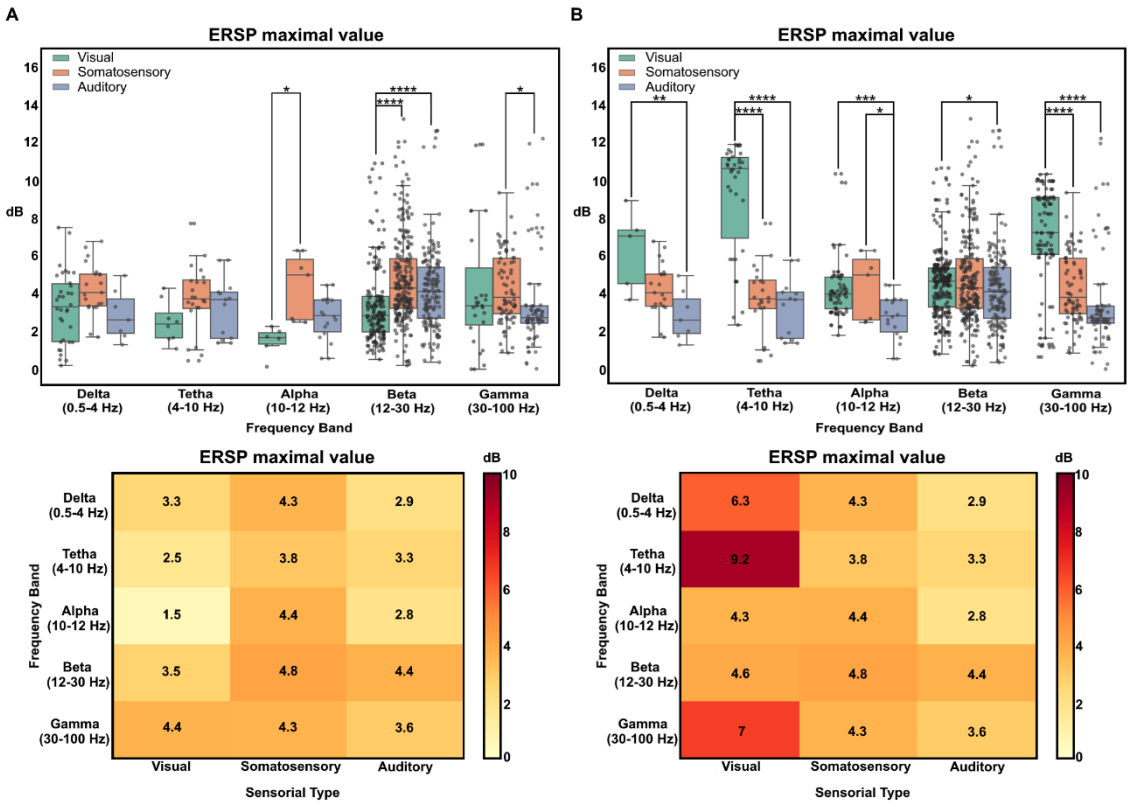

Figure 5. Maximum ERSP values across different frequency bands and sensory modalities.

In (A), visual stimulation is performed ipsilaterally to the recording site, whereas in (B), visual stimulation is contralateral. The other types of stimulation (somatosensory and auditory) remain the same in both conditions.

(A) and (B) top panels: Boxplots showing the distribution of maximum evoked spectral power (ERSP) values across different frequency bands: delta (0.5-4 Hz), theta (4-10 Hz), alpha (10-12 Hz), beta (12-30 Hz), and gamma (30-100 Hz) for three types of sensory stimulation: visual (green), somatosensory (orange), and auditory (blue). Each dot represents an individual ERSP value. The boxplots include the median, interquartile range, and outliers. Significant differences between conditions were assessed using

*a Dunn's post hoc test with Bonferroni correction. Statistical significance is indicated by asterisks: * $p < 0.05$, ** $p < 0.01$, *** $p < 0.001$, and **** $p < 0.0001$.*

(A) and (B) bottom panels: Heatmaps showing the average maximum ERSP values (in dB) for each frequency band (left axis) and sensory stimulation type (bottom axis). The colour scale represents the magnitude of the evoked power, where lighter tones indicate lower values and darker/red tones indicate higher values.

The application of visual stimulation to either the ipsilateral or contralateral eye resulted in distinct effects in the eLFP recordings from V1. As expected, no overall differences in power were observed across brain wave frequencies when ipsilateral visual stimulation was applied relative to the recorded hemisphere. However, some notable distinctions emerged, particularly in the alpha, beta, and gamma bands. Evoked differences were observed in response to visual and somatosensory stimulation for the alpha band, all three types of stimulation for the beta band, and only somatosensory and auditory stimulation for the gamma band (Figure 5A, top).

The mean of the maximum ERSP values highlights the beta band as the most responsive, with all three types of stimulation evoking power levels around 3.5 dB, with the highest response recorded for somatosensory stimulation at 4.8 dB. Similarly, gamma band power values exceeded 3.5 dB across conditions. Somatosensory stimulation consistently evoked responses around 4 dB across all frequency bands. Auditory stimulation notably elicited a power value of approximately 4.4 dB in the beta band, whereas in the other frequency bands, the evoked power values remained around 3 dB. In contrast, visual stimulation evoked a peak response of 4.4 dB in the gamma band, while in beta and delta, the values were close to 3.5 dB. In the theta and alpha bands, the evoked responses were around 2 dB, with the lowest recorded value being 1.5 dB in alpha (Figure 5A, bottom).

Contralateral visual stimulation elicited significant differences compared to the other types of stimulation across almost all studied frequency bands. Notably, gamma and theta bands showed the greatest significant differences in maximum power values compared to the other frequency bands (Figure 5B, top).

The mean power values revealed a distinct electrophysiological signature compared to those evoked by ipsilateral stimulation. Overall, the power evoked by visual stimulation across frequency bands was elevated, reaching a minimum of 4.3 dB in the alpha band and 4.6 dB in beta. However, the most relevant frequency bands, in terms of power values, were delta, theta, and gamma, with delta reaching an average of 6.3 dB, gamma 7 dB, and theta 9.2 dB. These

values exceeded those evoked by the other two types of stimulation, which maintained the same general response pattern in line with the ipsilateral visual stimulation experiments, because auditory and somatosensory stimuli are always presented on the contralateral side, the same data were used for both conditions in the graphs (Figure 5B, bottom).

4.2. Dynamics of ITC values in V1 response to trimodal stimulation

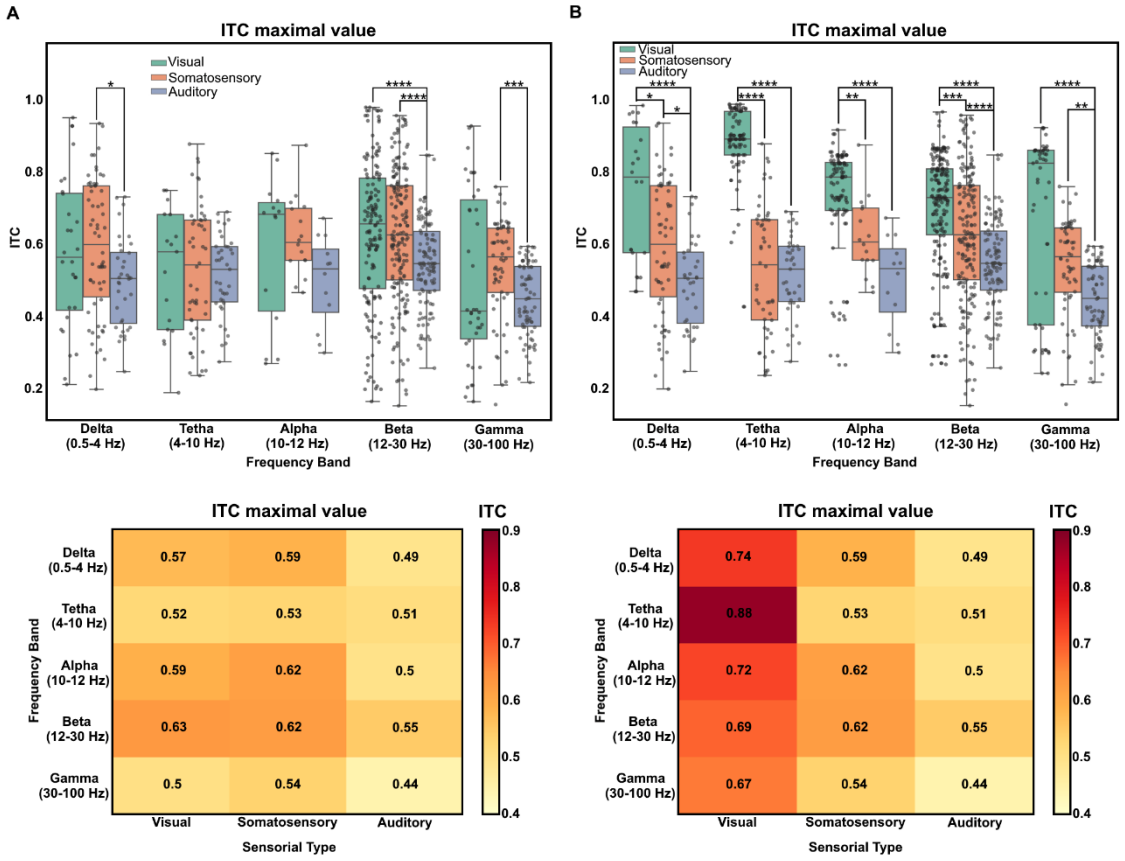

Figure 6. Maximum ITC values across different frequency bands and sensory modalities.

In (A), visual stimulation is ipsilateral to the recording site, whereas in (B), it is contralateral. The other types of stimulation (somatosensory and auditory) remain consistent across conditions.

*(A) and (B) top panels: Boxplots showing the distribution of maximum inter-trial coherence (ITC) values evoked by the three types of sensory stimulation—visual (green), somatosensory (orange), and auditory (blue)—across different frequency bands: delta (0.5-4 Hz), theta (4-10 Hz), alpha (10-12 Hz), beta (12-30 Hz), and gamma (30-100 Hz). Each dot represents an individual ITC value recorded in response to a specific stimulation type. The boxplots include the median, interquartile range, and outliers. Statistical significance of differences between conditions was assessed using Dunn's post hoc test with Bonferroni correction. Asterisks denote significance levels: * $p < 0.05$, ** $p < 0.01$, *** $p < 0.001$, and **** $p < 0.0001$.*

(A) and (B) bottom panels: Heatmaps showing the average maximum ITC values for each frequency band (left axis) and sensory stimulation type (bottom axis). The colour scale indicates ITC magnitude, where

lighter tones indicate lower values and darker/red tones indicate higher values. Notably, contralateral visual stimulation (B) elicits significantly higher ITC values, particularly in the delta, theta, and alpha bands. The highest coherence is observed in the theta band (0.88).

The ITC analysis further highlights significant differences between contralateral and ipsilateral visual stimulation, as only visual stimuli were presented either on the ipsilateral or contralateral side relative to the recording site. For ipsilateral stimulation, notably, somatosensory and auditory stimulation evoked the most substantial differences in the delta and gamma bands. In the beta band, visual stimulation also contributed to the evoked ITC values, which differed considerably from those induced by auditory stimulation, but not from those elicited by somatosensory stimulation (Figure 6A, top).

The ITC values evoked by auditory stimulation were the lowest across the entire frequency spectrum, whereas those induced by visual and somatosensory stimulation exhibited similar trends, particularly in the delta, alpha, and beta bands. However, none of these values exceeded a mean ITC of 0.7 (Figure 6A, bottom).

In contrast, contralateral visual stimulation evoked significantly higher ITC values compared to other types of stimulation, particularly in the delta, theta, and alpha bands, where values approached 1 (Figure 6B, top). The average maximum phase coherence values remained around 0.7 across most frequency bands. However, the theta band stands out with a coherence value of 0.88, indicating a phase-locking phenomenon in this frequency range (Figure 6B, bottom).

4.3. Study of V1 response latency to three different sensory stimuli

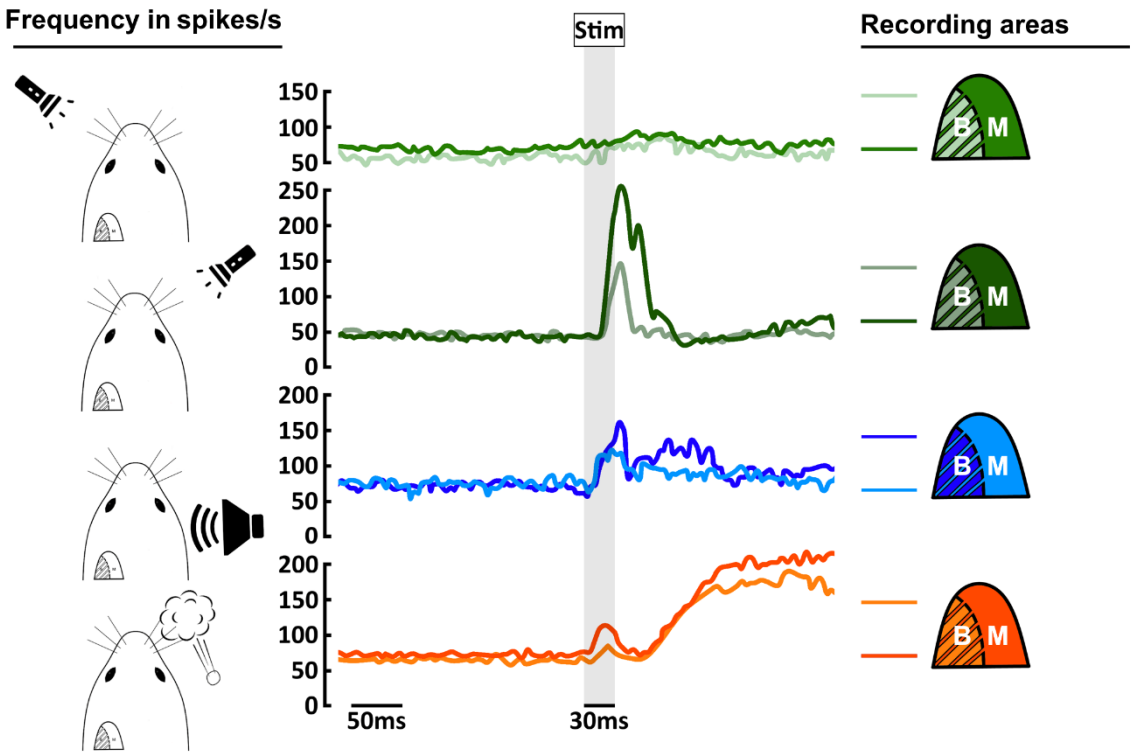

Figure 7. Analysis of single- and multi-unit frequency in V1 in response to different types of sensory stimulation.

The plots show the grand average of firing rate (spikes/s) over time (ms) in response to visual (green), auditory (blue), and somatosensory (orange) stimuli. The shaded area marks the stimulation period. On the left side of the figure, the different stimulation conditions are illustrated. The first represents ipsilateral visual stimulation, the second contralateral visual stimulation, the third contralateral auditory stimulation, though without preventing the animal from perceiving the sound with the ipsilateral ear, and the last depicts somatosensory stimulation applied to the contralateral whiskers. The colour palette on the right indicates the origin of each activity represented. The first set (bright green) corresponds to ipsilateral visual stimulation, where the darker shade represents activity in the monocular zone and the lighter shade in the binocular zone. The second set (shaded green) represents contralateral visual stimulation, following the same convention: the darker green corresponds to the monocular zone, while the lighter green corresponds to the binocular zone (non-stimulated eye was not covered; however, the stimulus was positioned to minimize contralateral visibility). For auditory stimulation (third row), blue shades are used: the darker blue represents the binocular region, while the lighter blue represents the monocular region. Lastly, for somatosensory stimulation (fourth row), orange shades are applied: the darker orange corresponds to the monocular region and the lighter orange to the binocular region.

The recording of single-unit and multi-unit activity in V1 allowed for the study of both the firing rate of these units per second and the response latency of V1 to the different types of stimulation.

Figure 7 illustrates the grand average of unit firing rates per second before and after the respective stimulation. Notably, ipsilateral visual stimulation appears to have evoked little to no effect on neural activity, whereas contralateral visual stimulation induced the most pronounced response across V1, affecting both the monocular and binocular zones.

Moreover, V1 exhibited responses to different types of stimulation at the level of unit firing frequency. Interestingly, both auditory and somatosensory stimulation evoked unit rate patterns more like those induced by contralateral visual stimulation than to those generated by ipsilateral visual stimulation.

Seventy milliseconds after stimulation, the recorded activity in V1 was associated with events beyond the direct afferent sensorial input, such as motor or reflexive responses. A clear example of this is somatosensory stimulation, which elicits a secondary increase in firing rate, suggesting the involvement of non-visual influences on V1 neuronal activity.

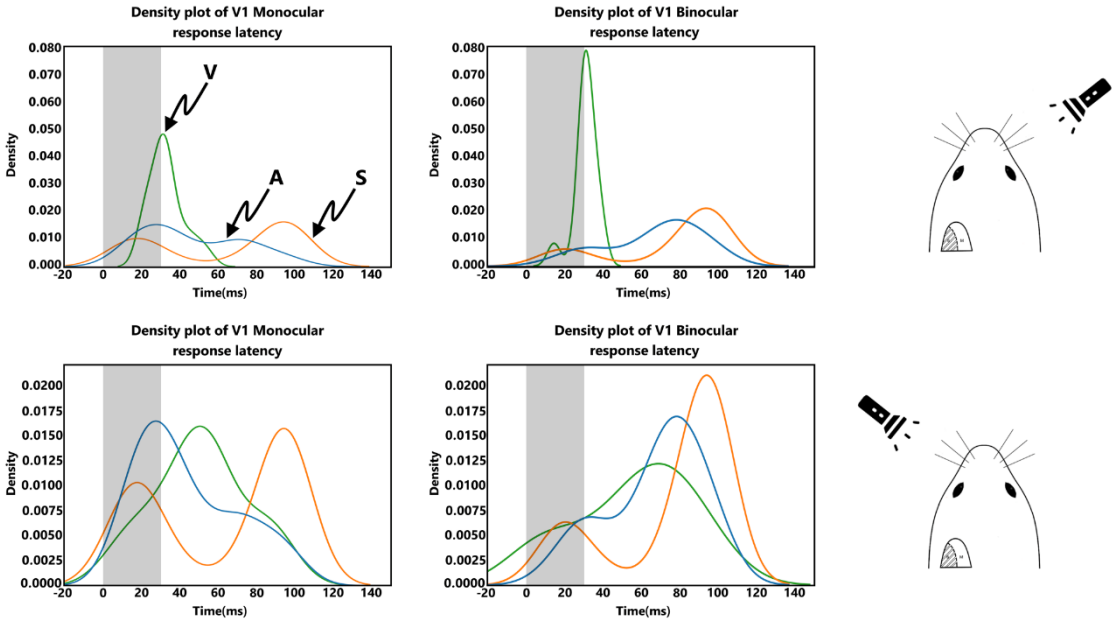

Figure 8. Kernel density plots of response latency in V1.

Kernel density estimation (KDE) plots representing response latencies in the V1 region for different sensory stimuli. KDE is used to visualise the continuous distribution of response times, highlighting peaks and patterns in latency. The plots are divided into monocular (left) and binocular (right) response distributions. The x-axis represents time in milliseconds (ms), and the y-axis indicates density. Each plot includes three curves corresponding to different sensory modalities: green for visual stimuli (V), blue for auditory stimuli (A), and orange for somatosensory stimuli (S). The shaded area marks the stimulation period.

A first set of kernel density plots for the response latency values of V1 under different types of stimulation reveal clear differences depending on whether the stimulation is contralateral or ipsilateral and whether the recording area is in the binocular or monocular zone (Figure 8). The latency values show a higher concentration around specific distributions, indicating distinct temporal processing characteristics for each condition. Contralateral visual stimulation evoked a response latency of 31 ms in both the monocular and binocular regions, indicating a fast and synchronous activation across V1. Ipsilateral visual stimulation, however, resulted in longer latencies, with responses at 50 ms in the monocular zone and 68 ms in the binocular zone, suggesting weaker and delayed activation compared to contralateral input.

Somatosensory stimulation evoked an initial response at 18 ms in the monocular zone, slightly delayed to 20 ms in the binocular zone. A second latency peak appeared at 94 ms, identical in both monocular and binocular regions.

Auditory stimuli elicited a response at 27 ms in the monocular zone and 33 ms in the binocular zone, following a latency pattern similar to early visual responses. A second response latency occurred at 71 ms in the monocular zone and 77 ms in the binocular zone (Figure 8).

These results indicate that V1 processes visual stimuli with the shortest latencies, especially for contralateral inputs, while auditory and somatosensory stimuli elicit responses at different, yet consistent, latency distributions. Additionally, the binocular zone exhibited slightly longer latencies compared to the monocular zone across all stimulation types, highlighting potential differences in integration times for sensory inputs in V1.

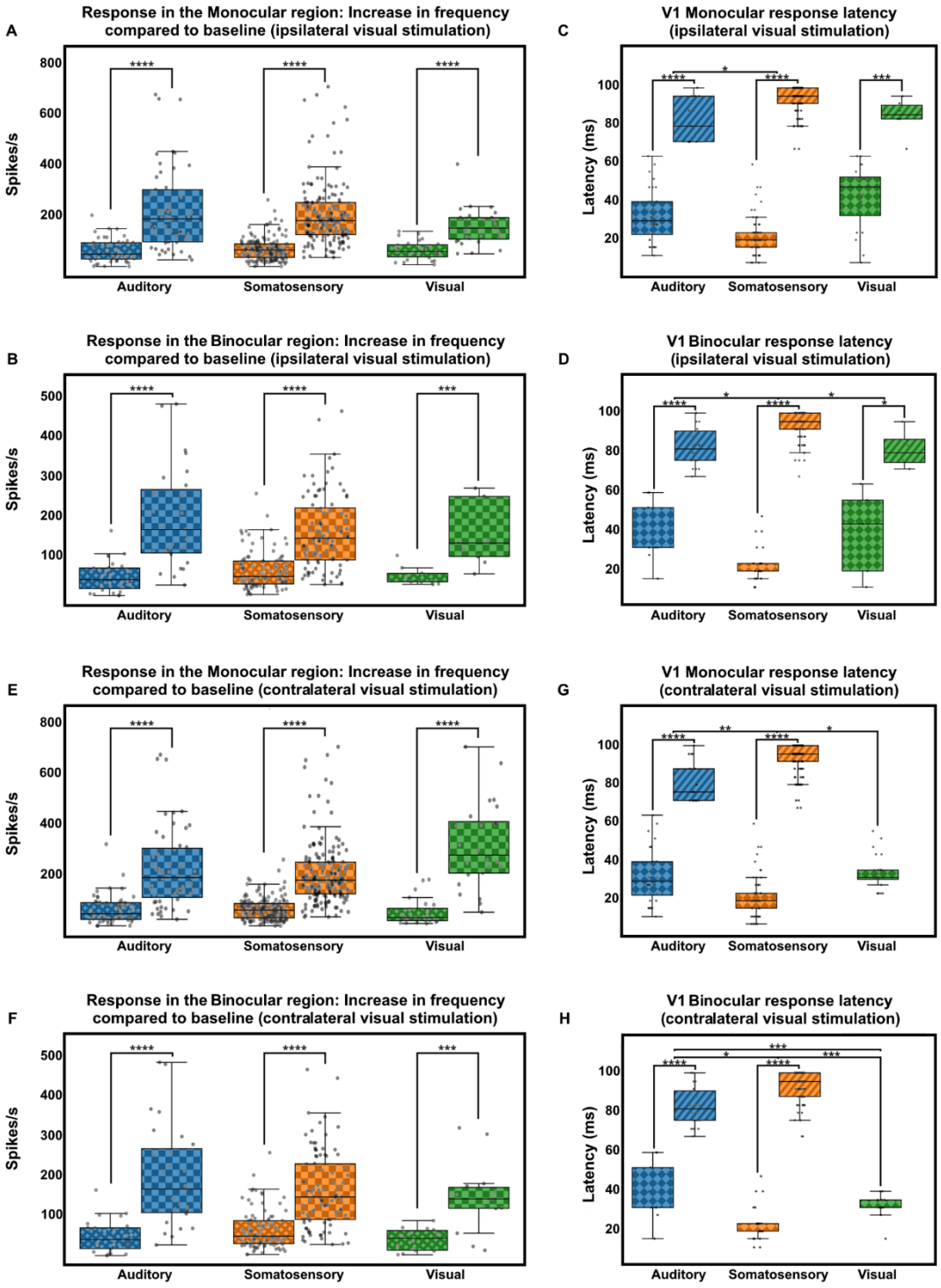

Figure 9. Analysis of single- and multi-unit activity frequency and response latency in V1 following auditory, somatosensory, and visual stimulation.

(A, B, E, F) Boxplots representing the increase in firing rate (spikes per second) compared to the baseline in the monocular (A, E) and binocular (B, F) regions of V1 in response to auditory (blue) and somatosensory (orange) stimulation. (A, B) correspond to ipsilateral visual stimulation (green), whereas (E, F) correspond to contralateral visual stimulation (green). The data indicate a highly significant increase in activity across all stimulation types, confirming that each modality can evoke a neural response

in both monocular and binocular areas. Statistical significance levels are denoted by asterisks ($p < 0.05$, ** $p < 0.01$, *** $p < 0.001$, **** $p < 0.0001$).*

(C, D, G, H) Boxplots showing the distribution of response latencies (ms) in the monocular (C, G) and binocular (D, H) regions of V1 for each sensory modality. (C, D) correspond to ipsilateral visual stimulation, whereas (G, H) correspond to contralateral visual stimulation.

An alternative methodology we proposed for analysing response latency used boxplots (Figure 9), along with calculating the median, mean, and standard deviation. This approach enables direct visualisation of data distribution and facilitates trend identification across experimental conditions. Comparing these results with the kernell density data from Figure 8 shows strong concordance, reinforcing both approaches' robustness and validating response time stability in V1.

Although minor differences in absolute values exist, the general trend of monocular and binocular responses remains stable, reflecting consistent neuronal activation based on stimulation type (Figure 9).

For contralateral visual stimulation, kernel density data show a 31 ms latency in both monocular and binocular zones, indicating rapid, synchronised V1 activation. Directly calculating the mean yields highly similar values: 32.89 ms in the monocular zone and 30.88 ms in the binocular zone, confirming response time stability. Similarly, the median latency in boxplots is 30.29 ms for both conditions, closely aligning with the kernel density estimates. Slight variability in contralateral visual latency appears in data dispersion, with standard deviations of 8.86 ms in the monocular zone and 5.81 ms in the binocular zone. This consistency across methodologies reinforces the reliability of early latency estimation in contralateral responses (Figure 9G, H).

For ipsilateral visual stimulation, kernel density data indicate a longer latency, with response times of 50 ms in the monocular zone and 68 ms in the binocular zone, suggesting delayed, less efficient activation compared to contralateral stimulation. Directly calculating the mean gives slightly lower values: 39.2 ms in the monocular zone and 35.9 ms in the binocular zone, although the median latency in boxplots (42.3 ms in both conditions) remains close to kernel density estimates. Greater dispersion in these response times appears in the standard deviation (18.9 ms in the monocular zone and 24.6 ms in the binocular zone), indicating neuronal response variability may explain part of the observed difference. Additionally, for late latency in ipsilateral stimulation, kernel density data report 68 ms in the binocular zone, while the directly calculated mean values show 80.3 ms in the binocular zone and 83.6 ms in the monocular zone, with medians of 78.4 ms

and 84.4 ms, respectively. Although these values are somewhat higher than kernel density estimates, both methods detecting a second latency suggest a stable, reproducible activation pattern for ipsilateral responses (Figure 9C, D).

For somatosensory stimulation, kernel density data show an initial latency of 18 ms in the monocular zone and 20 ms in the binocular zone, reflecting an early, efficient V1 response. Boxplot values are slightly higher, with a mean of 19.9 ms in the monocular zone and 22.4 ms in the binocular zone, maintaining the trend observed in kernel density estimates. The median values in boxplots are 18.2 ms in the monocular and 22.0 ms in the binocular zones, showing strong coherence with KDE (kernel density estimation) values. Moreover, kernel density data reveal a second somatosensory latency at 94 ms, indicating late activation characteristic of this sensory modality. This second peak also appears in boxplot values, with a mean of 92.3 ms in the monocular zone and 91.8 ms in the binocular zone, along with medians of 94.2 ms in both conditions. The standard deviation of approximately 8 ms in both conditions indicates low dispersion in this late latency, suggesting high stability in the somatosensory response (Figure 9C, D, G, H).

For auditory stimulation, kernel density data show a 27 ms latency in the monocular zone and 33 ms in the binocular zone, following an activation pattern similar to early visual responses. Boxplot values show slight differences but maintain the trend, with means of 30.7 ms in the monocular and 37.4 ms in the binocular zones, and medians of 28.3 ms and 30.2 ms, respectively. Similarly, kernel density estimates report a second auditory latency at 71 ms in the monocular zone and 77 ms in the binocular zone, reflecting subsequent auditory stimulus processing. This pattern also appears in boxplot values, with means of 78.7 ms in the monocular and 81.5 ms in the binocular zones, and medians of 74.5 ms and 80.32 ms. Data dispersion, reflected in standard deviations of 10-15 ms, may explain slight differences in absolute values (Figure 9C, D, G, H).

Next, we also analysed frequency in spikes per second, comparing the baseline before stimulation with the response period. As expected, frequency increased during the response period, but key differences emerged between ipsilateral and contralateral visual stimulation. The baseline median in the monocular zone was 53.6 Hz for ipsilateral (Figure 9A) and 27.9 Hz for contralateral (Figure 9E) stimulation. The response also showed substantial differences, reaching 145.7 Hz in ipsilateral (Figure 9A) and 275.2 Hz in contralateral (Figure 9E) stimulation, indicating contralateral visual stimulation elicits a higher spiking rate. In the binocular zone, the pattern was similar but less pronounced: the baseline was 31.5 Hz for ipsilateral (Figure 9B) and 39.6 Hz for contralateral (Figure 9F) stimulation, while the response reached 129.7 Hz in the ipsilateral (Figure 9B) and 138.9 Hz in the contralateral condition (Figure 9F), suggesting a smaller difference in this region.

For somatosensory stimulation, the baseline was 59.4 Hz in the monocular and 44.9 Hz in the binocular zone, while the response increased significantly to 175.7 Hz and 142.0 Hz, respectively, indicating strong activation. For auditory stimulation, baseline values were 42.7 Hz in the monocular and 36.6 Hz in the binocular zone, with the response reaching 182.4 Hz and 164.0 Hz, demonstrating a stable spike rate increase. While all sensory modalities increased neuronal activity relative to the baseline, contralateral visual stimulation in the monocular zone produced the highest unit rate increase, highlighting its role in V1 activation (Figure 9A, B, E, F).

4.4. Trimodal responses in V1 of mice: preferential processing of somatosensory stimuli

Our findings reveal how visual, auditory, and somatosensory stimuli are processed in the monocular and binocular regions of V1, highlighting differences in response latencies and firing rate increases. Visual stimulation shows clear latency differences. Contralateral stimulation elicited a response at 31 ms in both regions, while ipsilateral stimulation delayed responses to 50 ms (monocular) and 68 ms (binocular), suggesting weaker processing. Auditory stimulation evoked latencies of 27 ms (monocular) and 33 ms (binocular), with a secondary response at 71 ms and 77 ms, respectively. This distinct temporal profile suggests a later activation stage. Somatosensory stimulation elicited the earliest response at 18 ms (monocular) and 20 ms (binocular), reinforcing the importance of tactile cues in murine sensory processing. A second peak at 94 ms in both zones likely reflects later integrative mechanisms.

All stimuli significantly increase the firing rate, indicating V1's responsiveness beyond visual input. Contralateral visual stimulation elicited the strongest and most precise response, especially in the binocular region, aligning with its role in integrating visual information. Auditory and somatosensory stimuli evoked responses more similar to contralateral than ipsilateral visual activation, suggesting a shared influence on V1.

Our findings indicate that V1 is not exclusively visual, responding to auditory and somatosensory stimuli with structured latency patterns. Data suggest auditory and somatosensory inputs engage V1 through pathways overlapping with contralateral visual input, while ipsilateral input follows a distinct, less efficient route. This supports the hypothesis that mice rely heavily on somatosensory cues, with tactile processing showing the shortest latencies and highest firing rate, possibly due to the perception of motion induced by whisker deflection by air puff.

These results confirm that V1 exhibits a trimodal response to visual, auditory, and somatosensory stimuli, suggesting that non-visual cues contribute to sensory processing in mice, complementing traditional visual pathways.

5. Discussion

Overall, our findings confirm that V1 is primarily driven by contralateral visual input but can also be modulated by auditory and somatosensory stimuli, with notable differences in response latency and firing rate. Our observations support a growing body of literature challenging the traditional view that multisensory integration occurs exclusively in higher cortical stages following extensive processing in separate sensory areas. Recent electrophysiological and anatomical studies in humans and primates have clearly demonstrated that early cortical regions, classically regarded as unisensory, can integrate information from multiple sensory modalities at very early stages of cortical processing (Foxe & Schroeder, 2005; Schroeder & Foxe, 2005). These studies have revealed direct anatomical connections between primary auditory and visual cortices, as well as neuronal responses exhibiting characteristic feedforward processing profiles, indicating that direct and rapid mechanisms may underlie the multisensory responses observed in our investigation.

The contralateral visual stimulation primarily served as a control measure to verify the accurate positioning of our recordings in the mouse visual cortex. As expected, this type of stimulation elicited the most characteristic response in V1, confirming the proper localisation of our electrodes. A direct comparison between contralateral and ipsilateral visual stimulation revealed a clear dominance of contralateral input, with shorter response latencies and higher firing rates in both the monocular and binocular regions of V1.

However, what was particularly striking in our results was that both auditory and somatosensory stimulation evoked responses in V1 with shorter latencies than contralateral visual stimulation. This unexpected finding suggests that non-visual sensory modalities may engage V1 through not only distinct pathways but also possibly faster processing. These findings align with evidence from human studies suggesting that visual processing involves rapid and widespread activation across cortical areas. Foxe and Simpson (2002) demonstrated that activity propagates from early visual cortex to frontal regions within approximately 30 ms of stimulus onset, highlighting the existence of fast and distributed processing pathways in the human brain. The rapid activation following somatosensory and auditory stimulation raises intriguing questions about the extent of cross-modal integration in V1, particularly considering that the visual cortex is traditionally thought to be specialised for processing visual input. Although not directly investigated here, it is essential to explore whether specific oscillatory dynamics, particularly in the beta frequency range, contribute to the sensory integration observed in V1. Beta oscillations have been implicated in sensory processing across multiple cortical regions, suggesting a potential role in modulating visual perception and cross-modal interactions.

Our results indicate that theta-band activity in V1 not only exhibits the highest spectral power but also the greatest inter-trial coherence in response to repetitive contralateral visual stimulation.

Notably, ipsilateral stimulation did not evoke a theta response of comparable power or coherence in V1. This suggests that continuous exposure to visual patterns in the contralateral field may have induced plasticity in V1, akin to the findings of Zold and Shuler (2015), who reported that theta oscillations in V1 emerge with experience and may encode temporal information about relevant visual events.

An alternative explanation is that the observed theta activity in V1 was not exclusively generated locally but was instead modulated by hippocampal theta oscillations. Fournier et al. (2020) demonstrated that V1 activity can be phase-locked to theta oscillations recorded in CA1, suggesting an interaction between the hippocampus and the visual cortex during spatial tasks. Although our experiment did not involve active navigation, the animals moved on a running wheel, which may have influenced theta dynamics. Rhythmic locomotion has been associated with hippocampal theta oscillations, and it is possible that this movement contributed to the modulation of V1 activity, potentially reflecting hippocampal activity.

Although the precise origin of the pronounced theta activity observed in V1 remains undetermined, our findings suggest that these oscillations play a key role in visual processing in mice. This may be an emergent phenomenon in V1, shaped by experience with repetitive contralateral visual stimuli, as proposed by Zold and Shuler (2015), or it may reflect hippocampal modulation, consistent with Fournier et al. (2015). In either case, their strong presence and coherence highlight their relevance in structuring visual processing.

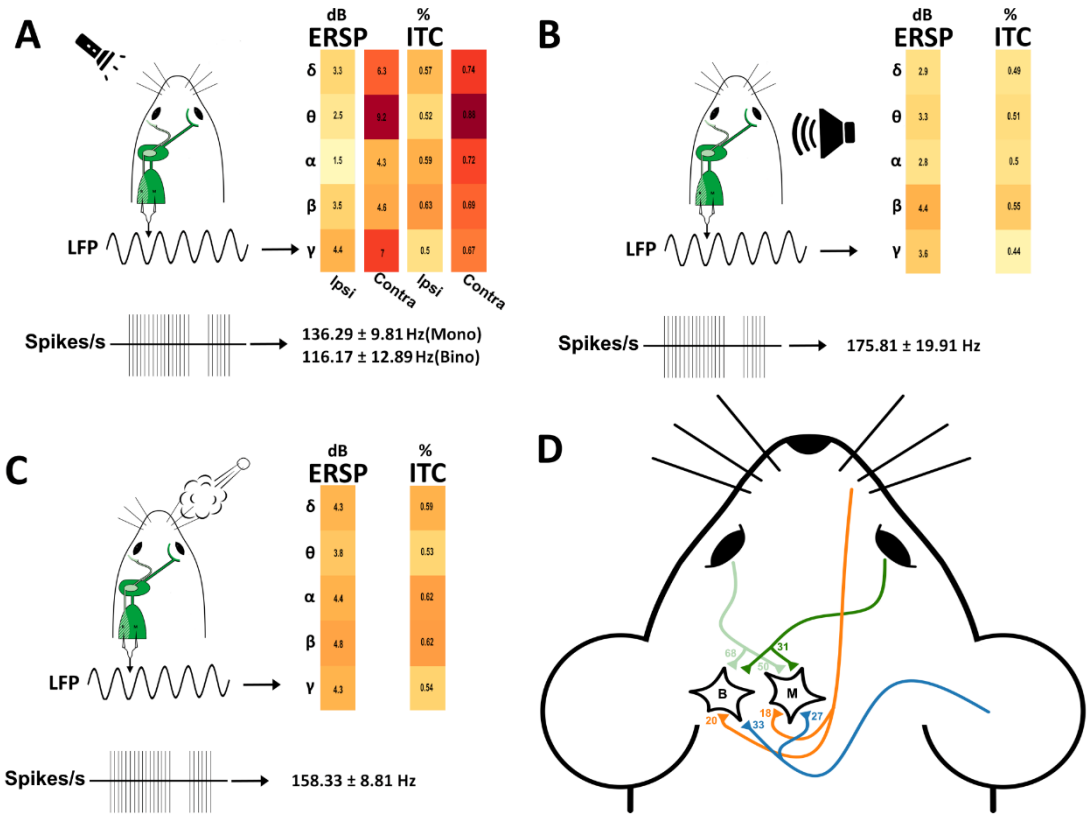

Figure 10. Differential processing of sensory stimuli in V1.

(A-C) Neural responses to ipsilateral visual, auditory, and somatosensory stimulation. Each panel illustrates the stimulus type (top), the corresponding local field potential (LFP) response, multi/single-unit firing rate, and spectral analysis of the evoked activity. Heatmaps show ERSP (dB) and inter-trial coherence (ITC) across different frequency bands (δ, θ, α, β, and γ).

(D) Example neurons from the monocular (M) and binocular (B) regions of V1 and their respective sensory inputs. Response latency diagram summarising the estimated latencies for each sensory modality. Somatosensory input exhibits the shortest response time (18 ms), auditory input activates V1 at 30 ms, while visual stimulation leads to longer latencies: 50-68 ms for ipsilateral stimulation and 31 ms for contralateral stimulation.

Other studies have investigated the role of beta waves in different cortices. For example, in the sensorimotor cortex, this frequency band plays a role in both sensory and motor integration, fulfilling higher functions, such as postural control (Baker, 2007; Lalo *et al.*, 2007). Therefore, in the V1, this frequency band could have a similar role in sensory integration to enhance environmental perception. In humans, a connection between beta waves and sensory gating has been described. It is proposed that the first stimulus generates a transient signal in a local neuronal assembly, modifying responses to subsequent stimuli, allowing inhibitory conditioning to occur (Hong *et al.*, 2008). In our mouse model reveals that ipsilateral visual stimulation and contralateral

somatosensory stimulation evokes an increase in beta wave phase coherence, similar to what occurs with somatosensory stimulation in humans (Figure 10A, C) (Cheron *et al.*, 2007), which is in line with our results. Beta waves are associated with improvements in concentration and visual perception in stroke rehabilitation, as demonstrated by Cho et al. (2015). These oscillations appear to lower the threshold for visual information transmission, facilitating visual stimuli processing during attentive states. Consequently, the present increase in beta activity may have a global role in modulating visual perception across different levels of the visual system (Wróbel, 2000; Dubey *et al.*, 2023). Except for somatosensory stimulation, ERS (Event-Related Synchronisation) alpha was the weakest, consistent with literature indicating that alpha activity tends to be suppressed during eye open state or active tasks (Toscani *et al.*, 2010). According to our results, visual stimulation is associated with greater gamma band activity (Figure 10A), reinforcing the importance of gamma oscillations in active visual processing during attentive states. These spectral patterns align with human EEG findings on intersensory switching. Vanneau et al. (2024) showed that switching modalities reduces alpha-band coherence in sensory cortices and increases frontal theta activity, reflecting less efficient processing and greater cognitive effort. Though V1 was not examined, these effects suggest attentional reconfiguration alters cortical synchrony. Our observed increase in theta coherence during repeated contralateral visual stimulation may indicate a similar mechanism in V1. The authors' priming-expectancy model supports this, as repeated inputs may enhance neural readiness and synchronization, while switching disrupts these anticipatory dynamics.

Overall, auditory stimulation evokes lower power and phase coherence compared to other modalities, with particularly low phase coherence values observed in high frequencies, such as gamma (Figure 10B). A potential concern is that the animals were unable to perceive the frequency band used for stimulation. However, from the outset we noted that C57BL/6J mice develop high-frequency hearing loss from 2-3 months of age. Heffner et al. (2001) showed that this loss begins above approximately 18 kHz and progressively worsens up to ≥30 kHz, without affecting the mid-to-low frequency range (≤10 kHz). Consequently, we ensured that our stimuli lay entirely within that mid-to-low band, and thus the high-frequency hearing loss in C57BL/6J mice should not have influenced our behavioural or temporal-processing results. This contrasts with somatosensory stimulation, where power and coherence values are generally higher. To further analyse phase consistency across trials, we examined ITC, which quantifies the stability of phase alignment across stimulus repetitions. Our results show that auditory stimulation exhibits significantly lower ITC values compared to somatosensory and visual stimulation, indicating weaker temporal synchronisation in V1 for auditory stimuli. It could be argued that our somatosensory air-puff stimulus also generates incidental auditory cues or subtle mechanical stimulation of the eyelid or eyeball, any of which might masquerade as a “visual” response in V1.

However, as detailed in the Methods, we confirmed via sound-level measurements that the air puff never exceeded 30 dB SPL against a 60-70 dB ambient background, and video monitoring revealed no systematic eyelid closure upon delivery. Thus, we minimised any cross-modal noise or tactile artefacts. Furthermore, the latency observed following the air puffas brief is consistent both with rapid transmission from the somatosensory to the visual cortex and with a subsomatosensory (non-whisker) pathway. Consequently, we cannot entirely exclude minor auditory or ocular mechanoreceptive contributions; nevertheless, these controls and the temporal signature leave open the possibility that V1 activation genuinely reflects somatosensory-system input.

Somatosensory stimulation evokes a generalised elevation in both parameters (ERSP and ITC), potentially due to the proximity of the primary somatosensory area and greater beta and gamma activity sensitivity to this stimulus type (Figure 10C) (Kisley & Cornwell, 2006). V1 significantly influences S1 activity in mice of the same strain as ours, but this influence has not been observed to be fully reciprocal, from S1 to V1 (Dinh *et al.*, 2024). The capacity of the visual cortex to respond actively to somatosensory stimulation could be explained by such connectivity (Massé *et al.*, 2016). Interestingly, early somatosensory evoked potentials (frontal N30 components) in humans increase when somatosensory stimulation is accompanied by visual observation of the stimulated hand, likely involving modulation in beta-band activity and reorganisation of ongoing oscillations (Rossi *et al.*, 2002; Cebolla & Cheron, 2015).

The beta frequency band is a gateway to multisensory plasticity. Evidence suggests beta oscillation plays a role in the primary visual cortex and can be elicited by any sensory stimulation tested, as reflected in both power and phase coherence. Cortical beta waves in awake primates are linked to phase-dependent mechanisms of short-term synaptic plasticity (Zanos *et al.*, 2018), potentially explaining the role of oscillations in attention, learning, and cortical reorganisation. Womelsdorf and Hoffman (2018) describe that synaptic plasticity (the strengthening or weakening of neuronal connections) depends on electrical stimulation synchronisation with beta oscillation phases in the brain. Stimulation during the beta depolarisation phase increases neuron sensitivity to incoming signals, promoting short-term synaptic strength changes through calcium-dependent mechanisms. These changes persist beyond the oscillations, demonstrating that phase synchronisation can influence synaptic plasticity. This finding might explain why this frequency band is present regardless of the type of stimulation (Mongillo *et al.*, 2008; Singer, 2017). However, the question remains: what would happen if visual input were suddenly lost? How would this event affect both beta frequency and synaptic plasticity?

Studies show that V1 neurons respond to visual stimuli and encode decision-making and rewards, indicating that V1 is a multisensory area integrating non-visual information (Zhang & Zador,

2023). This multisensory integration may relate to V1's heightened response to non-visual inputs. Similarly, integrating auditory and somatosensory stimuli in V1, as suggested by our findings, might demand a higher firing rate due to the complexity of interactions across sensory modalities. For instance, Meijer et al. (2017) observed V1 neurons modulating firing rates based on the temporal congruence of visual and auditory stimuli. Congruent stimuli raise firing rates, showing efficient integration, while incongruent stimuli suppress them, underlining temporal synchronisation's role in proper multisensory integration, as seen in monkeys (Wang *et al.*, 2008). A noteworthy point is how non-visual stimuli, like auditory and somatosensory inputs, evoke faster responses in V1 than visual ones. Early multisensory integration relies on a wide variety of anatomical routes (feedforward, feedback, and lateral) and occurs at multiple hierarchical levels, creating an extremely flexible and complex substrate for representing sensory information. Although it remains unclear to what extent feedforward convergence at low hierarchical levels contributes to conscious perception, it may nonetheless enhance the speed and accuracy of responses even without voluntary involvement. This diversity in space (which areas are connected), time (very short or longer latencies), and magnitude (signal strength) implies that the classic hierarchical model of "process separately first, then integrate" must be expanded to include anatomical and temporal dimensions, acknowledging that even the most "basic" sensory cortices participate in higher-order functions (Foxe & Schroeder, 2005). Research often finds auditory stimuli evoke earlier responses than visual. For example, Lohuis et al. (2024) found that V1 responds more quickly to auditory stimuli (latency ~27 ms) than to visual ones (~40 ms), aligning with our observation of shorter latencies for non-visual inputs. This may suggest V1's optimisation for efficiently integrating non-visual stimuli, essential for navigation and quick environmental responses in mice. Additionally, somatosensory stimulation elicits rapid responses in S1, within 10 ms, possibly explaining why V1 responds to somatosensory inputs in about 18 ms (Ahissar *et al.*, 2000) (Figure 10D). Other brain areas, like the auditory cortex, also show firing rate modulation in response to sensory modalities. Bizley et al. (2007) found that approximately 15% of neurons in the primary auditory cortex of ferrets are visually influenced, rising to nearly 50% in higher-level auditory areas. This underscores visual stimuli's impact on neuronal activity beyond V1, suggesting multisensory integration is not limited to one cortical region. Likewise, visual stimuli in mouse S1 modulate tactile processing through theta (4-8 Hz) and gamma (30-100 Hz) oscillations (Figure 10A, C), enhancing tactile processing under visual control. Inactivation of V1 with lidocaine reveals that V1-S1 connections are vital for oscillatory modulation, though tactile responses do not vanish, implying that subcortical circuits contribute to visual-tactile integration (Sieben *et al.*, 2013). Fu et al. (2003) observed, in the auditory cortex's caudomedial region in monkeys, that 72% of neurons responded to somatosensory stimuli, emphasising the auditory cortex's capacity for somatosensory integration.

Multisensory integration may link to neuronal plasticity facilitated by locomotion, as locomotion raises V1 neuron firing rates and improves visual stimulus encoding by reducing noise and response times. This suggests that during locomotion, V1 is better adapted to processing multisensory inputs efficiently. Though subjects could move freely, recordings were made only while stationary to ensure clear multisensory integration measurement without movement. This enhanced plasticity during locomotion may extend to auditory and somatosensory integration, supporting the idea of V1 being a highly adaptable cortical region (Stryker, 2014; Dadarlat & Stryker, 2017).

Studies on V1's inhibitory circuits suggest that multisensory integration may be modulated by specific interneuron networks. In particular, VIP interneurons (vasoactive intestinal peptide-expressing neurons), known for their role in cortical plasticity, might facilitate non-visual input integration in V1 by adjusting firing rates according to sensory stimuli (Fu *et al.*, 2015; Mesik *et al.*, 2015). Additionally, parvalbumin (PV+) interneurons contribute to sensory selection by synchronizing cortical activity through gamma oscillations (Womelsdorf *et al.*, 2014). While these inhibitory mechanisms could support multisensory processing in V1, their exact role requires further investigation.

Adaptations and perspectives on multisensory integration in V1 have deepened the understanding of multisensory integration in V1, revealing that it is not limited to visual processing but responds to a variety of sensory stimuli, including auditory and somatosensory inputs. Research on firing rates and response latencies in V1 suggests it plays a key role in efficiently integrating different sensory modalities, especially in rapid adaptation and processing contexts. This knowledge opens promising perspectives for therapeutic oscillation modulation in sensory damage conditions.

Our results position primary visual cortex not merely as a passive recipient of visual inputs but as a dynamic multisensory hub whose rapid, cross-modal engagement fundamentally shapes perceptual and behavioral outcomes. The finding that auditory and somatosensory signals reach V1 more quickly than contralateral vision highlights a mechanism for swift environmental monitoring, while the modality-specific oscillatory patterns, particularly in the theta and beta bands, suggest intrinsic temporal frameworks that gate information flow, facilitate short-term synaptic plasticity, and optimize stimulus discrimination under different attentional demands. Functionally, this implies that V1 contributes directly to sensorimotor coordination and expectation-driven processing, integrating disparate sensory streams to improve the speed and accuracy of responses. Moreover, the pervasive beta-band coherence across modalities points to a potential target for neuromodulation strategies in sensory rehabilitation and calls for a reappraisal of hierarchical models to recognize V1's role in higher-order functions such as predictive coding and cross-modal learning.

Author Contributions

A.C.T. conceived the study, designed the experiments, conducted all data collection, performed the primary data analysis, and wrote the manuscript. G.C. contributed to the experimental design and provided essential training in laboratory techniques, including the use of specialised equipment for neuronal detection and intracortical electrophysiological recordings. Their expertise was crucial for optimising data acquisition procedures and ensuring the reliability of the recorded signals. D.R. was responsible for the preprocessing and in-depth analysis of the raw signals recorded, applying advanced signal processing techniques to extract meaningful neural activity patterns. L.A. and L.R. actively participated in the discussion of results, critically evaluating the findings, identifying methodological improvements, and providing theoretical insights that helped refine the study's interpretations. L.R. and L.A. also provided overall supervision, secured funding, facilitated access to research infrastructure, guided the experimental strategy, and thoroughly reviewed and revised the manuscript to ensure scientific rigor and clarity.

CRediT Taxonomy:

Conceptualization: A.C.T. and L.R.

Methodology: A.C.T. (custom in vivo LFP setup), G.C. (specialized equipment training).

Investigation: A.C.T. (data collection).

Data Curation: D.R. (preprocessing of raw signals), A.C.T. (preprocessing of raw signals).

Formal Analysis: A.C.T. (primary data analysis), D.R. (advanced signal-processing).

Resources: G.C. (laboratory techniques, electrophysiology equipment), L.A. and L.R. (research infrastructure).

Writing - Original Draft: A.C.T.

Writing - Review & Editing: L.A., G.C. and L.R.

Visualization: D.R. and A.C.T.

Validation: L.A. and L.R. (critical evaluation of results, methodological feedback).

Supervision: L.A. and L.R.

Funding Acquisition: L.A. and L.R.

Acknowledgements

This work was made possible thanks to the generous support of the *Chaire Les Amis des Aveugles*, whose commitment to society and to improving the quality of life for visually impaired individuals has been both an inspiration and a driving force behind this research. Their support has reflected a deep dedication to scientific progress in service of a more inclusive and equitable society. We thank E. Toussaint and T. Peteau for expert technical assistance and insightful discussions. We are grateful to the Université de Mons (Belgium) for providing access to facilities and materials to carry out these experiments. We also thank the staff of the Mons Animal Facility for their excellent animal care. Finally, we gratefully acknowledge the financial support of the Belgian National Fund for Scientific Research (FNRS), the Brain and Society Foundation, and the Research Fund of the Université de Mons (Belgium).

Conflict of Interest

The authors declare that they have no conflict of interest.

Data Accessibility statement

The raw neurophysiological data supporting the findings of this study have been deposited in Zenodo and are available at https://doi.org/10.5281/zenodo.15800088

Abbreviations

AP: anteroposterior (in stereotaxic coordinates)

CEBEA: Committee on Animal Ethics and Welfare (Comité d'éthique et du bien-être animal)

dB: decibels

dB SPL: sound pressure level

EEG: electroencephalography or electroencephalogram

eLFP: evoked local field potential

ERSP: event-related spectral perturbation

ERP: event-related potential

ERS: event-related synchronization

fMRI: functional magnetic resonance imaging

Hz: hertz

ITC: inter-trial coherence

KDE: kernel density estimation

KU: Katholieke Universiteit

L: lateral (in stereotaxic coordinates)

LFP: local field potential

LNMB: Laboratory of Neurophysiology and Movement Biomechanics

MUA: multi-unit activity

ms: milliseconds

µm: micrometers

PFA: paraformaldehyde

PLLS: extrastriate visual cortex

PSTH: peri-stimulus time histogram

PV+: parvalbumin-positive cells

SEM: standard error of the mean

SUA: single-unit activity

TF: time-frequency

ULB: Université Libre de Bruxelles

UMONS: University of Mons

UK: United Kingdom

USA: United States of America

V1: primary visual cortex

VIP: vasoactive intestinal peptide-expressing neurons

Bibliography

Ahissar, E., Sosnik, R., & Haidarliu, S. (2000) Transformation from temporal to rate coding in a somatosensory thalamocortical pathway. *Nature*, 406, 302–306.

Allman, B.L. & Meredith, M.A. (2007) Multisensory Processing in "Unimodal" Neurons: Cross-Modal Subthreshold Auditory Effects in Cat Extrastriate Visual Cortex. *J. Neurophysiol.*, 98, 545-549.

Alwashmi, K., Meyer, G., Rowe, F., & Ward, R. (2024) Enhancing learning outcomes through multisensory integration: A fMRI study of audio-visual training in virtual reality. *NeuroImage*, 285, 120483.

Baker, S.N. (2007) Oscillatory interactions between sensorimotor cortex and the periphery. *Curr. Opin. Neurobiol.*, 17, 649-655.

Bastos, G., Holmes, J.T., Ross, J.M., Rader, A.M., Gallimore, C.G., Wargo, J.A., Peterka, D.S., & Hamm, J.P. (2023) Top-down input modulates visual context processing through an interneuron-specific circuit. *Cell Rep.*, 42, 113133.

Bertonati, G., Amadeo, M.B., Campus, C., & Gori, M. (2023) Task-dependent spatial processing in the visual cortex. *Hum. Brain Mapp.*, 44, 5972-5981.

Bizley, J.K., Nodal, F.R., Bajo, V.M., Nelken, I., & King, A.J. (2007) Physiological and Anatomical Evidence for Multisensory Interactions in Auditory Cortex. *Cereb. Cortex*, 17, 2172-2189.

Cambiaghi, M., Teneud, L., Velikova, S., Gonzalez-Rosa, J.J., Cursi, M., Comi, G., & Leocani, L. (2011) Flash visual evoked potentials in mice can be modulated by transcranial direct current stimulation. *Neuroscience*, 185, 161-165.

Cebolla, A.M. & Cheron, G. (2015) Sensorimotor and cognitive involvement of the beta-gamma oscillation in the frontal N30 component of somatosensory evoked potentials. *Neuropsychologia*, 79, 215-222.

Chen, G., Rasch, M.J., Wang, R., & Zhang, X. (2015) Experience-dependent emergence of beta and gamma band oscillations in the primary visual cortex during the critical period. *Sci. Rep.*, 5, 17847.

Cheron, G., Cebolla, A.M., De Saedeleer, C., Bengoetxea, A., Leurs, F., Leroy, A., & Dan, B. (2007) Pure phase-locking of beta/gamma oscillation contributes to the N30 frontal component of somatosensory evoked potentials. *BMC Neurosci.*, 8, 75.

Cho, H.-Y., Kim, K., Lee, B., & Jung, J. (2015) The effect of neurofeedback on a brain wave and visual perception in stroke: a randomized control trial. *J. Phys. Ther. Sci.*, 27, 673-676.

Dadarlat, M.C. & Stryker, M.P. (2017) Locomotion Enhances Neural Encoding of Visual Stimuli in Mouse V1. *J. Neurosci.*, 37, 3764-3775.

Davies, P.L. (2010) Middle and late latency ERP components discriminate between adults, typical children, and children with sensory processing disorders. *Front. Integr. Neurosci.*, 4.

Delorme, A. & Makeig, S. (2004) EEGLAB: an open source toolbox for analysis of single-trial EEG dynamics including independent component analysis. *J. Neurosci. Methods*, 134, 9-21.

DiCarlo, J.J., Lane, J.W., Hsiao, S.S., & Johnson, K.O. (1996) Marking microelectrode penetrations with fluorescent dyes. *J. Neurosci. Methods*, 64, 75-81.

Dinh, T.N.A., Moon, H.S., & Kim, S.-G. (2024) Separation of bimodal fMRI responses in mouse somatosensory areas into V1 and non-V1 contributions. *Sci. Rep.*, 14, 6302.

Dubey, A., Markowitz, D.A., & Pesaran, B. (2023) Top-down control of exogenous attentional selection is mediated by beta coherence in prefrontal cortex. *bioRxiv*,.

Fournier, J., Saleem, A.B., Diamanti, E.M., Wells, M.J., Harris, K.D., & Carandini, M. (2020) Mouse Visual Cortex Is Modulated by Distance Traveled and by Theta Oscillations. *Curr. Biol.*, 30, 3811-3817.e6.

Foxe, J. & Simpson, G. (2002) Flow of activation from V1 to frontal cortex in humans. *Exp. Brain Res.*, 142, 139-150.

Foxe, J.J. & Schroeder, C.E. (2005) The case for feedforward multisensory convergence during early cortical processing: *NeuroReport*, 16, 419-423.

Franklin, K.B.J. & Paxinos, G. (2019) *Paxinos and Franklin's the Mouse Brain in Stereotaxic Coordinates, Compact: The Coronal Plates and Diagrams*. Elsevier Science.

Fu, K.-M.G., Johnston, T.A., Shah, A.S., Arnold, L., Smiley, J., Hackett, T.A., Garraghty, P.E., & Schroeder, C.E. (2003) Auditory Cortical Neurons Respond to Somatosensory Stimulation. *J. Neurosci.*, 23, 7510-7515.

Fu, Y., Kaneko, M., Tang, Y., Alvarez-Buylla, A., & Stryker, M.P. (2015) A cortical disinhibitory circuit for enhancing adult plasticity. *eLife*, 4, e05558.

Galvez, R., Weible, A.P., & Disterhoft, J.F. (2007) Cortical barrel lesions impair whisker-CS trace eyeblink conditioning. *Learn. Mem.*, 14, 94-100.

Galvez, R., Weiss, C., Cua, S., & Disterhoft, J. (2009) A novel method for precisely timed stimulation of mouse whiskers in a freely moving preparation: Application for delivery of the conditioned stimulus in trace eyeblink conditioning. *J. Neurosci. Methods*, 177, 434-439.

Ghazanfar, A. & Schroeder, C. (2006) Is neocortex essentially multisensory? *Trends Cogn. Sci.*, 10, 278-285.

Grandchamp, R. & Delorme, A. (2011) Single-Trial Normalization for Event-Related Spectral Decomposition Reduces Sensitivity to Noisy Trials. *Front. Psychol.*, 2.

Hayden, D.J., Finnie, P.S.B., Thomazeau, A., Li, A.Y., Cooke, S.F., & Bear, M.F. (2023) Electrophysiological Signatures of Visual Recognition Memory across All Layers of Mouse V1. *J. Neurosci.*, 43, 7307-7321.

Heffner, R.S., Koay, G., & Heffner, H.E. (2001) Focus: Sound-Localization Acuity Changes with Age in C57BL/6J Mice. In *Handbook of Mouse Auditory Research*. CRC Press eBooks, pp. 45-50.

Helfrich, R.F. & Knight, R.T. (2019) Cognitive neurophysiology: Event-related potentials. In *Handbook of Clinical Neurology*. Elsevier, pp. 543-558.

Hong, L.E., Buchanan, R.W., Thaker, G.K., Shepard, P.D., & Summerfelt, A. (2008) Beta (∼16 Hz) frequency neural oscillations mediate auditory sensory gating in humans. *Psychophysiology*, 45, 197-204.

Javitt, D.C., Siegel, S.J., Spencer, K.M., Mathalon, D.H., Hong, L.E., Martinez, A., Ehlers, C.L., Abbas, A.I., Teichert, T., Lakatos, P., & Womelsdorf, T. (2020) A roadmap for development of neuro-oscillations as translational biomarkers for treatment development in neuropsychopharmacology. *Neuropsychopharmacology*, 45, 1411-1422.

Kaan, E. (2007) Event-Related Potentials and Language Processing: A Brief Overview. *Lang. Linguist. Compass*, 1, 571-591.

Katzner, S., Nauhaus, I., Benucci, A., Bonin, V., Ringach, D.L., & Carandini, M. (2009) Local Origin of Field Potentials in Visual Cortex. *Neuron*, 61, 35-41.

Kayser, C. & Logothetis, N.K. (2007) Do early sensory cortices integrate cross-modal information? *Brain Struct. Funct.*, 212, 121-132.

Kisley, M.A. & Cornwell, Z.M. (2006) Gamma and beta neural activity evoked during a sensory gating paradigm: Effects of auditory, somatosensory and cross-modal stimulation. *Clin. Neurophysiol.*, 117, 2549-2563.

Krebber, M., Harwood, J., Spitzer, B., Keil, J., & Senkowski, D. (2015) Visuotactile motion congruence enhances gamma-band activity in visual and somatosensory cortices. *NeuroImage*, 117, 160-169.

Lalo, E., Gilbertson, T., Doyle, L., Lazzaro, V.D., Cioni, B., & Brown, P. (2007) Phasic increases in cortical beta activity are associated with alterations in sensory processing in the human. *Exp. Brain Res.*, 177, 137-145.

Laramée, M.E., Kurotani, T., Rockland, K.S., Bronchti, G., & Boire, D. (2011) Indirect pathway between the primary auditory and visual cortices through layer V pyramidal neurons in V2L in mouse and the effects of bilateral enucleation: A1-V2L-V1 pathway in the mouse. *Eur. J. Neurosci.*, 34, 65-78.

Levakova, M., Tamborrino, M., Ditlevsen, S., & Lansky, P. (2015) A review of the methods for neuronal response latency estimation. *Biosystems*, 136, 23-34.

Lopez, L., Brusa, A., Fadda, A., Loizzo, S., Martinangeli, A., Sannita, W.G., & Loizzo, A. (2002) Modulation of flash stimulation intensity and frequency: effects on visual evoked

potentials and oscillatory potentials recorded in awake, freely moving mice. *Behav. Brain Res.*, 131, 105-114.

Makeig, S., Westerfield, M., Jung, T.-P., Enghoff, S., Townsend, J., Courchesne, E., & Sejnowski, T.J. (2002) Dynamic Brain Sources of Visual Evoked Responses. *Science*, 295, 690-694.

Marenna, S., Castoldi, V., d'Isa, R., Marco, C., Comi, G., & Leocani, L. (2019) Semi-invasive and non-invasive recording of visual evoked potentials in mice. *Doc. Ophthalmol.*, 138, 169-179.

Masimore, B., Kakalios, J., & Redish, A.D. (2004) Measuring fundamental frequencies in local field potentials. *J. Neurosci. Methods*, 138, 97-105.

Massé, I.O., Ross, S., Bronchti, G., & Boire, D. (2016) Asymmetric Direct Reciprocal Connections Between Primary Visual and Somatosensory Cortices of the Mouse. *Cereb. Cortex*, cercor;bhw239v1.

Meijer, G.T., Mertens, P.E.C., Pennartz, C.M.A., Olcese, U., & Lansink, C.S. (2019) The circuit architecture of cortical multisensory processing: Distinct functions jointly operating within a common anatomical network. *Prog. Neurobiol.*, 174, 1-15.

Meijer, G.T., Montijn, J.S., Pennartz, C.M.A., & Lansink, C.S. (2017) Audiovisual Modulation in Mouse Primary Visual Cortex Depends on Cross-Modal Stimulus Configuration and Congruency. *J. Neurosci.*, 37, 8783-8796.

Mesik, L., Ma, W., Li, L., Ibrahim, L.A., Huang, Z.J., Zhang, L.I., & Tao, H.W. (2015) Functional response properties of VIP-expressing inhibitory neurons in mouse visual and auditory cortex. *Front. Neural Circuits*, 09.

Mongillo, G., Barak, O., & Tsodyks, M. (2008) Synaptic Theory of Working Memory. *Science*, 319, 1543-1546.

Murray, M.M., Thelen, A., Thut, G., Romei, V., Martuzzi, R., & Matusz, P.J. (2016) The multisensory function of the human primary visual cortex. *Neuropsychologia*, 83, 161-169.

Oude Lohuis, M.N., Marchesi, P., Olcese, U., & Pennartz, C.M.A. (2024) Triple dissociation of visual, auditory and motor processing in mouse primary visual cortex. *Nat. Neurosci.*, 27, 758-771.

Porciatti, V., Pizzorusso, T., & Maffei, L. (2002) Electrophysiology of the postreceptoral visual pathway in mice. *Doc. Ophthalmol. Adv. Ophthalmol.*, 104, 69-82.

Rossi, S., Tecchio, F., Pasqualetti, P., Ulivelli, M., Pizzella, V., Romani, G.L., Passero, S., Battistini, N., & Rossini, P.M. (2002) Somatosensory processing during movement observation in humans. *Clin. Neurophysiol.*, 113, 16-24.

Rossi Sebastiano, A., Poles, K., Gualtiero, S., Romeo, M., Galigani, M., Bruno, V., Fossataro, C., & Garbarini, F. (2024) Balancing the Senses: Electrophysiological Responses Reveal the Interplay between Somatosensory and Visual Processing During Body-Related Multisensory Conflict. *J. Neurosci.*, 44, e1397232024.

Rugg, M.D. & Coles, M.G.H. (1996) *Electrophysiology of Mind*. Oxford University Press.

Sánchez-León, C.A., Campos, G.S.-G., Fernández, M., Medina, J.F., & Márquez-Ruiz, J. (2025) Somatodendritic orientation determines tDCS-induced neuromodulation of Purkinje cell activity in awake mice. *bioRxiv*,.

Schroeder, C.E. & Foxe, J. (2005) Multisensory contributions to low-level, 'unisensory' processing. *Curr. Opin. Neurobiol.*, 15, 454-458.

Sieben, K., Röder, B., & Hanganu-Opatz, I.L. (2013) Oscillatory Entrainment of Primary Somatosensory Cortex Encodes Visual Control of Tactile Processing. *J. Neurosci.*, 33, 5736-5749.

Singer, W. (2017) Synchronous Oscillations and Memory Formation ☆. In *Learning and Memory: A Comprehensive Reference*. Elsevier, pp. 591-597.

Stryker, M.P. (2014) A Neural Circuit That Controls Cortical State, Plasticity, and the Gain of Sensory Responses in Mouse. *Cold Spring Harb. Symp. Quant. Biol.*, 79, 1-9.

Sur, S. & Sinha, V. (2009) Event-related potential: An overview. *Ind. Psychiatry J.*, 18, 70.

Taberner, A.M. & Liberman, M.C. (2005) Response Properties of Single Auditory Nerve Fibers in the Mouse. *J. Neurophysiol.*, 93, 557-569.

Toscani, M., Marzi, T., Righi, S., Viggiano, M.P., & Baldassi, S. (2010) Alpha waves: a neural signature of visual suppression. *Exp. Brain Res.*, 207, 213-219.

Van Brussel, L., Gerits, A., & Arckens, L. (2009) Identification and localization of functional subdivisions in the visual cortex of the adult mouse. *J. Comp. Neurol.*, 514, 107-116.

Vanneau, T., Quiquempoix, M., Foxe, J.J., & Molholm, S. (2024) Neural Mechanisms of Intersensory Switching: Evidence for Delayed Sensory Processing and Increased Cognitive Effort.

Wang, Y., Celebrini, S., Trotter, Y., & Barone, P. (2008) Visuo-auditory interactions in the primary visual cortex of the behaving monkey: Electrophysiological evidence. *BMC Neurosci.*, 9, 79.

Womelsdorf, T. & Hoffman, K. (2018) Latent Connectivity: Neuronal Oscillations Can Be Leveraged for Transient Plasticity. *Curr. Biol.*, 28, R879-R882.

Womelsdorf, T., Valiante, T.A., Sahin, N.T., Miller, K.J., & Tiesinga, P. (2014) Dynamic circuit motifs underlying rhythmic gain control, gating and integration. *Nat. Neurosci.*, 17, 1031-1039.

Wróbel, A. (2000) Beta activity: a carrier for visual attention. *Acta Neurobiol. Exp. (Warsz.)*, 60, 247-260.

Xu, X., Hanganu-Opatz, I.L., & Bieler, M. (2020) Cross-Talk of Low-Level Sensory and High-Level Cognitive Processing: Development, Mechanisms, and Relevance for Cross-Modal Abilities of the Brain. *Front. Neurorobotics*, 14, 7.

Zanos, S., Rembado, I., Chen, D., & Fetz, E.E. (2018) Phase-Locked Stimulation during Cortical Beta Oscillations Produces Bidirectional Synaptic Plasticity in Awake Monkeys. *Curr. Biol.*, 28, 2515-2526.e4.

Zhang, A. & Zador, A.M. (2023) Neurons in the primary visual cortex of freely moving rats encode both sensory and non-sensory task variables. *PLOS Biol.*, 21, e3002384.

Zold, C.L. & Hussain Shuler, M.G. (2015) Theta Oscillations in Visual Cortex Emerge with Experience to Convey Expected Reward Time and Experienced Reward Rate. *J. Neurosci.*, 35, 9603-9614.